UNIVERSITAT POLITÈCNICA DE VALÈNCIA

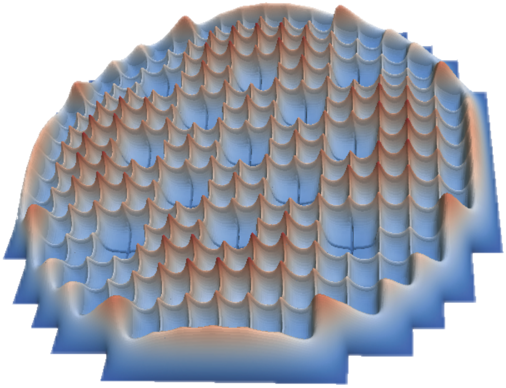

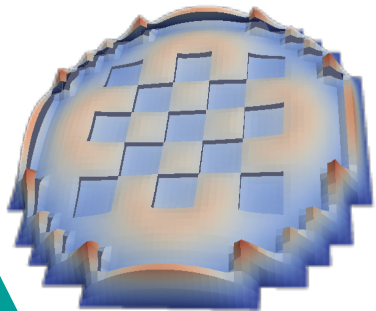

PhD Thesis

Development of a Finite Element Method for Neutron Transport Equation Approximations

Author:
Antoni Vidal

Supervisors:
Damián Ginestar
Gumersindo Verdú

València, January 2018

UNIVERSITAT
POLITÈCNICA
DE VALÈNCIA

PhD THESIS

Development of a finite element method for neutron transport equation approximations

January 2018

Author: Antoni Vidal Ferràndiz

Supervisors: Damián Ginestar Peiró
Gumersindo Verdú Martín

Ací em pariren i ací estic.
I com que he investigat certes coses,
ací les conte, ací les dic.

Abstract

The neutron transport equation describes the neutron population and the nuclear reactions inside a nuclear reactor core. First, this equation is introduced and its assumptions are stated. Then, the stationary neutron diffusion equation which is the most useful approximation of this equation, is studied. This approximation leads to a differential eigenvalue problem. To solve the neutron diffusion equation, a $h-p$ finite element method is investigated. To improve the efficiency of the method a Restricted Additive Schwarz preconditioner is implemented.

Once the solution for the steady state neutron distribution is obtained, it is used as initial condition for the time integration of the neutron diffusion equation. To test the behaviour of the method, rod ejection accidents are numerically simulated. However, a non-physical behaviour appears when a cell is partially rodded: this is, the rod cusping effect, which is solved by using a moving mesh scheme. In other words, the mesh follows the movement of the control rod. Numerical results show that the rod cusping effect is corrected with this scheme.

After that, the simplified spherical harmonics approximation, SP_N, is developed to solve the steady state problem. This approximation extends the spherical harmonics approximation, P_N, in one dimensional geometries to multidimensional geometries with strong assumptions. It improves the diffusion theory results but does not converge as N tends to infinity. The advantages and limitations of this approximation are tested on several one-, two- and three-dimensional reactors.

Finally, the spatial homogenization in the context of the finite element method is studied. Homogenization consists in replacing heterogeneous subdomains by homogeneous ones, in such a way that the homogenized problem provides fast and accurate average results. Discontinuous solutions were proposed in the Generalized Equivalence Theory. Here, a discontinuous Galerkin finite element method where the jump condition for the neutron flux is imposed in a weak sense using interior penalty terms is introduced. Also, the use of discontinuity factors for the correction of the homogenization error when using the SP_N equations is investigated.

Resumen

La ecuación del transporte neutrónico describe la población de neutrones y las reacciones nucleares dentro de un reactor nuclear. Primero, introducimos esta ecuación y las aproximaciones de la misma. Entonces, estudiamos la ecuación de la difusión neutrónica, la aproximación al transporte más utilizada. Para el caso estacionario, esta aproximación da lugar a un problema diferencial de valores propios. Para resolver la ecuación de la difusión se ha desarrollado un método de elementos finitos $h-p$. Para mejorar la eficiencia del método se ha implementado un precondicionador del tipo *Restricted Additive Schwarz*.

Una vez hemos obtenido la distribución neutrónica en estado estacionario, usamos esta solución como condición inicial para integrar la ecuación de la difusión. Para probar el comportamiento del método propuesto, hemos simulado numéricamente ejecciones accidentales de barras de control. Sin embargo, cuando una celda tiene parcialmente introducida una barra de control aparece un comportamiento no físico, el efecto *rod cusping*. Para mitigar este efecto proponemos un esquema de malla móvil, es decir, la malla sigue el movimiento de las barras de control. Los resultados muestran que el efecto *rod cusping* disminuye con el esquema expuesto.

Después, desarrollamos la aproximación de armónicos esféricos simplificados, SP_N, para simular el comportamiento del núcleo del reactor el problema en estado estacionario. Esta aproximación extiende los armónicos esféricos en geometrías unidimensionales, P_N, a geometrías multidimensionales usando fuertes aproximaciones. Las ecuaciones SP_N mejoran la teoría de la difusión pero no convergen cuando $N \to \infty$. Probamos las ventajas y limitaciones de esta aproximación en diversos reactores.

Finalmente, estudiamos la homogenización espacial en el contexto de los elementos finitos. La homogenización consiste en cambiar subdominios heterogéneos por homogéneos, de forma que el problema homogeneizado da eficientemente resultados promedios. La Teoría Generalizada de la Equivalencia para la homogenización propone factores de discontinuidad. Así pues, se ha introducido un método de elementos finitos de Galerkin discontinuo donde la condición de discontinuidad se impone de forma débil usando términos de penalización. También, hemos investigado el uso de factores de discontinuidad para la corrección de errores de homogenización cuando se usan la ecuaciones SP_N.

Resum

L'equació del transport neutrònic descriu la població de neutrons i les reaccions nuclears dins del nucli d'un reactor nuclear. Primer, introduïm aquesta equació i les seues principals aproximacions. Aleshores, estudiem l'equació de la difusió neutrònica, l'aproximació al transport neutrònic més utilitzada. Aquesta equació genera un problema diferencial de valors propis. Per a resoldre l'equació de la difusió s'ha desenvolupat un mètode d'elements finits $h-p$. Per millorar l'eficiencia del mètode s'ha implementat un precondicionador del tipus *Restricted Additive Schwarz*.

Una vegada hem obtingut la distribució neutrònica en estat estacionari, usem aquesta solució com a condició inicial per integrar l'equació de la difusió depenent del temps. Amb la voluntat de provar el comportament del mètode proposat, hem simulat numèricament expusions accidentals de barres de control. Però, quan un node té parcialment introduïda una barra de control apareix un comportament no físic, l'efecte *rod cusping*. Per mitigar aquest efecte proposem un esquema de malla mòbil, és a dir, la malla segueix el moviment de les barres de control. Els resultats numèrics mostren que l'efecte *rod cusping* disminueix amb l'esquema exposat.

Després, desenvolupem l'aproximació d'harmònics esfèrics simplificats, SP_N, per a resoldre el problema en estat estacionari. Aquesta equació estén l'aproximació d'harmònics esfèrics en geometries unidimensionals, P_N, a geometries multidimensionals usant fortes aproximacions. Les equacions SP_N milloren la teoria de la difusió però no convergeixen quan $N \to \infty$. Provem els avantatges i limitacions d'aquesta aproximació en diversos reactors.

Finalment, estudiem l'homogeneïtzació espacial en el context dels elements finits. L'homogeneïtzació consisteix en canviar subdominis heterogenis per homogenis, de forma que el problema homogeneïtzat dóna eficientment resultats mitjos. La Teoria Generalitzada de l'Equivalència per a l'homogeneïtzació proposa factors de discontinuïtat. Així, s'ha introduït un mètode d'elements finits de Galerkin discontinu on la condició de discontinuïtat per al flux neutrònic s'imposa de forma dèbil usant termes de penalització. També, hem investigat l'ús de factors de discontinuïtat per a la correcció dels errors d'homogeneïtzació quan usen les equacions SP_N.

Agraïments

Per damunt de tot, vull agrair l'ajuda, el consell i la instrucció dels meus directors de tesi Damián Ginestar i Gumersindo Verdú. Aquesta tesi és tant meua com seua.

Molt especialment vull donar les gracies a Sebastián González que des de Chalmers University of Technology ha participat en casi totes les idees que aquesta tesi presenta. Sense ell, aquesta tesi seria molt menys rigorosa matemàticament i la programació hauria costat molt més. Aquest agraïment el faig extensiu a totes les persones de la Division of Nuclear Engineering del Department of Physics de Chalmers University a Göteborg que em van ajudar durant la meua estada a Suècia.

Un especial reconeixement als companys del Institut de Matemàtica Multidisciplinar (IMM). En especial a Philip, Clara, Nikita, David, Ragab i Muaz amb els quals he compartit tantes vivències. També voldria agrair als professors Juan Carlos Cortés, Rafael Villanueva, Sergio Blanes i Dolores Roselló per acollir-me a l'institut.

De la mateixa forma, vull reconéixer a tot el personal del Departament d'Enginyeria Química i Nuclear per la seua ajuda. En especial, voldria recordar-me'n d'Amanda Carreño per la seua col·laboració en moltes investigacions presents i futures. També, voldria agrair a Sofia Carlos per haver confiat en mi per donar les meues primeres classes a la universitat.

Voldria mencionar el meu amic Ricardo Sanz per tots els cafés que hem compartit, els quals són el combustible d'aquest treball. Agraïsc el bon treball de Lorena Gil dissenyant la portada d'aquesta tesi. També, done les gracies a Susanna per compartir la nostra felicitat junts. Finalment, seria injust no mencionar la meua família, als quals dec tot el que sóc.

Antoni Vidal
anvifer2@upv.es

Contents

List of Symbols

Acronyms

ADFs Problem with assembly DFs and assembly homogenized cross sections

ANM Analytical Nodal Method

BWR Boiling Water Reactor

CPU Central processing unit

ENDF Evaluated Nuclear Data Files

EPS Eigenvalues Problem Solver

FEM Finite Element Method

FVM Finite Volume Method

GMRES Generalized Minimal Residual Method

ILU Incomplete LU descomposition

IP-FEM Interior Penalty Finite Element Method

IRAM Implicit Restarted Arnoldi Method

LU Lower Upper descomposition

LWR Light Water Reactor

NEM Nodal Expansion Method

No DFs Problem without DFs and assembly homogenized cross sections

PDFs Problem with pin DFs and pin homogenized cross section

PETSc Portable, Extensible Toolkit for Scientific computations

PWR Pressurized Water Reactor

RDFs Problem with reference DFs and reference homogenized cross sections

RXSs Problem without DFs and assembly homogenized cross sections

SLEPc Scalable Library for Eigenvalue Problem computations

SPH Superhomogenization procedure

SpMVs Sparse Matrix-Vector multiplications

VVER Water-Water Energetic Reactor

Symbols

$\bar{\varepsilon}$ Mean relative error

β Total fraction of delayed neutrons

β_p Fraction of delayed neutrons of group p

χ Fision spectrum

Δk_{eff} Multiplicative factor error in (pcm)

$\Delta\lambda$ Eigenvalue error in (pcm)

Γ Problem frontier

Γ_k Subdomain boundary which is part of the problem frontier

λ Eigenvalue

λ_p Neutron precursors decay constant

$\mathcal{M}$ Neutron production differential operator

$\mathcal{N}_i$ Shape function of the i-th support point

μ Cosine of angle of the neutron velocity

μ_0 Cosine of angle scattering

ν Mean number of born neutron per fission

Ω Problem domain

Ω_k Mesh subdomain or cell

ϕ Scalar neutron flux

ϕ_g Scalar neutron flux of group g

ψ	Angular neutron flux
σ	Microscopic cross section
Σ_a	Macroscopic absorption cross section
Σ_f	Macroscopic fission cross section
Σ_r	Macroscopic removal cross section
Σ_s	Macroscopic scattering cross section
Σ_t	Macroscopic total cross section
θ_e	Symmetrizing coeficient
$\varepsilon_{\max}$	Maximum absolute error
φ	Test function
$\vec{\Omega}$	Direction of the neutron
$\vec{J}$	Net current vector
$\vec{r}$	Spatial position coordinates
$\lvert\mathbf{J^k}\rvert$	Jacobian of the afine transformation
D	Diffusion coefficient
E	Energy of the neutron
$f(E)$	Energy dependent spectral weighting function
f_e	Discontinuity factor
f_{ins}	Volume fraction of insertion of the rod in the cell
h_k	Adimensional cell size
$J^{\pm}$	Neutron partial current
J_n	Net current through direction n
$J_n^{\pm}$	Partial currents through direction n
k_{eff}	Multiplicative factor or fundamental eigenvalue
l_I^p	Lagrange basis polynomial of degree p

N	Neutron density probability distribution
N_0	Avogadro's number, 6.022×10^{23}
N_d	Density number
P	Preconditioner
p	Polynomial degree of the shape functions of the finite element method
P_{RAS}	Restricted Aditive Schwarz preconditioner
P_D	Jacobi preconditioner
P_n	Legendre polynomial of order n
P_V	Vertices preconditioner
P_{VEF}	Vertices, edges and faces preconditioner
q_{ex}	Emission density of neutrons of an external source
R	Reaction rate
R_k	Restriction operator
RMS	Root Mean Square
RPP	Relative power peaking error
S	Schur Complement matrix
s_e	Penalty coeficient
u_n^g	Pseudo flux moment n of energy group g
V_t	Total volume of the problem
$\mathcal{L}$	Neutron loss differential operator
C_p	Concentration of delayed neutron precursors of group p
G	Number of neutron energy groups
K	Number of finite element cells
N_{DoFs}	Number of degrees of freedom
N_p	Number of precursor groups

1 Introduction

1.1 Motivation and Objectives

In thesis, it is proposed the development of a high order finite element method to solve the neutron transport equation. Different approximation to this equation are developed as the diffusion equation and the simplified spherical harmonics. A fast and accurate solution of these equations is basic for the design and safe operation of nuclear reactor and other nuclear system.

The thesis objectives can be summarized as follows.

1. To implement a finite element code with $h-p$ adaptivity to solve the diffusion equation in steady state. The code must be able to deal with multidimensional geometries of all kind.
2. To optimize the resolution of the eigenvalue through the study of different refinement strategies and the application of different eigenvalue solvers.
3. To solve the time dependent diffusion equation.
4. To develop approximations of the neutron transport equation with a higher angular discretization as the simplified spherical harmonics equation.
5. To study pin-wise and assembly-wise spatial homogenization techniques in the context of the finite element method.

1.2 Thesis Outline

The thesis dissertation is organized in 7 chapters and 2 appendices. Next chapter is dedicated to introduce the neutron transport equation and the basic neutron reactor physics concepts and magnitudes. Then, the stationary neutron diffusion equation is studied in Chapter 3, the most used approximation of this equation. To solve the neutron diffusion equation a $h-p-$ finite element method is investigated. Also, to improve the efficiency of the method a Restricted Additive Schwarz preconditioner is developed in Section 3.8.

In Chapter 4 the solution for the steady state neutron distribution is used as initial condition for the time integration of the neutron diffusion equation. To test the behaviour of the time integration, rod ejection accidents are numerically simulated. However, a non-physical behaviour appears when a cell is partially rodded, the rod cusping effect, which is solved using a moving mesh scheme. Numerical results show that the rod cusping effect is corrected with this scheme. Chapter 5 develops the simplified spherical harmonics approximation, SP_N, to solve the steady state problem. This approximation extends the spherical harmonics approximation, P_N, in one dimensional geometries to multidimensional geometries with strong assumptions. The advantages and limitations of this approximation are tested on several one-, two- and three-dimensional reactors.

Chapter 6 is devoted to the spatial homogenization in the context of the finite element method. Homogenization consists in replacing heterogeneous subdomains by homogeneous ones, in such a way that the homogenized problem provides fast and accurate average results. Discontinuous solutions were proposed in the Generalized Equivalence Theory. Here, a discontinuous Galerkin finite element method where the jump condition for the neutron flux is imposed in a weak sense using interior penalty terms is introduced. Also, the use of discontinuity factors for the correction of the homogenization error when using the SP_N equations is investigated. Finally, the main conclusions and results of the dissertation are summarized in Chapter 7.

Appendix A develops the analytic solution of a bidimensional homogeneous reactor in the diffusion approximation with two energy groups. Finally, Appendix B is dedicated to compile all the information related to the numerical benchmarks used along the dissertation.

2

The Neutron Transport Equation

The nuclear physics inside a nuclear reactor core is governed by the transport of neutrons and the interactions between neutrons and nucleus. Therefore, the design, analysis and control of a nuclear reactor requires solving the neutron transport equation in an approximated manner. The solution of the neutron transport equation determines the neutron distribution in the reactor and hence, it permits to validate and verify the safety parameters.

The root of transport theory goes back more than a century to the Boltzmann equation, first formulated for the study of the kinetic theory of gases. Until the 1940s with the development of nuclear chain reactors the interest arose in solving neutron particle transport problems in the broad range of geometrical configurations found in nuclear reactors and radiation shielding applications.

The behaviour of a nuclear reactor is modelled by means of the neutron distribution in the reactor core as a function depending on the neutron position, direction, energy and time. Within the transport theory the neutrons are considered classical point particles in the sense that they are zero dimensional points determined by means of their position and its velocity. In other words, particles are considered points that travel in straight lines between collisions and neutron-neutron interactions are neglected.

There are mainly two types of calculations associated with the neutron transport equation. First, static calculations to determine the Lambda modes associated with a given configuration of the reactor. This is a generalized eigenvalue problem associated with a differential operator with given boundary conditions. The determination of the fundamental mode allows us to describe the behaviour of the reactor in steady state. The second type of calculations are those made for

the determination of a transient from a perturbation made on a stationary configuration of the reactor, using for that the time dependent neutron transport equation.

This chapter is organized as follows. We start with the cross sections definition in Section 2.1. Then, the elemental magnitudes in reactor physics are introduced in Section 2.2. After that, we present the time dependent transport equations in its integro-differential form in Section 2.3. Finally, Section 2.4 derives the steady state neutron transport equation and the criticality problems.

2.1 Cross Section Definition

Before the transport equation can be stated, the probability distribution laws governing the neutrons and nuclei iteration must be reviewed. The probability of a nuclear reaction taking place is expressed in terms of *microscopic cross sections* as

$$\sigma \equiv \frac{R}{n\mathrm{v}N_n} \tag{2.1}$$

which denotes the probable reaction rate R, for n neutrons travelling with speed v in a material with N_n nucleus per unit volume. The units of σ are area that refers to the concept of cross-sectional area of interaction presented to the neutron by the nucleus for a particular reaction process. However, this cross-sectional area can be much greater than the geometric cross section of the nucleus. Microscopic cross section are usually measured in barns for historical reasons, 1 barn = 10^{-24} cm^2 (Stacey, 2007).

The *macroscopic cross section* is defined as

$$\Sigma \equiv N_d\sigma = \frac{\rho N_0}{A}\sigma\,, \tag{2.2}$$

where N_d is the density number, $N_0 = 6.022 \times 10^{23}$ is the Avogadro's number, ρ is the material density and A is the atomic number. The macroscopic cross section represents the probability of iteration of a neutron per unit path length, and thus, it has units of $1/cm$. From now on, all cross section mentioned in this thesis are macroscopic avoiding the details of the interaction process inside the core. Moreover, the nuclear reactions are considered instantaneous because their real duration is less than 10^{-6}s (Demazière, 2014). The only exception of any practical significance is in the fission reaction in which a small fraction of the fission products decay by neutron emission after some delay.

The fission cross section, $\Sigma_f(\vec{r}, E', t)$, is a measure of the probability that a neutron and a nucleus interact to form a compound nucleus which then splits into two lighter nuclei, called fission fragments. Such splitting is accompanied by the release of new neutrons and γ rays. It is assumed that the neutrons are isotropically emitted. The probability that a compound nucleus will be formed is greatly enhanced if the relative energy of the neutron and the original nucleus, plus the reduction in the nuclear binding energy, corresponds to the difference in energy of the ground state and an excited state of the compound nucleus, so that the energetics are just right for formation of a compound nucleus in an excited state (Stacey, 2007).

The neutrons shortly emitted after the scission ($\sim 10^{-7}$) are called prompt neutrons. The fission fragments are usually neutron-rich and in excited states and thus decay into less excited atoms via β^- decay or γ emission. Such neutrons emitted by β^- decay of the fission fragments are called delayed neutrons and the corresponding fission fragments are named neutron precursors. Many precursors of delayed neutrons exist, each having its own neutron decay constant, λ_p. Usually, similar precursors, in terms of their decay constant, are grouped into several groups described by their average properties. Six groups are typically used. The fraction of delayed neutron, β_p, represents the number of delayed neutron belonging to group p divided by the total number of neutrons emitted. The total fraction of delayed neutrons, β, is given by

$$\beta = \sum_{p=1}^{N_p} \beta_p \,. \tag{2.3}$$

This delayed fraction is small, ranging from 0.0065 for U-235 to about 0.0021 for Pu-239. χ indicates the spectrum of the neutrons produced by fission such that $\chi \mathrm{d}E$ indicates the fraction of neutrons emitted with and energy between E and $E + \mathrm{d}E$. This spectrum fulfils,

$$\int_0^\infty \mathrm{d}E\, \chi(E) = 1 \tag{2.4}$$

Finally, $\nu(E)$ represents the average number of neutrons emitted per fission.

The absorption cross section, $\Sigma_a(\vec{r}, E, t)$, is the probability that a neutron gets captured by a nucleus. The most relevant of this nuclear reactions are the radiative capture where only a gamma ray is emitted. Also, the absorption of a neutron that begins a fission reactor is taken into account in this cross section.

The scattering reaction occurs when a neutron collides on a nucleus and changes its energy and/or direction after the collision. For scattering cross section, $\Sigma_s(\vec{r}, \vec{\Omega}\cdot$

$\vec{\Omega}',\, E \to E',\, t)$, both elastic and inelastic cross sections exist. Elastic scattering interactions are governed by the laws of conservation of momentum and kinetic energy. Inelastic scattering results in a loss of kinetic energy of the neutron due to an increase of the energy state of the nucleus.

Based on the definitions given above, the *total cross section* is introduced as

$$\Sigma_t(\vec{r},\, E,\, t) = \Sigma_a(\vec{r},\, E,\, t) + \int\limits_{(4\pi)} \mathrm{d}\vec{\Omega}' \int\limits_{0}^{\infty} \mathrm{d}E'\, \Sigma_s(\vec{r},\, \vec{\Omega}\cdot\vec{\Omega}',\, E \to E',\, t)\,, \qquad (2.5)$$

where Σ_t is the probability of a neutron to have an iteration of any kind with a nucleus if it travels one centimetre.

The energy dependence of cross section is very strong. As reasonably low energies of incident neutrons, cross sections are frequently quite smooth in energy. However as the neutron energy increases, the cross section frequently are dominated by resonance peaks that results from unstable states of the compound nucleus formed by the target nuclide and the neutron. The resonances may be scattering , capture and fission depending on weather the state decays by neutron or gamma emission or results in a fission (Lewis and Miller, 1984).

The complex behaviour of neutron cross sections cannot be calculated from first principles using properties of the nucleus (Weinberg, Wigner, and Wigner, 1958). Hence, data must be determined empirically as a function of energy for each nuclide and for each reaction. The determination of the neutron cross sections has required years of effort in measuring, calculating and evaluating cross sections for hundreds of isotopes. These efforts are collected in *evaluated nuclear data files* (ENDF) containing sections of all reactions of importance, as well as energy and angular distributions of the resulting secondary particles. Nowadays, the most comprehensive compilation of experimental results is EXFOR computer library (McLane, 2000) that contains the major evaluated nuclear data files: United States Evaluated Nuclear Data File (END/B-VII.1), Joint Evaluated File of NEA Countries (JEFF-3.2), Japanese Evaluated Nuclear Data Library (JENDL-4.0) and Russian Evaluated Nuclear Data File (BROND-3.1), among others.

2.2 Elementary magnitudes in reactor physics

The definition of the distribution of neutrons requires seven independent variables: three spatial coordinates, $\vec{r}$, two angles specifying the particle direction of travel, $\vec{\Omega}$, the particle energy, E, or the particle velocity, v, and time t.

The *neutron density probability distribution*, $N(\vec{r},\, E,\, \vec{\Omega},\, t)$, is defined such that $N(\vec{r},\, E,\, \vec{\Omega},\, t)\, \mathrm{d}V\, \mathrm{d}\vec{\Omega}\, \mathrm{d}E$ is the expected number of neutrons in a differential volume element $\mathrm{d}V$ about $\vec{r}$ travelling in the cone of directions $\mathrm{d}\vec{\Omega}$ around $\vec{\Omega}$ with energies between E and $E+\mathrm{d}E$ at time t. For most purposes, it is more economical to formulate the transport problems in terms of the *angular flux*,

$$\psi(\vec{r},\, E,\, \vec{\Omega},\, t) \equiv \upsilon N(\vec{r},\, E,\, \vec{\Omega},\, t)\,. \tag{2.6}$$

The angular flux can be defined as the total path travelled during $\mathrm{d}t$ by all particles in the differential phase space volume $\mathrm{d}V\, \mathrm{d}\vec{\Omega}\, \mathrm{d}E$.

Usually, the direction of the particles is not important in the calculation of reaction rates. Then, the *scalar flux* is defined as the integral of ψ over all directions,

$$\phi(\vec{r},\, E,\, t) = \int\limits_{(4\pi)} \mathrm{d}\vec{\Omega}\, \psi(\vec{r},\, \vec{\Omega},\, E, t)\,. \tag{2.7}$$

The scalar neutron flux can be interpreted as the number of neutrons per unit area, energy and time. However, it does not represent a flow of neutrons through a surface, it corresponds to the total length travelled by all neutrons per unit time and volume. As the macroscopic cross section, $\Sigma_\alpha(\vec{r},\, E)$ is defined as the probability per unit path length that a particle of energy E will cause a reaction of type α. The total number of reactions per unit time in $\mathrm{d}V\, \mathrm{d}E\, \mathrm{d}\vec{\Omega}$ is

$$R = \Sigma_\alpha(\vec{r},\, E,\, t)\phi(\vec{r},\, E,\, \vec{\Omega},\, t)\,. \tag{2.8}$$

The *net current vector* is defined as

$$\vec{J}(\vec{r},\, E,\, t) \equiv \int\limits_{(4\pi)} \mathrm{d}\vec{\Omega}\, \vec{\Omega}\, \psi(\vec{r},\, \vec{\Omega},\, E,\, t)\,. \tag{2.9}$$

For a given position, energy and time the product

$$J_n(\vec{r},\, E,\, t) \equiv \vec{n} \cdot \vec{J}(\vec{r},\, \vec{\Omega},\, E,\, t) = \int\limits_{(4\pi)} \mathrm{d}\vec{\Omega}\, (\vec{n} \cdot \vec{\Omega})\psi(\vec{r},\, \vec{\Omega},\, E,\, t) \tag{2.10}$$

gives the net number of particles crossing per unit area of surface per unit time, per unit energy and in the positive direction of the normal vector. In some situations it is desirable to divide the current into *partial currents* of neutrons crossing the surface in the positive and negative directions,

$$J_n(\vec{r},\, E,\, t) = J_n^+(\vec{r},\, E,\, t) - J_n^-(\vec{r},\, E,\, t)\,, \tag{2.11}$$

where

$$J_n^+ = \int_{\vec{\Omega}\cdot\vec{n}>0} \mathrm{d}\vec{\Omega}\, \vec{n}\cdot\vec{\Omega}\, \psi\,, \tag{2.12}$$

$$J_n^- = \int_{\vec{\Omega}\cdot\vec{n}<0} \mathrm{d}\vec{\Omega}\, \vec{n}\cdot\vec{\Omega}\, \psi\,, \tag{2.13}$$

2.3 Neutron transport equation

Once we have described the main magnitudes in the neutron transport physics we can study the *neutron transport equation*. This equation is stated as the balance of the neutron distribution in a control volume. In this way, the increment of the neutron distribution is equal to the sum of emission densities in the control volume (Lewis and Miller, 1984),

$$\begin{aligned}\frac{1}{\mathrm{v}}\frac{\partial\psi}{\partial t} =& -\vec{\Omega}\cdot\vec{\nabla}\,\psi(\vec{r},\,E,\,\vec{\Omega},\,t) - \Sigma_t(\vec{r},\,E,\,t)\psi(\vec{r},\,E,\vec{\Omega},\,t) + q_{\text{ex}}(\vec{r},\,E,\,\vec{\Omega},\,t)\\ &+ \int_0^\infty dE' \int_{(4\pi)} \mathrm{d}\vec{\Omega}'\,\Sigma_s(\vec{r},\,E'\to E,\,\vec{\Omega}'\cdot\vec{\Omega},\,t)\,\psi(\vec{r},E',\vec{\Omega}',t)\\ &+ (1-\beta)\chi(E)\int_{(4\pi)} \mathrm{d}\vec{\Omega}' \int_0^\infty \mathrm{d}E'\nu\Sigma_f(\vec{r},\,E',\,t)\,\psi(\vec{r},\,E',\,\vec{\Omega}',\,t)\\ &+ \sum_{p=1}^{N_p}\lambda_p\frac{\chi(E)}{4\pi}\mathcal{C}_p(\vec{r},\,t).\end{aligned} \tag{2.14}$$

The left hand side, $\frac{1}{\mathrm{v}}\frac{\partial\psi}{\partial t}$, represents the rate of increment in the neutron distribution. The first term on the right hand of the equation, $\vec{\Omega}\cdot\vec{\nabla}\,\psi(\vec{r},E,\vec{\Omega},t)$, takes into account the neutron advection flowing out the phase control volume, where $\vec{\Omega}$ is the unit vector denoting the direction of the going neutrons. The second term, $\Sigma_t(\vec{r},E,t)\,\psi(\vec{r},\,E,\,\vec{\Omega},\,t)$, describes the rate at which neutrons are absorbed or scattered to other energies or directions. $q_{\text{ex}}(\vec{r},E,\vec{\Omega},t)$ denotes the emission density of neutrons of a possible external source. The fourth term describes the neutrons introduced into the volume element by scattering from other energies and directions. The fifth term indicates the number of prompt neutrons introduced into the volume element by fission processes that assumes isotropic fission distribution. The quantity of delayed neutrons appearing in the volume from the precursors decay is taken into account by the last term.

The concentration of delayed neutron precursors in each precursors group p satisfies the following balance equation

$$\frac{\partial \mathcal{C}_p}{\partial t}(\vec{r},t) = \beta_p \int_0^{\infty} dE \int_{(4\pi)} \mathrm{d}\vec{\Omega}\, \nu\Sigma_f(\vec{r},E,t)\, \psi(\vec{r},E,\vec{\Omega},t) - \lambda_p \mathcal{C}_p(\vec{r},t), \tag{2.15}$$

where ν is the average number of neutrons arising from fission, and $p = 1, \ldots, N_p$.

The transport equation is an integro-differential equation in both the steady-state and time dependent forms. The time dependent solution is unique and non-negative provided all cross sections, sources and non negative initial and boundary condition (Lewis and Miller, 1984).

Now, the energy variable is discretized into G intervals as show in Figure 2.1 that states the multigroup formalism. In this Figure, $E_G = 0$ and E_0 is a sufficiently large energy. The neutrons in group g are taken to be just those with energies between E_g and E_{g-1} where $E_g < E_{g-1}$. Our objective is to obtain the transport equation in terms of the group angular flux defined as,

$$\psi_g(\vec{r},\vec{\Omega}) = \int_{E_g}^{E_{g-1}} \mathrm{d}E\, \psi_g(\vec{r},\, \vec{\Omega},\, E)\,. \tag{2.16}$$

We suppose that within each energy group the angular flux can be approximated as the product of a known normalization function of energy $f(E)$ and the group flux

$$\psi(\vec{r},\, \vec{\Omega},\, E) \approx f(E)\psi_g(\vec{r},\, \vec{\Omega})\,, \tag{2.17}$$

where the energy-dependent spectral weighting function $f(E)$ is normalized as

$$\int_{E_g}^{E_{g-1}} \mathrm{d}E f(E) = 1\,. \tag{2.18}$$

It has to be emphasized that the quantities that need to be preserved when transforming the neutron transport equation with the multi-group formalism are the

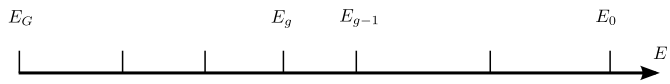

Figure 2.1: Discretization of the energy into G energy groups.

reaction rates and neutron currents. In a similar way, the spatial homogenization studied in Chapter 6 aims to preserve the same quantities. If equation (2.14) is integrated for each energy group, the multigroup neutron transport equation is written as

$$\begin{aligned}\frac{1}{v_g}\frac{\partial \psi_g}{\partial t} = &- \vec{\Omega}\cdot\vec{\nabla}\,\psi_g(\vec{r},\,\vec{\Omega},\,t) - \Sigma_{tg}(\vec{r},\,t)\psi_g(\vec{r},\vec{\Omega},\,t) + q_{\text{ex},\,g} \\ &+ \sum_{g'=1}^{G}\int_{(4\pi)} \Sigma_{s,\,g'\to g}(\vec{r},\,\vec{\Omega}'\cdot\vec{\Omega},\,t)\,\psi_g(\vec{r},\vec{\Omega}',t)\,d\vec{\Omega}' \\ &+ \sum_{g'=1}^{G}(1-\beta)\frac{\chi_g}{4\pi}\nu_g\Sigma_{fg'}(\vec{r},t)\phi_{g'}(\vec{r},\,t) \\ &+ \sum_{p=1}^{N_p}\lambda_p\frac{\chi_g}{4\pi}\mathcal{C}_p(\vec{r},\,t)\end{aligned} \tag{2.19}$$

and the concentration on neutron precursors

$$\frac{\partial \mathcal{C}_p}{\partial t}(\vec{r},t) = \beta_p\sum_{g'=1}^{G}\int_{(4\pi)}\mathrm{d}\vec{\Omega}\,\nu\Sigma_{fg'}(\vec{r},\,t)\,\psi_{g'}(\vec{r},\,\vec{\Omega},\,t) - \lambda_p\mathcal{C}_p(\vec{r},\,t)\,. \tag{2.20}$$

The energy integrated quantities are defined as

$$\phi_g(\vec{r},\, t) = \int_{E_g}^{E_{g-1}} \phi(\vec{r},\, E,\, t)\,\mathrm{d}E\,, \tag{2.21}$$

$$\frac{1}{\mathrm{v}_g(E)} = \int_{E_g}^{E_{g-1}} \frac{1}{\mathrm{v}(E)} f(E)\,\mathrm{d}E\,, \tag{2.22}$$

$$\Sigma_{tg}(\vec{r},\, \vec{\Omega},\, t) = \int_{E_g}^{E_{g-1}} \Sigma_t(\vec{r},\, E,\, t) f(E)\,\mathrm{d}E\,, \tag{2.23}$$

$$\Sigma_{s,\,g'\to g}(\vec{r},\, \vec{\Omega}'\cdot\vec{\Omega},\, t) = \int_{E_g}^{E_{g-1}} \mathrm{d}E \int_{E'_g}^{E_{g'-1}} \mathrm{d}E' \Sigma_s(\vec{r},\, E'\to E,\, \vec{\Omega}'\cdot\vec{\Omega},\, t) f(E)\ , \tag{2.24}$$

$$\nu_g \Sigma_{f,\,g}(\vec{r},\, t) = \int_{E_g}^{E_{g-1}} \nu\Sigma_f(\vec{r},\, E,\, t) f(E)\,\mathrm{d}E\,, \tag{2.25}$$

$$\chi_g = \int_{E_g}^{E_{g-1}} \chi(E)\,\mathrm{d}E\,, \tag{2.26}$$

$$q_{\mathrm{ex},\,g} = \int_{E_g}^{E_{g-1}} q_{\mathrm{ex}} f(E)\,\mathrm{d}E\,. \tag{2.27}$$

Before multigroup transport calculations can be carried out, values of the multigroup cross sections $\Sigma_{a\,g}$, $\nu\Sigma_{f\,g}$ and $\Sigma_{s\,gg'}$ must be available. As indicated by the definitions in equations (2.22) through (2.25). However, the evaluation of group cross sections requires that both the detailed energy dependence of the cross section and the spectral weighting function $f(E)$ be known. These date are given in the evaluated data files. In this way, $f(E)$ is guessed depending on the characteristics of the system under analysis and the computational models that are available for the description of that system. Usually a guess of the neutron flux spectrum is chosen as the normalization function where three energetic zones are distinguished, fission energies, slowing-down energies and decimalisation energies; (Demazière, 2014). The exact energy dependent spectral weighting function used is outside the scope of this thesis.

2.3.1 Boundary Conditions

To solve the Partial Differential Equation (PDE) given by the transport equation (2.14) or equation (2.19) in the domain V surrounded by the surface Γ, boundary conditions are needed to be known a priori. Specifically, the flux distribution entering V across $\vec{\Omega}$ or at least a relation between the incoming and outgoing fluxes must be known. The most usual boundary condition are summarized as:

- *Vacuum boundary or free surface boundary conditions* are expressed

$$\psi(\vec{r}_B, \vec{\Omega}_{\text{in}}) = 0, \qquad \text{for } \vec{\Omega}_{\text{in}} \cdot \vec{n} < 0,\ \vec{r}_B \in \Gamma\,. \tag{2.28}$$

- *Albedo boundary conditions*: The incoming flux on the boundary is equal to a known isotropic albedo coefficient α times the outgoing flux in the direction corresponding to a spectral reflection.

$$\psi(\vec{r}_B, \vec{\Omega}_{\text{in}}) = \alpha\, \psi(\vec{r}_B, \vec{\Omega}_{\text{out}}), \qquad \text{for } \vec{\Omega}_{\text{in}} \cdot \vec{n} < 0,\ r_B \in \Gamma\,, \tag{2.29}$$

  where, if the outgoing direction $\vec{\Omega}_{\text{out}}$ is represented as a sum between its component normal to the surface at the boundary point and a tangential component by the incidence angle $\vec{\Omega}_{\text{out},\,\perp}$, i.e.

$$\vec{\Omega}_{\text{out}} = |\vec{\Omega}_{\text{out}} \cdot \vec{n}|\, \vec{n} + \vec{\Omega}_{\text{out},\,\perp}\,, \tag{2.30}$$

  the ingoing direction, $\vec{\Omega}_{\text{in}}$, is then given as

$$\vec{\Omega}_{\text{in}} = -|\vec{\Omega}_{\text{out}} \cdot \vec{n}|\vec{n} + \vec{\Omega}_{\text{out},\,\perp}\,. \tag{2.31}$$

- *Specular reflective boundary conditions* can be defined as

$$\psi(\vec{r}_B, \vec{\Omega}_{\text{in}}) = \psi(\vec{r}_B, \vec{\Omega}_{\text{out}}) \qquad \text{for } \vec{\Omega}_{\text{in}} \cdot \vec{n} < 0,\ r_B \in \Gamma\,. \tag{2.32}$$

  This boundary condition is an special case of albedo boundary conditions with $\alpha = 1$, as all outgoing particles are reflected back like a perfect mirror.

- *White boundary conditions*: All neutrons leaving the system through the boundary are isotropically emitted back into the domain.

$$\psi(\vec{r}_B, \vec{\Omega}_{\text{in}}) = \frac{\int\limits_{\vec{\Omega}\cdot\vec{n}>0} \mathrm{d}\vec{\Omega}\, |\vec{\Omega} \cdot \vec{n}|\, \psi(\vec{r}_B, \vec{\Omega})}{\int\limits_{\vec{\Omega}\cdot\vec{n}>0} \mathrm{d}\vec{\Omega}\, |\vec{\Omega} \cdot \vec{n}|} = \frac{J^+(\vec{r}_B)}{\pi}, \tag{2.33}$$
$$\text{for } \vec{\Omega}_{\text{in}} \cdot \vec{n} < 0,\ r_B \in \Gamma\,.$$

2.4 Steady State Neutron Transport Equation

A reactor is said to be critical if there is a self-sustaining time-independent chain reaction in the absence of external sources of neutrons, $q_{\text{ex}} = 0$. If such an equilibrium cannot be established, the asymptotic distribution of neutrons, called the fundamental mode, will not be in steady state and will either increase or decrease exponentially. The system is then supercritical or subcritical, respectively.

The k_{eff} form of the criticality problem or the lambda modes problem is written dividing the fission source of neutrons by λ. Hence, the multigroup neutron transport equation in steady state can be written

$$\begin{aligned}
&\vec{\Omega} \cdot \vec{\nabla}\, \psi_g(\vec{r},\, \vec{\Omega}) + \Sigma_{tg}(\vec{r})\, \psi_g(\vec{r}, \vec{\Omega}) \\
&= \sum_{g'=1}^{G} \int_{(4\pi)} \mathrm{d}\vec{\Omega}'\, \Sigma_{s,\, g' \to g}(\vec{r},\, \vec{\Omega}' \cdot \vec{\Omega})\, \psi_{g'}(\vec{r}, \vec{\Omega}') \\
&+ \frac{1}{\lambda} \sum_{g'=1}^{G} \chi_g \int_{(4\pi)} \mathrm{d}\vec{\Omega}' \nu_g \Sigma_{f g'}(\vec{r})\, \psi_{g'}(\vec{r},\, \vec{\Omega}')\,, \\
&\qquad\qquad\qquad\qquad\qquad\qquad g = 1,\, \ldots,\, G.
\end{aligned} \tag{2.34}$$

Equation (2.34) is a differential eigenvalue problem, where λ is the eigenvalue and $(\psi_1,\, \psi_2,\, \ldots,\, \psi_G)$ is the eigenvector. The fundamental eigenvalue, the one with the largest magnitude or k_{eff}, shows the criticality of the reactor core and its corresponding eigenfunction describes the steady state neutron distribution in the core. Next sub-critical eigenvalues and their corresponding eigenfunctions are interesting because they have been successfully used to develop modal methods to integrate the time dependent neutron diffusion equation in Miró et al., (2002). Also the sub-critical modes have been used to classify BWR instabilities by March-Leuba and Rey, (1993) and Ginestar et al., (2011).

Clearly the system is critical if this largest eigenvalue is $k_{\text{eff}} = 1$. A value $k_{\text{eff}} < 1$ implies that the system is subcritical because not enough neutrons are produced by fission. In the other way, $k_{\text{eff}} > 1$ implies that the system is supercritical. Also k_{eff} can be interpreted as the asymptotic ratio of the number of neutrons in one generation and the number in the next (Lewis and Miller, 1984). Despite the lambda modes equation is the most used equation in order to solve the critical state of a reactor, some other eigenvalue problems exist that are useful for similar applications (Ronen, Shvarts, and Wagschal, 1976; Velarde, Ahnert, and Aragonés, 1978; Carreño et al., 2017).

2.4.1 Neutron Diffusion Equation

The main approximation of the neutron transport equation is the neutron diffusion equation that states that the neutron current is proportional to the gradient of the scalar neutron flux by means of a diffusion coefficient. This approximation is analogous to the Fick's law in species diffusion and to the Fourier law in heat transfer.

$$\vec{J}_g(\vec{r}) = D_g \vec{\nabla} \phi_g(\vec{r}), \tag{2.35}$$

where $\vec{J}_g$ is the current vector for the group g.

Integrating equation (2.34) over all directions and applying approximation (2.35), the neutron diffusion equation is written as

$$\begin{aligned} &- \vec{\nabla} \cdot \left(D_g \vec{\nabla}\, \phi_g(\vec{r}) \right) + \Sigma_{tg}(\vec{r})\, \phi_g(\vec{r}) \\ &= \sum_{\substack{g'=1 \\ g' \neq g}}^{G} \Sigma_{s,\, g' \to g}(\vec{r})\, \phi'_g(\vec{r}) + \frac{1}{\lambda} \sum_{g'=1}^{G} \chi_g \nu_g \Sigma_{f g'}(\vec{r})\, \phi_{g'}(\vec{r}), \\ &\qquad\qquad\qquad\qquad\qquad\qquad\qquad\qquad\qquad\qquad g = 1, \ldots, G. \end{aligned} \tag{2.36}$$

Diffusion theory provides a valid description of the neutron flux when their three main assumptions made in its derivation are satisfied. The first condition is that absorption is much less likely than scattering. This condition is satisfied for most of the moderating and structural materials found in a nuclear reactor but not for the fuel and control elements. The second condition is the linear spatial variation of the neutron distribution. This condition is satisfied a few mean free paths away from the boundary of large, compared to the mean free path, homogeneous media. The third condition is an isotropic scattering distribution. It is satisfied for scattering from heavy nuclei (Stacey, 2007).

Then, as a modern nuclear reactor consists of thousands of small elements, many of them highly absorbing diffusion theory is not strictly valid. However diffusion theory is widely used in nuclear reactor analysis and makes accurate predictions. The key is that a more accurate transport approximations are used to make useful diffusion theory where it would be expected to fail. The many small elements in a large regions are replaced by homogenized mixture with effective averaged cross sections and diffusion coefficients, thus creating a computational model for which diffusion theory is valid.

3

h-p-Finite Element Method for the Static Neutron Diffusion Equation

3.1 Introduction

The neutron diffusion equation is an approximation of the neutron transport equation that states that the neutron current is proportional to the gradient of the neutron flux by means of a diffusion coefficient. For a given configuration of a nuclear reactor core, it is always possible to force its criticality dividing the neutron production rate by a positive number, λ, obtaining a neutron balance equation. This equation is known as the Lambda modes problem (Henry, 1975; Ginestar, 1995),

$$\mathcal{L}\Phi = \frac{1}{\lambda}\mathcal{M}\Phi\,, \tag{3.1}$$

where $\mathcal{L}$ is the neutron loss differential operator and $\mathcal{M}$ is the neutron production operator.

Different methods have been proposed to spatially solve the neutron diffusion equation. Core-level codes traditionally use nodal methods. In these methods, the diffusion equation is integrated over large homogenized regions known as nodes to obtain a balance with average surface currents and fluxes as unknowns. Modern nodal methods usually rely on the Nodal Expansion Method, NEM, (Finnemann, 1975; Singh, Mazumdar, and Pandey, 2014) and the Analytical Nodal Method,

ANM, (Smith, 1979; Hébert, 1987) to overcome the problem in the recalculation of coupling coefficients. Also, a nodal collation method based on the expansion of the neutron in terms of orthogonal polynomials has been extensively used to deal with rectangular geometries (Verdú et al., 1994; Verdú et al., 1999; Ginestar, Marín, and Verdú, 2001; Verdú et al., 2005). The Finite Volume Method, FVM, has also been considered to calculate the neutronic steady state of a nuclear power (Bernal et al., 2014).

Finite element methods have been also used to study reactors with rectangular geometry, as PWR and BWR reactors (Hébert, 2008) and hexagonal geometries as VVER reactors (González-Pintor, Ginestar, and Verdú, 2009). Adaptivity is one of the main advantages in the use of the finite element method. *h*-adaptable meshes have been proposed to be used to obtain the static configuration of a nuclear reactor core with the use of triangular finite elements (Baker et al., 2013) and rectangular elements (Wang, Bangerth, and Ragusa, 2009). Also unstructured grid schemes (Theler, 2013) have been developed to solve the problem in non standard geometries.

Here, an *h*-*p* finite element method is used to obtain the dominant Lambda modes associated with a configuration of a reactor core. In order to increase the accuracy of the solution of the finite element method, it is necessary to refine the mesh used. Two main different refinement techniques exist such as *h*-refinement and *p*-refinement. In *h*-refinement, the cells of the mesh are spatially subdivided into smaller ones, keeping the original element boundaries intact. *p*-refinement increases the polynomial degree of the basic functions used in the expansions of the high order finite element method increasing the exactitude of the solution. Most of the literature, for example Wang and Ragusa, (2009), advises to use *h*-refinement in regions where the solution is rough or possesses singularities. Otherwise, the *p*-refinement is advised in regions where the solution is smooth. Sometimes, it is possible to combine efficiently the *h*- and *p*-refinements and call it the *h*-*p*-refinement. In this procedure both the size of elements h and their degree of polynomial p are altered. To select which cells are refined an error estimator is used. Thus, all the process is automatic leading to Automatic Mesh Refinement (AMR). Also, with the *h*-refinement is possible to solve the neutron diffusion equation with cross sections assembly averaged for the majority of fuel assemblies and pin-cell averaged for a particular fuel assembly of interest.

The *h*-*p* finite element method has been implemented using the open source finite elements library *deal.II* (Bangerth, Hartmann, and Kanschat, 2007; Bangerth and Kayser-Herold, 2009). With the help of the library, the code proposed is dimension independent and can manage different cell sizes and different types of finite elements. In order to solve the resulting algebraic eigenvalue problem

from the spatial discretization of the Lambda modes problem the SLEPc library (Hernandez, Roman, and Vidal, 2005) is used.

The rest of the chapter is organized as follows. Next the spatial discretization using the finite element method using the two energy groups approximation of the neutron diffusion equation is developed. Then, the multigroup treatment inside the FEM is summarized. Once the Lambda modes problem is written in algebraic matrix form, the eigenvalue problem is solved in Section 3.4. To solve the problem with the desired accuracy and automatically refine the meshes, it is necessary to define an error estimator as shown in Section 3.5. In Section 3.6, some numerical results of the code are presented. Finally, two optimizations of the code as the matrix-free methods and a preconditioning study are explained in Sections 3.7 and 3.8. This chapter rewrites the methods and results presented in Vidal-Ferràndiz et al., (2014) and Vidal-Ferràndiz et al., (2017).

3.2 The Finite Element Method

The Lambda modes equation in the approximation of two groups of energy is considered. This equation, if it is assumed that there is no upscattering from the thermal to the fast group, can be expressed as (Henry, 1975),

$$\begin{pmatrix} -\vec{\nabla}(D_1\vec{\nabla}) + \Sigma_{a1} + \Sigma_{12} & 0 \\ -\Sigma_{12} & -\vec{\nabla}(D_2\vec{\nabla}) + \Sigma_{a2} \end{pmatrix} \begin{pmatrix} \phi_1 \\ \phi_2 \end{pmatrix} = \frac{1}{\lambda} \begin{pmatrix} \nu\Sigma_{f1} & \nu\Sigma_{f2} \\ 0 & 0 \end{pmatrix} \begin{pmatrix} \phi_1 \\ \phi_2 \end{pmatrix}, \tag{3.2}$$

where D_g, $g = 1, 2$ are the diffusion coefficients, Σ_{ag}, Σ_{fg} and Σ_{12} are the macroscopic cross sections of absorption, fission and scattering, respectively. ϕ_1 and ϕ_2 are the fast and thermal neutron fluxes, respectively. The weak formulation of this equation is obtained by pre-multiplying by a test function, $\varphi^T = (\varphi_1, \quad \varphi_2)$, and integrating over the domain, Ω, defining the reactor core,

$$\int_{\Omega} \begin{pmatrix} \varphi_1 & \varphi_2 \end{pmatrix} \begin{pmatrix} -\vec{\nabla}(D_1\vec{\nabla}) + \Sigma_{a1} + \Sigma_{12} & 0 \\ -\Sigma_{12} & -\vec{\nabla}(D_2\vec{\nabla}) + \Sigma_{a2} \end{pmatrix} \begin{pmatrix} \phi_1 \\ \phi_2 \end{pmatrix} \mathrm{d}V$$
$$= \frac{1}{\lambda} \int_{\Omega} \begin{pmatrix} \varphi_1 & \varphi_2 \end{pmatrix} \begin{pmatrix} \nu\Sigma_{f1} & \nu\Sigma_{f2} \\ 0 & 0 \end{pmatrix} \begin{pmatrix} \phi_1 \\ \phi_2 \end{pmatrix} \mathrm{d}V \,. \tag{3.3}$$

The vectorial identity, $\vec{\nabla} \cdot \left(u\vec{\nabla}v\right) = \left(\vec{\nabla}u\right) \cdot \left(\vec{\nabla}v\right) + u\left(\vec{\nabla} \cdot \vec{\nabla}v\right)$, is applied and expression (3.3) is rewritten as

$$\begin{aligned} &\int_{\Omega} \vec{\nabla}\varphi_1 D_1 \vec{\nabla}\phi_1 \mathrm{d}V - \int_{\Omega} \vec{\nabla} \cdot \left(\varphi_1 D_1 \vec{\nabla}\phi_1\right) \mathrm{d}V + \int_{\Omega} \varphi_1 \left(\Sigma_{a1} + \Sigma_{12}\right) \phi_1 \mathrm{d}V \\ &+ \int_{\Omega} \vec{\nabla}\varphi_2 D_2 \vec{\nabla}\phi_2 \mathrm{d}V - \int_{\Omega} \vec{\nabla} \cdot \left(\varphi_2 D_2 \vec{\nabla}\phi_2\right) \mathrm{d}V + \int_{\Omega} \varphi_2 \Sigma_{a2} \phi_2 \mathrm{d}V \\ &- \int_{\Omega} \varphi_2 \Sigma_{12} \phi_1 \mathrm{d}V = \frac{1}{\lambda} \left(\int_{\Omega} \varphi_1 \nu\Sigma_{f1} \phi_1 \mathrm{d}V + \int_{\Omega} \varphi_1 \nu\Sigma_{f2} \phi_2 \mathrm{d}V \right). \end{aligned} \tag{3.4}$$

Using Gauss Divergence theorem, $\int_{\Omega} \vec{\nabla} \cdot \vec{F} \mathrm{d}V = \int_{\Gamma} \vec{F} \mathrm{d}\vec{S}$, to eliminate second order derivatives,

$$\begin{aligned} &\int_{\Omega} \vec{\nabla}\varphi_1 D_1 \vec{\nabla}\phi_1 \mathrm{d}V - \int_{\Gamma} \varphi_1 D_1 \vec{\nabla}\phi_1 \mathrm{d}\vec{S} + \int_{\Omega} \varphi_1 \left(\Sigma_{a1} + \Sigma_{12}\right) \phi_1 \mathrm{d}V \\ &+ \int_{\Omega} \vec{\nabla}\varphi_2 D_2 \vec{\nabla}\phi_2 \mathrm{d}V - \int_{\Gamma} \varphi_2 D_2 \vec{\nabla}\phi_2 \mathrm{d}\vec{S} + \int_{\Omega} \varphi_2 \Sigma_{a2} \phi_2 \mathrm{d}V \\ &- \int_{\Omega} \varphi_2 \Sigma_{12} \phi_1 \mathrm{d}V = \frac{1}{\lambda} \left(\int_{\Omega} \varphi_1 \nu\Sigma_{f1} \phi_1 \mathrm{d}V + \int_{\Omega} \varphi_1 \nu\Sigma_{f2} \phi_2 \mathrm{d}V \right), \end{aligned} \tag{3.5}$$

is obtained, where Γ is the boundary of the domain defining the reactor.

Finally, the reactor domain Ω is divided into cells or subdomains Ω_k $(k = 1, \ldots, K)$ where it is assumed that the nuclear cross sections remain constant due to a previous spatial homogenization strategy. The cross sections for each cell k are denoted by the superscript $^{(k)}$. For further details about the homogenization strategies the reader is referred to Chapter 6. Γ_k is also defined as the corresponding subdomain surface which is part of the reactor frontier Γ. Equation (3.5) is rewrit-

ten as

$$\sum_{k=1}^{K}\left(D_1^{(k)}\int_{\Omega_k}\vec{\nabla}\varphi_1\vec{\nabla}\phi_1\mathrm{d}V - D_1^{(k)}\int_{\Gamma_k}\varphi_1\vec{\nabla}\phi_1\mathrm{d}\vec{S} + (\Sigma_{a1}^{(k)}+\Sigma_{12}^{(k)})\int_{\Omega_k}\varphi_1\phi_1\mathrm{d}V\right.$$
$$+ D_2^{(k)}\int_{\Omega_k}\vec{\nabla}\varphi_2\vec{\nabla}\phi_2\mathrm{d}V - D_2^{(k)}\int_{\Gamma_k}\varphi_2\vec{\nabla}\phi_2\mathrm{d}\vec{S} + \Sigma_{a2}^{(k)}\int_{\Omega_k}\varphi_2\phi_2\mathrm{d}V$$
$$\left. - \Sigma_{12}^{(k)}\int_{\Omega_k}\varphi_2\phi_1\mathrm{d}V\right) = \frac{1}{\lambda}\sum_{k=1}^{K}\left(\nu\Sigma_{f1}^{(k)}\int_{\Omega_k}\varphi_1\phi_1\mathrm{d}V + \nu\Sigma_{f2}^{(k)}\int_{\Omega_k}\varphi_1\phi_2\mathrm{d}V\right). \tag{3.6}$$

It has to be noted that there are several surface integrals over the boundary of the subdomains, Γ_k, that rely on the boundary conditions and that will be studied in Section 3.2.1. The solution ϕ_g is approximated through an usual trial solution as sum of shape functions, $\mathcal{N}_j$, multiplied by their corresponding coefficients associated with the support points values $\tilde{\phi}_{gj}$.

$$\phi_g \approx \sum_{j=0}^{N_{\text{DoFs}}}\mathcal{N}_j\,\tilde{\phi}_{gj}\,, \tag{3.7}$$

where N_{DoFs} is the total number of degrees of freedom or nodes.

In the same way, a continuous Galerkin method (Zienkiewicz, Taylor, and Zhu, 2005) is used assuming that the test functions belong to the finite set of shape functions. Introducing these expressions in equation (3.6) and eliminating redundant coefficients to obtain continuous solutions using a condensation process (see, for example, González-Pintor, Ginestar, and Verdú, (2009) for more details) in terms of global coefficients, the procedure leads to an algebraic eigenvalue problem of the form

$$\begin{pmatrix}\mathbf{L_{11}} & 0\\ \mathbf{L_{21}} & \mathbf{L_{22}}\end{pmatrix}\begin{pmatrix}\tilde{\phi}_1\\ \tilde{\phi}_2\end{pmatrix} = \frac{1}{\lambda}\begin{pmatrix}\mathbf{M_{11}} & \mathbf{M_{12}}\\ 0 & 0\end{pmatrix}\begin{pmatrix}\tilde{\phi}_1\\ \tilde{\phi}_2\end{pmatrix}, \tag{3.8}$$

where the matrices elements are given by

$$
\begin{aligned}
\mathbf{L_{11}}_{(ij)} &= \sum_{k=1}^{K} D_1^{(k)} \int_{\Omega_k} \vec{\nabla}\mathcal{N}_i \vec{\nabla}\mathcal{N}_j \mathrm{d}V - D_1^{(k)} \int_{\Gamma_k} \mathcal{N}_i \vec{\nabla}\mathcal{N}_j \mathrm{d}\vec{S} + (\Sigma_{a1}^{(k)} + \Sigma_{12}^{(k)}) \int_{\Omega_k} \mathcal{N}_i \mathcal{N}_j \mathrm{d}V \,, \\
\mathbf{L_{22}}_{(ij)} &= \sum_{k=1}^{K} D_2^{(k)} \int_{\Omega_k} \vec{\nabla}\mathcal{N}_i \vec{\nabla}\mathcal{N}_j \mathrm{d}V - D_2^{(k)} \int_{\Gamma_k} \mathcal{N}_i \vec{\nabla}\mathcal{N}_j \mathrm{d}\vec{S} + \Sigma_{a2}^{(k)} \int_{\Omega_k} \mathcal{N}_i \mathcal{N}_j \mathrm{d}V \,, \\
\mathbf{L_{12}}_{(ij)} &= \sum_{k=1}^{K} -\Sigma_{12}^{(k)} \int_{\Omega_k} \mathcal{N}_i \mathcal{N}_j \mathrm{d}V \,, \\
\mathbf{M_{11}}_{(ij)} &= \sum_{k=1}^{K} \nu\Sigma_{f1}^{(k)} \int_{\Omega_k} \mathcal{N}_i \mathcal{N}_j \mathrm{d}V \,, \\
\mathbf{M_{12}}_{(ij)} &= \sum_{k=1}^{K} \nu\Sigma_{f2}^{(k)} \int_{\Omega_k} \mathcal{N}_i \mathcal{N}_j \mathrm{d}V \,.
\end{aligned}
\tag{3.9}
$$

These integrals only have non-zero value when shape functions $\mathcal{N}_i$ and $\mathcal{N}_j$ collide inside the same cell, therefore highly sparse global matrices are obtained.

3.2.1 Boundary conditions

Implemented boundary conditions are zero-flux, zero-current and albedo boundary conditions. This last case are mixed boundary conditions of the form,

$$
\vec{n}\vec{\nabla}\phi_g(\vec{x}) + \frac{1}{D_g}\frac{1-\gamma}{2(1+\gamma)}\phi_g(\vec{x}) = 0 \,, \qquad \vec{x} \in \Gamma \,. \tag{3.10}
$$

where $\vec{n}$ is a normal vector to the boundary pointing outwards, γ is the albedo factor going from 0, leading to vacuum boundary conditions, to 1.0, giving zero current frontier conditions.

If zero-flux boundary conditions are assumed the nodal values on the frontier are explicitly fixed to zero. Thus, their related shape function are not in the algebraic problem of equation (3.8) because their flux is restricted to zero. On the other hand, if the boundary conditions are zero-current boundary conditions the surface integral terms are equal to zero and the finite element formulation takes care of these conditions without restrictions in the nodes. Zero-current boundary conditions take care of symmetry conditions in the neutron diffusion equation. Albedo boundary conditions are treated in a weak form by pre-multiplying the

condition by the test function and integrating over the surface of the domain,

$$- D_g \int_\Gamma \varphi_g \vec{\nabla} \phi_g \mathrm{d}\vec{S} = \frac{1}{2} \frac{1-\gamma}{1+\gamma} \int_\Gamma \varphi_g \phi_g \mathrm{d}\vec{S} \,. \tag{3.11}$$

Hence, the boundary integrals that appear in equation (3.9) are substituted by,

$$\sum_{k=1}^{K} -D_g \int_{\Gamma_k} \mathcal{N}_i \vec{\nabla} \mathcal{N}_j \mathrm{d}\vec{S} = \sum_{k=1}^{K} \frac{1}{2} \frac{1-\gamma}{1+\gamma} \int_{\Gamma_k} \mathcal{N}_i \mathcal{N}_j \mathrm{d}\vec{S}, \qquad g = 1,\, 2\,. \tag{3.12}$$

3.2.2 Reference element

As it has been already mentioned, the whole reactor domain is discretized into subdomains also called cells. In order to define these subdomains always over the same reference cell an affine mapping is used to map each physical element to the reference element. An example of this process for a bidimensional cell is shown in Figure 3.1.

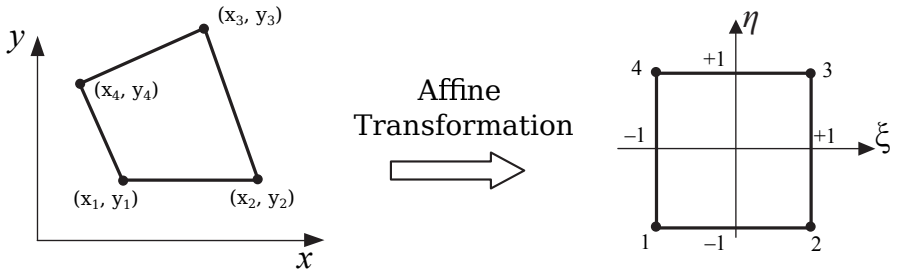

Figure 3.1: Affine transformation mapping the physical element into the reference element.

This change of variables relates physical coordinates (x, y), with the coordinates of the reference domain (ξ, η) and it is given by

$$\begin{aligned} x(\xi,\eta) = \frac{1}{4} \big(&(1-\xi)(1-\eta)x_1 + (1-\xi)(1+\eta)x_2 \\ &+ (1+\xi)(1-\eta)x_3 + (1-\xi)(1+\eta)x_4 \big) \,, \end{aligned} \tag{3.13}$$

$$\begin{aligned} y(\xi,\eta) = \frac{1}{4} \big(&(1-\xi)(1-\eta)y_1 + (1-\xi)(1+\eta)y_2 \\ &+ (1+\xi)(1-\eta)y_3 + (1-\xi)(1+\eta)y_4 \big) \,. \end{aligned} \tag{3.14}$$

This affine mapping helps to compute the integrals defining the matrix elements taking into account the Jacobian of the transformation $|\mathbf{J^k}|$. Since

$$\mathrm{d}V = \mathrm{d}x\mathrm{d}y = \begin{vmatrix} \frac{\partial x}{\partial \xi} & \frac{\partial y}{\partial \xi} \\ \frac{\partial x}{\partial \eta} & \frac{\partial y}{\partial \eta} \end{vmatrix} \mathrm{d}\xi\mathrm{d}\eta = |\mathbf{J^k}|\mathrm{d}\xi\mathrm{d}\eta\,. \tag{3.15}$$

3.2.3 Lagrange finite elements

For simplicity, Lagrange finite elements (Zienkiewicz, Taylor, and Zhu, 2005) are used. These elements have their nodes distributed forming a regular mesh over the cell. Their shape functions are defined with *Lagrange polynomials* for every dimension. These polynomials have a value of unity at the corresponding nodal point and zero at the other nodes and they satisfy all inter-element continuity conditions. Lagrange polynomials are defined as

$$l_I^p(\xi) = \frac{(\xi-\xi_1)\ldots(\xi-\xi_{I-1})(\xi-\xi_{I+1})\ldots(\xi-\xi_{p+1})}{(\xi_I-\xi_1)\ldots(\xi_I-\xi_{I-1})(\xi_I-\xi_{I+1})\ldots(\xi_I-x_{p+1})} = \prod_{\substack{k=0\\k\neq I}}^{p+1} \frac{\xi-\xi_k}{\xi_I-\xi_k}\,, \tag{3.16}$$

where p is the polynomial degree of the expansion which characterizes the finite element method, and ξ_i is the position of every node in the element. Multidimensional versions of these elements are obtained by tensor product of one-dimensional elements. Thus, in two coordinates, if the node is labelled by its column and row number I, J,

$$\mathcal{N}_{I,J}(\xi,\eta) = l_I^p(\xi) l_J^p(\eta)\,. \tag{3.17}$$

Figure 3.2 shows the shape functions of some one-dimensional Lagrange elements and an example of these shape functions in a bidimensional element is displayed in Figure 3.3. The number of nodes in each cell, which is function of the finite element degree p, is the number of degrees of freedom in each cell. The total number of degrees of freedom of the problem is calculated multiplying the number of nodes per cell by the number of cells and removing the repeated nodes in the interface between cells. Finally, it should be noted that to compute the integrals of the weak formulation in each cell a Gauss quadrature is used (Golub and Welsch, 1969). The degree of the quadrature is selected with $p+2$ quadrature points, ensuring an exact integration inside the approximation of polynomial shape functions.

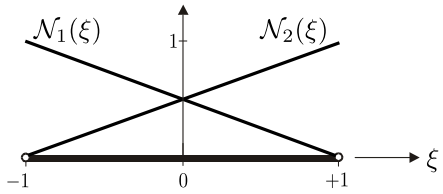

$$\begin{aligned}\mathcal{N}_1(\xi) &= \tfrac{1}{2}(1-\xi)\\ \mathcal{N}_2(\xi) &= \tfrac{1}{2}(1+\xi)\end{aligned}$$

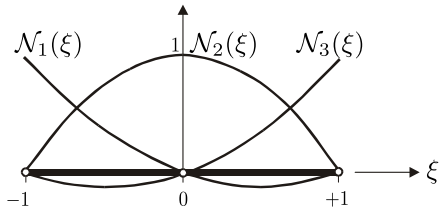

$$\begin{aligned}\mathcal{N}_1(\xi) &= \tfrac{1}{2}\xi(1-\xi)\\ \mathcal{N}_2(\xi) &= 1-\xi^2\\ \mathcal{N}_3(\xi) &= \tfrac{1}{2}\xi(1+\xi)\end{aligned}$$

Figure 3.2: Example of unidimensional shape functions used, linear and quadratic.

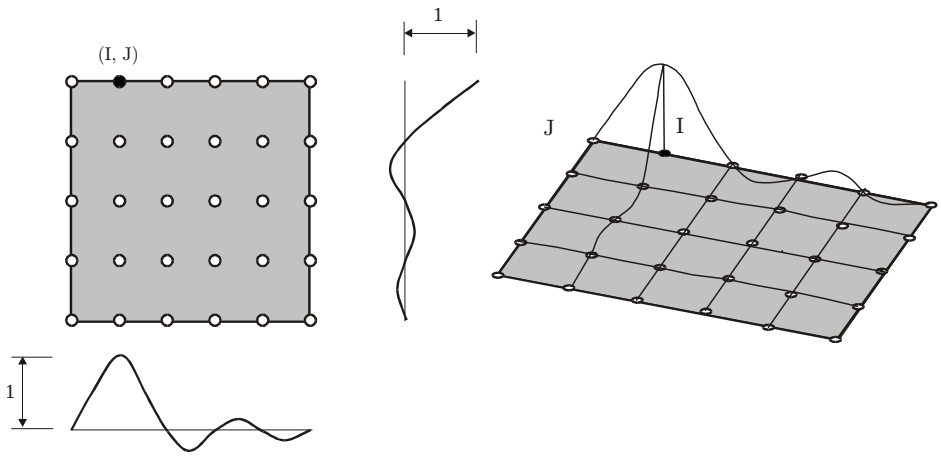

Figure 3.3: A shape function for a 2D Lagrangian element, ($I = 2$, $J = 5$, $p = 4$).

3.3 Multigroup treatment

Even though the two energy groups discretization of the diffusion equation is the most popular choice for full reactor calculations, it is also possible to solve the diffusion equation for an arbitrary number of groups, G.

This equation has a well-defined block structure due to the neutron energy discretization of the problem. The equation for the energy groups has the following form

$$\mathcal{L}_{gg}\phi_g + \sum_{\substack{h=1 \\ h\neq g}}^{G} \mathcal{L}_{gh}\phi_h = \frac{1}{\lambda}\sum_{h=1}^{G} \mathcal{M}_{gh}\phi_h\,, \qquad g = 1,\,\ldots,\,G, \tag{3.18}$$

where

$$\begin{aligned} \mathcal{L}_{gg}\phi_g &:= -\vec{\nabla}\left(D_g\vec{\nabla}\phi_g\right) + \Sigma_{r,g}\phi_g, \\ \mathcal{L}_{gh}\phi_g &:= -\Sigma_{s,h\to g}\phi_h, \\ \mathcal{M}_{gh}\phi_g &:= \chi_g\nu\Sigma_{f,h}\phi_h. \end{aligned} \tag{3.19}$$

Here ϕ_g is the neutron flux for the g-th energy group, D_g is the diffusion coefficient, $\Sigma_{r,g}$ is the macroscopic removal cross section (absorption plus outscattering), $\Sigma_{s,g\to h}$ is the macroscopic scattering cross section from group g to h, $\nu\Sigma_{f,g}$ is the fission cross section, χ_g is the neutron energy spectrum of fission and λ is the multiplicative factor defined before. The cross sections and the diffusion coefficient are space dependent functions, usually defined as piecewise constants because of a previous homogenization procedure has been used (see Chapter 6 for more details).

3.3.1 Finite Element Method discretization

Using a similar procedure to the one explained in Section 3.2, the multigroup diffusion equation leads to the following algebraic generalized eigenvalue problem

$$\mathbf{L}\tilde{\phi} = \frac{1}{\lambda}\mathbf{M}\tilde{\phi}\,, \tag{3.20}$$

where each block is composed by,

$$\begin{aligned}
\mathbf{L_{gg}}_{(ij)} &= \sum_{k=1}^{K} D_g \int_{\Omega_k} \vec{\nabla}\mathcal{N}_i \vec{\nabla}\mathcal{N}_j \mathrm{d}V - D_g \int_{\Gamma_k} \mathcal{N}_i \vec{\nabla}\mathcal{N}_j \mathrm{d}\vec{S} + \Sigma_{r,g} \int_{\Omega_k} \mathcal{N}_i \mathcal{N}_j \mathrm{d}V \,, \\
\mathbf{L_{gh}}_{(ij)} &= \sum_{k=1}^{K} \Sigma_{s,h\to g} \int_{\Omega_k} \mathcal{N}_i \mathcal{N}_j \,\mathrm{d}V \,, \qquad\qquad \text{for } g \neq h \,, \\
\mathbf{M_{gh}}_{(ij)} &= \sum_{k=1}^{K} \chi_g \nu \Sigma_{f,h} \int_{\Omega_k} \mathcal{N}_i \mathcal{N}_j \,\mathrm{d}V \,.
\end{aligned} \tag{3.21}$$

3.4 Eigenvalue Solver

In the most general case, the eigenvalue problem (3.20) is traditionally solved using the power iteration method with a combination of inner and outer iterations (Ferguson and Derstine, 1977). The inner iterations update the neutron flux, from faster to slower energy groups, using a fixed source as follows

$$\mathbf{L_{gg}}\tilde{\phi}_g^{(i)} = Q_g^{(i-1)}, \tag{3.22}$$

where the fixed source for group g, Q_g, is generated using the updated neutron flux for the up-scattering terms and the previous neutron flux for the down-scattering and for the fission terms

$$Q_g^{(i-1)} = \sum_{h=1}^{g-1} \mathbf{L_{gh}}\tilde{\phi}_h^{(i)} + \sum_{h=g+1}^{G} \mathbf{L_{gh}}\tilde{\phi}_h^{(i-1)} + \frac{1}{\lambda^{(i-1)}} \sum_{h=1}^{G} \mathbf{M_{gh}}\tilde{\phi}_h^{(i-1)}. \tag{3.23}$$

Once the inner-iteration has finished, by performing either one single loop through the energy groups or iterating until convergence, the outer iteration updates the eigenvalue by using the actual flux and the previous flux with the previous eigenvalue, as follows

$$\lambda^{(i)} = \lambda^{(i-1)} \frac{||\mathbf{M}\tilde{\phi}^{(i)}||}{||\mathbf{M}\tilde{\phi}^{(i-1)}||} \,, \tag{3.24}$$

where $||\cdot||$ is the norm in $(L^2(\Omega))^G := \overbrace{L^2(\Omega) \times \ldots \times L^2(\Omega)}^{G}$. For this general scenario, the solution of equation (3.22) is the most demanding step from the computational point of view. Thus, the preconditioning of a finite element discretization of equation (3.22) is essential in order to accelerate the whole algorithm.

3.4.1 Two energy group optimization

A usual situation is accounted where the Lambda modes problem is approximated using only two energy groups and assuming that the neutrons are born from fission in the fast group, $\chi_1 = 1.0, \chi_2 = 0.0$, and there is no up-scattering, $\Sigma_{s2\to1} = 0$. Thus, we obtain a block lower triangular form of the operator that can be used to solve the system more efficiently. This scenario is widely considered because it provides a good approximation, at low cost, for simulating standard LWR type reactor cores.

This problem can be solved more efficiently than the general multigroup approximation if the generalized eigenvalue problem (3.8) is reduced to an ordinary eigenvalue problem,

$$\mathbf{L_{11}^{-1}}\left(\mathbf{M_{11}} - \mathbf{M_{12}}\,\mathbf{L_{22}^{-1}}\,\mathbf{L_{21}}\right)\tilde{\phi}_1 = \lambda\,\tilde{\phi}_1\,, \tag{3.25}$$

which is solved for the n dominant eigenvalues and their corresponding eigenvectors using a Krylov-Schur method (Stewart, 2002) from the library SLEPc (Hernandez, Roman, and Vidal, 2005). Other methods as the Implicit Restarted Arnoldi Method (IRAM) (Verdú et al., 1999) and the Jacobi Davidson methods (Verdú et al., 2005) have also been used in the literature. To avoid the calculation of the inverse of sparse matrices, that leads to dense matrices, for each matrix-vector product requested by the eigenvalues problem solver (EPS), two linear systems associated with matrices $\mathbf{L_{11}}$ and $\mathbf{L_{22}}$ are solved. These systems are solved by means of an iterative scheme as the preconditioned conjugate gradient method (Saad, 2003). Particularly, a reversed Cuthill-McKee reordering (Cuthill and McKee, 1969) is performed to reduce the bandwidth of the matrices, together with an *incomplete LU* factorization, ILU(0), of the matrices, which is used as preconditioning. For more information about preconditioning these systems the readers is referred to Section 3.8.

Once the ordinary eigenvalue problem involving $\tilde{\phi}_1$ is solved, the thermal group is calculated as

$$\tilde{\phi}_2 = \mathbf{L_{22}^{-1}}\,\mathbf{L_{21}}\tilde{\phi}_1\,. \tag{3.26}$$

3.4.2 Normalization

Once the fluxes are obtained other practical magnitudes are computed as the neutron power that is defined as a weighted sum of the neutron fluxes

$$P = \kappa \sum_{g=1}^{G} \Sigma_{fg}|\phi_g|\,. \tag{3.27}$$

The thermal power is proportional to the neutron power generated by the reactor since it is assumed that every fission generates a constant average amount of energy, κ. The absolute value is introduced in this definition to generalize the neutron power for the subcritical modes where the fluxes have positive and negative values. In addition, the eigenvectors should be normalized through some criteria. The most usual one is

$$\frac{1}{V_t}\sum_{g=1}^{G}\int_{\Omega}\Sigma_{fg}\,|\phi_g|\,\mathrm{d}V = 1\,. \tag{3.28}$$

If values for Σ_{fg} are not available it is common to use $\nu\Sigma_{fg}$ in equation (3.28) instead. This approximation considers that ν is constant for all the materials in the core and all energy groups.

3.5 Refinement and error estimator

After the problem is solved, it is convenient to estimate if the obtained solution has enough accuracy and if, this is not the case, to refine the mesh accordingly. In this way, two types of refinements are considered, a uniform refinement, where all cells are refined, and an adaptive refinement, where only part of the cells are refined. To choose which cells are refined a modified version of the error estimator proposed in Kelly et al., (1983) is used. This estimator, η_k, is extended for non-constant diffusion coefficients in Wang, Bangerth, and Ragusa, (2009) and generalized for a multigroup approximation as

$$\eta_k = \sqrt{\frac{h_k}{24}}\sum_{g=1}^{G}\left(\Sigma_{fg}^{(k)}\int_{\mathcal{T}_k}\left(D_g\vec{\nabla}\phi_g\right)\mathrm{d}\vec{S}\right)\,, \tag{3.29}$$

where $\mathcal{T}_k$ denotes all interior boundaries of the element k and h_k is the adimensional cell size. In other words, we are using the jump in the net current weighted by the fission cross sections as the error estimator in the neutron power. Even though, this is an error estimator for the Poisson's equation, i.e. $\nabla^2\varphi = f$, this indicator is widely used as a heuristic refinement indicator and it is considered a good choice in the absence of actual estimators for a particular equation (Bangerth and Kayser-Herold, 2009).

3.6 Numerical Results

To study the performance of the *h-p* finite element method exposed above to determine the Lambda modes of a nuclear reactor, three different benchmark

problems have been considered. To compare the performance of the method using different types of meshes, refinement sizes and strategies, different errors have been employed. These errors are defined in Table 3.1 where $\bar{P}_i$ and $\bar{P}_i^*$ are the obtained power and the reference power in the i-th coarse cell (cell averaged), respectively. V_i is the volume of the coarse cell i and V_t is the total volume of the reactor. λ_n is the n-th computed eigenvalue and λ_n^* is the reference eigenvalue.

Table 3.1: Definition of the different errors employed to compare the accuracy of the different methods.

Relative power Error	$\varepsilon_i = \dfrac{\lvert\bar{P}_i - \bar{P}_i^*\rvert}{\lvert\bar{P}_i^*\rvert}$
Mean Relative Error	$\bar{\varepsilon} = \dfrac{1}{V_t}\sum_i \varepsilon_i V_i$
Maximum Absolute Error	$\varepsilon_{\max} = \max\lvert\bar{P}_i - \bar{P}_i^*\rvert$
Relative Power Peaking error	$RPP = \dfrac{\max\lvert\bar{P}_i\rvert - \max\limits_i\lvert\bar{P}_i^*\rvert}{\max\lvert\bar{P}_i^*\rvert}$
Eigenvalue Error (pcm)	$\Delta\lambda = 10^5 \times \lvert\lambda_n - \lambda_n^*\rvert$

To validate the results of the implemented code a 2D homogeneous reactor has been studied, since an analytical solution can be found for this problem. Also more realistic reactors, as the BIBLIS 2D reactor and the IAEA 3D reactor have been studied. The number of eigenvalues requested has been set to 4 with a relative tolerance of 10^{-7} in all the examples. The code has been written in C++ and executed in a computer with an Intel®i3-3220 @ 3.30GHz processor with 12 Gb of RAM running Ubuntu GNU/Linux 14.04.

3.6.1 Homogeneous Reactor

First a theoretical reactor is considered. It consists of a two dimensional rectangular homogeneous material with zero flux boundary conditions Even though this problem is completely theoretical, it is relevant because it can be solved analytically for all its eigenvalues. This analytical solution is developed in Appendix A. The material cross sections for the (40 cm $\times$ 40 cm) rectangular reactor are shown in Table 3.2 where it is assumed a constant $\nu = 2.5$.

Table 3.3 shows the eigenvalue results using different number of cells and different polynomial degrees for the basis of the finite element method. The power distribution for the dominant eigenvalue using a very coarse mesh (16 cells $p = 1$)

Table 3.2: Cross section values for the homogeneous reactor.

$\mathbf{D_1}$ (cm)	$\mathbf{D_2}$ (cm)	$\boldsymbol{\Sigma_{a1}}$ (1/cm)	$\boldsymbol{\Sigma_{a2}}$ (1/cm)	$\boldsymbol{\Sigma_{12}}$ (1/cm)	$\boldsymbol{\nu\Sigma_{f1}}$ (1/cm)	$\boldsymbol{\nu\Sigma_{f2}}$ (1/cm)
1.32	0.2772	0.0026562	0.071596	0.023106	0.0074527	0.13236

Table 3.3: Eigenvalue results for the homogeneous reactor using uniform meshes.

Number of cells	**p**	**Number of DoFs**	**1st Mode** λ_1	$\Delta\lambda$	**2nd Mode** λ_2	$\Delta\lambda$
16	1	25	1.12178	2507	0.60706	7910
256	1	289	1.14528	157	0.68091	525
4096	1	4225	1.14675	10	0.68583	33
16	2	81	1.14660	25	0.68323	293
256	2	1089	1.14685	0	0.68615	1
16	3	169	1.14685	0	0.68611	5
16	4	289	1.14685	0	0.68616	0
Analytical			1.14685		0.68616	

is shown in Figure 3.4a and the relative error in the power distribution, ε_i, is shown in Figure 3.4b. It should be noted that the maximum difference with the analytical solution is up to 11% but the averaged relative error ($\bar{\varepsilon}$) is only about 3.04%. Figure 3.5 compares the power distribution along the center line $y = 20$ cm for the first two dominant eigenvalues. It is observed a good agreement with the analytical solutions as the number of cells or the polynomial expansion degrees are increased. It must be also noted that the eigenvalue error and the relative power error are very low compared to the next, more realistic, benchmarks in terms of the number of cells and degrees of freedom involved in the calculation. This explains that the heterogeneity between cells is the main source of error.

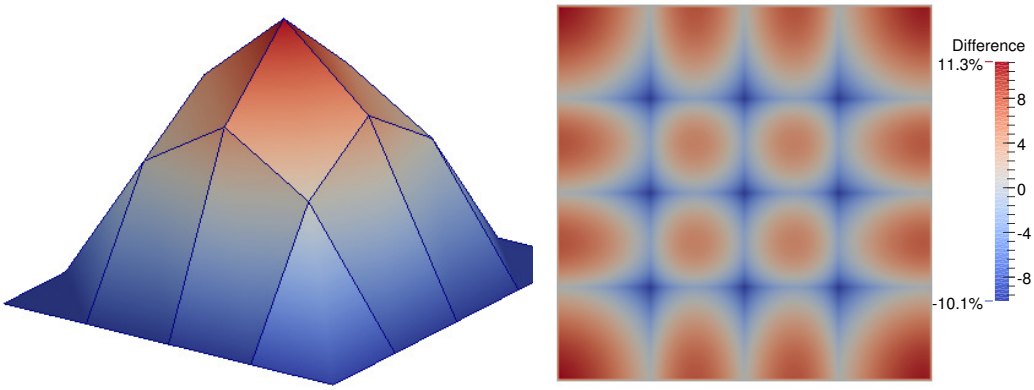

(a) Power distribution. **(b)** Error distribution.

Figure 3.4: Fundamental mode power distribution and its error distribution for homogeneous reactor with zero-flux boundary conditions.

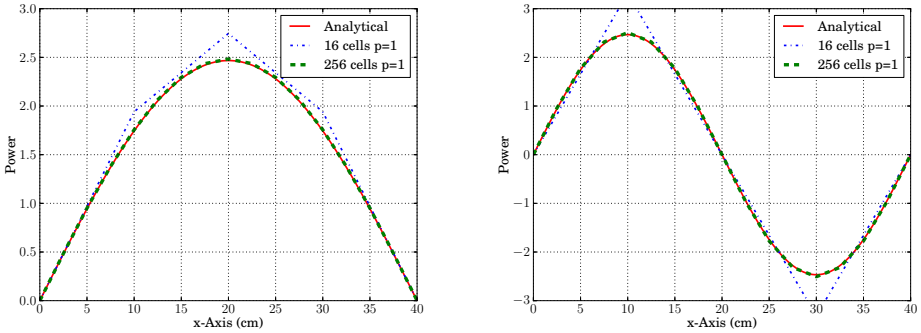

(a) 1st Mode. **(b)** 2nd Mode.

Figure 3.5: Power distribution along the line $y = 20\ cm$ for the homogeneous reactor.

3.6.2 BIBLIS 2D Reactor

Here, a more realistic two-dimensional example is chosen, the BIBLIS 2D benchmark. This is a classical two-group neutron diffusion problem taken as a benchmark for different numerical codes (Hébert, 1985). It has 257 different assemblies including 64 cells modelling the reflector. The definition of the benchmark can be found in Appendix B.6. The reference values for the first mode are extracted from Müller and Weiss, (1991). For the second mode the reference values are extracted from the most converged solution computed, using 16448 cells with $p = 4$.

Figure 3.6 shows the neutron power distribution for the four dominant modes of this reactor. Tables 3.4 and 3.6 display the eigenvalue results for uniform refined meshes and *h*-refined meshes. Tables 3.5 and 3.7 show the power distribution errors obtained using different meshes and different polynomial degrees, p, together with the CPU time needed to compute 4 eigenvalues[1]. Figure 3.7 displays the error distribution, ε_i, for 257 elements with $p = 3$ for the first mode. As an example of automated adaptive refinement, Figure 3.8, displays the meshes generated in 6 different iterations of the code using the error estimator defined in (3.29). It is observed that the code refines the cells with the highest error that are pointed out correctly by the error estimator. Also, it can be noted that the algorithm refines the cells near the locations where the material changes, particularly in the last iterations.

In Figures 3.9 and 3.10, the mean relative error for the two dominant eigenvalues is displayed as a function of the execution time for different meshes and degrees of the finite element method. From these Figures, it can be seen that the errors follow a typical exponential convergence with the computation time. Also, it can be concluded that the errors in the power distribution do not depend on which eigenvalue is being calculated. These Figures and Tables show that the local or uniform *h*-refinement is not a better strategy than increasing the polynomial uniformly because of the smoothness in the fluxes solutions and the computational cost of the evaluation of the error estimator. For example, a coarse mesh with 257 elements with $p = 3$ gives better results, $\bar{\varepsilon}_1 = 1.29\%$ and $\Delta\lambda_1 = 25$ pcm, than a *h*-refined mesh with 4280 cells and $p = 1$, $\bar{\varepsilon}_1 = 1.87\%$ and $\Delta\lambda_1 = 65$ pcm; even though the cubic approximation is faster to be solved, 0.22 s against 0.51 s. These results partially contradict the results given in Wang, Bangerth, and Ragusa, (2009) because of the use here of full core reactor benchmarks where the solution maintain a significant smoothness. In Figure 3.11, a convergence graph is shown

[1] To understand the velocity of the Krylov-Schur method implemented in C++, it is compared with an standard eigenvalue solver as the `eigs()` function from Matlab®. While `eigs()` takes 0.81 s to solve the system for the $p = 3$ case without refinement, our code takes 0.22 s.

for the relative power peaking error versus the time of execution. Although this error is important nuclear reactor engineering, the power peaking relative error shows a behaviour which is less smooth than the mean error between meshes and different polynomial degrees of finite elements.

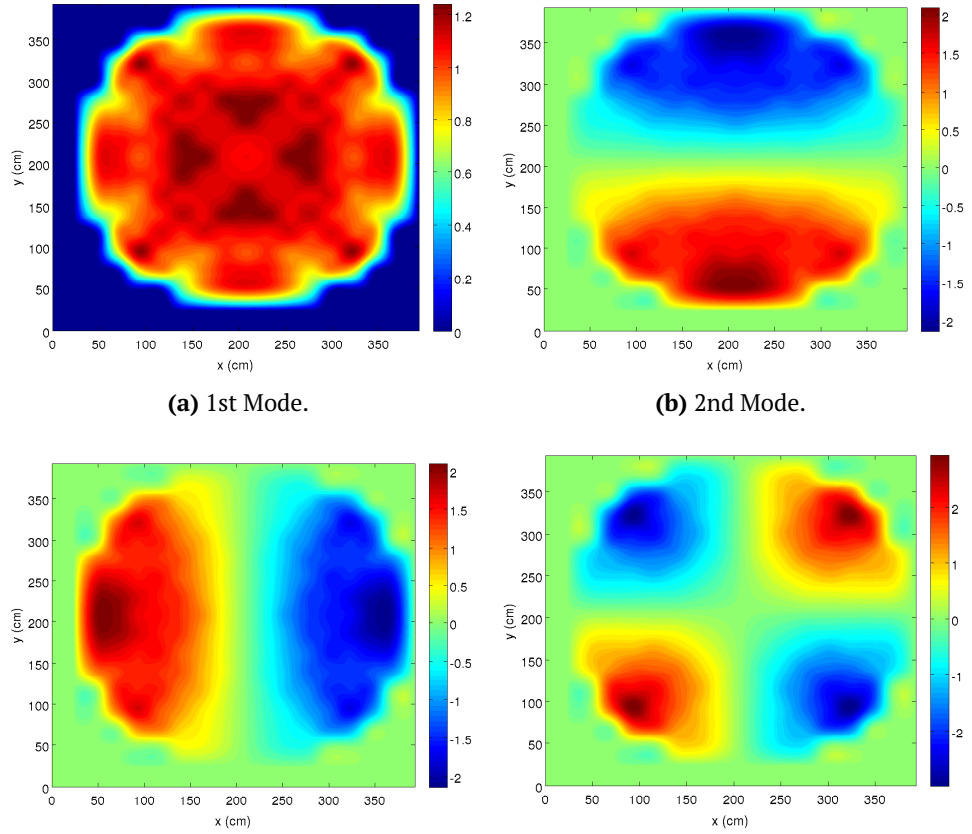

(a) 1st Mode.

(b) 2nd Mode.

(c) 3rd Mode.

(d) 4th Mode.

Figure 3.6: Power distribution for the four dominant modes of the BIBLIS reactor.

Table 3.4: Eigenvalue results with uniform refined meshes in BIBLIS Reactor.

Number of cells	p	Number of DoFs	CPU time (s)	1st Mode λ_1	1st Mode $\Delta\lambda$	2nd Mode λ_2	2nd Mode $\Delta\lambda$
257	1	292	2.0e−2	1.02179	331	1.01380	419
4112	1	4249	2.8e−1	1.02490	20	1.01780	19
65 792	1	66 337	1.7e+1	1.02508	2	1.01797	2
257	2	1097	8.0e−2	1.02540	30	1.01832	33
4112	2	37 417	2.0	1.02534	24	1.01809	10
16 448	2	66 337	1.7e+1	1.02510	0	1.01800	1
257	3	2416	2.2e−1	1.02535	25	1.01822	23
4112	3	37 417	8.1	1.02510	0	1.01798	1
Reference				1.02510		1.01799	

Table 3.5: Power distribution errors with uniform refined meshes in BIBLIS Reactor.

Number of cells	p	1st Mode $\bar{\varepsilon}$ (%)	1st Mode $\varepsilon_{\max}$	2nd Mode $\bar{\varepsilon}$ (%)	2nd Mode $\varepsilon_{\max}$
257	1	7.03	1.7e−1	6.40	2.5e−1
4112	1	0.55	5.5e−2	0.56	1.4e−2
65 792	1	0.04	8.4e−4	0.05	4.7e−2
257	2	1.72	3.7e−2	1.69	5.5e−2
4112	2	0.16	3.6e−3	0.14	4.0e−3
16 448	2	0.02	3.7e−4	0.01	3.7e−4
257	3	1.29	3.0e−2	1.18	5.6e−2
4112	3	0.01	1.8e−4	0.01	1.9e−4

Table 3.6: Eigenvalue results with *h*-refined meshes in BIBLIS Reactor.

Number of cells	p	Number of DoFs	CPU time (s)	1st Mode λ_1	1st Mode $\Delta\lambda$	2nd Mode λ_2	2nd Mode $\Delta\lambda$
644	1	732	6.0e−2	1.022 18	292	1.01440	358
4280	1	4736	5.1e−1	1.024 43	67	1.01729	70
28 613	1	30 982	8.7	1.024 99	11	1.01786	13
72 866	1	68 646	3.4e+1	1.025 01	9	1.01786	13
647	2	2861	3.0e−1	1.025 13	3	1.01812	13
4064	2	18 139	4.8	1.025 10	0	1.01800	1
10 187	2	57 881	1.8e+1	1.025 10	0	1.01798	1
Reference				1.025 10		1.01799	

Table 3.7: Power distribution errors with *h*-refined meshes in BIBLIS Reactor.

Number of cells	p	1st Mode $\bar{\varepsilon}$ (%)	1st Mode $\varepsilon_{\max}$	2nd Mode $\bar{\varepsilon}$ (%)	2nd Mode $\varepsilon_{\max}$
644	1	4.56	9.2e−2	4.58	1.3e−1
4280	1	1.87	9.1e−2	1.65	4.8e−2
28 613	1	0.21	2.2e−3	0.19	1.9e−1
72 866	1	0.05	2.8e−3	0.05	1.5e−3
647	2	1.09	2.7e−2	1.05	4.1e−2
4064	2	0.23	8.2e−3	0.19	7.9e−3
10 187	2	0.04	1.4e−3	0.03	3.2e−2

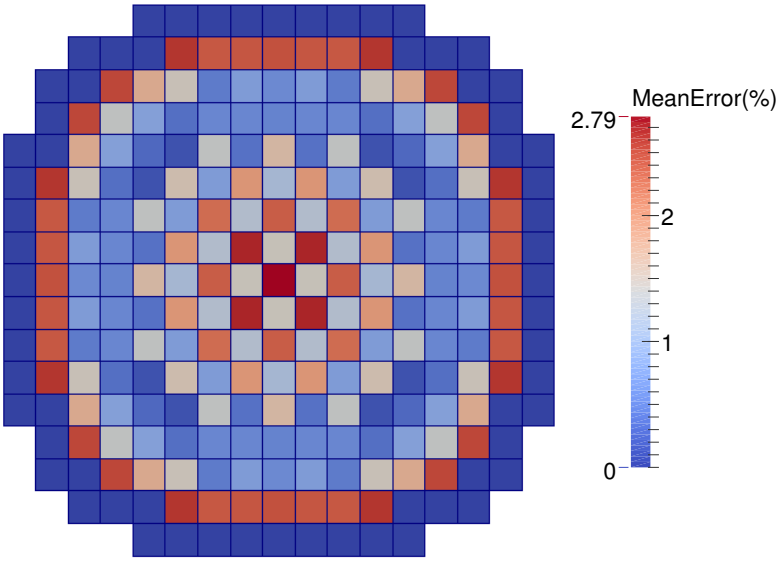

Figure 3.7: Relative error distribution using a mesh with 257 elements $p = 3$ in 1st mode of BIBLIS Reactor.

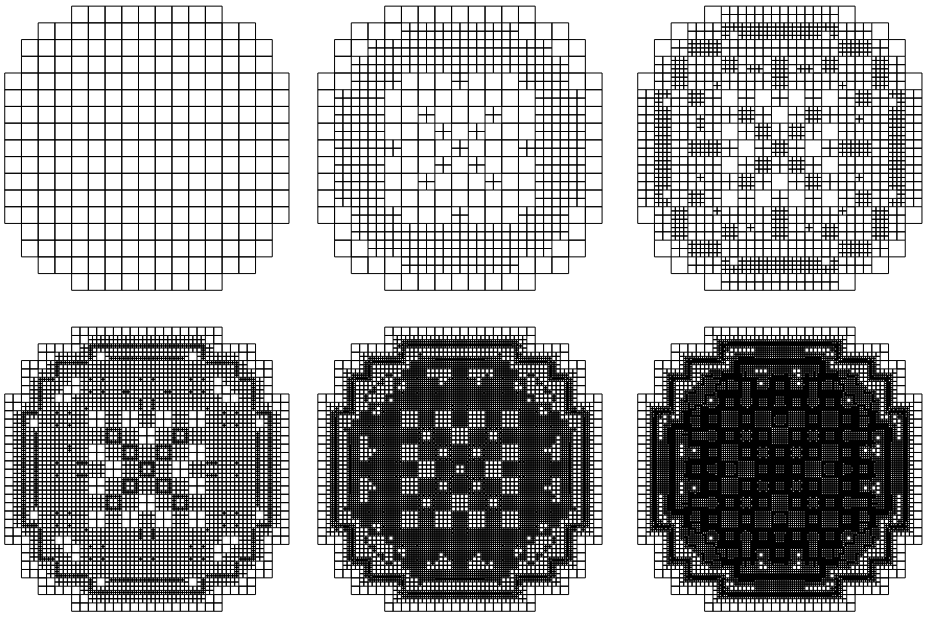

Figure 3.8: Example of 6 iterations in the refination process, refining for the 1st Mode.

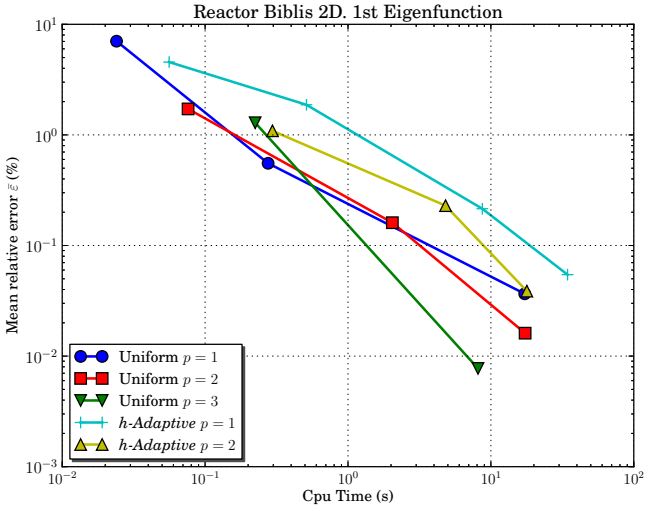

Figure 3.9: Mean error against CPU time for 1st eigenvalue of the BIBLIS Reactor.

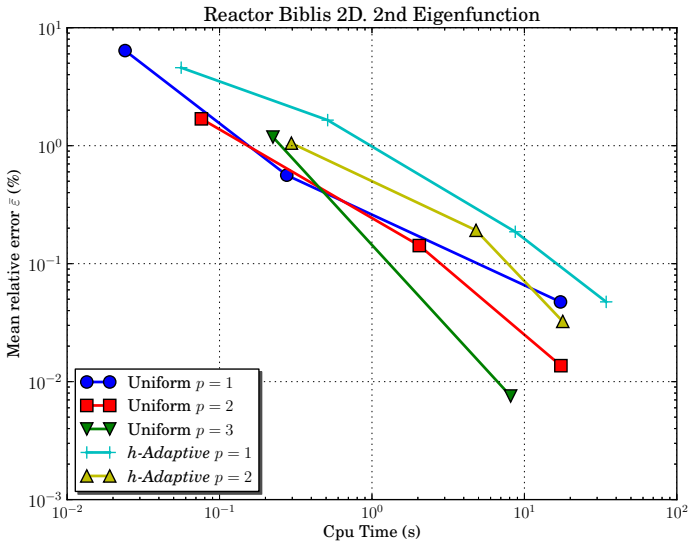

Figure 3.10: Mean error against CPU time for 2nd eigenvalue of the BIBLIS Reactor.

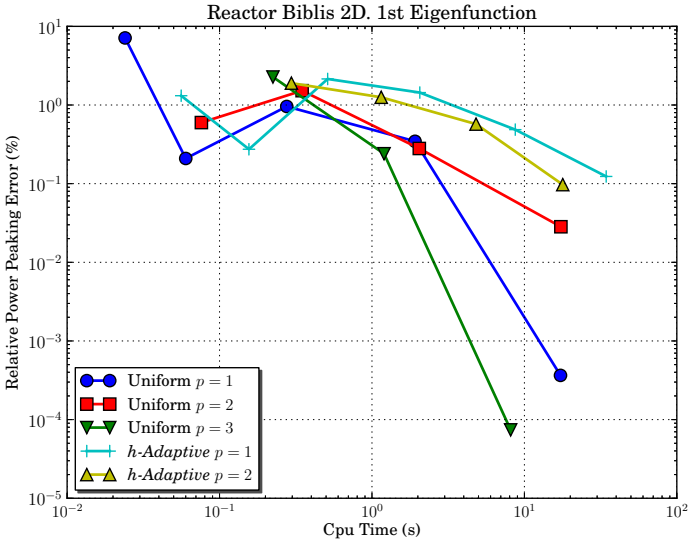

Figure 3.11: Relative power peaking error against CPU time for 1st eigenvalue of the BIBLIS Reactor.

3.6.3 IAEA 3D Reactor

The IAEA PWR 3D benchmark has been solved as an example of a three dimensional reactor. The core is composed of 241 assemblies including 64 assemblies modelling the reflector. The definition of this benchmark is exposed in Appendix B.8. The reference values for the first mode are extracted from American Nuclear Society, (1977) and for the second mode they are extracted from the most converged solution computed, using $36\,632$ elements with $p = 3$.

Figure 3.12 shows the averaged power distribution for the three dominant modes of this reactor. Tables 3.8 and 3.10 display the eigenvalue results for uniform refined meshes and *h*-refined meshes. Also, Tables 3.8 and 3.10 show the power distribution errors for different computation parameters. Figures 3.13 and 3.14 display the convergence graphs (mean cell error against time of execution) for the two dominant eigenvalues. To make hardware independent comparisons of the algorithms, the mean error against the number of the degrees of freedom (DoF) is represented in Figure 3.15. Figure 3.16 shows the computation times against the number of degrees of freedom in order to confirm the relationship. These Figures and Tables show that also for this three dimensional problem the local *h*-refinement is not a better strategy than increasing the polynomial degree uniformly because of the smoothness in the solutions for the fluxes and the computational cost of evaluating the error estimator. For example, a coarse mesh with 4579 cells with $p = 3$ gives better results, $\bar{\varepsilon} = 0.79\%$ and $\Delta\lambda = 8.1$ pcm, than a *h*-refined mesh with 20609 cells and $p = 2$, $\bar{\varepsilon} = 1.54\%$ and $\Delta\lambda = 87$ pcm; even though the first one is faster, 97.5 s against 108.2 s. Also, it is observed that the errors behaviour for the first eigenvalue and its corresponding eigenvector are similar to the errors for the second eigenvector. It can be concluded then, that the best strategy in this case, with a moderate computational cost, is to use finite elements with cubic polynomials with a coarse mesh.

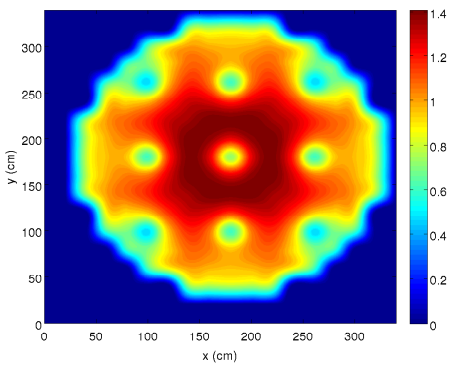

(a) 1st mode (average plane)

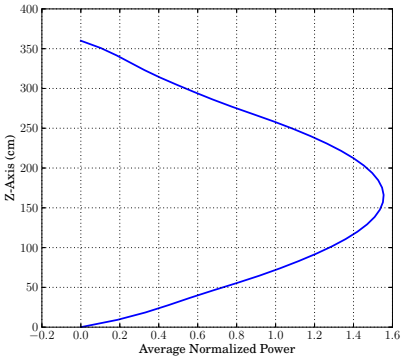

(b) 1st mode (axial profile)

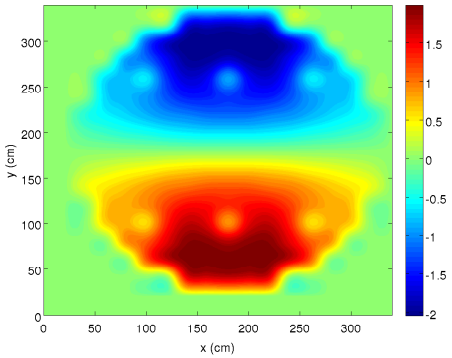

(c) 2nd mode (average plane)

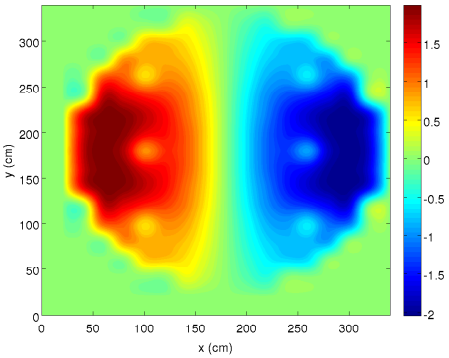

(d) 3rd mode (average plane)

Figure 3.12: Power distribution for the three dominant modes of the IAEA 3D reactor.

Table 3.8: Eigenvalue results with uniform refined meshes in IAEA 3D reactor.

Number of cells	p	**Number of DoF**	**CPU time (s)**	**1st Mode** λ_1	$\Delta\lambda$	**2nd Mode** λ_2	$\Delta\lambda$
4579	1	5520	1.1	1.05039	2069	1.04627	2915
36 632	1	40287	8.7	1.03060	150	1.02061	349
293 056	1	307461	1.1e+2	1.02925	15	1.01773	61
4579	2	40287	1.5e+1	1.03017	107	1.01934	222
36 632	2	307461	1.7e+2	1.02908	2	1.01723	11
4579	3	131776	9.7e+1	1.02914	4	1.01717	5
Reference				1.02910		1.01712	

Table 3.9: Power distribution errors with uniform refined meshes in IAEA 3D reactor.

Number of cells	p	1st Mode $\bar{\varepsilon}$ (%)	1st Mode $\varepsilon_{\max}$	2nd Mode $\bar{\varepsilon}$ (%)	2nd Mode $\varepsilon_{\max}$
4579	1	71.19	2.1	56.41	3.4
36 632	1	11.43	3.4e−1	10.68	4.6e−1
293 056	1	1.76	5.9e−2	2.01	7.7e−2
4579	2	5.78	1.8e−1	5.80	2.1e−1
36 632	2	0.70	9.2e−3	0.92	3.7e−2
4579	3	0.79	2.5e−1	0.79	7.7e−2

Table 3.10: Eigenvalue results with *h*-refined meshes in IAEA 3D reactor.

Number of cells	p	Number of DoFs	CPU time (s)	1st Mode λ_1	1st Mode $\Delta\lambda$	2nd Mode λ_2	2nd Mode $\Delta\lambda$
20 609	1	24 698	5.1	1.02961	51	1.02019	302
103 818	1	125 214	3.6e+1	1.02882	28	1.01752	35
20 609	2	193 466	1.1e+2	1.02992	87	1.01878	161
Reference				1.02910		1.01717	

Table 3.11: Power distribution errors with *h*-refined refined meshes in IAEA 3D reactor.

Number of cells	p	1st Mode $\bar{\varepsilon}$ (%)	1st Mode $\varepsilon_{\max}$	2nd Mode $\bar{\varepsilon}$ (%)	2nd Mode $\varepsilon_{\max}$
20 609	1	25.20	5.6e−1	23.70	6.7e−1
103 818	1	8.22	1.4e−1	9.26	3.2e−1
20 609	2	1.54	2.9e−2	1.64	1.7e−2

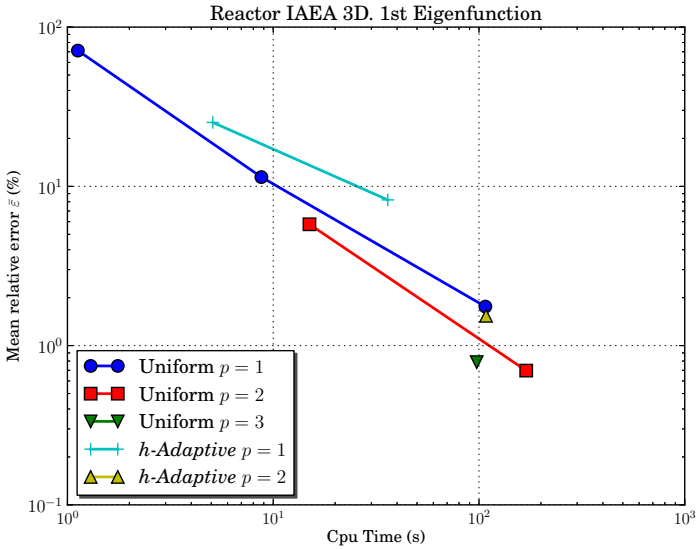

Figure 3.13: Mean error against CPU time for 1st mode of the IAEA 3D reactor.

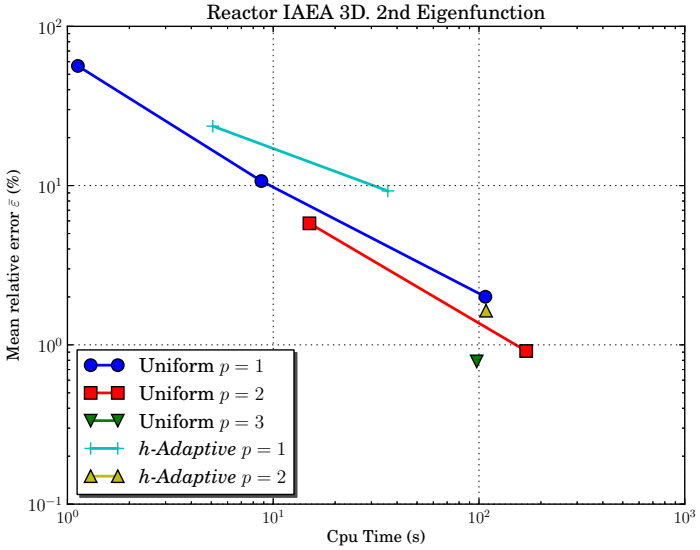

Figure 3.14: Mean error against CPU time for the 2nd mode of the IAEA 3D reactor.

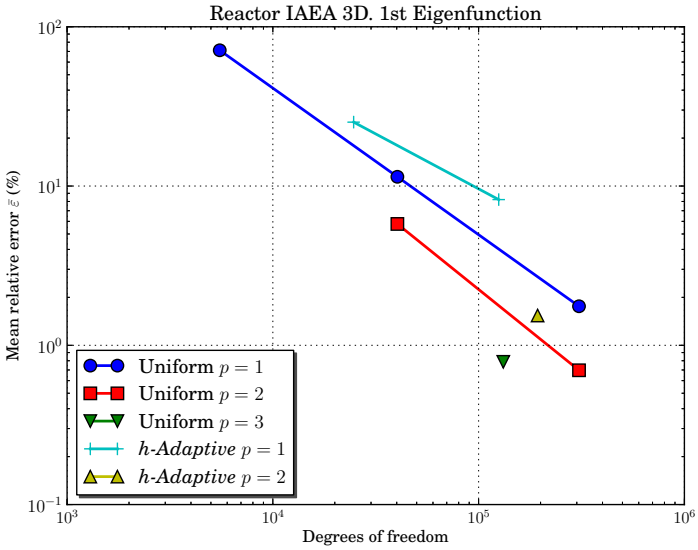

Figure 3.15: Mean relative error against number of degrees of freedom for the 1st mode of the IAEA 3D reactor.

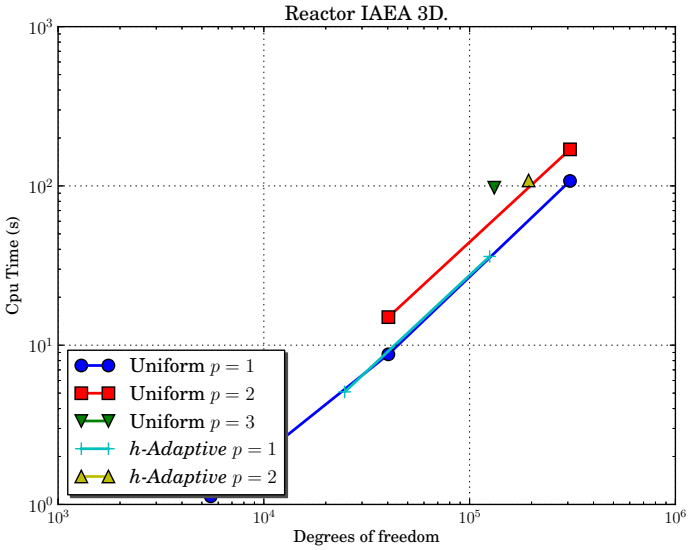

Figure 3.16: CPU time against degrees of freedom for the IAEA 3D reactor.

3.7 Matrix Free Methods

It has been shown above that the *Lambda modes* problem is solved by evaluating discrete differential operators. This makes the operator evaluation and, in particular, matrix-vector products, the central and usually most time-consuming component in a finite element method (FEM) code, as can be seen in the numerical results presented in the previous Section. It must be noted that solving iteratively a linear system, can be seen as computing a certain number of matrix-vector products. Thus, we focus on restructuring this basic operation.

Also, one of the main drawbacks of the presented *h-p*-finite element method is the quantity of memory used to store the matrix elements, despite of they are saved in a sparse way. Instead of assembling a sparse matrix and using it for matrix–vector products, this operation can be applied by cell-wise quadrature (Kronbichler and Kormann, 2012). The evaluation of shape functions can be implemented with a sum-factorization approach. In this Section, it is presented a framework that exploits the special structure of the finite element operation as the differential operator is applied. Instead of assembling a global sparse matrix, we only store the unit cell shape function information, the enumeration of degrees of freedom, and the transformation from unit to the real cell. Recently, cell-based strategies without explicit matrix storage have been considered for GPU programming (Komatitsch et al., 2010).

The number of nonzero elements per row in the matrix for a $(p-1)$*th* order finite element in d dimensions is proportional to p^d, rendering high order methods increasingly expensive. If we split the application of the FEM operator into a function evaluation and integration step described by unit cell shape functions and derivatives, the shape information can be applied for one dimension at a time for basis functions that are derived from a tensor product. This restructuring reduces the computational complexity to d^2p operations per degree of freedom and is usually referred to as sum-factorization (Melenk, Gerdes, and Schwab, 2001).

The cell-based without explicit matrix storage implementation of a matrix-vector product can be summarized as,

$$v = \mathbf{A}u = \sum_{k=1}^{K} R_k^T \mathbf{A_k} \left(R_k u\right) = \sum_{k=1}^{K} \mathbf{A_k} u_k \,, \tag{3.30}$$

where R_k denotes the restriction operation from the global ordering and the cell ordering and $\mathbf{A_k}$ is the local matrix related to cell k. In order to see the implementation details to efficiently compute the local matrix-vector product, $\mathbf{A_k}u_k$, the reader is refereed to Kronbichler and Kormann, (2012).

The main problem derived from the matrix-free implementation is that linear systems cannot be solved with traditional preconditioners as the matrix elements are not stored explicitly. As preconditioning is essential to solve the linear system related to the eigenvalue problem solver iterations in reasonable computational times, only mass-matrices are used in a matrix-free way. Thus, $\mathbf{L_{gg}}$ diagonal blocks are stored explicitly and all the other blocks are computed in a matrix-free fashion. This implementation reduces significantly the memory used to store the matrices without affecting negatively the computational times.

As explained in Kronbichler and Kormann, (2012) matrix-free implementation of matrix-vector product can be faster than usual sparse matrix-vector multiplication (SpMVs) due to the reduction of memory requirements and cache memory optimization. A reduced memory requirement of the matrix-vector product promises improved wall times through higher Gflop rates (billion arithmetic operations per second) because spares matrix-vector multiplication are usually limited by memory bandwidth rather than arithmetic throughput. Even though attempts have been made to tune kernels (Williams et al., 2007), Gflops rates rarely exceed 2–20% of peak arithmetic throughput.

Table 3.12 shows a comparison between the proposed matrix-free implementation and the SpMVs implementation. The Table presents the CPU time and memory used by the program for the IAEA 3D reactor using different finite element polynomial degrees. The results show that the total memory used is reduced more than 50% when the matrix storage is the most demanding process. Particularly, 47% for $p = 2$, 52% for $p = 3$ and 55% for $p = 4$. Also, the computational time has been slightly reduced about a 10% due to the optimization of the values stored in the cache memory.

Table 3.12: SpMVs and matrix-Free comparison in the IAEA 3D reactor.

		SpMVs		**Matrix-Free**	
p	**Number of DoFs**	**CPU Time** (s)	**Memory** (MB)	**CPU Time** (s)	**Memory** (MB)
1	5520	1.1	6.4e+1	9.2e−1	5.4e+1
2	40 287	1.5e+1	4.3e+2	1.3e+1	2.3e+2
3	131 776	9.7e+1	2.3e+3	8.9e+1	1.1e+3
4	307 461	5.2e+2	8.9e+3	4.7e+2	4.0e+3

3.8 Preconditioning

Because of the discretization with the FEM, the block matrices of the diagonal are large, sparse, symmetric and positive definite. Thus, the related linear systems are well suited to be solved with an iterative Krylov subspace method, as the conjugate gradient method. As we have to solve several linear systems with the diagonal block-matrices, $\mathbf{L_{gg}}$, it pays off to spend a bit more time once to create a good preconditioner for these matrices.

In general terms, a preconditioner is any form of modification of an original linear system which makes it "easier" to solve by a given iterative method (Saad, 2003). In other words, the original linear system

$$Ax = f\,, \tag{3.31}$$

is transformed into

$$(P\,A)\,x = Pf = c\,, \tag{3.32}$$

such that the new system matrix $(P\,A)$ has a smaller condition number than A or it increases the convergence rate of the iterative method. The classical preconditioning of matrices derived from FEM discretization are based on an incomplete matrix factorization. Nevertheless, the computation of such factorizations requires to store the sparse matrices in the computer memory, in addition to the computed preconditioners, which results in large requirements of memory resources. These memory requirements can be lowered by different fill-in or threshold criteria for the preconditioner, although the minimum memory requirement remains large if a fast preconditioner is used. To solve this problem, alternative preconditioning techniques are studied, which are based on the domain decomposition methodology, aiming at lowering the memory requirements when high order Finite Element Methods are used.

Domain decomposition methods were first proposed by Schwarz (Schwarz, 1870) as an analytical tool. A renewed interest in this kind of methods was noticed with the appearance of parallel computers (Smith, Bjorstad, and Gropp, 2004). These methods were first proposed to solve partial differential equations on complex domains and later these techniques were extended to solve linear equations (see (Gander, 2008) and references therein). The algebraic Schwarz methods are based on partitioning the vector of unknowns into subsets, which correspond to a partition of the coefficients matrix, typically associated with different subdomains in the continuous problem. The solution of the whole system is achieved by solving the systems associated with the different blocks of the partitioned matrix, which are simpler problems than the original one. Schwarz methods to solve linear systems are not as competitive as other alternative methods such as multi-grid

solvers, but they can be used as efficient preconditioners of Krylov methods, at the cost of a few more iterations.

Domain decomposition methods in nuclear engineering have been receiving increasing attention for the last years due to their potential to solve large problems by using a *divide-and-conquer* strategy. For example, a Schur complement is used to accelerate the core solver in Barrault et al., (2011). In Jamelot, Baudron, and Lautard, (2012); Jamelot and Ciarlet, (2013) a method based on the Schwarz iterative algorithm is studied to solve the mixed neutron diffusion and the simplified spherical harmonics neutron equation. Finally, the response matrix method that implements a two-level model, a global and a local level, was analysed in Cossa, Giusti, and Montagnini, (2010) and in Rathkopf and Martin, (1986). The local level is defined on a mesh fine enough to provide accurate results while the global level is defined on a coarse mesh which accelerates the convergence of the method. The methodology for linking the local and global solutions is the key aspect of the response matrix method.

In this Section, some of the classical preconditioning methods are reviewed starting by direct solvers, the ultimate preconditioner, and incomplete factorizations of the coefficient matrices (Saad, 2003). Then, the Schur complement method to separate the interior unknowns from the rest of the unknowns is studied in Section 3.8.3. To solve the Schur complement system substructuring preconditioners are defined in Section 3.8.4. Advanced versions of substructuring preconditioners, the Restricted Additive Schwarz preconditioner is described in Section 3.8.5. The chapter is concluded with a comparison among these preconditioners in a two dimensional and a tree dimensional benchmark.

3.8.1 Direct Solvers

Direct methods to solve sparse linear systems perform an LU factorization of the original matrix and try to reduce cost by minimizing *fill-ins*, i.e., nonzero elements introduced during the elimination process in positions which were initially zeros. (Saad, 2003). In order to compute fast LU factorizations, for example, UMFPACK library (Davis, 2004) or SuperLu library (Demmel et al., 1999) can be used.

A typical sparse direct solver for positive definite matrices consists of four phases. First, preordering is applied to reduce fill-in. Two popular methods are used: minimum degree ordering and nested-dissection ordering. Second, a symbolic factorization is performed. This means that the factorization is processed only symbolically, i.e., without numerical values. Third, the numerical factorization,

in which the actual factors L and U are formed, is processed. Finally, the forward and backward triangular sweeps are executed for each different right-hand side.

It must be noted that a direct method is the fastest solver for one dimensional and two dimensional problems, even though they use more memory than most of the other preconditioners. In two dimensional geometries, we can use complete LU factorizations because even reasonably large problems rarely have more than a few $100\,000$ unknowns with relatively few nonzero entries per row. Furthermore, the bandwidth of matrices is $\mathcal{O}(\sqrt{N})$ and therefore moderate. For such matrices, sparse factors can be computed in a matter of a few seconds. As a point of reference, computing the sparse factors of a matrix of size N and bandwidth B takes $\mathcal{O}(NB^2)$ operations. In two dimensional geometries, this is $\mathcal{O}(N^2)$; though this is a higher complexity than, for example, assembling the linear system which takes $\mathcal{O}(N)$, the constant for computing the decomposition is so small that it doesn't become the dominating factor in the entire program until we get to very large numbers of unknowns in the high $100\,000$ or more (Bangerth, Hartmann, and Kanschat, 2007).

The situation changes when we compute three dimensional problems because the number of unknowns and the bandwidth of the matrix, quickly increase. In this case the matrix bandwidth, which determines the number of fill-ins, is $O(N^{2/3})$. This makes using a sparse direct solver inefficient because the memory requirements become impractical. Usually, what we do in that case is to use an incomplete LU decomposition (ILU) as a preconditioner combined with an iterative method, rather than actually computing the complete LU factorization.

3.8.2 Incomplete Factorization Methods

One of the simplest ways of defining a preconditioner is to perform an incomplete factorization of the original matrix A. An incomplete factorization seeks triangular matrices L, U such that $A \approx LU$ rather than $A = LU$ in a complete factorization. Solving for $LUx = b$ can be done quickly but does not yield the exact solution to $Ax = b$ so it can be used only as preconditioner of an iterative method . If L and U have the same nonzero structure as the lower and upper parts of A, this factorization is known as ILU(0) and it is the less expensive to compute. If the underlying matrix structure can be referenced by pointers instead of copied, the only extra memory required is for the entries of L and U. On the other hand, it leads to a crude approximation which may result in the iterative solver requiring several iterations to converge.

To remedy this, several alternative incomplete factorizations have been developed by allowing more fill-in in L and U. A common choice is to use the sparsity pattern of A^2 instead of A; this matrix is appreciably more dense than A, but still sparse over all. This preconditioner is called ILU(1). One can then generalize this procedure; the ILU(k) preconditioner of a matrix A is the incomplete LU factorization with the sparsity pattern of the matrix A^{k+1}. More accurate ILU preconditioners require more memory, to such an extent that eventually the running time of the algorithm increases even though the total number of iterations decreases. Consequently, there is a cost/accuracy trade-off that users must evaluate, typically on a case-by-case basis depending on the family of linear systems to be solved.

Computing the ILU takes a time that only depends on the number of non-zero entries in the sparse matrix, or that we are willing to fill in the LU factors, if these should be more than the ones in the matrix, but is independent of the bandwidth of the matrix. It is therefore an operation that can efficiently also be computed for three dimensional problems. To see more details about the incomplete LU factorization and more sophisticated versions as the ILUT the reader is referred to Saad, 2003, Chapter 10.

3.8.3 Schur Complement Method

Lagrange polynomials used in the high order finite element method, as stated in Section 3.2.3, provide a natural partition of the set of degrees of freedom (DoFs) into vertices, edges, faces and interior shape functions as can be seen in Figure 3.17. Figure 3.17 shows a representation of the substructuring decomposition for a two-dimensional domain using polynomials of degree 3. Thus, after the spatial discretization, the linear system $Ax = f$ can be expressed as

$$\begin{pmatrix} A_{II} & A_{IV} & A_{IE} & A_{IF} \\ A_{IV}^T & A_{VV} & A_{VE} & A_{VF} \\ A_{IE}^T & A_{VE}^T & A_{EE} & A_{EF} \\ A_{IF}^T & A_{VF}^T & A_{EF}^T & A_{FF} \end{pmatrix} \begin{pmatrix} x_I \\ x_V \\ x_E \\ x_F \end{pmatrix} = \begin{pmatrix} f_I \\ f_V \\ f_E \\ f_F \end{pmatrix} \tag{3.33}$$

where the subscript I refers to the degrees of freedom related to the interior of the cells, and the subscripts V, E and F refer to the degrees of freedom related with the vertices, edges and faces, respectively.

We notice here that the interior DoFs of each cell are decoupled from the interior DoFs of the other cells. Thus, it allows us to apply the Schur complement method

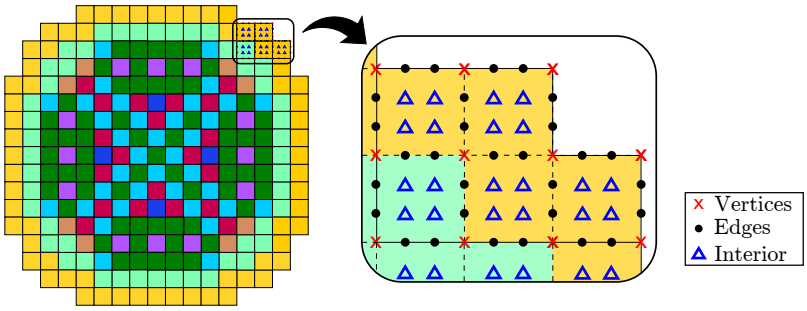

Figure 3.17: A model of a reactor and the representation of the different degrees of freedom using cubic polynomials in a two-dimensional problem.

as

$$\begin{pmatrix} A_{II} & A_{IB} \\ A_{IB}^T & A_{BB} \end{pmatrix} \begin{pmatrix} x_I \\ x_b \end{pmatrix} = \begin{pmatrix} f_I \\ f_B \end{pmatrix} , \tag{3.34}$$

where the block A_{II} is a block diagonal matrix, every block being the block matrix of the cell local interior nodes, i.e,

$$A_{II} = \text{diag}\{A_{1,\,II},\ \ldots,\ A_{k,\,II},\ \ldots,\ A_{K,\,II}\} , \tag{3.35}$$

and the matrix A_{BB} is composed of the matrices for the interfaces. In other words, the matrix contains the terms related with the vertices, edges and faces. Then we solve the system for the interior DoFs, which is block diagonal and thus easy to invert using a complete Cholesky factorization, and obtain a system for the boundary degrees of freedom, which is written as

$$S x_B = f_S , \tag{3.36}$$

where

$$S = A_{BB} - A_{IB}^T A_{II}^{-1} A_{IB} , \quad f_S = f_B - A_{IB} A_{II}^{-1} f_I .$$

Once the Schur complement system (3.36) is solved, the interior unknowns can be obtained by simple matrix multiplication,

$$x_I = A_{II}^{-1}(f_I - A_{IB}^T x_B) .$$

Inside a finite element partitioning the Schur complement matrix can be built locally as a sum of the contribution in each cell, S_k, as follows (Saad, 2003),

$$S = \sum_{k=1}^{K} S_k = \sum_{k=1}^{K} \left(A_{k,\,BB} - A_{k,\,IB}^T A_{k,\,II}^{-1} A_{k,\,IB} \right) , \tag{3.37}$$

where $A_{k,\_}$ is the corresponding local block matrix associated with the cell k. Then, the system matrix A does not need to be built explicitly to construct its Schur complement matrix.

It is worth to notice here that since the Schur complement is the stiffness matrix associated with a subspace of the space generated by the original basis, its condition number is bounded by the condition number of the complete matrix A and is typically far better (Sherwin and Casarin, 2001).

A disadvantage of this approach is the additional expense of constructing the Schur complement matrix. For a single system this expense can outweigh the advantage of solving a better conditioned system for low order in the polynomial expansions (Pardo et al., 2015). However, for the resolution of the *Lambda modes problem* each matrix has to be solved several times with different right hand sides. Thus, the computational cost of constructing the Schur complement matrix is overcome by the number of linear systems to be solved.

3.8.4 Substructuring preconditioners

In the same way as the original matrix, the Schur complement matrix has a structure that can be algebraically separated into vertices, edges and faces degrees of freedom. The methods based on this kind of partition of the high order finite element shape functions are called substructuring methods. We use this partition of the DoFs to provide the Schur complement system (3.36) with the following structure

$$\begin{pmatrix} S_{VV} & S_{VE} & S_{VF} \\ S_{VE}^T & S_{EE} & S_{EF} \\ S_{VF}^T & S_{EF}^T & S_{FF} \end{pmatrix} \begin{pmatrix} x_{B,V} \\ x_{B,E} \\ x_{B,F} \end{pmatrix} = \begin{pmatrix} f_{S,V} \\ f_{S,E} \\ f_{S,F} \end{pmatrix} , \tag{3.38}$$

Thus, a substructuring preconditioner for this system can be defined as,

$$P = \begin{pmatrix} B_{VV} & 0 & 0 \\ 0 & B_{EE} & 0 \\ 0 & 0 & B_{FF} \end{pmatrix}^{-1} . \tag{3.39}$$

where different substructuring preconditioners for the Schur complement matrix are defined in the next subsections by different choices for B_{VV}, B_{EE}, B_{FF}.

Preconditioner P_D

The simplest preconditioner for the Schur complement matrix is to use only use the diagonal of the local matrices for preconditioning, i.e.,

$$\begin{aligned} B_{VV} &= \text{diag}\left(S_{VV}\right), \\ B_{EE} &= \text{diag}\left(S_{EE}\right), \\ B_{FF} &= \text{diag}\left(S_{FF}\right), \end{aligned}$$

implementing a Diagonal Jacobi preconditioner.

Preconditioner P_V

As with the original matrix, A, the preconditioner can be improved if the sub-matrix of vertices is solved in the preconditioner. This matrix is also explicitly assembled and Cholesky factorized. In this case, the preconditioner sub-matrices are defined as,

$$\begin{aligned} B_{VV} &= S_{VV}, \\ B_{EE} &= \text{diag}\left(S_{EE}\right), \\ B_{FF} &= \text{diag}\left(S_{FF}\right). \end{aligned}$$

Preconditioner P_{VEF}

Similarly to the original matrix, the sub-matrices S_{EE} and S_{FF} represent the whole set of edges and faces degrees of freedom, respectively. For the Schur complement preconditioner P_{VEF} each edge and each face is considered independently. Thus, B_{EE} and B_{FF} also have a block diagonal structure. The preconditioner blocks are defined by,

$$\begin{aligned} B_{VV} &= S_{VV}, \\ B_{EE} &= \text{block-diag}\left(S_{EE}\right), \\ B_{FF} &= \text{block-diag}\left(S_{FF}\right). \end{aligned}$$

3.8.5 Restricted Additive Schwarz Preconditioner

Another possibility of preconditioning the system (3.38) consists of introducing overlapping between the subdomains by including the degrees of freedom related

to the vertices and edges in the different blocks, referred as Additive Schwarz preconditioner. This preconditioner is an extension of the classical alternating Schwarz method at the continuous level (Schwarz, 1870), formulated by Schwarz in 1870. This method sequentially solves the Laplace equation in two continuous subdomains. The projection interpretation of the alternating Schwarz method led to the Additive Schwarz preconditioner defined at the matrix level. It should be noted that the additive Schwarz method will not converge in general, but nevertheless can be efficiently used to accelerate a Krylov subspace method (Saad, 2003).

In this work, a Restricted Additive Schwarz (RAS), as the one defined as in Cai and Sarkis, (1999), is used to accelerate the Schur complement system of equation (3.36). In (Efstathiou and Gander, 2003) it is studied from a theoretical point of view why this preconditioner usually has better convergence properties than the unrestricted Additive Schwarz. The RAS is defined as,

$$P_{\text{RAS}} = \sum_{k=1}^{K} R_k^T X_k \left(R_k S R_k^T \right)^{-1} R_k, \tag{3.40}$$

where k is the index running the finite element cells. R_k denotes the restriction operator from the global domain to the cell k. R_k^T is the corresponding interpolation operator, from the local to the global domain. Finally, X_k is a partition of unity matrix that scales the contribution of each degree of freedom depending on the number of subdomains where it is present. The partition of the unity matrix is the key aspect which distinguishes the restricted version from the unrestricted version of the additive Schwarz preconditioner (Cai and Sarkis, 1999). It is important to note that the RAS preconditioner yields to non-symmetric iterations even for symmetric matrices. Thus, iterative solvers capable of dealing with non-symmetric system must be used, as the GMRES method.

The main difference between substructuring preconditioner and the RAS preconditioner is the presence of overlapping between subdomains in the RAS, building a preconditioner more complicated than a simple block Jacobi preconditioner. Figure 3.18 shows the subdomain decomposition of the block Jacobi preconditioner and the Additive Schwarz preconditioner for the Schur complement matrix. This type of partitioning is similar to the one used in (Carvalho, Giraud, and Le Tallec, 2001).

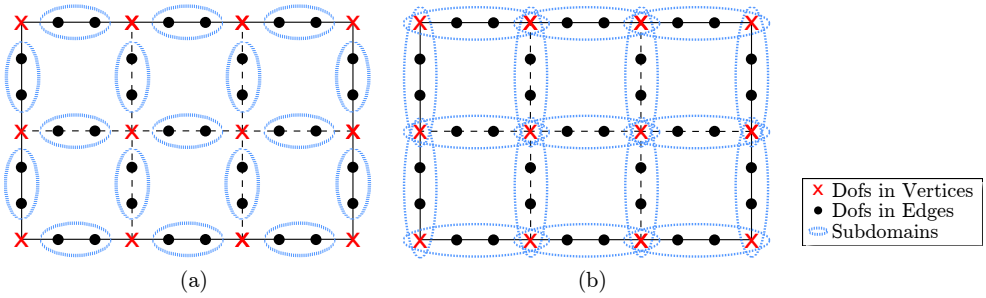

Figure 3.18: Subdomains decomposition of (a) substructuring preconditioner and (b) the Additive Schwarz preconditioner.

3.8.6 Numerical Results

A two-dimensional and a three-dimensional problems in the approximation of two energy groups have been considered to study the performance of the proposed preconditioners to accelerate the solution of the linear systems associated with every iteration of the eigenvalue problem solver. To compare the performance of the different preconditioners the average number of iterations needed to solve the systems related to $\mathbf{L_{11}}$ and $\mathbf{L_{22}}$ in the eigenvalue calculation is used. Also the memory used by the matrix objects and the preconditioners is shown.

2D BIBLIS Reactor

First, the BIBLIS 2D benchmark defined in Appendix B.6 is considered. In Table 3.4, it is shown the accuracy obtained with the finite element method using different FEM polynomial degrees (p). It is observed that it is necessary to use high degree polynomials in the finite element method to obtain solutions of the problem with high accuracy. The eigenvalue calculation is performed with the Krylov-Schur method for the first 4 eigenvalues. It must be noted that every linear system related to $\mathbf{L_{11}}$ and $\mathbf{L_{22}}$ will be solved 48 times since the eigenvalues problem solver needs 48 iterations to converge the problem with the desired relative tolerance.

Tables 3.13 and 3.14 display the performance of the different preconditioners for the Schur complement matrix in terms of the average number of iterations, memory used by the matrix related elements, and CPU time used to compute the solution for $p = 3$ and $p = 5$ degrees in the finite element method. These numer-

ical results show a decrease of the number of iterations as the preconditioners become more complete. However, this improvement in the number of iterations does not represent an improvement in the computational time. The reason is that this benchmark is not big enough to show a time reduction in the Schwarz methodology, compensating the extra overhead needed to assemble and decompose the different sub-matrices. The ILU(0) preconditioner is not the best neither, due to the fact that the diagonal preconditioner P_d is very fast to compute, so that the small reduction of the iteration counts is enough when considering the reduced cost of applying and computing the preconditioner. Moreover, it can be observed that the reduction in the number of iterations for the matrix $\mathbf{L_{11}}$ is different from the reduction obtained for $\mathbf{L_{22}}$, i.e., the preconditioners used here are sensitive to the coefficients of the equation. As it has been mentioned above, the best performance is obtained if a direct method based on the LU decomposition is used.

Figures 3.19a and 3.19b show the average number of iterations for solving the system related to the matrix $\mathbf{L_{11}}$ and $\mathbf{L_{22}}$, respectively using finite elements from degree 1 to degree 9. In these Figures, it can be seen that the number of iterations grows as the finite element degree increases in an almost linear way. This can be explained because when p is increased the number of non-zeros inside the matrix is enlarged and thus its condition number. However, the number of iterations show a particular behaviour for low degree finite elements because of the relative importance of the degrees of freedom related to the vertices in these matrices.

Table 3.13: Preconditioners performance for BIBLIS reactor with $p = 3$.

Preconditioner	**Avg. its. $\mathbf{L_{11}}$**	**Avg. its $\mathbf{L_{22}}$**	**Memory** (MB)	**Time** (s)
None	18.9	22.0	0.86	0.27
P_D	16.1	13.0	0.86	0.20
P_V	16.1	11.9	0.98	0.29
P_{VEF}	15.1	11.0	1.1	0.51
P_{RAS}	13.0	9.5	1.1	0.44
$P_{\text{ILU(0)}}$	7.0	5.0	1.6	0.22
LU	-	-	2.7	0.16

Table 3.14: Preconditioners performance for BIBLIS reactor with $p = 5$.

Preconditioner	**Avg. its.** $\mathbf{L_{11}}$	**Avg. its** $\mathbf{L_{22}}$	**Memory** (MB)	**Time** (s)
None	25.0	23.3	3.9	0.80
P_D	23.0	13.0	3.9	0.69
P_V	23.2	13.0	4.1	0.74
P_{VEF}	20.9	12.5	4.3	1.10
P_{RAS}	17.8	10.0	4.4	0.92
$P_{\text{ILU(0)}}$	9.0	6.0	6.0	0.75
LU	-	-	10.2	0.62

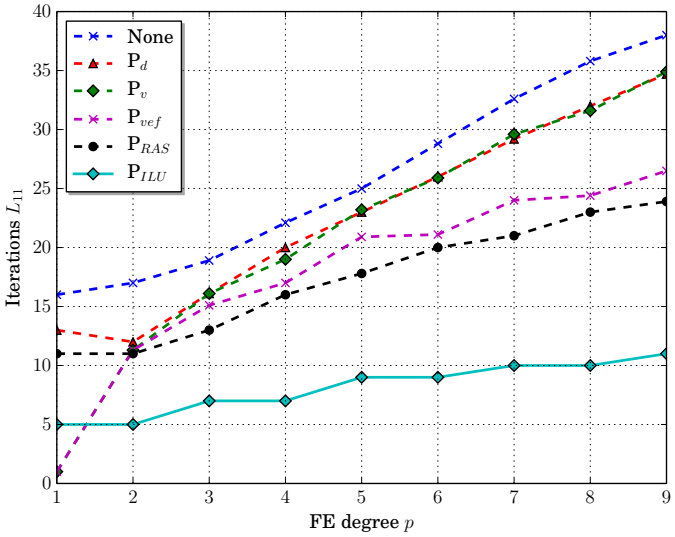

(a) Iterations for $\mathbf{L_{11}}$ system.

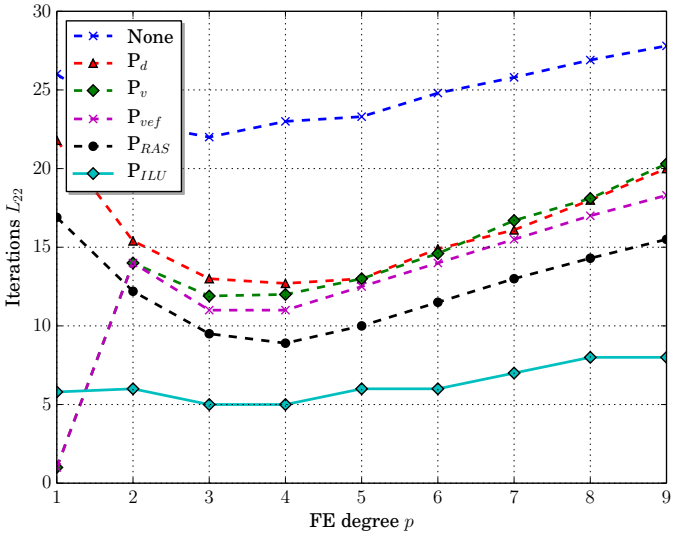

(b) Iterations for $\mathbf{L_{22}}$ system.

Figure 3.19: Averaged number of iterations depending on the finite element degree used for BIBLIS reactor.

3D IAEA Reactor

As a second problem, the IAEA PWR 3D benchmark (American Nuclear Society, 1977) is considered. Table 3.8 shows a summary of the size of the problem and the accuracy of the solutions for different degrees of the polynomials, p, used in the finite element method. As in the case of the previous benchmark, to obtain accurate solutions it is necessary to use high degree polynomials in the finite element method.

Tables 3.15 and 3.16 display the performance of the different preconditioners in terms of the average number of iterations, memory used by the matrix related elements and the CPU time needed to solve the eigenvalue problem when the degrees $p = 3$ and $p = 5$ are used in the finite element method. These Tables show a decrease of the number of iterations as the preconditioners become more complete. However, this improvement in the number of iterations does not always represent a decrease in the computational time because of the extra overhead needed to build and apply the preconditioner. Also, it can be seen that the partial preconditioner including the vertices, P_V, does not present significant improvement with respect to the previous preconditioners P_D, which is much faster to build and apply. However, when the preconditioner includes the terms related with the vertices edges and face, P_{VEF}, a significant improvement is achieved. It must be also noted, that the use of the direct method based of a LU decomposition is a bad choice for this three dimensional problem. Due the high memory requirements, about 45 GB, the complete LU decomposition is not computed for $p = 5$.

Nevertheless, for this benchmark, the fastest preconditioner is the proposed $\mathrm{P}_{\mathrm{RAS}}$, where the gain in CPU time is larger for the highest polynomial degree used. Here, although the number of iterations needed by the preconditioner based on the ILU(0) decomposition is smaller, the time used to construct this preconditioner and to apply it, is larger than for the preconditioner based on the Schwarz method. It means that the saving in the memory usage is also improving the calculation time, because a smaller preconditioner is not only much faster to build, but also faster to apply.

Figures 3.20a and 3.20b show the average number of iterations for solving the system related to the matrix $\mathbf{L_{11}}$ and $\mathbf{L_{22}}$, respectively using finite elements from degree 1 to degree 6. In these Figures, it can be seen that the number of iterations grows as the finite element degree increases in an almost constant way. This can be explained because increasing p enlarges the number of non-zeros inside the matrix and thus its condition number. However, the number of iterations show

a particular behaviour for low degree finite elements, $p = 1$ and $p = 2$, because these matrices are almost composed of degrees of freedom related to the vertices.

Table 3.15: Preconditioners performance for IAEA 3D reactor using $p = 3$.

Preconditioner	**Avg. its. $\mathbf{L_{11}}$**	**Avg. its $\mathbf{L_{22}}$**	**Memory** (MB)	**Time** (s)
None	36.6	42.6	220	130
P_D	23.0	17.3	220	60
P_V	22.4	16.6	230	63
P_{VEF}	21.9	15.0	240	63
P_{RAS}	16.0	11.2	290	53
$P_{\text{ILU(0)}}$	8.0	6.0	500	72
LU	-	-	4800	699

Table 3.16: Preconditioners performance for IAEA 3D reactor with $p = 5$.

Preconditioner	**Avg. its. $\mathbf{L_{11}}$**	**Avg. its $\mathbf{L_{22}}$**	**Memory** (MB)	**Time** (s)
None	48.7	47.6	2500	1500
P_D	35.1	25.1	2500	1200
P_V	34.8	24.8	2500	1200
P_{VEF}	29.0	22.1	2500	890
P_{RAS}	23.9	17.9	2800	800
$P_{\text{ILU(0)}}$	11.0	8.9	4600	1280

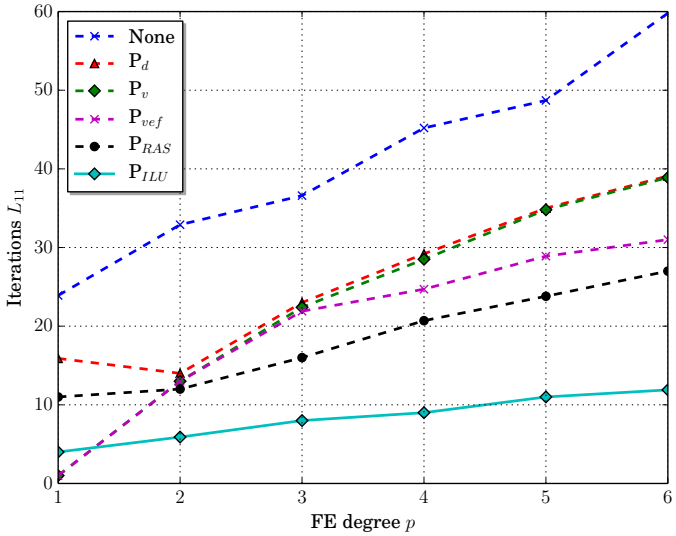

(a) Iterations for $\mathbf{L_{11}}$ system.

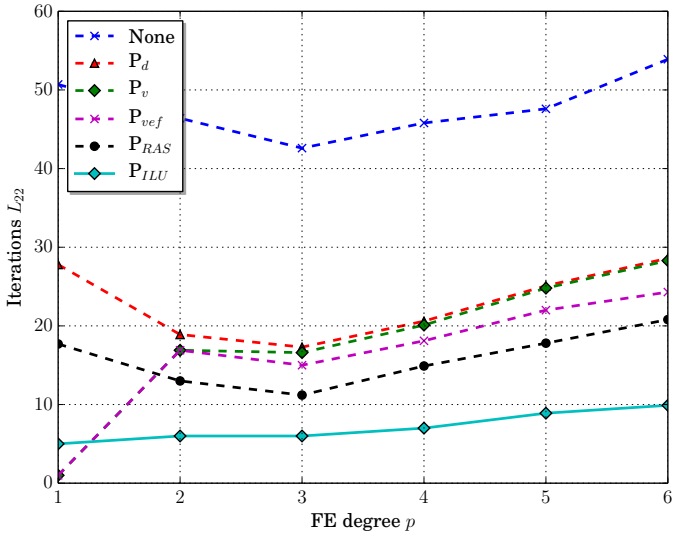

(b) Iterations for $\mathbf{L_{22}}$ system.

Figure 3.20: Averaged number of iterations depending on the finite element degree used for the IAEA 3D reactor.

4 Time Dependent Neutron Diffusion Equation

4.1 Introduction

For a given transient, the balance of neutrons inside a nuclear reactor core can be modelled using the time dependent neutron transport equation. This equation is usually approximated with the diffusion equation with two energy groups assuming that fission neutrons are born in the fast group and there is no up-scattering (Stacey, 2007). This approximation is of the form of

$$[\mathrm{v}^{-1}]\frac{\partial \Phi}{\partial t} + \mathcal{L}\Phi = (1-\beta)\mathcal{M}\Phi + \sum_{p=1}^{N_p} \lambda_p \chi \mathcal{C}_p \quad , \tag{4.1}$$

$$\frac{\partial \mathcal{C}_p}{\partial t} = \beta_p \left(\nu\Sigma_{f1}\ \nu\Sigma_{f2}\right)\Phi - \lambda_p \mathcal{C}_p\,, \quad p = 1,\ \ldots,\ N_p, \tag{4.2}$$

where, N_p is the number of delayed neutron precursor groups considered and the matrix operators are defined as

$$\mathcal{L} = \begin{pmatrix} -\vec{\nabla}\cdot(D_1\vec{\nabla}) + \Sigma_{a1} + \Sigma_{12} & 0 \\ -\Sigma_{12} & -\vec{\nabla}\cdot(D_2\vec{\nabla}) + \Sigma_{a2} \end{pmatrix}, \ [\mathrm{v}^{-1}] = \begin{pmatrix} \frac{1}{\mathrm{v}_1} & 0 \\ 0 & \frac{1}{\mathrm{v}_2} \end{pmatrix},$$

$$\mathcal{M} = \begin{pmatrix} \nu\Sigma_{f1} & \nu\Sigma_{f2} \\ 0 & 0 \end{pmatrix}, \quad \Phi = \begin{pmatrix} \phi_1 \\ \phi_2 \end{pmatrix}, \quad \chi = \begin{pmatrix} 1 \\ 0 \end{pmatrix},$$

where ϕ_1 and ϕ_2 are the fast and thermal neutron fluxes, respectively. The diffusion constants and cross-sections, D_g, Σ_{12}, Σ_{ag}, $\nu\Sigma_{fg}$, $g = 1,\ 2$, appearing in the

equations depend on the reactor materials, that is, they are position and time dependent functions. $\mathcal{C}_p$ is the concentration of neutron precursors, β_p is the yield of delayed neutrons in the p-th precursors group and λ_p is the corresponding decay constant. These coefficients are related to the delayed neutron precursor decay.

The spatial discretization of the neutron diffusion equation has been studied in Chapter 3. There, an *h-p*-finite element method has been studied to solve the *Lambda modes problem* and to study the steady state of a nuclear reactor core.

Different methods have been proposed for the time discretization of the time-dependent neutron diffusion equation (Verdú et al., 1995). Standard methods use backward difference formulas (Ginestar et al., 1998). These methods, for each time step, need to solve a system of linear equations, which is large and sparse. Preconditioned iterative methods are used to solve these systems (Bru et al., 2002), (González-Pintor, Ginestar, and Verdú, 2014). Other kind of methods such as modal methods (Miró et al., 2002) or the quasi-static method (Dulla, Mund, and Ravetto, 2008) have been also used in the nuclear engineering field.

Some transient calculations in reactor cores are based on dynamic changes in the reactor configuration due to the movement of control rods, which are usual manoeuvres in the reactor operation. The simulation of these transients presents what is known as the *rod-cusping* problem. This problem is a non-physical behaviour of different magnitudes as the neutron power and the multiplicative constant of the reactor along the transient. This problem is caused by the use of fixed mesh schemes and averaged material properties for the partially rodded node, as Figure 4.1 represents. When a control rod is partially inserted in a node, this node is divided into two parts: the upper part of the node, where the cross sections are modified due to the effect of the control rod, and the lower part of the node, which has the cross sections without modifications and the cross sections of the whole node are calculated by means of an interpolation procedure taking into account the position of the control rod tip.

In this Chapter, a moving mesh strategy is developed to reduce the rod-cusping problem. This method is based on the use of different spatial meshes for the different time steps following the movement of the control rod avoiding the necessity of the use of averaged material properties, as it is observed in Figure 4.2. To avoid problems with hanging nodes (Šolín, Červený, and Doležel, 2008), the spatial mesh is refined in the same way for all the axial plane. The solutions obtained in each time step for the physical quantities are interpolated to a new spatial mesh in each time step. This Chapter rewrites some methods and results presented in Vidal-Ferràndiz et al., (2016a).

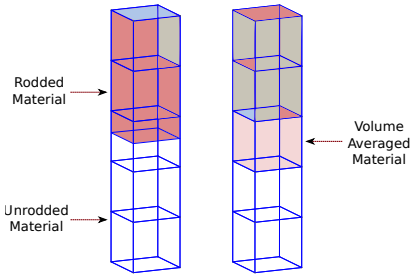

Figure 4.1: Rod-cusping problem in a fixed mesh scheme.

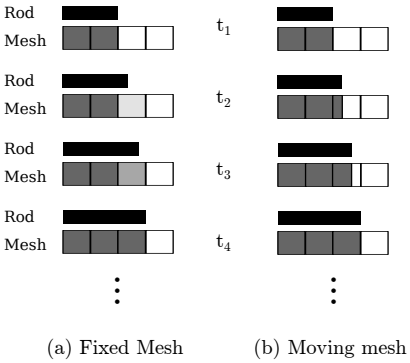

Figure 4.2: 1D representation of fixed and moving mesh schemes.

The rest of the Chapter is organized as follows, in Section 4.2, the spatial discretization used for the neutron diffusion equation is briefly presented. Then the time discretization of the problem is explained in Section 4.3. Different approaches to solve the rod-cusping effect and the interpolation used for the moving mesh scheme are presented in Section 4.4. To test the performance of the method, several benchmarks are analysed in Section 4.5.

4.2 Spatial Discretization

For a given transient analysis in a core reactor, usually, a static configuration of the reactor is considered as initial condition. Associated with the time dependent neutron diffusion equation, (4.1) and (4.2), there is the generalized eigenvalue

problem

$$\mathcal{L}\Phi = \frac{1}{\lambda}\mathcal{M}\Phi\,. \tag{4.3}$$

The fundamental eigenvalue, the largest one, k_{eff}, is the multiplicative constant of the reactor core and its corresponding eigenfunction describes the steady state spatial neutron distribution in the core. In this way, the calculation of the stationary neutron flux distribution is the first step for any transient analysis. To solve both problems (4.1), (4.2) and (4.3), a spatial discretization of the equations has to be selected as it has been exposed in Chapter 3. A high order continuous Galerkin finite element method (Zienkiewicz, Taylor, and Zhu, 2005) is used here leading to an algebraic eigenvalue problem associated with the discretization of equation (4.3) with the following block structure,

$$\begin{pmatrix} L_{11} & 0 \\ L_{21} & L_{22} \end{pmatrix} \tilde{\Phi} = \frac{1}{\lambda} \begin{pmatrix} M_{11} & M_{12} \\ 0 & 0 \end{pmatrix} \tilde{\Phi}\,, \tag{4.4}$$

where $\tilde{\Phi} = \left(\tilde{\phi}_1,\ \tilde{\phi}_2\right)^T$ are the algebraic vectors of weights associated with the fast and thermal neutron fluxes.

4.3 Time discretization

Once the spatial discretization has been selected, a discrete version of the time dependent neutron diffusion equation is solved. Since the system of ordinary differential equations resulting from the discretization of the neutron diffusion equations is stiff, implicit methods are usually used. Particularly, a first order backward method is used as the one introduced in Ginestar et al., (1998), needing this method to solve a large system of linear equations for each time step.

Once the spatial discretization is performed, the semi-discrete two energy groups time dependent neutron diffusion equation together with the neutron precursors concentration equations are of the form

$$[\tilde{v}^{-1}]\frac{d\tilde{\Phi}}{dt} + L\tilde{\Phi} = (1-\beta)M\tilde{\Phi} + \sum_{p=1}^{N_p} \lambda_p X C_p\,, \tag{4.5}$$

$$P\frac{dC_p}{dt} = \beta_p\,(M_{11}M_{21})\,\tilde{\Phi} - \lambda_p P C_p, \quad k = 1,\ \ldots\ ,\ N_p\,, \tag{4.6}$$

where L and M are the matrices obtained from the static spatial discretization of operators $\mathcal{L}$ and $\mathcal{M}$, whose elements are given by equations (3.9). Matrix X and

$[\tilde{\mathrm{v}}^{-1}]$ are defined as

$$X = \begin{pmatrix} P \\ 0 \end{pmatrix}, \qquad [\tilde{\mathrm{v}}^{-1}] = \begin{pmatrix} P\,\mathrm{v}_1^{-1} & 0 \\ 0 & P\,\mathrm{v}_2^{-1} \end{pmatrix},$$

where matrix P is the mass matrix of the spatial discretization, which appears due to the fact that the polynomial basis used in the finite element method is not orthogonal. The matrix elements of P are given by

$$P_{ij} = \sum_{k=1}^{K} \int_{\Omega_k} \mathcal{N}_i \mathcal{N}_j \mathrm{d}V\,. \tag{4.7}$$

where K is the number of finite elements, N_i is the shape function for the i support point and Ω_k is the volume of the k finite element.

The time discretization of the precursors equations (4.6), is done by using a one-step implicit finite differences scheme. To obtain this scheme, we make the change of function

$$PC_p = e^{-\lambda_p t} B_p\,, \tag{4.8}$$

obtaining

$$\frac{dB_p}{dt} = e^{\lambda_p t} \beta_p \left(M_{11} M_{12}\right) \tilde{\Phi}(t)\,. \tag{4.9}$$

Integrating between t_n and t,

$$B_p(t) = B_p^n + \int_{t_n}^{t} e^{\lambda_p \tau} \beta_p \left(M_{11} M_{12}\right) \tilde{\Phi}(\tau)\, d\tau. \tag{4.10}$$

Making use of the change (4.8), C_p^{n+1} can be expressed as

$$PC_p^{n+1} = e^{-\lambda_p \Delta t_n} PC_p^n + e^{-\lambda_p t_{n+1}} \int_{t_n}^{t_{n+1}} e^{\lambda_p \tau}\, \beta_p \left(M_{11} M_{12}\right) \tilde{\Phi}(\tau)\, d\tau\,. \tag{4.11}$$

where $\Delta t_n = t_{n+1} - t_n$. The term $\left(M_{11} M_{12}\right) \tilde{\Phi}(t)$ inside the integral is approximated by its value at the instant t_{n+1} obtaining

$$PC_p^{n+1} = PC_p^n e^{-\lambda_p \Delta t_n} + \frac{\beta_p}{\lambda_p} \left(1 - e^{-\lambda \Delta t_n}\right) \left(M_{11}^{n+1} M_{12}^{n+1}\right)\, \tilde{\Phi}^{n+1}\,. \tag{4.12}$$

In the same way, Euler's backward method is used in equation (4.5) obtaining,

$$[\tilde{\mathrm{v}}^{-1}] \frac{1}{\Delta t_n} \left(\tilde{\Phi}^{n+1} - \tilde{\Phi}^n\right) + L^{n+1} \tilde{\Phi}^{n+1} = (1-\beta) M^{n+1} \tilde{\Phi}^{n+1} + \sum_{p=1}^{N_p} \lambda_p X C_p^{n+1}\,. \tag{4.13}$$

Taking into account equation (4.12), equation (4.13) is rewritten as the system of linear equations

$$T^{n+1}\tilde{\Phi}^{n+1} = R^n\tilde{\Phi}^n + \sum_{p=1}^{N_p} \lambda_p e^{-\lambda_p \Delta t_n} X C_p^n = E^n \,, \tag{4.14}$$

where the matrices are defined as,

$$T^{n+1} = \frac{1}{\Delta t_n}[\mathrm{v}^{-1}] + L^{n+1} - \hat{a}M^{n+1} \,,$$
$$R^n = \frac{1}{\Delta t_n}[\mathrm{v}^{-1}] = \frac{1}{\Delta t_n}\begin{pmatrix} P\,\mathrm{v}_1^{-1} & 0 \\ 0 & P\,\mathrm{v}_2^{-1} \end{pmatrix} \,,$$

and the coefficient $\hat{a}$ is

$$\hat{a} = 1 - \beta + \sum_{p=1}^{N_p} \beta_p \left(1 - e^{-\lambda_p \Delta t_n}\right) \,.$$

This system of equations is large, sparse and has to be solved for each time step. The preconditioned GMRES method (Saad, 2003) has been chosen to solve these systems and the preconditioner used has been a incomplete LU preconditioner, ILU(0), together with a reversed Cuthill-McKee reordering (Cuthill and McKee, 1969) to reduce the bandwidth of the matrices.

4.4 Rod cusping effect

To avoid the *rod-cusping effect*, different strategies have been developed. In this Section, we summarize the most relevant ones. In addition to these, some approaches have been discussed to estimate the flux distribution inside the partially rodded node as in Yamamoto, (2004). Other strategy presented in Gilbert et al., (2008) is based on interpolating the solution on refined meshes near the moving control rod.

4.4.1 Volume Flux Weighting Method

The simplest method to deal with partially inserted nodes is based on weighting the cross sections of the rodded (R) and unrodded (NR) part with the volume fraction inserted,

$$\bar{\Sigma} = (1 - f_{\text{ins}})\Sigma_{\text{NR}} + f_{\text{ins}}\Sigma_{\text{R}} \,, \tag{4.15}$$

where f_{ins} is the volume fraction of insertion of the rod in the cell.

4.4.2 Approximate Flux Weighting Method

Gehin, (1992) introduced a simple correction model of the rod-cusping effect using the surrounding averaged cell values. A similar method was developed in González-Pintor, Verdú, and Ginestar, (2011). In absence of the average flux in the unrodded and rodded fractions of the node, they are approximated by the following relations,

$$\phi_{\mathrm{NR}} = \frac{\Delta z_{k-1}\phi_{k-1} + (1 - f_{\mathrm{ins}})\Delta z_k \phi_k}{\Delta z_{k-1} + (1 - f_{\mathrm{ins}})\Delta z_k}\,, \tag{4.16}$$

$$\phi_{\mathrm{R}} = \frac{\Delta z_{k+1}\phi_{k+1} + f_{\mathrm{ins}}\Delta z_k \phi_k}{\Delta z_{k+1} + f_{\mathrm{ins}}\Delta z_k}\,, \tag{4.17}$$

where ϕ_k is the average neutron flux in the axial cell k and Δz_k is the size of the node in the vertical direction z. With this definitions, the cross sections of the partially inserted node, $\bar{\Sigma}$, are given by

$$\bar{\Sigma} = \frac{(1 - f_{\mathrm{ins}})\Sigma_{\mathrm{NR}}\phi_{\mathrm{NR}} + f_{\mathrm{ins}}\Sigma_{\mathrm{R}}\phi_{\mathrm{R}}}{(1 - f_{\mathrm{ins}})\phi_{\mathrm{NR}} + f_{\mathrm{ins}}\phi_{\mathrm{R}}}\,. \tag{4.18}$$

4.4.3 Analytical Flux Weighting Method

In Smith et al., (1992), the flux inside the partially rodded cell is computed by solving a one dimensional two regions problem using the neutron current resulting from the previous solution as boundary conditions. The intranodal flux shapes are integrated analytically to obtain flux-volume-weighted cross sections. Additionally, axial discontinuity factors for the top and bottom of the partially rodded node are used. They are computed by taking the ratios of the heterogeneous to homogeneous boundary fluxes.

4.4.4 Bilinear Weighting Method

According to Kim and Cho, (1990) and Cho, Kim, and Lee, (2001) for a partially rodded cell, the equivalent homogenized cross sections can be calculated as

$$\bar{\Sigma} = \frac{\int_0^{\Delta z_k} \phi\,\Sigma\,\phi^{\dagger}\mathrm{d}z}{\int_0^{\Delta z_k} \phi\,\phi^{\dagger}\mathrm{d}z}\,, \tag{4.19}$$

where ϕ and $\phi^{\dagger}$ are the heterogeneous forward and adjoint fluxes inside the partially rodded node.

4.4.5 Equivalence Method

In Dall'Osso, (2002) and in Bennewitz, Finnemann, and Wagner., (1975) an equivalence method is studied. The main idea that lies behind these methods is to try to reproduce the reaction rates in the partially inserted cell as if the node was divided into two nodes. The rod cross section weighting factors are computed by forcing the reaction rates of the classical nodal expansion to match the reaction rates of the reference nodal expansion. This condition is not sufficient because it guarantees only the equivalence of the average cell equations. To complete the equivalence a correction to the weighted residual equations is also computed.

4.4.6 Moving Mesh strategy

Traditionally the time dependent neutron diffusion equation is solved using a spatial mesh that is fixed along all the transient. As it has been already mentioned, the simulation of transients where the control rod banks move suffer from the *rod-cusping* problem because averaged cross sections are used for the partially rodded nodes. We propose the use of a spatial mesh that changes each time step following the control rod, in such a way, that we do not have partially rodded nodes. This scheme requires the interpolation of the physical solutions of the equations, which are continuous functions, from the old mesh in step n to the next mesh corresponding to step $n+1$. The mesh interpolation process consists of finding the solution in the new support point values corresponding to the new mesh by polynomial interpolation of the values of the solution in the old mesh. To maintain the accuracy of the solution this interpolation is done using a polynomial interpolation of the same degree as the degree used in the high order finite element method used for the spatial discretization.

To formalise the method we use the superscript notation to refer to the time step number and the subscript notation to the mesh number step. Then, Φ^n_m refers to the neutronic flux at time step n defined in the mesh m. The interpolation process is implemented by means of a function f, and can be written as

$$\Phi^n_{m+1} = f(\Phi^n_m)\,, \tag{4.20}$$

$$C^n_{p,m+1} = f(C^n_{p,m})\,. \tag{4.21}$$

Figure 4.3 shows an example of the neutron flux interpolation $\Phi^n(z)$ between two consecutive meshes m and $m+1$. This interpolation is similar to the one used in h-refined finite elements codes to interpolate from the coarse mesh to the fine mesh and accelerate the convergence of solution in the fine mesh (Bangerth, Hartmann,

and Kanschat, 2007). However in the moving mesh method, the support points of the mesh are moved and not only coarse cells are subdivided into finer cells.

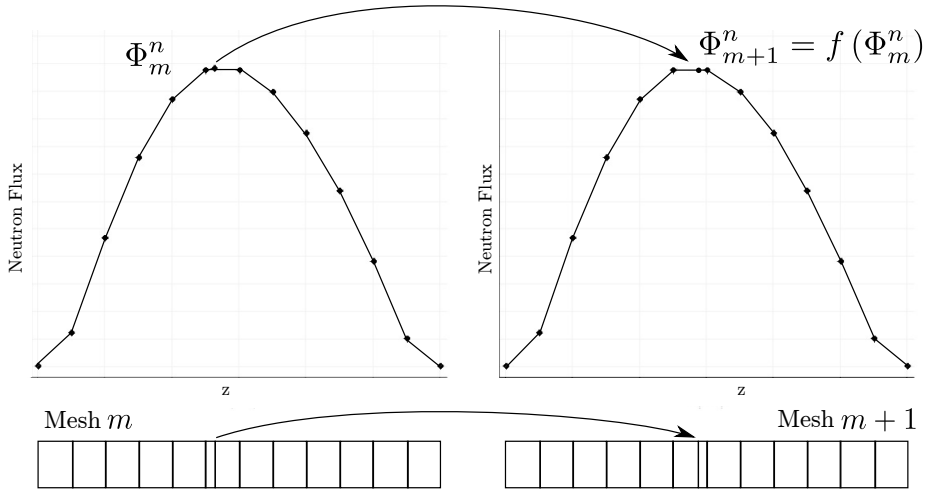

Figure 4.3: 1D Mesh interpolation example.

In the moving mesh interpolation, only physical quantities, which are continuous, can be interpolated adequately. However, from equation (4.12) the obtained quantity is PC_p^n and the physical magnitude needed for the interpolation is C_p^n. To avoid the computationally expensive task of inverting matrix P, a mass lumping technique is considered (Zienkiewicz, Taylor, and Zhu, 2005). This procedure mainly consists in approximating matrix P by the lumped matrix $\hat{P}$, a diagonal matrix whose elements are the result of adding all the elements of each row of the mass matrix (row-sum method).

Given a mass matrix, P, and its lumped matrix, $\hat{P}$, the essential requirement of preservation of mass is satisfied i.e.

$$\sum_j \sum_i M_{ij} = \sum_i \hat{P}_{ii} \,. \tag{4.22}$$

The row-sum method is equivalent to calculate the integrals involving polynomials up to order s approximately with a quadrature rule up to order $s-1$ for Lagrange finite elements (Karniadakis and Sherwin, 2005). In other words, the procedure is equivalent to use an inexact quadrature rule where its evaluation points coincide with the support points of the finite element. In general, the use

of lumped mass matrices is only a convenient numerical device if the considerable efficiency improvement trades off for any loss in accuracy. However, we note that occasionally mass lumping can improve accuracy of some problems by error cancellation. It can be shown that in the transient approximation the lumping process introduces additional viscous dissipation and this can help in cancelling out numerical oscillations (Hinton, Rock, and Zienkiewicz, 1976).

As the lumped mass matrix is diagonal, its inverse is trivially calculated as

$$\hat{P}_{ii}^{-1} = \frac{1}{\sum_{j=1}^{N_{\text{DoFs}}} \sum_{k=1}^{K} \int_{\Omega_k} \mathcal{N}_i \mathcal{N}_j \mathrm{d}V} \,. \tag{4.23}$$

In the usual fixed mesh scheme, it is not necessary to know the value of C_p^n because it is enough to obtain PC_p^n for each time step.

The steps necessary for the implementation of the moving mesh procedure are summarized in the scheme shown in Figure 4.4. The computation starts with an eigenvalue computation to obtain the stationary configuration of the reactor core, which is used as initial condition. Then, the dynamic calculation starts. First, the neutron precursors concentration is solved in the initial mesh. Afterwards, the control rods and the mesh are moved and the neutronic flux and the precursors distribution are interpolated to the new mesh. Next, the system associated with the numerical scheme is solved obtaining the next flux distribution. This is clearly the most time consuming part of the computation. Finally, the stopping criterion is checked and if it is not fulfilled the dynamic computation is repeated for the next time step.

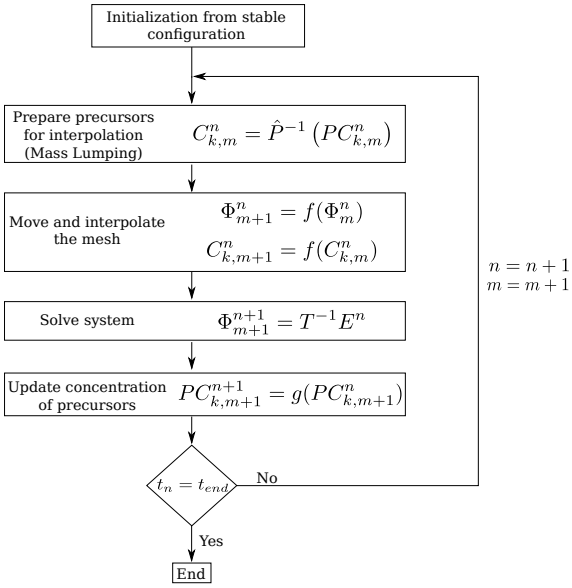

Figure 4.4: Scheme of the moving mesh time integration scheme.

4.5 Numerical Results

To study the performance of the moving mesh method proposed above, several benchmarks are studied. The first benchmark consists of a one dimensional problem where a control rod is ejected to a given velocity and then inserted back. The second benchmark is a small three dimensional hexagonal reactor where a rod ejection accident is also studied. Finally, realistic rectangular and hexagonal three dimensional benchmarks are solved.

To compare the performance of the method, different errors are used. They have been previously defined in Table 3.1.

4.5.1 One-dimensional problem

To validate the code a simple one-dimensional reactor is considered, which represents a simplified model for a rod-ejection accident. This reactor consists of 12 cells composed of different materials and it is defined in Appendix B.3.

The initial static results obtained for the dominant eigenvalue k_{eff} using different polynomial degrees for the finite element method, p, are shown in Table 4.1. In this Table, the number of degrees of freedom (DoFs) is also shown for the reduced eigenvalue problem in order to have an idea of the size of the problem solved. Also the mean relative error and maximum absolute error per cell for the neutron power is shown for the initial configuration of the problem. It can be seen that with $p = 2$ and $p = 3$, we obtain enough accurate results to simulate this reactor because we get less than 1% of relative error in the power.

Table 4.1: Dominant eigenvalue and power distribution results for the 1D reactor.

p	Number of DoFs	k_{eff}	Δk_{eff} (pcm)	Power $\bar{\varepsilon}$ (%)	$\varepsilon_{\max}$
1	13	0.97843	38	2.48	0.04
2	25	0.97876	5	0.41	0.01
3	37	0.97880	1	0.09	0.00
	PARCS	0.978811			

Figure 4.5 shows a detail of the evolution of the normalized mean power, $\bar{P}(t)$,

$$\bar{P}(t) = \frac{\int_\Omega \left(\Sigma_{f1}\phi_1(t) + \Sigma_{f2}\phi_2(t)\right) \mathrm{d}V}{\int_\Omega \left(\Sigma_{f1}\phi_1(0) + \Sigma_{f2}\phi_2(0)\right) \mathrm{d}V} \,, \tag{4.24}$$

during the transient computed using a classical fixed mesh scheme (volume averaged) with 12 axial nodes, the moving mesh scheme presented in this work and the reference values. All the transient calculations are made using cubic polynomials in the finite element method and a simulation stop time of $10\,\mathrm{s}$. Reference results for the neutronic flux and the k_{eff} of the problem are computed with the neutronic code PARCS (Downar et al., 2009), using a fixed mesh with 120 cells where the rod-cusping problem is insignificant. As can be seen in Figure 4.5, the fixed mesh computations present some non-physical jumps in the normalized mean power, mainly when the control rod is in the middle of a cell. However the rod-cusping problem is mitigated with the moving mesh scheme reducing the mean error in the normalized mean power about three times, from 0.3% to 0.13%. Moreover, the relative errors for the reactor mean power for each one of the time steps obtained with the fixed mesh scheme and the moving mesh scheme are shown in Figure 4.6. Figure 4.7 shows the errors in the computation of the dominant eigenvalue (Δk_{eff}) solving an static problem for every time step of the transient. As it can be seen in these Figures, the errors for the k_{eff} and the mean reactor power have very similar behaviours.

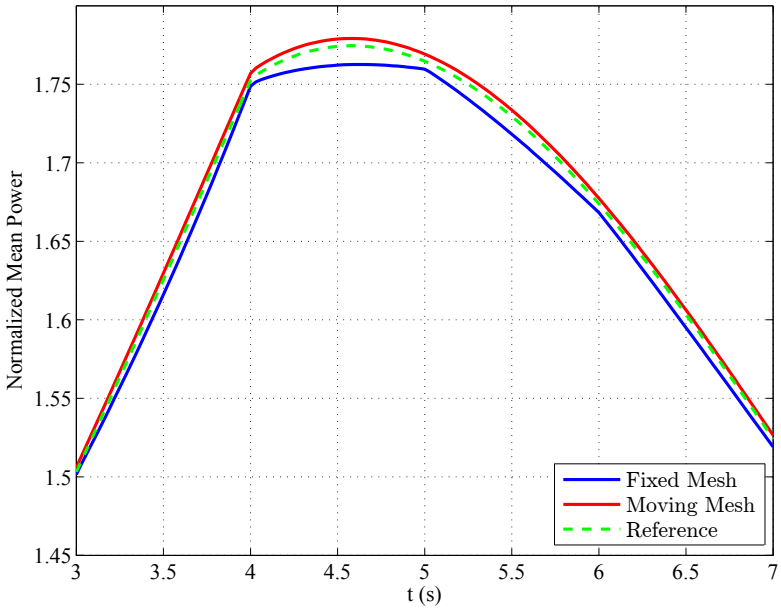

Figure 4.5: Normalized power evolution for the 1D reactor from 3s to 7s.

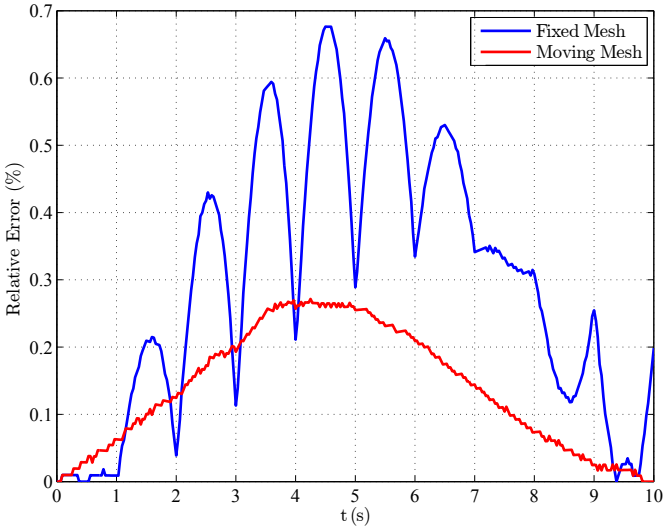

Figure 4.6: Comparative of errors over time in 1D reactor.

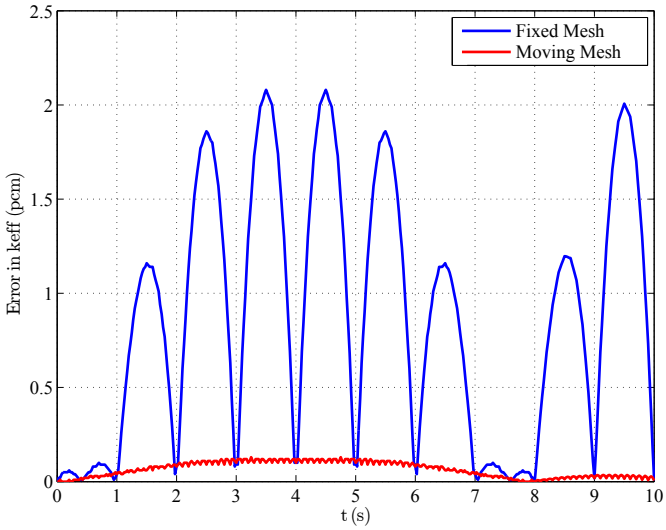

Figure 4.7: Errors in k_{eff} during the transient.

4.5.2 Small Hexagonal Rector

To test the performance of the method in three dimensional reactors, a small hexagonal reactor that presents a large rod-cusping problem is studied (González-Pintor, Verdú, and Ginestar, 2011). This reactor is defined in Appendix B.10. As the Deal.II library cannot handle hexagonal finite elements, each hexagon is subdivided into 3 quadrilaterals with the help of the mesh generation code Gmsh (Geuzaine and Remacle, 2009), as it is shown in Figure 4.8. Thus, the used mesh for this reactor has a total of 684 cells.

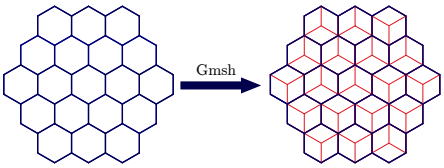

Figure 4.8: Hexagonal cells transformed into quadrilaterals with Gmsh.

The results obtained for the dominant eigenvalue using different polynomial degrees for the finite element method, p, are shown in Table 4.2. In this Table, the mean relative errors and maximum absolute errors per cell in the power for the initial configuration of the reactor are also shown. It can be seen that with $p = 2$ we obtain enough accurate results to simulate this reactor because we get less than 0.5% of relative error in the power.

Table 4.2: Dominant eigenvalue and power distribution results for the small 3D reactor.

p	Number of DoFs	k_{eff}	Δk_{eff} (pcm)	Power $\bar{\varepsilon}$ (%)	Power ε_{max}
1	949	0.80190	1563	2.08	0.17
2	6475	0.81664	89	0.29	0.03
3	20 683	0.81737	16	0.06	0.01
	PARCS	0.81753			

Figure 4.9 shows the time evolution of the normalized mean power of the reactor in the first 0.15 seconds. In this Figure, the results obtained with the moving mesh scheme proposed in this work, are compared with the results obtained with the classical fixed mesh scheme. While the fixed mesh scheme considers 12 axial planes, the moving mesh computation has 13 axial planes (12 fixed and 1 moving). In addition, the reactor is also solved with a fixed mesh scheme using 120

axial planes where the rod-cusping problem is very small and the results of this computation are taken as a reference. All transient calculations are made using cubic polynomials in the finite element method.

The relative errors for the reactor mean power for each one of the time steps obtained with the fixed mesh scheme and the moving mesh scheme are shown in Figure 4.10. Thus, the moving mesh scheme reduces the mean error from 5.7% to 0.50%. As it can be seen in these Figures, the moving mesh scheme produces better results than the fixed mesh scheme when a small number of axial planes are considered for the spatial discretization.

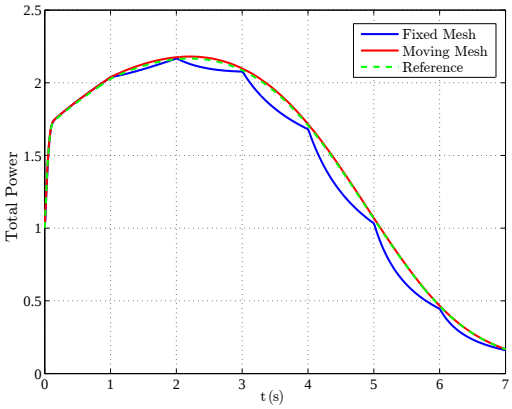

Figure 4.9: Normalized mean power evolution for the small 3D reactor.

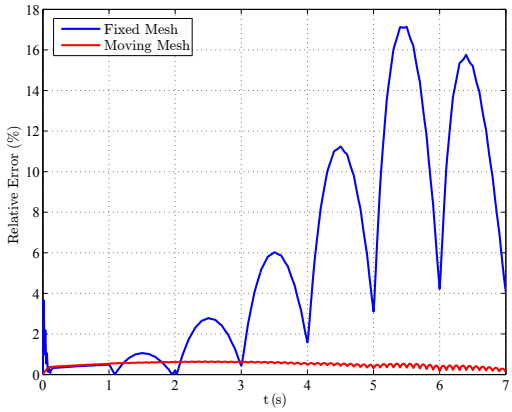

Figure 4.10: Normalized mean power error for the small 3D reactor.

4.5.3 Langenbuch Reactor

To the validate the performance of the method in a rectangular reactor the Langenbuch benchmark (Langenbuch, Maurer, and Werner, 1977) is used. The transient simulates the accidental ejection of a group of control rods at a slow velocity of 3 cm/s. This benchmark is fully specified in Appendix B.9.

Table 4.3 shows a comparison of the static results for this reactor using different polynomials degrees related to the finite element method. It can be seen that, at least quadratic shape functions, $p = 2$, must be used to ensure reasonable results and only with cubic polynomials the mean error is reduced to less than 1%. For this reason, all transient simulations are done with cubic finite element polynomials.

Figure 4.11 shows the normalized mean power evolution along the first 60 seconds of simulation. Reference results are extracted using 100 axial planes in order to minimize the rod-cusping effect. In this way, the fixed mesh scheme considers 10 axial planes and the moving mesh computation has 11 axial planes (10 fixed and 1 moving). Figure 4.12 shows the relative error results of the previous graph. It can be seen that the moving mesh strategy reduces the error of the simulation from 2.5% to 0.5% of mean error.

Table 4.3: Dominant eigenvalue and power distribution results for the Langenbuch Reactor.

p	Number of DoFs	k_{eff}	Δk_{eff} (pcm)	Power $\bar{\varepsilon}$ (%)	$\varepsilon_{\max}$
1	949	1.00076	111	3.78	0.11
2	10 773	1.00039	74	1.24	0.05
3	34 720	0.99990	25	0.39	0.01
	PARCS	0.99965			

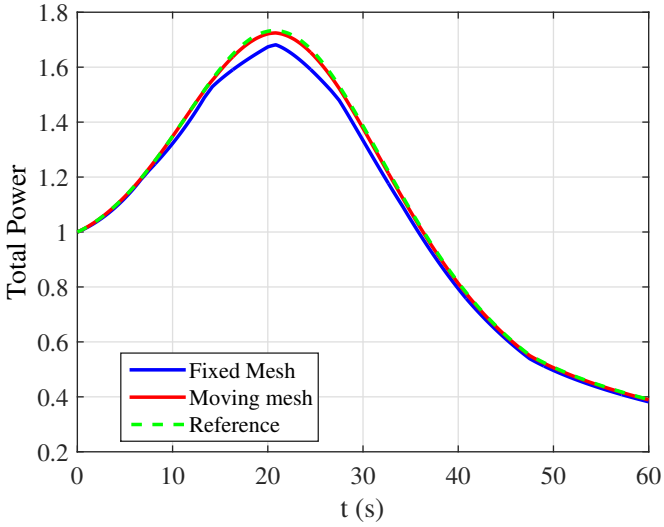

Figure 4.11: Normalized mean power for Langenbuch reactor.

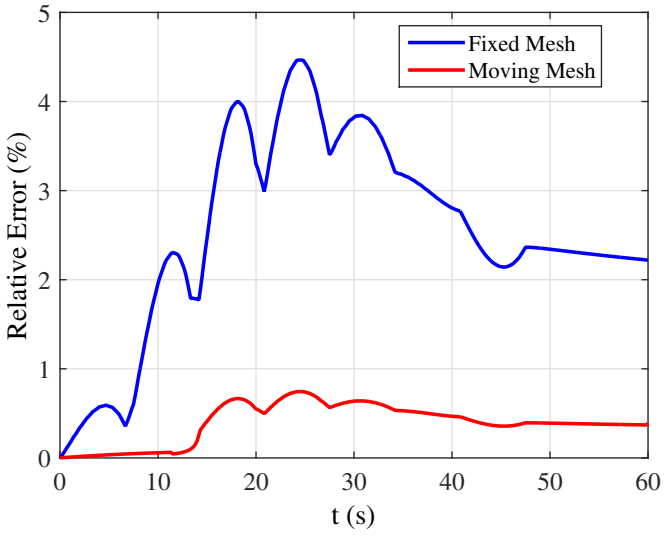

Figure 4.12: Normalized mean power relative error for Langenbuch reactor.

4.5.4 AER Benchmark

To test the performance of the proposed method in a realistic reactor, the transient benchmark AER-DYN-001 proposed in Keresztúri and Telbisz, (1992) has been studied. This problem corresponds to an asymmetric control rod ejection accident in a VVER-440 core. This benchmark is fully specified in Appendix B.11.

In Figure 4.13, the total power evolution is presented for several calculations. First, the power evolution has been computed with the nodal code PARCS (Downar et al., 2009) using 12 axial planes. This computation presents a strong rod-cusping effect. In the same way, the finite element method with a fixed mesh presents a similar behaviour when 12 axial planes are used in the computations. To avoid the rod-cusping we have computed the transient using the moving mesh scheme with 13 axial planes (12 fixed and 1 moving). In this case, the power evolution is comparable to the behaviour obtained with the PARCS code using axial 120 planes. To be self-consistent, a reference finite element solution, with fixed mesh and 60 axial planes, is also shown. All the calculation have been performed with a maximum time step of 0.01s because this is the maximum time step that achieves sufficiently converged results.

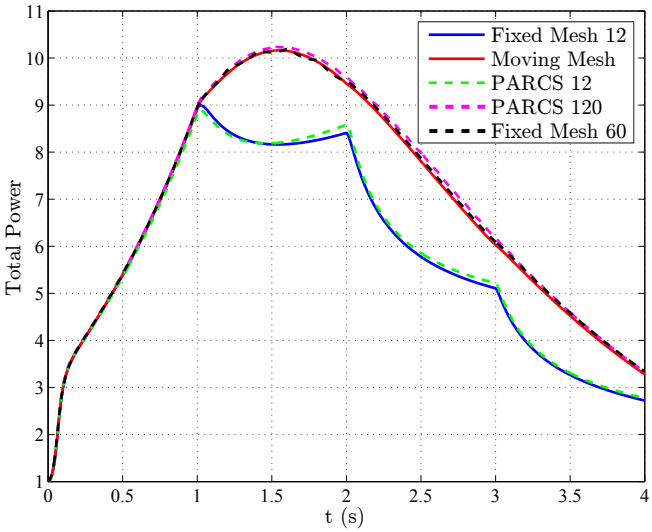

Figure 4.13: Power evolution for the VVER-440 reactor.

5 Simplified Spherical Harmonics Equations

5.1 Introduction

The accuracy of the diffusion theory for describing the neutron population in a nuclear reactor is limited for a variety of situations: when strong material and/or flux gradients are present, when neutron streaming is significant or when neutron scattering contains a strongly anisotropic component. These situations usually take place when complex fuel assemblies exist or calculation at assembly level are carried out. Also, new nuclear fuels designed for Generation IV reactors are producing these situations more often. To improve the results of diffusion theory for situations such as those mentioned, higher-order approximations for the angular dependence of the neutron transport equation must be employed.

In this chapter we investigate the simplified spherical harmonics approximation (SP_N). Spherical harmonics approximation or P_N is developed by the expansion of the angular flux in terms of Legendre polynomials. As the multidimensional P_N approximation is a complicated set of equations, Gelbard showed that one dimensional P_N equations could be extended to multidimensional geometries substituting the one-dimensional derivatives by a multidimensional gradient. This ad-hoc approximation, called Simplified P_N (SP_N), gives accurate results compared to its computational cost to solve. Theoretical basis for the SP_N equations were provided decades after by Brantley and Larsen, (2000), showing that these equations are high-order asymptotic solutions of the transport equation when diffusion theory is the leading-order approximation in the dominant direction.

Unlike the standard spherical harmonics approximation, the simplified spherical harmonics solution does not converge to the exact transport solution as $N \to \infty$. However, it is more accurate than the diffusion approximation for usual reactor configurations within acceptable computing times. The main advantage of the SP_N approximation is the number of equations to be solved, which is smaller than the complete P_N number of equations, and the resulting system of elliptic equations that is readily solvable with small modifications of the standard diffusion solvers. The number of equations increases quadratically as $(N+1)^d$ for spherical harmonics, while it increases linearly as $(N+1)/2$ for SP_N. In addition the SP_N approximation does not suffer from the ray effects that can adversely affect the discrete ordinates method, S_N, for certain configurations (Lewis and Miller, 1984).

In the simplified spherical harmonics method, odd order approximations have found a broader acceptance than even order approximations because nuclear cross sections are usually available for odd order approximations. Furthermore nuclear cross sections have only as many linear independent fields as the next lower approximation, which is and odd order approximation. We focus our study in SP_1, SP_3 and SP_5 approximations as higher N approximations do not produce considerable better results than these approximations for full core reactor calculations.

In this Chapter, a $h-p-$Finite Element Method is used to obtain the stationary neutron flux and the multiplicative factor associated with the configuration of a reactor core using the SP_N approximation. The accuracy of the simplified P_N approximation is compared to diffusion approximation and discrete ordinates codes.

The rest of the Chapter is organized as follows. In Section 5.2, the one dimensional P_N approximation is developed for a general N. Section 5.3 describes the Simplified P_N approximation for multidimensional geometries. In Section 5.4, the finite element discretization of these equations is summarized. Section 5.5 shows some numerical results of the method employed including two one-dimensional benchmarks and more realistic three dimensional reactors.

5.2 One Dimensional P_N equations

We consider the eigenvalue problem associated with the steady-state, multi-group, linear neutron transport equation in slab geometry (Henry, 1975),

$$\left(\mu\frac{\mathrm{d}}{\mathrm{d}x}+\Sigma_t^g(x)\right)\psi^g(x,\mu)=$$
$$\sum_{g'=1}^{G}\int_{-1}^{1}\Sigma_s^{gg'}(x,\mu_0)\psi^{g'}(x,\mu')\mathrm{d}\mu'+\frac{1}{\lambda}\sum_{g'=1}^{G}\frac{\chi^g(x)}{2}\nu\Sigma_f^{g'}(x)\int_{-1}^{1}\psi^{g'}(x,\mu')\mathrm{d}\mu',$$
$$g=1,\,\ldots,\,G,\qquad x\in[0,\,L_t]\,, \tag{5.1}$$

with vacuum boundary conditions at the extremes of the domain, $x = 0$ and $x = L_t$,

$$\psi^g(0,\mu_{in})=0\,,\qquad \psi^g(L_t,\mu_{in})=0\,. \tag{5.2}$$

G is the total number of energy groups considered, θ is the angle between the direction of the incident neutron velocity and the x axis, $\mu = cos(\theta)$, θ_0 is the angle between the incident neutrons and the scattered neutrons, $\mu_0 = cos(\theta_0)$. μ_{in} is the set of directions cosines that are incident at a given boundary, in other words, at $x = 0$, $0 < \mu_{in} \leq 1$ and at $x = L_t$, $-1 \leq \mu_{in} < 0$. In this Chapter, we have marked the energy group index as superscript in order to distinguish it from the moment index.

The solutions of this eigenvalue problem are known as the *Lambda modes* of the transport equation. The dominant eigenvalue, $\lambda = k_{\text{eff}}$, is the multiplicative factor of the system and measures its criticality and the corresponding eigenvector is the stationary angular flux distribution inside the domain.

Different angular discretizations are commonly used to solve this problem, as the discrete ordinates or the spherical harmonics expansion of the angular variable (Lewis and Miller, 1984). Both discretizations provide equivalent solutions with an appropriate choice of the quadrature set that defines the discrete ordinates method, (Gast, 1958; Cullen, 2001), and have simplified second order forms, where odd moments are formally solved and substituted back into the equations, providing a simplified formulation where the number of unknown fields is reduced.

The P_N approximation to the neutron transport equation (5.1) assumes that the angular dependence of both the angular neutron flux distribution and the scattering cross-section can be expanded in terms of $N + 1$ Legendre polynomials,

$P_n(\mu)$, where N is odd in this work, as

$$\psi^g(x,\mu) = \sum_{n=0}^{N} \frac{2n+1}{2} \phi_n^g(x)\, P_n(\mu)\ , \tag{5.3}$$

$$\Sigma_s^{gg'}(x,\mu_0) = \sum_{n=0}^{L} \frac{2n+1}{2} \Sigma_{sn}^{gg'}(x)\, P_n(\mu_0)\ . \tag{5.4}$$

where ϕ_n^g is the n-th angular moment of the neutron flux of energy group g and $\Sigma_{sn}^{gg'}$ is the scattering cross sections moment. Using expansions (5.3) and (5.4) into equation (5.1) and the orthogonality relations for these polynomials, the following P_N equations are obtained (Capilla et al., 2005),

$$\frac{\mathrm{d}\phi_1^g}{\mathrm{d}x} + \sum_{g'=1}^{G} \left(\Sigma_t^g - \Sigma_{s0}^{gg'}\right) \phi_0^{g'} = \frac{1}{\lambda} \sum_{g'=1}^{G} \chi^g \nu \Sigma_f^{g'} \phi_0^{g'}\,, \tag{5.5}$$

$$\frac{\mathrm{d}}{\mathrm{d}x}\left(\frac{n}{2n+1}\phi_{n-1}^g + \frac{n+1}{2n+1}\phi_{n+1}^g\right) + \sum_{g'=1}^{G} (\delta_{gg'}\Sigma_t^g - \Sigma_{sn}^{gg'})\phi_n^{g'} = 0\,, \quad \text{for } n = 1,\ \ldots,\ N\,, \quad g = 1,\ \ldots,\ G, \tag{5.6}$$

where we have considered the expansion order for the angular flux, N, to be larger than the order of anisotropic scattering, L. In this formulation, we consider the components of the scattering equal to zero for moments higher than L, but we have kept them in the formulation for simplicity. The P_N equations (5.5) and (5.6) constitute a set of $N+1$ equations with $N+2$ unknowns. This problem is usually solved setting the derivative of the highest order moment to zero $\frac{\mathrm{d}}{\mathrm{d}x}\phi_{N+1} = 0$. This closure is the most common and straightforward one but can be problematic for some time dependent applications, so other closures have also been developed in the literature (Hauck and McClarren, 2010).

Equations (5.5) and (5.6) are more easily expressed in matrix notations as,

$$\frac{\mathrm{d}\,\Phi_1}{\mathrm{d}x} + \mathbf{\Sigma_0}\Phi_0 = \frac{1}{\lambda}\mathbf{F}\Phi_0\,, \tag{5.7}$$

$$\frac{\mathrm{d}}{\mathrm{d}x}\left(\frac{n}{2n+1}\Phi_{n-1} + \frac{n+1}{2n+1}\Phi_{n+1}\right) + \mathbf{\Sigma_n}\Phi_n = 0\,, \quad \text{for } n = 1,\ \ldots,\ N\,. \tag{5.8}$$

where,

$$\boldsymbol{\Sigma_n} = \begin{pmatrix} \Sigma_t^1 - \Sigma_{sn}^{11} & -\Sigma_{sn}^{12} & \dots & -\Sigma_{sn}^{1G} \\ -\Sigma_{sn}^{21} & \Sigma_t^2 - \Sigma_{sn}^{22} & \dots & -\Sigma_{sn}^{2G} \\ \vdots & \vdots & \ddots & \vdots \\ -\Sigma_{sn}^{G1} & -\Sigma_{sn}^{G2} & \dots & \Sigma_t^G - \Sigma_{sn}^{GG} \end{pmatrix},$$

$$\mathbf{F} = \begin{pmatrix} \chi^1\nu\Sigma_f^1 & \chi^1\nu\Sigma_f^2 & \dots & \chi^1\nu\Sigma_f^G \\ \chi^2\nu\Sigma_f^1 & \chi^2\nu\Sigma_f^2 & \dots & \chi^2\nu\Sigma_f^G \\ \vdots & \vdots & \ddots & \vdots \\ \chi^G\nu\Sigma_f^1 & \chi^G\nu\Sigma_f^2 & \dots & \chi^G\nu\Sigma_f^G \end{pmatrix},$$

$$\Phi_n = \left(\phi_n^1, \phi_n^2, \dots, \phi_n^G\right)^T .$$

It must be noted that in many nuclear applications, as in usual static full reactor calculations, the scattering cross section, Σ_s, is considered isotropic and a transport correction is typically introduced (Hamilton and Evans, 2015). Thus, considering isotropic scattering, i.e. $L = 0$ in equation (5.4), the matrix $\boldsymbol{\Sigma_n}$ is diagonal for $n > 0$. Substituting the equations related to the odd moments of the flux, equation (5.8) yields to

$$\begin{aligned} -\frac{\mathrm{d}}{\mathrm{d}x}\Bigg(& \frac{n\,\boldsymbol{\Sigma_{n-1}}^{-1}}{(2n+1)(2n-1)}\frac{\mathrm{d}}{\mathrm{d}x}\left((n-1)\Phi_{n-2} + n\Phi_n\right) \\ + & \frac{(n+1)\boldsymbol{\Sigma_{n+1}}^{-1}}{(2n+1)(2n+3)}\frac{\mathrm{d}}{\mathrm{d}x}\left((n+1)\Phi_n + (n+2)\Phi_{n+2}\right)\Bigg) + \boldsymbol{\Sigma_n}\Phi_n = \frac{1}{\lambda}\mathbf{F}\Phi_n\delta_{n0}\,, \\ & \text{for } n = 0,\ 2,\ \dots,\ N-1\,. \end{aligned} \tag{5.9}$$

Equation (5.9) defines an eigenvalue problem associated with a linear system of $(N+1)/2$ elliptic, second-order equations. This eigenvalue problem can be converted into a problem composed of a set of diffusion-like equations if the following linear change of variables is performed,

$$U_n = (n+1)\,\Phi_n + (n+2)\,\Phi_{n+2}, \qquad n = 0,\ 2,\ \dots,\ N-1\,, \tag{5.10}$$

$$U = (U_0,\, U_2,\, \dots,\, U_{N-1})^T\,, \tag{5.11}$$

and each element of U contains the group dependent diffusive pseudo-moments

$$U_n = (u_n^1,\, u_n^2,\, \dots,\, u_n^G)^T\,. \tag{5.12}$$

For example, the set of P_5 equations are

$$\begin{aligned}
-\frac{\mathrm{d}}{\mathrm{d}x}\left(\frac{1}{3}{\boldsymbol{\Sigma_1}}^{-1}\frac{\mathrm{d}}{\mathrm{d}x}\left(\Phi_0+2\Phi_2\right)\right)+\boldsymbol{\Sigma_0}\Phi_0&=\frac{1}{\lambda}\mathbf{F}\Phi_0\,,\\
-\frac{\mathrm{d}}{\mathrm{d}x}\left(\frac{2}{15}{\boldsymbol{\Sigma_1}}^{-1}\frac{\mathrm{d}}{\mathrm{d}x}\left(\Phi_0+2\Phi_2\right)+\frac{3}{35}{\boldsymbol{\Sigma_3}}^{-1}\frac{\mathrm{d}}{\mathrm{d}x}\left(3\Phi_2+4\Phi_4\right)\right)+\boldsymbol{\Sigma_2}\Phi_2&=0\,,\\
-\frac{\mathrm{d}}{\mathrm{d}x}\left(\frac{4}{63}{\boldsymbol{\Sigma_3}}^{-1}\frac{\mathrm{d}}{\mathrm{d}x}\left(3\Phi_2+4\Phi_4\right)+\frac{5}{99}{\boldsymbol{\Sigma_5}}^{-1}\frac{\mathrm{d}}{\mathrm{d}x}\left(5\Phi_4+6\Phi_6\right)\right)+\boldsymbol{\Sigma_4}\Phi_4&=0\,.
\end{aligned} \tag{5.13}$$

Using the change of variables,

$$U_0=\Phi_0+2\Phi_2\,,\quad U_2=3\Phi_2+4\Phi_4\,,\quad U_4=5\Phi_4+6\Phi_6\,, \tag{5.14}$$

the system (5.13) is rewritten as the eigenvalue problem,

$$-\frac{\mathrm{d}}{\mathrm{d}x}\left(\mathbf{D}\frac{\mathrm{d}}{\mathrm{d}x}U\right)+\mathbf{A}U=\frac{1}{\lambda}\mathbf{M}U\,, \tag{5.15}$$

where the effective diffusion matrix, $\mathbf{D}$, the absorption matrix, $\mathbf{A}$, and the fission matrix, $\mathbf{M}$, are defined as,

$$\mathbf{D}=\begin{pmatrix}\frac{1}{3}{\boldsymbol{\Sigma_1}}^{-1}&0&0\\0&\frac{1}{5}{\boldsymbol{\Sigma_3}}^{-1}&0\\0&0&\frac{1}{7}{\boldsymbol{\Sigma_5}}^{-1}\end{pmatrix}=\begin{pmatrix}\mathbf{D_0}&0&0\\0&\mathbf{D_1}&0\\0&0&\mathbf{D_2}\end{pmatrix}\,, \tag{5.16}$$

$$\mathbf{A}_{ij}=\sum_{m=1}^{3}\mathbf{c}_{ij}^{(\mathbf{m})}\boldsymbol{\Sigma}_{\mathbf{m}}\,, \tag{5.17}$$

$$\mathbf{M}_{ij}=\mathbf{c}_{ij}^{(\mathbf{1})}\mathbf{F}\,, \tag{5.18}$$

and the coefficients matrix, $\mathbf{c}^{(\mathbf{m})}$,

$$\mathbf{c}^{(\mathbf{1})}=\begin{pmatrix}1&-\frac{2}{3}&\frac{8}{15}\\-\frac{2}{3}&\frac{4}{9}&-\frac{16}{45}\\-\frac{8}{15}&-\frac{16}{45}&\frac{64}{225}\end{pmatrix},\quad \mathbf{c}^{(\mathbf{2})}=\begin{pmatrix}0&0&0\\0&\frac{5}{9}&-\frac{4}{9}\\0&-\frac{4}{9}&\frac{16}{45}\end{pmatrix},\quad \mathbf{c}^{(\mathbf{3})}=\begin{pmatrix}0&0&0\\0&0&0\\0&0&\frac{9}{25}\end{pmatrix}. \tag{5.19}$$

5.2.1 Boundary Conditions in one-dimensional P_N

To approximate the vacuum boundary conditions for the one-dimensional P_N equations, we shall consider Marshak's conditions (Stacey, 2007). These boundary

conditions impose a restriction in the flux odd moments at each boundary, x_B, either $x_B = 0$ or $x_B = L_T$, are given by

$$\int_{\mu_{in}} P_n(\mu)\,\psi^g(x_B,\mu)\mathrm{d}\mu = 0, \qquad g = 1,\ 2,\ \ldots,\ G, \quad n = 1,\ 3,\ \ldots, N. \tag{5.20}$$

Expanding $\psi(x_B,\mu)$ using equation (5.3),

$$\int_{\mu_{in}} P_n(\mu) \sum_{n'=0}^{N} \frac{2n'+1}{2}\phi^g_{n'}(x_B,\mu)P_{n'}(\mu)\mathrm{d}\mu = 0\,, \qquad g = 1,\ 2,\ \ldots,\ G, \quad n = 1,\ 3,\ \ldots,\ N. \tag{5.21}$$

Using the orthogonality relationship of Legendre polynomials and setting $N = 5$, the Marshak's boundary condition are,

$$\begin{aligned} \frac{1}{2}\Phi_0 + \frac{5}{8}\Phi_2 - \frac{3}{16}\Phi_4 &= -\Phi_1\,,\\ -\frac{1}{8}\Phi_0 + \frac{5}{8}\Phi_2 - \frac{81}{128}\Phi_4 &= -\Phi_3\,,\\ \frac{1}{16}\Phi_0 - \frac{25}{128}\Phi_2 - \frac{81}{128}\Phi_4 &= -\Phi_5\,. \end{aligned}$$

Applying the change of variables proposed in equation (5.10), the vacuum condition in the P_5 approximation can be applied as

$$-\hat{n}\,\mathbf{D}\frac{\mathrm{d}}{\mathrm{d}x}U(x_B) = \mathbf{B}U(x_B)\,, \tag{5.22}$$

where matrix $\mathbf{B}$ is given by the Kronecker product of matrix $\mathbf{b}$ by an $(G \times G)$ identity matrix,

$$\mathbf{B} = \mathbf{b} \otimes \mathbf{I}_{(G\times G)}\,, \qquad \mathbf{b} = \begin{pmatrix} \frac{1}{2} & -\frac{1}{8} & \frac{1}{16} \\ -\frac{1}{8} & \frac{7}{24} & -\frac{41}{384} \\ \frac{1}{16} & -\frac{41}{384} & \frac{407}{1920} \end{pmatrix}, \tag{5.23}$$

and $\hat{n}$ is the normal direction of the boundary, either 1 or -1 in one dimensional geometries.

On the other hand, reflective boundary conditions are imposed if all the flux odd moments are set to zero.

$$\phi^g_n(x_B) = 0, \qquad g = 1,\ 2,\ \ldots,\ G, \quad n = 1,\ 3,\ \ldots,\ N\,. \tag{5.24}$$

Thus, reflective boundary conditions are set imposing,

$$\frac{\mathrm{d}}{\mathrm{d}x}u_n^g(x_B) = 0, \qquad g = 1,\ 2,\ \ldots,\ G, \quad n = 0,\ 2,\ \ldots,\ N\,. \tag{5.25}$$

These treatments yield to $(N+1)/2$ equations in the boundary that effectively closes the system. We note that both of these boundary conditions treatments contain asymmetric components when N is even. Thus, only odd sets of $\mathrm{P_N}$ equations are considered. It must be noted that for each group the $\mathrm{P_N}$ system of equations (5.15) is symmetric because the coefficients $\mathbf{c}^{(\mathbf{m})}$ and $\mathbf{B}$ are symmetric.

5.3 Simplified $\mathrm{P_N}$

For multidimensional problems, the $\mathrm{SP_N}$ approximation is obtained substituting the x derivative operator by the corresponding two- or three-dimensional gradient operator in equations (5.7) and (5.8).

$$\vec{\nabla}\Phi_1 + \boldsymbol{\Sigma}_\mathbf{0}\Phi_0 = \frac{1}{\lambda}\mathbf{F}\Phi_0\,, \tag{5.26}$$

$$\vec{\nabla}\left(\frac{n}{2n+1}\Phi_{n-1} + \frac{n+1}{2n+1}\Phi_{n+1}\right) + \boldsymbol{\Sigma}_\mathbf{n}\Phi_n = 0\,, \quad \text{for } n = 1,\ \ldots,\ N\,. \tag{5.27}$$

This approximation may seen ad-hoc, but in Brantley and Larsen, (2000) a theoretical basis is provided. Brantley and Larsen show that these equations are high-order asymptotic solutions of the transport equation when diffusion theory is the leading-order approximation as it is the usual case in full reactor simulations. However the $\mathrm{SP_N}$ approximation does not converge to the true transport solution when $N \to \infty$.

The main advantage of the Simplified $\mathrm{P_N}$ approximation towards complete $\mathrm{P_N}$ equations is that the resulting system of equations is a set of elliptic, diffusion-like second order differential equations. These equations can be easily implemented using numerical methods suited for the diffusion equation without major changes.

As an example of the form of SP_N equations, the set of SP_5 equations yields to

$$\begin{aligned}
-\vec{\nabla}\left(\frac{1}{3}{\boldsymbol{\Sigma_1}}^{-1}\vec{\nabla}\left(\Phi_0+2\Phi_2\right)\right)+\boldsymbol{\Sigma_0}\Phi_0&=\frac{1}{\lambda}\mathbf{F}\Phi_0\,,\\
-\vec{\nabla}\left(\frac{2}{15}{\boldsymbol{\Sigma_1}}^{-1}\vec{\nabla}\left(\Phi_0+2\Phi_2\right)+\frac{3}{35}{\boldsymbol{\Sigma_3}}^{-1}\vec{\nabla}\left(3\Phi_2+4\Phi_4\right)\right)+\boldsymbol{\Sigma_2}\Phi_2&=0\,,\\
-\vec{\nabla}\left(\frac{4}{63}{\boldsymbol{\Sigma_3}}^{-1}\vec{\nabla}\left(3\Phi_2+4\Phi_4\right)+\frac{5}{99}{\boldsymbol{\Sigma_5}}^{-1}\vec{\nabla}\left(5\Phi_4+6\Phi_6\right)\right)+\boldsymbol{\Sigma_4}\Phi_4&=0\,. \qquad (5.28)
\end{aligned}$$

Performing the same change of variables as stated in equation (5.10), the SP_5 equation set of equations can be expressed as

$$-\vec{\nabla}\left(\mathbf{D}\,\vec{\nabla}U\right)+\mathbf{A}U=\frac{1}{\lambda}\mathbf{M}U\,, \qquad (5.29)$$

where the matrix operators $\mathbf{D}$, $\mathbf{A}$ and $\mathbf{M}$ are the same as the one defined in equations (5.16), (5.17) and (5.18).

5.3.1 Boundary Conditions in SP_N

In the same way as it has been done in Section 5.2.1, boundary conditions for SP_N equations are given substituting the x derivative operator by the two- or three dimensional gradient operator in equations (5.22) and (5.25). Making use of equation (5.20), vacuum boundary conditions for the Simplified P_N equations are

$$-\vec{n}\,\mathbf{D}\,\vec{\nabla}U(x_B)=\mathbf{B}\,U(x_B)\,, \qquad (5.30)$$

where matrix $\mathbf{B}$ is given in equation (5.23) and $\vec{n}$ is the normal direction to the boundary.

Additionally, reflective boundary conditions are given by

$$\vec{\nabla}u_n^g(x_B)=0,\qquad g=1,\,2,\,\ldots,\,G,\qquad n=0,\,2,\,\ldots,\,N\,. \qquad (5.31)$$

5.4 Finite Element Discretization

As it was reviewed in the last section the SP_N approximation consists of a set of diffusion-like equations for which the solution for the unknown fluxes moments is required. Thus, the finite element discretization (FEM), that was developed for the diffusion equation in Chapter 3, can be applied without major changes.

Hence, a continuous Galerkin finite element discretization has been applied to equation (5.29) leading to an algebraic generalized eigenvalue problem. To discretize the problem the reactor domain, Ω, has been partitioned into cells Ω_k, $k = 1, 2, \ldots, K$, where the nuclear cross sections are assumed to be constant. In the same way, Γ_k is the set of the corresponding cell surfaces which are part or the external reactor boundary, Γ.

To simplify the notation, in this Section only one group of energy is considered. Thus, the discretization of SP_5 equations can be written as the generalized algebraic eigenvalue problem,

$$\begin{pmatrix} \mathbf{L_{00}} & \mathbf{L_{01}} & \mathbf{L_{02}} \\ \mathbf{L_{10}} & \mathbf{L_{11}} & \mathbf{L_{12}} \\ \mathbf{L_{20}} & \mathbf{L_{21}} & \mathbf{L_{22}} \end{pmatrix} \begin{pmatrix} \tilde{u}_0 \\ \tilde{u}_2 \\ \tilde{u}_4 \end{pmatrix} = \frac{1}{k_{\text{eff}}} \begin{pmatrix} \mathbf{S_{00}} & \mathbf{S_{01}} & \mathbf{S_{02}} \\ \mathbf{S_{10}} & \mathbf{S_{11}} & \mathbf{S_{12}} \\ \mathbf{S_{20}} & \mathbf{S_{21}} & \mathbf{S_{22}} \end{pmatrix} \begin{pmatrix} \tilde{u}_0 \\ \tilde{u}_2 \\ \tilde{u}_4 \end{pmatrix}, \tag{5.32}$$

where $\tilde{u}_0$, $\tilde{u}_2$ and $\tilde{u}_4$ are the algebraic vectors representing u_0, u_2 and u_4 and the matrix blocks are constructed as,

$$\begin{aligned} (\mathbf{L_{nn}})_{ij} &= \sum_{k=1}^{K} D_n(\vec{\nabla}\mathcal{N}_i,\, \vec{\nabla}\mathcal{N}_j)_{\Omega_k} - D_n(\vec{\nabla}\mathcal{N}_i,\, \mathcal{N}_j)_{\Gamma_k} + A_{nn}(\mathcal{N}_i,\, \mathcal{N}_j)_{\Omega_k}, \\ (\mathbf{L_{nn'}})_{ij} &= \sum_{k=1}^{K} A_{nn'}(\mathcal{N}_i,\, \mathcal{N}_j)_{\Omega_k}, \qquad \text{if } \; n' \neq n \\ (\mathbf{S_{nn'}})_{ij} &= \sum_{k=1}^{K} M_{nn'}(\mathcal{N}_i,\, \mathcal{N}_j)_{\Omega_k}, \end{aligned}$$

where the common notation for the scalar product, $(a,\, b)_\Omega = \int_\Omega a\, b \,\mathrm{d}V$ has been used and the surface integrals $\int_\Gamma a\, b \,\mathrm{d}\vec{S}$ are denoted by $(a,\, b)_\Gamma$. D_n, $A_{nn'}$ and $M_{nn'}$ were previously defined in equations (5.16), (5.17) and (5.18), respectively. $\mathcal{N}_i$ is the prescribed shape function associated with the i-th degree of freedom or support point. The shape functions used are part of the Lagrange finite elements, previously defined in Section 3.2.3.

To solve the algebraic eigenvalue problem (5.32) for the dominant eigenvalue k_{eff} and its corresponding eigenvector, the power iteration method is used as defined in Section 3.4.

Finally, the solution fluxes must be normalized. Usually, it is forced that

$$1 = \frac{1}{V} \sum_{g=1}^{G} \int_\Omega \Sigma_{fg} \phi_0^g \,\mathrm{d}V. \tag{5.33}$$

5.5 Numerical Results

5.5.1 One dimensional homogeneous reactor

First, a one dimensional homogeneous slab of 2 cm thick with vacuum boundary conditions is considered. The material properties of the reactor are defined in Appendix B.1. This problem has been selected because has a simple analytic solution for the P_N approximation (Capilla et al., 2005) thus, it can be used to validate the solution of the FEM implementation. This problem is also relevant because it shows a bad behaviour when the diffusion approximation, P_1, is used due to the strong spatial variation of the neutronic flux.

Table 5.1 shows the fundamental eigenvalue and those corresponding to the subcritical modes obtained for the P_1, P_3 and P_5 approximations compared to the exact analytical values of the same neutron transport approximations. It can be seen that FEM results and analytic results are almost equal. Also, the results from the discrete-ordinates code ONEDANT (O'Dell, Brinkley, and Marr, 1982) with an angular quadrature order of S_{96} is included to be used as reference. This is a very good approximation to the exact transport solution but the computational cost of this method is very high to be used in more realistic problems. Hence, we can see an important improvement of P_3 eigenvalue results compared with P_1 results.

Table 5.1: First four dominant eigenvalues for the one dimensional homogeneous reactor.

	FEM Results			
	P_1	**P_3**	**P_5**	**S_{96}**
k_{eff}	0.5874890	0.6529562	0.6605229	0.662951
2nd	0.1491351	0.2077446	0.2233791	
3rd	0.0583796	0.0960912	0.0113888	
4th	0.0296016	0.0531219	0.0680403	
	Analytical Results			
k_{eff}	0.587489	0.652956	0.660523	
2nd	0.149135	0.207745	0.223379	
3rd	0.058380	0.096091	0.113889	
4th	0.029602	0.053122	0.068040	

Figure 5.1 shows the scalar flux from the P_N reference solution versus the P_N obtained with the FEM code. It can be noted that for the fundamental mode, the P_1 does not represent the transport solution accurately enough. In this way, P_3 and P_5 calculations follow the transport solutions very accurately. In Figures

5.2, 5.3 and 5.4 the solutions of the scalar flux associated with the next three subcritical modes are shown.

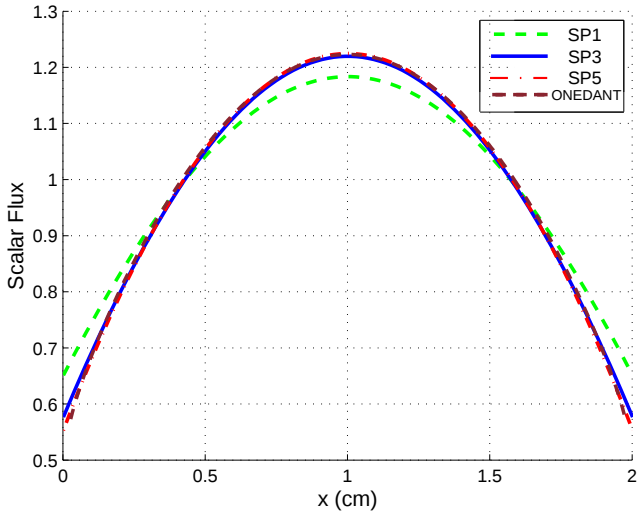

Figure 5.1: Scalar flux for the 1D homogeneous slab.

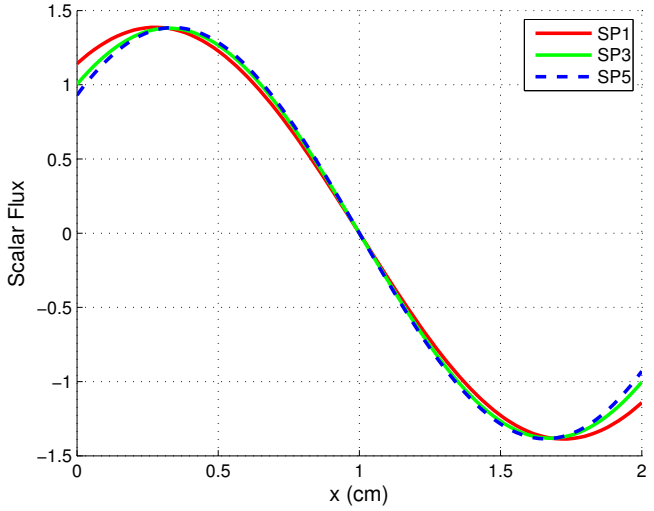

Figure 5.2: 2nd subcritical mode of the 1D homogeneous slab.

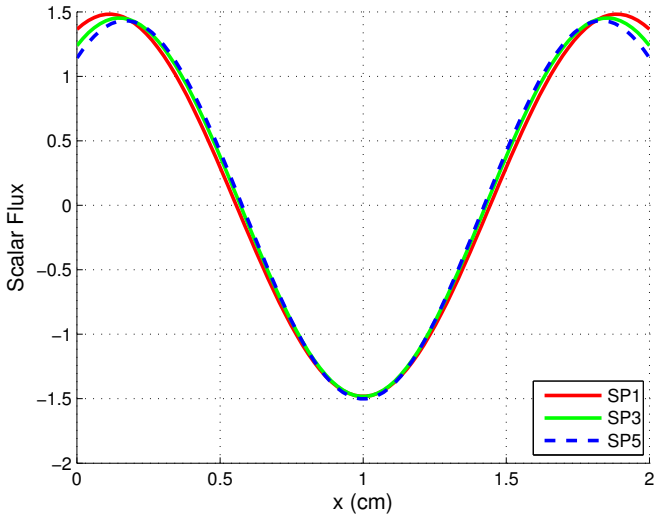

Figure 5.3: 3rd subcritical mode of the 1D homogeneous slab.

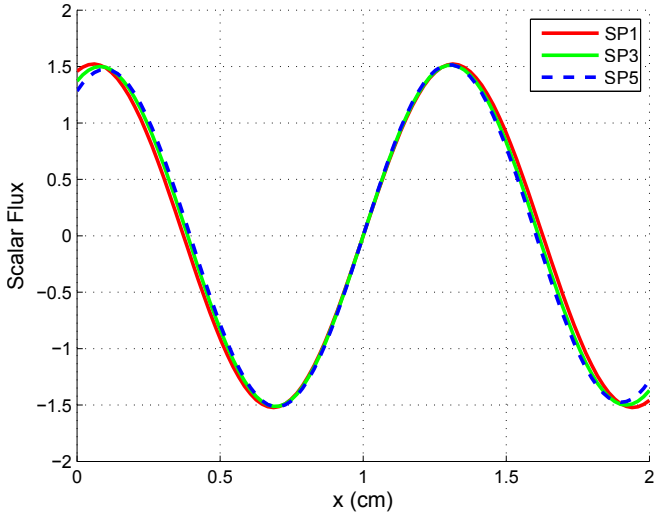

Figure 5.4: 4th subcritical mode of the 1D homogeneous slab.

5.5.2 One dimensional heterogeneous reactor

A more realistic example is a seven-region slab of 18 cm thick, with vacuum boundary conditions for the leftmost and rightmost faces. As before, this benchmark is defined in Appendix B.2.

Table 5.2 shows the first four eigenvalues computed with the finite element method for the P_N approximation with ($N = 1, 3, 5$). All FEM calculations have been computed with cubic shape functions because a high accuracy is demonstrated without an excessive number of degrees of freedom (DoFs) as stated in Vidal-Ferràndiz et al., (2014). Also it is included a reference k_{eff} calculation using the discrete ordinates code ONEDANT (O'Dell, Brinkley, and Marr, 1982) with an angular quadrature order of S_{96}, with 500 fine cells in each region and a convergence tolerance of 1e-6. In Figure 5.5a, the normalized scalar flux for the fundamental mode is plotted for the P_1, P_3 and P_5 approximations. Also, Figure 5.5 shows the second, third and fourth subcritical modes. It can be seen that P_3 and P_5 approximations give very accurate results close to the transport solution. However diffusion solution, here P_1, does not give enough accurate results for this assembly calculation.

Table 5.2: First four eigenvalues for the one dimensional heterogeneous reactor.

	FEM Results			
	P_1	**P_3**	**P_5**	**S_{96}**
k_{eff}	1.113872	1.148744	1.157360	1.16224
2nd	0.658651	0.735036	0.746618	
3rd	0.423944	0.527645	0.541952	
4th	0.109235	0.165305	0.188148	

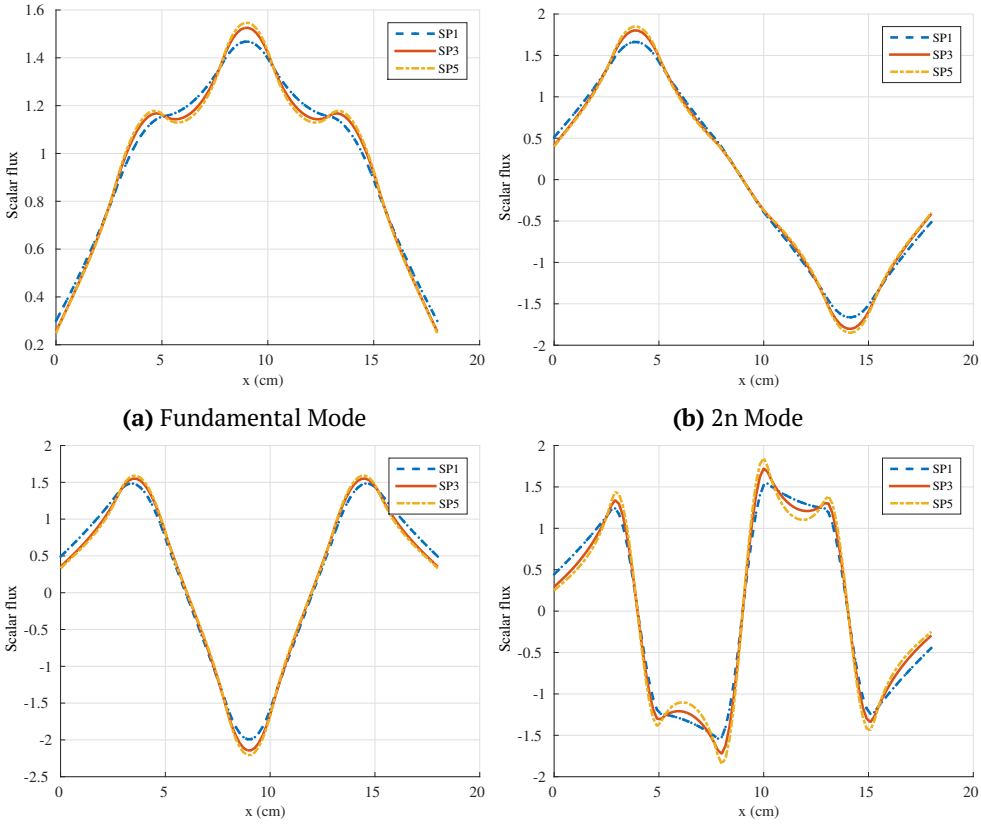

(a) Fundamental Mode

(b) 2n Mode

(c) 3rd Mode

(d) 4th Mode

Figure 5.5: Fluxes for the 1D heterogeneous slab.

5.5.3 BIBLIS 2D Reactor

In order to study the SP_N performance in a more realistic reactor the classical two dimensional BIBLIS benchmark is computed. This reactor is fully defined in Appendix B.6.

Table 5.3 shows the eigenvalue error and power errors for this reactor. Reference values are extracted from the SP_5 calculation. SP_1 calculation presents a small but considerable error in comparison with calculation involving more spherical harmonics. However, SP_3 is almost equal to SP_5 calculation so, SP_5 does not worth the extra computational effort. Figure 5.6 displays the relative power error per cell between SP_1 and SP_5 calculation. It can be seen that the error is located in

the cells near the boundary, where the power is underestimated, and in the center of the reactor, where the power is over estimated by the SP_1 calculation.

Table 5.3: Comparative results for BIBLIS reactor.

N	DoFs	k_{eff}	Δk_{eff} (pcm)	$\bar{\varepsilon}$ (%)	$\varepsilon_{\max}$
SP_1	4832	1.02535	49	1.44	0.04
SP_3	9664	1.02584	0	0.02	0.00
SP_5	14 496	1.02584			

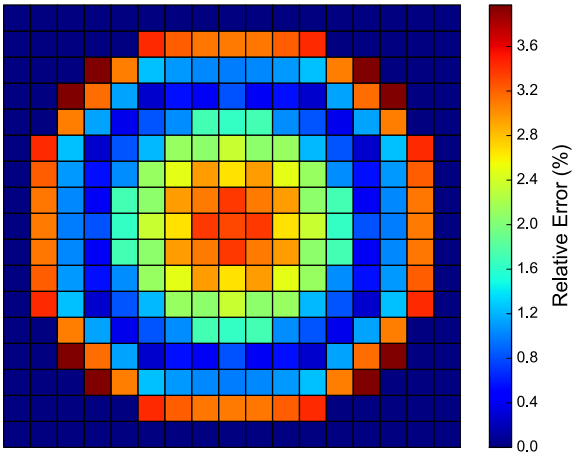

Figure 5.6: Relative error per assembly between SP_1 and SP_5 in BIBLIS 2D.

5.5.4 AER Benchmark

The performance of the SP_N approximation is also studied for the three dimensional hexagonal VVER-440 reactor. This reactor is defined in Appendix B.11.

Table 5.4 shows the results obtained for the fundamental eigenvalue, k_{eff}, using SP_1, SP_3 and SP_5 approximations. Also, the number of DoFs is shown and the mean relative and maximum relative difference for the axial power between both SP_1, SP_3 approximation and SP_5 approximation are displayed for the reactor configuration. The radial distribution of the error is shown in Figure 5.7. Also, the relative error using the SP_3 option of PARCS code (Downar et al., 2009) are included in this Figure. Figure 5.8 shows the axial power distribution for the SP_N approximation in this reactor. The axial difference in neutronic power distribution between both SP_1 and SP_3 approximations and SP_5 are shown also in Figure 5.9. It can be seen that SP_1 approximation has a maximum axial error above 1.6% while SP_3 and SP_5 almost present identical results, their axial difference is less than 0.1%.

Table 5.4: Comparative results for VVER-440 reactor.

N	DoFs	k_{eff}	Δk_{eff} (pcm)	$\bar{\varepsilon}$ (%)	$\varepsilon_{\max}$
1	857 882	1.01138	127	1.56	0.05
2	1 715 764	1.01261	4	0.04	0.00
3	2 573 646	1.01265	0		

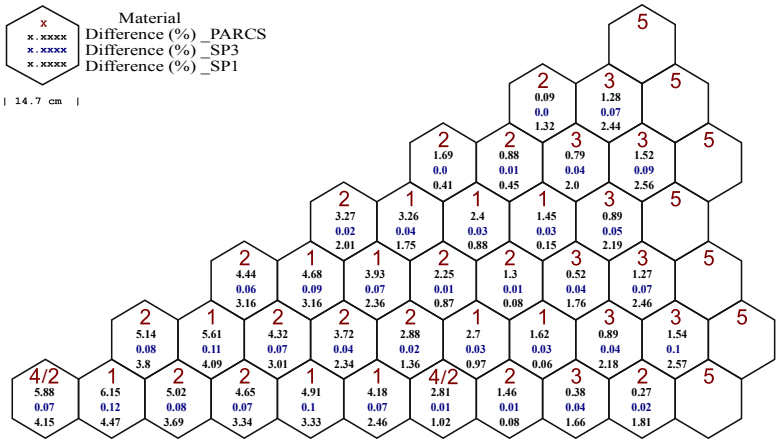

Figure 5.7: Radial distribution of errors for VVER-440 reactor.

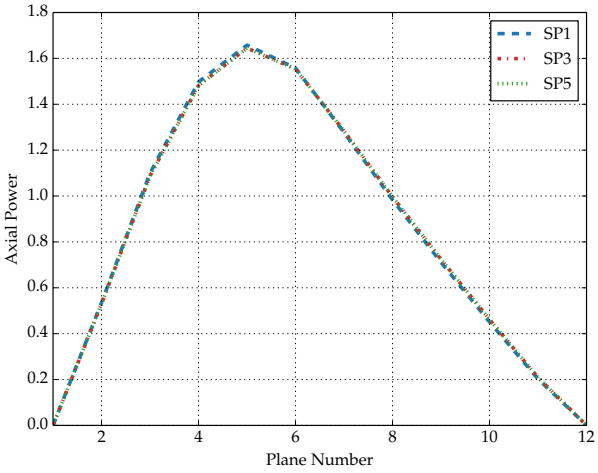

Figure 5.8: Axial power distribution for VVER-440 reactor.

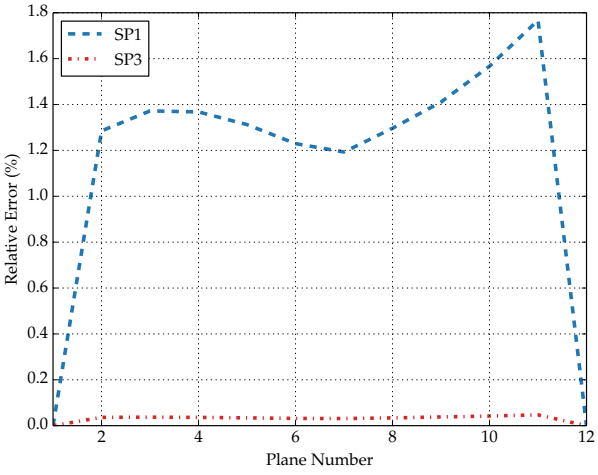

Figure 5.9: Axial errors distribution for VVER-440 reactor.

5.5.5 IAEA 3D

The performance of the SP_N approximation is also studied for the three dimensional IAEA-3D reactor with rectangular geometry (American Nuclear Society, 1977). This reactor is defined in Appendix B.8.

Table 5.5 shows the results obtained for the fundamental eigenvalue, k_{eff}, using SP_1, SP_3 and SP_5 approximations. The radial distribution of the error is shown in Figure 5.10 and Figure 5.11 shows the axial power distribution for the SP_N $(N = 1, 3, 5)$ approximations. The axial difference in neutronic power distribution between both SP_1 and SP_3 approximations and SP_5 are shown in Figure 5.12. It can be seen that SP_1 approximation has a maximum axial error above 1.2% while SP_3 and SP_5 almost present identical results, their axial difference is less than 0.1%. Again we can observe that SP_3 approximation improves diffusion theory result without an excessive increment of the computational cost. SP_5 does not give any relevant improvement compared to SP_3 .

Table 5.5: Comparative results for IAEA 3D reactor.

N	DoFs	k_{eff}	Δk_{eff} (pcm)	$\bar{\varepsilon}$ (%)	$\varepsilon_{\max}$
1	263 552	1.02913	59	0.79	0.02
2	527 104	1.02971	1	0.03	0.00
3	790 656	1.02972	0	0.00	0.00

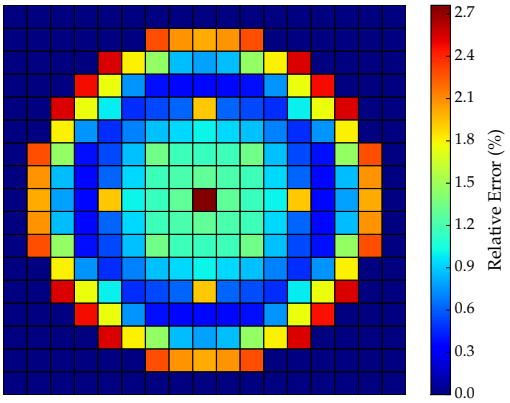

Figure 5.10: Radial distribution of errors for IAEA 3D reactor.

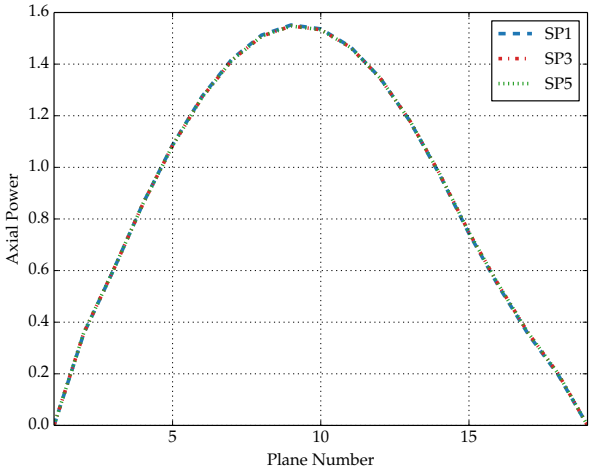

Figure 5.11: Axial power distribution for IAEA 3D reactor.

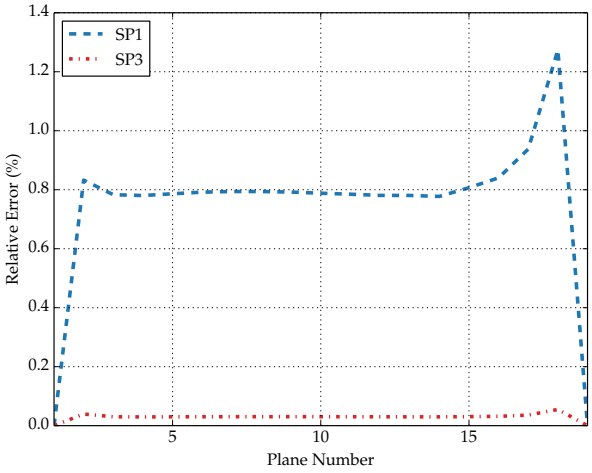

Figure 5.12: Axial errors distribution for IAEA 3D reactor.

6 Homogenization and Discontinuity Factors

6.1 Introduction

A nuclear core typically consists of around 150 to 700 fuel assemblies measuring from 10 cm to 30 cm in radial size and slightly less than 4 m axially. Also, each one of the fuel assemblies is constituted by typically hundreds of solid fuel pins containing fissile nuclei surrounded by cladding regions, coolant, structural elements, burnable poisons, water channels, control rods, and so on (Stacey, 2007). In other words, hundreds of thousands of heterogeneous regions.

To solve a full heterogeneous reactor core is computationally challenging and most of the times unaffordable because of the complexity of the spatial domain and the fine angular and energy discretization required to accurately solve it. To reduce the computational cost, this problem is usually solved with a scheme consisting on two stages of calculation for different scales through a homogenization process. The first stage is a very detailed energy and spatial calculation on a reference domain to obtain cross sections averaged over energy and space, which can be later used in few group global core calculations in the second stage of the method.

In this way, spatial homogenization consists in replacing heterogeneous subdomains by homogeneous ones, in such a way that the homogenized problem provides fast and accurate average results. Nuclear engineering homogenization makes use of the periodicity of the geometry of the core. Even though each assem-

bly and pin contains different nuclear enrichments, they have the same geometry and similar neutron flux behaviour. Because the homogenized function to be calculated is smoother than the heterogeneous one, the original exact transport operator can be replaced with a low-order transport operator that eliminates some of the complexity of the original problem (Sanchez, 2009). For full core calculations the neutron diffusion equation in the approximation of two energy groups is usually employed. For more precision, SP_3 neutron transport approximation with up to 8 energy groups can be used. Then, the global solution can be reconstructed approximately using the previously computed isolated heterogeneous subdomain solutions multiplied by the average values of the solution on the subdomain obtained from the homogenized problem over the whole domain.

A first step in a homogenization methodology is to choose heterogeneous reactor properties that should be reproduced when the homogenized problem is solved. Usually, these quantities are the subdomain averaged reaction rates, the surface-averaged net currents and the multiplicative constant of the reactor, which is implicitly conserved if the two aforementioned quantities are preserved.

In the generalized equivalence theory (Smith, 1986), which is an extension of Koebke's homogenization method (Wagner and Koebke, 1983), flux discontinuity factors are introduced, forcing a jump for the neutron flux between different homogenized regions. Different homogenization strategies and definitions of discontinuity factors exist, such as the flux discontinuity ratios (Sanchez, Dante, and Zmijarevic, 2013), the current discontinuity factors (Sanchez, 2009) or the consistent discontinuity factors (Trahan and Larsen, 2015), among others. In another way, the *superhomogenization* procedure (SPH) introduces corrective factors to normalize the homogenized cross sections to produce the correct reaction rates in the homogenized problem (Kavenoky, 1978; Hébert, 1981; Hébert and Mathonniere, 1993; Hébert, 1993). The SPH corrective factors are calculated through an iterative procedure that maintains the continuity of the solution in the homogenized problem. Also, different mathematical justifications of the homogenization process in periodic lattices have been developed (Allaire and Bal, 1999; Allaire and Capdeboscq, 2000).

Discontinuity factor methodologies were developed for nodal methods because a discontinuity in the neutron flux while maintaining continuous the neutron current can be forced in a natural way in these methods. Most of finite element methods look for the neutronic flux as a continuous function in the reactor core. Thus, it is difficult to implement in such a methodology forced discontinuities between adjacent subdomains. In this Chapter, an approach is proposed to use a high order discontinuous Galerkin finite element method where the jump condition for the neutron flux is imposed in a weak sense using interior penalty terms.

For a long time, the preferred low order operator used for whole core calculations has been the neutron diffusion equation and the homogenized regions have been subdomains of the size of a fuel assembly. Because the computational resources available have increased, the homogenized regions have decreased to the size of a single pin and the low order operator relying on diffusion theory is being abandoned so that transport effects that occur at these smaller scales can be taken into account. One could, for instance, use the Simplified P_N (SP_N) formulation (Larsen, Morel, and McGhee, 1996). Homogenization errors for pin computations are the main concern in these approximations, and they have been recently studied for different problems (Kozlowski et al., 2011; Yu, Lu, and Chao, 2014). The main issue has been the definition of the discontinuity factors for the SP_N approximation in two- or three-dimensional problems (Yu and Chao, 2015; Chao, 2016b; Chao, 2016a; Yamamoto, Sakamoto, and Endo, 2016). On the other hand, the SP_N approximation has been implemented using the finite element method (FEM) for the spatial discretization (Turcksin, Ragusa, and Bangerth, 2010; Ragusa, 2010; Zhang, Ragusa, and Morel, 2013). In this Chapter, we also investigate the use of classical discontinuity factors for the correction of the homogenization error in a FEM when using SP_N as low order operator for pin-wise homogenization.

The rest of the Chapter is structured as follows. Section 6.2 summarizes the Generalized Equivalence theory for the diffusion theory. Then, Section 6.3 explains the Discontinuous Galerkin method with interior penalties in order to force the desired discontinuities between reactor regions. In Section 6.4, the method to calculate the reference (exact) discontinuity factor is explained. In Section 6.5, numerical results for the Discontinuous Galerkin method in one-dimensional and two-dimensional problems for the diffusion equation are presented. In Section 6.6, we extended the homogenization procedure to the SP_N approximation. In Section 6.7, we test the performance of the SP_N neutron transport approximation using one-dimensional problems against the SP_N solution with IP-FEM without discontinuity factors, and against the classical diffusion theory with discontinuity factors in order show the importance of using discontinuity factors for the homogenized equation. This Chapter rewrites the works published Vidal-Ferràndiz et al., (2016b) and Vidal-Ferràndiz et al., (2018).

6.2 Generalized Equivalence Theory

A first step in a homogenization methodology is to choose the heterogeneous reactor properties that would be reproduced when the homogenized problem is solved. Usually, these quantities are the node averaged group reaction rates, the surface-averaged group currents and the k-effective of the reactor, which

is implicitly conserved if the two aforementioned quantities are preserved. In this way, for every energy group g and every nuclear cross section $\Sigma_{\alpha\, g}$, the equations (Smith, 1986),

$$\int_{V_{hr}} \hat{\Sigma}^{hr}_{\alpha\, g} \hat{\phi}_g(\vec{r})\, \mathrm{d}\vec{r} = \int_{V_{hr}} \Sigma_{\alpha\, g}(\vec{r}) \phi_g(\vec{r})\, \mathrm{d}\vec{r}\,, \tag{6.1}$$

and

$$\int_{S_{hr}} \left(\hat{D}^{hr}_g \vec{\nabla} \hat{\phi}_g(\vec{r}) \right)\, \mathrm{d}\vec{S} = \int_{S_{hr}} \left(D_g(\vec{r}) \vec{\nabla} \phi_g(\vec{r}) \right)\, \mathrm{d}\vec{S}\,, \tag{6.2}$$

must be satisfied, where V_{hr} and S_{hr} are the volume of the homogenized region hr and its limiting surface, respectively; ϕ_g is the solution of the heterogeneous problem and $\hat{\phi}_g$ is the solution obtained using the homogenized parameters $\hat{\Sigma}^{hr}_{\alpha\, g}$ and $\hat{D}^{hr}_g$.

The determination of the homogenized parameters from equation (6.1) requires the knowledge of the heterogeneous solution, ϕ_g and the homogenized solution $\hat{\phi}_g$, which depends on the homogenized parameters. To overcome this difficulty, an approximation must be done. The homogenized parameters are considered to be constant for every region V_k, thus, expression (6.1) can be rewritten as

$$\hat{\Sigma}^{hr}_{\alpha\, g} = \frac{\int_{V_{hr}} \Sigma_{\alpha\, g}(\vec{r}) \phi_g(\vec{r})\, \mathrm{d}\vec{r}}{\int_{V_{hr}} \phi_g(\vec{r})\, \mathrm{d}\vec{r}}\,, \tag{6.3}$$

where the average value of the homogeneous flux has been approximated by the average value of the heterogeneous flux, i.e.,

$$\int_{V_{hr}} \hat{\phi}_g(\vec{r})\, \mathrm{d}\vec{r} \approx \int_{V_{hr}} \phi_g(\vec{r})\, \mathrm{d}\vec{r}\,, \tag{6.4}$$

and the diffusion coefficient can be expressed

$$\hat{D}^{hr}_g = \frac{\int_{S_{hr}} \left(D_g(\vec{r}) \vec{\nabla} \phi_g(\vec{r}) \right)\, \mathrm{d}\vec{S}}{\int_{S_{hr}} \vec{\nabla} \hat{\phi}_g(\vec{r})\, \mathrm{d}\vec{S}}\,. \tag{6.5}$$

When looking at the homogenized diffusion coefficients in equation (6.5), we see that they are, in general, different for each surface, and this makes impossible to define constant diffusion coefficients in each homogenized region. To solve this problem, some conditions imposed to the solution of the homogenized region have to be relaxed. Different approaches to relax these conditions lead to different homogenization methods. In the generalized equivalence theory (Smith,

1986), which is an extension of Koebke's homogenization method (Wagner and Koebke, 1983), flux discontinuity factors are introduced, relaxing the condition of continuity of the neutron flux in the interior faces of the homogenized regions.

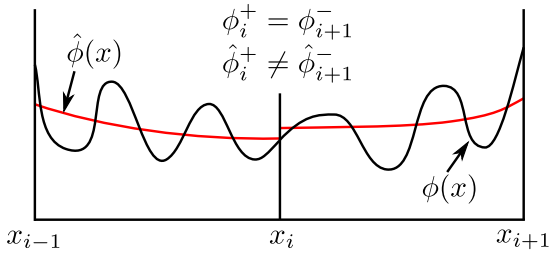

Figure 6.1: Reference discontinuity factors.

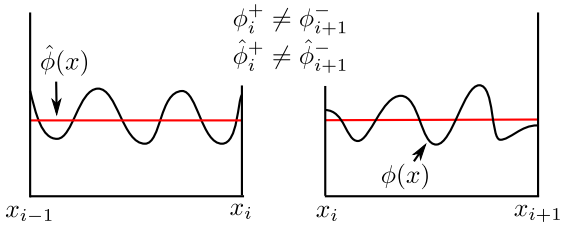

Figure 6.2: Assembly or pin discontinuity factors.

In this theory, the homogenized diffusion coefficients are computed as flux-volume weighted parameters, that is,

$$\frac{1}{\hat{D}_g} = \frac{\int_{V_{hr}} \frac{1}{D_g(\vec{r})} \phi_g(\vec{r})\, d\vec{r}}{\int_{V_{hr}} \phi_g(\vec{r})\, d\vec{r}}\,, \tag{6.6}$$

where we have used the equation (6.4) to avoid the homogeneous flux in the formulation.

For a given interface S_j limiting two adjacent homogenized regions, the energy-dependent discontinuity factors are defined as interface constants $f_{g,j}^-$, $f_{g,j}^+$, such

that

$$f_{g,j}^{-} \int_{S_j} \hat{\phi}_g^{-}(\vec{r}) dS = f_{g,j}^{+} \int_{S_j} \hat{\phi}_g^{+}(\vec{r}) dS \,, \tag{6.7}$$

where $\hat{\phi}_g^{-}(\vec{r})$ and $\hat{\phi}_g^{+}(\vec{r})$ are the lateral (directional) limits of the homogenized flux in the surface S_j viewed from the two different regions sharing this surface (see Figures 6.1 and 6.2). A possible definition of these discontinuity factors is

$$f_{g,j}^{-} = \frac{\int_{S_j} \phi_g^{-} \, dS}{\int_{S_j} \hat{\phi}_g^{-} \, dS} \,, \quad f_{g,j}^{+} = \frac{\int_{S_j} \phi_g^{+} \, dS}{\int_{S_j} \hat{\phi}_g^{+} \, dS} \,, \tag{6.8}$$

so continuity for the heterogeneous reconstructed flux is enforced. Condition (6.7) deals with averaged values in the surface S_j, so the generalized equivalence theory can be easily implemented into nodal methods, which use nodal-average fluxes and surface-average currents (Smith, 1986).

At this point we need the value of the heterogeneous and homogeneous fluxes, $\phi_g(\vec{r})$ and $\hat{\phi}_g(\vec{r})$ respectively, to generate the discontinuity factors and the homogenized cross sections. Different choices for these fluxes generate different homogenization parameters. Two techniques are considered in this work. The first one consists of using the heterogeneous flux calculated for the whole reactor for generating the Reference Cross Sections (RXS), and appropriate fixed current boundary conditions from the heterogeneous solution, together with the global k_{eff} and these RXS to generate the homogeneous flux in a particular region considered here as a fuel assembly. Thus, Reference Discontinuity Factors (RDF) are generated using equation (6.8) (See Figure 6.1). This technique provides exact homogenized parameters, but it requires the solution of the whole heterogeneous problem to generate the homogenized parameters, what makes it not practical. However, because of its reduced homogenization error, it is used here to verify that the discontinuity factors technique is successfully implemented within the interior penalty finite element method.

To circumvent the need of the whole core heterogeneous solution, the second technique studied here consists of considering that the heterogeneous flux is calculated for a single assembly or pin with reflective boundary conditions. This approach would be accurate if the different assemblies composing the core were similar to the assembly being homogenized. Thus, with the assembly or pin heterogeneous flux, we generate the Assembly homogenized Cross Sections (AXSs) or Pin homogenized Cross Section (PXSs), and the homogenized flux will be the solution of the homogenized problem with reflective boundary conditions, so we can define the Assembly Discontinuity Factors (ADFs) or Pin Discontinuity Factors (PDFs) with these fluxes (See Figure 6.2). This approach avoids to need

the heterogeneous solution for the whole core, but it introduces homogenization errors, which can be very large in a situation where the assemblies composing the core are very different to each other. The accuracy of the homogenized parameters can be increased by iterating between the solution of the homogenized problem and the homogenization process, using more accurate boundary conditions for the single assembly calculations that take into account the neighbourhood of the assembly. This kind of technique is not considered here, because the main focus of this work is the introduction of the flux discontinuity factors in the finite element formulation.

6.3 Discontinuous Galerkin method with interior penalty

Discontinuous Galerkin methods, were introduced in the early seventies to study neutron transport equations in Reed and Hill, (1973) and Lesaint and Raviart, (1974). They have become very popular to solve problems arising from hyperbolic type partial differential equations. Because of the versatility of these methods, they have been also applied to elliptic and parabolic problems (Arnold et al., 2000; Arnold et al., 2002).

Discontinuous Galerkin (DG) methods define an approximation to the solution by means of a variational formulation that tries to enforce the partial differential equation of the model together with the boundary and continuity conditions for the solution in a weak sense (Brezzi et al., 2006a). In this way, the DG method establishes a linear relationship between the residual of the approximation inside each element and its jumps across inter-element boundaries. This yields a formalism, that in a natural way, allows imposing jumps across the element interfaces without affecting the current as proposed in the generalized equivalence theory for homogenized reactors. It makes possible to use the finite element method for coarse-mesh reactor calculation after the homogenization procedure together with discontinuity factors, providing a suitable theoretical framework for developing new methodologies and more advanced schemes for the approximation of the homogenized neutron diffusion equation.

In the following, we present the Discontinuous Galerkin method proposed for the neutron diffusion equation with discontinuity factors, both for one and multi-dimensional problems.

6.3.1 One-dimensional problems

To show the method, we start with a source problem associated with the mono-energetic one-dimensional diffusion equation

$$-\frac{\partial}{\partial x}\left(D\frac{\partial\phi}{\partial x}\right)+\Sigma_a\phi=q\,, \tag{6.9}$$

for a reactor Ω. We choose a partition of the one-dimensional domain into K subdomains (Ω_k) with edges x_0, x_1, ..., x_K. Multiplying equation (6.9) by a test function, v, and integrating over Ω we obtain

$$-\int_\Omega v\frac{\partial}{\partial x}\left(D\frac{\partial\phi}{\partial x}\right)dx+\int_\Omega v\Sigma_a\phi\,dx=\int_\Omega vq\,dx\,. \tag{6.10}$$

Integrals defined over the whole domain in equation (6.10) can be written as the sum of integrals over each sub-domain as follows

$$-\sum_{e=1}^{K}\int_{x_{e-1}}^{x_e} v\frac{\partial}{\partial x}\left(D\frac{\partial\phi}{\partial x}\right)dx+\sum_{e=1}^{K}\int_{x_{e-1}}^{x_e} v\Sigma_a\phi\,dx=\sum_{e=1}^{K}\int_{x_{e-1}}^{x_e} vq\,dx\,. \tag{6.11}$$

After integrating by parts, equation (6.11) can be written as

$$\begin{aligned}\sum_{e=1}^{K}\int_{x_{e-1}}^{x_e}\frac{\partial v}{\partial x}D\frac{\partial\phi}{\partial x}\,dx-\sum_{e=1}^{K}\int_{x_{e-1}}^{x_e}\frac{\partial}{\partial x}\left(vD\frac{\partial\phi}{\partial x}\right)dx\\ +\sum_{e=1}^{K}\int_{x_{e-1}}^{x_e} v\Sigma_a\phi\,dx=\sum_{e=1}^{K}\int_{x_{e-1}}^{x_e} vq\,dx\,.\end{aligned} \tag{6.12}$$

Assuming that the neutronic flux and the diffusion coefficients can be discontinuous and making use of lateral limits, expression (6.12) is expressed as

$$\begin{aligned}-\sum_{e=1}^{K}\left(v_{e+1}^{-}D_{e+1}^{-}\frac{\partial\phi_e^{-}}{\partial x}-v_e^{+}D_k^{+}\frac{\partial\phi_e^{+}}{\partial x}\right)+D_e\sum_{e=1}^{K}\int_{x_{e-1}}^{x_e}\frac{\partial v}{\partial x}\frac{\partial\phi}{\partial x}\,dx\\ +\sum_{e=1}^{K}\int_{x_{e-1}}^{x_e} v\Sigma_a\phi\,dx=\sum_{e=1}^{K}\int_{x_{e-1}}^{x_e} vq\,dx.\end{aligned} \tag{6.13}$$

where the piece-wise constant diffusion coefficient D_e has moved outside of the integral, and $\phi_e^{\pm}$ is defined as the lateral limit of the flux at point x_e (considering the flux as belonging to the previous or posterior subdomain), i.e.,

$$\phi_e^{\pm}=\lim_{x\to x_e^{\pm}}\phi(x)\,. \tag{6.14}$$

The first term of this equation, may be written as

$$\begin{aligned} T(\phi) &= \sum_{e=1}^{K} \left(v_e^+ D_e^+ \frac{\partial \phi_e^+}{\partial x} - v_{e+1}^- D_{e+1}^- \frac{\partial \phi_e^-}{\partial x} \right) \\ &= v_0^+ D_0^+ \frac{\partial \phi_0^+}{\partial x} + \sum_{e=1}^{K} \left(v_e^+ D_e^+ \frac{\partial \phi_e^+}{\partial x} - v_e^- D_e^- \frac{\partial \phi_e^-}{\partial x} \right) - v_K^- D_K^- \frac{\partial \phi_K^-}{\partial x} \,. \end{aligned} \tag{6.15}$$

Using the identity

$$\begin{aligned} v_e^+ D_e^+ \frac{\partial \phi_e^+}{\partial x} - v_e^- D_e^- \frac{\partial \phi_e^-}{\partial x} = &-\frac{1}{2} \left(v_e^+ + v_e^- \right) \left(D_e^- \frac{\partial \phi_e^-}{\partial x} - D_e^+ \frac{\partial \phi_e^+}{\partial x} \right) \\ &-\frac{1}{2} \left(v_e^- - v_e^+ \right) \left(D_e^+ \frac{\partial \phi_e^+}{\partial x} + D_e^- \frac{\partial \phi_e^-}{\partial x} \right) , \end{aligned}$$

and introducing the notation

$$\begin{aligned} \{v\}_e &= \frac{1}{2} \left(v_e^+ + v_e^- \right) , & \left\{ D \frac{\partial \phi}{\partial x} \right\}_e &= \frac{1}{2} \left(D_e^+ \frac{\partial \phi_e^+}{\partial x} + D_e^- \frac{\partial \phi_e^-}{\partial x} \right) , \\ [\![v]\!]_e &= v_e^- - v_e^+ , & \left[\!\!\left[D \frac{\partial \phi}{\partial x} \right]\!\!\right]_e &= D_e^- \frac{\partial \phi_e^-}{\partial x} - D_e^+ \frac{\partial \phi_e^+}{\partial x} , \end{aligned}$$

the term (6.15), is rewritten as

$$\begin{aligned} T(\phi) = v_0^+ D_0^+ \frac{\partial \phi_0^+}{\partial x} - \sum_{e=1}^{K} \left(\{v\}_e \left[\!\!\left[D \frac{\partial \phi}{\partial x} \right]\!\!\right]_e \right) - \sum_{e=1}^{K} \left([\![v]\!]_e \left\{ D \frac{\partial \phi}{\partial x} \right\}_e \right) \\ - v_K^- D_K^- \frac{\partial \phi_K^-}{\partial x} \,. \end{aligned}$$

We are looking for solutions of the neutron diffusion equation that satisfy the continuity of the neutron current in the interior vertices of the mesh and that satisfy also the discontinuity factors condition in these vertices. That is,

$$\left[\!\!\left[D \frac{\partial \phi}{\partial x} \right]\!\!\right]_e = 0 \,, \tag{6.16}$$

$$[\![\phi]\!]_{f,\,e} = f_e^- \phi_e^- - f_e^+ \phi_e^+ = 0 \,, \quad e = 1,\, 2,\, \ldots,\, K, \tag{6.17}$$

where f_e^+ and f_e^- are the right and left discontinuity factors for vertex x_e, respectively.

Using the continuity condition for the current in the interior vertices from equation (6.16), the term (6.15) can be expressed as

$$T(\phi) = v_0^+ D_0^+ \frac{\partial \phi_0^+}{\partial x} - \sum_{e=1}^{K} \left([\![v]\!]_e \left\{ D \frac{\partial \phi}{\partial x} \right\}_e \right) - v_K^- D_K^- \frac{\partial \phi_K^-}{\partial x} \,, \tag{6.18}$$

while preserving the consistency of the formulation (the weak formulation is satisfied by the solution of the original strong formulation defined by equation (6.9)).

To stabilize this method, a penalty term is introduced (Brezzi et al., 2006a),

$$P(\phi) := \sum_{e=1}^{K} s_e \left([\![\phi]\!]_{f,\,e} [\![v]\!]_e \right) \,, \tag{6.19}$$

which does not affect the consistency of the formulation ($P(\phi) = 0$ when ϕ satisfies the discontinuity factors condition (6.17)), and the new term $T^{sp}(\phi) := T(\phi) + P(\phi)$ is written as

$$\begin{aligned} T^{sp}(\phi) =& v_0^+ D_0^+ \frac{\partial \phi_0^+}{\partial x} - v_K^- D_K^- \frac{\partial \phi_K^-}{\partial x} \\ & - \sum_{e=1}^{K} \left(\left\{ D \frac{\partial \phi}{\partial x} \right\}_e [\![v]\!]_e \right) + \sum_{e=1}^{K} s_e \left([\![\phi]\!]_{f,\,e} [\![v]\!]_e \right) \,. \end{aligned} \tag{6.20}$$

Then, equation (6.13) is rewritten as

$$\begin{aligned} & \sum_{e=1}^{K} \int_{x_{e-1}}^{x_e} \frac{\partial v}{\partial x} D \frac{\partial \phi}{\partial x} \, dx + \sum_{e=1}^{K} \int_{x_{e-1}}^{x_e} v \Sigma_a \phi \, dx - \sum_{e=1}^{K} \left(\left\{ D \frac{\partial \phi}{\partial x} \right\}_e [\![v]\!]_e \right) \\ & + \sum_{e=1}^{K} s_e \left([\![\phi]\!]_{f,\,e} [\![v]\!]_e \right) + v_0^+ D_0^+ \frac{\partial \phi_0^+}{\partial x} - v_K^- D_K^- \frac{\partial \phi_K^-}{\partial x} = \sum_{e=1}^{K} \int_{x_{e-1}}^{x_e} v q \, dx \,. \end{aligned} \tag{6.21}$$

Boundary conditions remain to be introduced in the method to be completely defined. The boundary conditions are imposed in a weak form (Rivière, 2008) and this can be made modifying the terms,

$$v_0^+ D_0^+ \frac{\partial \phi_0^+}{\partial x} - v_K^- D_K^- \frac{\partial \phi_K^-}{\partial x}, \tag{6.22}$$

in equation (6.21). Hence, if zero current conditions are imposed, these terms are identically zero. If zero flux boundary conditions are imposed these terms remain unaltered. And if albedo boundary conditions are considered,

$$-D_0^+ \frac{\partial \phi_0^+}{\partial x} = \alpha_0 \phi_0^+ , \qquad D_K^- \frac{\partial \phi_K^-}{\partial x} = \alpha_K \phi_K^- .$$

Thus, the terms (6.22) are substituted by

$$- v_0^+ \alpha_0 \phi_0^+ - v_K^- \alpha_K \phi_K^-. \tag{6.23}$$

This scheme requires the user to specify a parameter, s_e, which is known as a penalty parameter. This parameter can be viewed as a Lagrange multipliers condition to enforce the discontinuity factor condition in the finite element formulation. If the value of this parameter is not sufficiently large, the approximate solution is unstable. On the other hand, for an arbitrarily large value of the penalty parameter the condition number for the resulting matrices of the discretization would degenerate (Shahbazi, 2005). The development of optimal lower bounds for these parameters is out of the scope of this work, so here the penalty parameters are chosen, based in the expressions provided by Epshteyn and Rivière, (2007) and Shahbazi, (2005), as a large enough parameter ensuring convergence for the method.

Using the discontinuity factor condition (6.17), also a *symmetrizing* term could be introduced in the method, which is identically zero for the exact solution of the problem,

$$\theta \sum_{e=1}^{K} \left([\![\phi]\!]_{f,\,e} \left\{ D \frac{\partial v}{\partial x} \right\}_e \right), \tag{6.24}$$

thus equation (6.21) can be substituted by

$$\begin{aligned} &\sum_{e=1}^{K} \int_{x_{e-1}}^{x_e} \frac{\partial v}{\partial x} D \frac{\partial \phi}{\partial x}\, dx + \sum_{e=1}^{K} \int_{x_{e-1}}^{x_e} v \Sigma_a \phi \, dx \\ &- \sum_{e=1}^{K} \left(\left\{ D \frac{\partial \phi}{\partial x} \right\}_e [\![v]\!]_e \right) + \theta \sum_{e=1}^{K} \left([\![\phi]\!]_{f,\,e} \left\{ D \frac{\partial v}{\partial x} \right\}_e \right) + \sum_{e=1}^{K} s_e \left([\![\phi]\!]_{f,\,e} [\![v]\!]_e \right) \\ &+ v_0^+ D_0^+ \frac{\partial \phi_0^+}{\partial x} - v_K^- D_K^- \frac{\partial \phi_K^-}{\partial x} = \sum_{e=1}^{K} \int_{x_{e-1}}^{x_e} vq \, dx \,, \end{aligned} \tag{6.25}$$

where different values for the parameter $\theta = \{-1, 0, 1\}$ can be selected, obtaining different methods (Sun and Wheeler, 2005). Selecting $\theta = -1$ a method similar to the Symmetric Interior Penalty Galerkin (SIPG) method is obtained. For $\theta = 1$ it gives the analogous to the Non-symmetric Interior Penalty Galerkin (NIPG) method, and $\theta = 0$ corresponds to the Incomplete Interior Penalty Galerkin (IIPG) method. The symmetrizing term (6.24) is different from the one used in interior penalty methods, because it has the jump with respect to the discontinuity factors instead of the classical jump respect to the continuity of the solution. Thus, it

does not provide symmetry for the linear systems when using the SIPG method, and has not known advantages for the NIPG method. because no known reason justifies using one of the other methods, $\theta = 0$ is considered in our formulation.

6.3.2 Multidimensional problems

The interior penalty finite element method can be generalized to problems with multidimensional geometry. For this kind of problems, equation (6.9) is written as

$$-\vec{\nabla} D \vec{\nabla}\phi + \Sigma_a \phi = q\,. \tag{6.26}$$

This equation is defined for a reactor Ω, which is divided into subdomains Ω_1, Ω_2, $\ldots$, Ω_N, where the homogenized cross sections are considered as constant values.

Multiplying equation (6.26) by a test function, v, and integrating over Ω, it is obtained

$$-\int_\Omega v\vec{\nabla} D\vec{\nabla}\phi\,\mathrm{d}\vec{r} + \int_\Omega v\Sigma_a\phi\,\mathrm{d}\vec{r} = \int_\Omega vq\,\mathrm{d}\vec{r},$$

which can be rewritten as

$$-\sum_{k=1}^{K}\int_{\Omega_k} v\vec{\nabla} D\vec{\nabla}\phi\,\mathrm{d}\vec{r} + \int_\Omega v\Sigma_a\phi\,\mathrm{d}\vec{r} = \int_\Omega vq\,\mathrm{d}\vec{r}. \tag{6.27}$$

Integrating by parts the first term and using Green's theorem, we rewrite the first term of equation (6.27) as

$$-\int_{\Omega_k} v\vec{\nabla} D\vec{\nabla}\phi\,\mathrm{d}\vec{r} = D\int_{\Omega_k}\vec{\nabla} v\vec{\nabla}\phi\,\mathrm{d}\vec{r} - \int_{\partial\Omega_k} vD\vec{\nabla}\phi\,\vec{n}\mathrm{d}S\,.$$

In this way, equation (6.27), can be written as

$$\sum_{k=1}^{K} D\int_{\Omega_k}\vec{\nabla} v\vec{\nabla}\phi\,\mathrm{d}\vec{r} - \sum_{k=1}^{K}\int_{\partial\Omega_k} vD\vec{\nabla}\phi\,\vec{n}\mathrm{d}S + \int_\Omega v\Sigma_a\phi\,\mathrm{d}\vec{r} = \int_\Omega vq\,\mathrm{d}\vec{r}. \tag{6.28}$$

We decompose the surface integrals as a sum over the different faces limiting each node, distinguishing the set of interior faces $\mathcal{E}_h^0$ from the set of faces placed at the boundary of the reactor, $\mathcal{E}_h^\partial$. In this way, the set of all points that define the partition into subintervals $\mathcal{E}_h := \mathcal{E}_h^0 \cup \mathcal{E}_h^\partial$. For two adjacent elements Ω_i and

Ω_j, sharing the interior face e, the average and jump operators are defined by

$$\begin{aligned} \left\{D\vec{\nabla}\phi\right\}_e &= \frac{1}{2}\left(D_i\vec{\nabla}\phi_i^- + D_j\vec{\nabla}\phi_j^+\right), & \{v\}_e &= \frac{1}{2}\left(v_i^- + v_j^+\right), \\ \left[\!\left[D\vec{\nabla}\phi\right]\!\right]_e &= D_i\vec{\nabla}\phi_i^-\ \vec{n}_i + D_j\vec{\nabla}\phi_j^+\ \vec{n}_j, & [\![v]\!]_e &= v_i^-\vec{n}_i + v_j^+\vec{n}_j, \end{aligned} \tag{6.29}$$

where D_i, $\phi_i^{\pm}$, $v_i^{\pm}$ are the lateral limits in the surface e of D, ϕ and v in the node Ω_i; and $\vec{n}_i$ is the normal vector to the face e pointing outwards of node Ω_i[1]. Collecting together the integrals over the same face and operating in a similar way as it has been done for the one-dimensional case, using the definitions (6.29), we set

$$\begin{aligned} -\sum_{k=1}^{K}\int_{\partial\Omega_k} vD\vec{\nabla}\phi\,\vec{n}\,\mathrm{d}S = &-\sum_{b\in\mathcal{E}_h^{\partial}}\int_b vD\vec{\nabla}\phi\,\vec{n}\,\mathrm{d}S \\ &-\sum_{e\in\mathcal{E}_h^0}\int_e \left\{D\vec{\nabla}\phi\right\}_e [\![v]\!]_e\ \vec{n}\,\mathrm{d}S - \sum_{e\in\mathcal{E}_h^0}\int_e \left[\!\left[D\vec{\nabla}\phi\right]\!\right]_e \{v\}_e\ \vec{n}\,\mathrm{d}S\,. \end{aligned} \tag{6.30}$$

We are looking for a solution, ϕ, of the neutron diffusion equation (6.26) on each of the subdomains Ω_k such that in each interior surface, e that is shared by subdomains Ω_i and Ω_j, the neutron current is continuous and the assembly discontinuity factors condition is satisfied. These conditions can be expressed as

$$\left[\!\left[D\vec{\nabla}\phi\right]\!\right]_e = 0\,, \tag{6.31}$$

$$[\![\phi]\!]_{f,\,e} = f_i^-\phi_i\vec{n}_i + f_j^+\phi_j\vec{n}_j = 0\,, \tag{6.32}$$

which are imposed in a weak form in the interior penalty method.

Using the current continuity condition (6.31), equation (6.30) is rewritten as

$$-\sum_{k=1}^{K}\int_{\Omega_e} vD\vec{\nabla}\phi\,\vec{n}\,\mathrm{d}S = -\sum_{b\in\mathcal{E}_h^{\partial}}\int_b vD\vec{\nabla}\phi\,\vec{n}\,\mathrm{d}S - \sum_{e\in\mathcal{E}_h^0}\int_e \left\{D\vec{\nabla}\phi\right\}_e [\![v]\!]_e\ \vec{n}\mathrm{d}S. \tag{6.33}$$

[1] In the jump operator each addend have different sign as $\vec{n}_i = -\vec{n}_j$ for the same edge.

As in the one-dimensional case, using the assembly discontinuity factors condition (6.32), a penalty term is introduced, thus,

$$
\begin{aligned}
-\sum_{k=1}^{K}\int_{\Omega_e} vD\vec{\nabla}\phi\,\mathrm{d}\vec{r} = &-\sum_{b\in\mathcal{E}_h^{\partial}}\int_b vD\vec{\nabla}\phi\vec{n}\,\mathrm{d}S \\
&-\sum_{e\in\mathcal{E}_h^0}\int_e \left\{D\vec{\nabla}\phi\right\}_e [\![v]\!]_e\ \vec{n}\,\mathrm{d}S\ +\sum_{e\in\mathcal{E}_h^0}\int_e s_e\,[\![\phi]\!]_{f,\,e}\,[\![v]\!]_e\ \mathrm{d}S\,.
\end{aligned}
\tag{6.34}
$$

Inserting the expression (6.34) into equation (6.28) the multidimensional interior penalty method for the neutron diffusion equation is obtained.

$$
\begin{aligned}
&\sum_{k=1}^{K} D\int_{\Omega_e}\vec{\nabla}v\vec{\nabla}\phi\,\mathrm{d}\vec{r}+\int_{\Omega} v\Sigma_a\phi\,\mathrm{d}\vec{r}-\sum_{e\in\mathcal{E}_h^0}\int_e\left\{D\vec{\nabla}\phi\right\}_e [\![v]\!]_e\ \vec{n}\,\mathrm{d}S \\
&+\sum_{e\in\mathcal{E}_h^0}\int_e s_e\,[\![\phi]\!]_{f,\,e}\,[\![v]\!]_e\ \vec{n}\,\mathrm{d}S\ -\sum_{b\in\mathcal{E}_h^{\partial}}\int_b vD\vec{\nabla}\phi\vec{n}\,\mathrm{d}S=\int_{\Omega} vq\,\mathrm{d}\vec{r}.
\end{aligned}
\tag{6.35}
$$

The boundary conditions in the method affect the surface integrals over the external faces, $\mathcal{E}_h^{\partial}$, and the changes are similar to the ones exposed in the one-dimensional case.

The penalty parameters s_e are chosen as a large enough parameter ensuring convergence for the method, based in the expressions provided by Epshteyn and Rivière, (2007) and Shahbazi, (2005).

As in the one-dimensional case, using the discontinuity factors condition (6.32), a *symmetrizing* term could be introduced, obtaining

$$
\begin{aligned}
&\sum_{k=1}^{K} D\int_{\Omega_e}\vec{\nabla}v\vec{\nabla}\phi\,\mathrm{d}\vec{r}+\int_{\Omega} v\Sigma_a\phi\,\mathrm{d}\vec{r} \\
&-\sum_{e\in\mathcal{E}_h^0}\int_e\left\{D\vec{\nabla}\phi\right\}_e [\![v]\!]_e\ \vec{n}\,\mathrm{d}S\ +\theta\sum_{e\in\mathcal{E}_h^0}\int_e [\![\phi]\!]_{f,\,e}\left\{D\vec{\nabla}v\right\}_e\ \vec{n}\,\mathrm{d}S \\
&+\sum_{e\in\mathcal{E}_h^0}\int_e s_e\,[\![\phi]\!]_{f,\,e}\,[\![v]\!]_e\ \mathrm{d}S\ -\sum_{b\in\mathcal{E}_h^{\partial}}\int_e vD\vec{\nabla}\phi\,\vec{n}\,\mathrm{d}S=\int_{\Omega} vq\,\mathrm{d}\vec{r}.
\end{aligned}
\tag{6.36}
$$

Nevertheless, for the same reason as in one-dimensional problems, no symmetrizing term is considered in our formulation ($\theta = 0$).

6.4 Reference calculations

In order to calculate the best possible homogenized parameters, the heterogeneous solution over the whole reactor is used to calculate the reference values of the homogenized coefficients (cross sections and discontinuity factors). The computed parameters are called reference homogenized cross sections (RXS) and reference discontinuity factors (RDFs) to differentiate them from the isolated assembly or pin parameters, which are computed using the heterogeneous flux in an isolated assembly with reflective boundary conditions. Obviously, this reference homogenized calculation does not have any practical application because the full heterogeneous reactor is must be solved first. However, the reference homogenized solution can be used to distinguish between the error when solving the homogenized problem, and the error of the homogenization procedure.

To compute the reference cross sections, the neutron diffusion equation is solved taking into account the heterogeneous composition of each one of the assemblies composing the reactor, obtaining the heterogeneous neutron flux, $\phi_g(\vec{r})$. Reference cross sections have been calculated with the usual flux-weighting method by means of equation (6.3) and (6.6) (Smith, 1986). A calculation method of the reference discontinuity factors has been proposed in one dimensional homogenized regions and its extension to multidimensional homogenized regions.

6.4.1 One-dimensional homogenized regions

First, the solution for the heterogeneous whole core reactor is obtained, $\phi_g(x)$. Using this flux, the reference homogenized cross sections, $\hat{\Sigma}_{\alpha,\,g}$ and $\hat{D}_g$ are obtained for the different homogenized regions. The reference discontinuity factors at vertex x_i are defined as

$$f^{-}_{g,\,i} = \frac{\phi^{-}_g(x_i)}{\hat{\phi}^{-}_g(x_i)}, \qquad f^{+}_{g,\,i-1} = \frac{\phi^{+}_g(x_i)}{\hat{\phi}^{+}_g(x_i)}, \tag{6.37}$$

depending also on the homogenized flux. This homogenized flux is the solution of a boundary value problem, defined in one-group of energy (see Figure 6.3) as

$$-\hat{D}_i \frac{\mathrm{d}^2}{\mathrm{d}x^2}\hat{\phi}(x) + \hat{\Sigma}_{a,\,i}\,\hat{\phi}(x) - \frac{1}{\lambda}\nu\hat{\Sigma}_{f,\,i}\,\hat{\phi}(x) = 0 \tag{6.38}$$

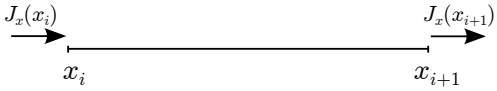

Figure 6.3: One dimensional homogenized region.

with the boundary conditions

$$-\hat{D}_i \frac{\mathrm{d}\hat{\phi}}{\mathrm{d}x}(x_i) = \hat{J}_x(x_i),$$
$$-\hat{D}_i \frac{\mathrm{d}\hat{\phi}}{\mathrm{d}x}(x_{i+1}) = \hat{J}_x(x_{i+1}).$$

These boundary conditions and the λ present in equation (6.38) are obtained from the whole core heterogeneous reactor calculation, using

$$\hat{J}_x(x_i) \approx J_x(x_i) = D_i \frac{\mathrm{d}\phi}{\mathrm{d}x}(x_i)\,,$$
$$\hat{J}_x(x_{i+1}) \approx J_x(x_{i+1}) = D_i \frac{\mathrm{d}\phi}{\mathrm{d}x}(x_{i+1})\,.$$

Although, problem (6.38) has an analytical solution for one energy group approximation, the solution of the same problem for the multigroup approximation has to be computed numerically. The numerical method selected to solve this problem has been a high-order continuous finite element method as the one presented by Vidal-Ferràndiz et al., (2014). The weak form of this problem for a test function φ can be written as

$$\hat{D}_i \int_{x_{i-1}}^{x_i} \frac{\mathrm{d}\varphi}{\mathrm{d}x}\frac{\mathrm{d}\hat{\phi}}{\mathrm{d}x}\,\mathrm{d}x + \left(\hat{\Sigma}_{a,\,i} - \frac{\nu\hat{\Sigma}_{f,\,i}}{\lambda}\right)\int_{x_{i-1}}^{x_i} \varphi\,\hat{\phi}\,\mathrm{d}x = \varphi\,\hat{J}_x(x_i) - \varphi\,\hat{J}_x(x_{i+1}) \quad (6.39)$$

which after spatial discretization becomes the algebraic linear system

$$A\Phi = b\,, \quad (6.40)$$

where Φ is the vector of coefficients of the polynomial expansion of the homogeneous neutron flux. The elements of the matrix A and the right hand side vector

b are given by

$$A_{lm} = \hat{D}_i \int_{x_{i-1}}^{x_i} \frac{\mathrm{d}N_l}{\mathrm{d}x}\frac{\mathrm{d}N_m}{\mathrm{d}x}\mathrm{d}x + \left(\hat{\Sigma}_{a,\,i} - \frac{\nu\hat{\Sigma}_{f,\,i}}{\lambda}\right)\int_{x_{i-1}}^{x_i} N_l\, N_m\, \mathrm{d}x\,,$$

$$b_l = \begin{cases} +N_l\hat{J}_x(x_i) & \text{if } l = 0, \\ 0 & \text{if } l \neq 0,\ p, \\ -N_l\hat{J}_x(x_{i+1}) & \text{if } l = p. \end{cases}$$

where N_l are the shape function considered and p is the polynomial truncation order chosen.

6.4.2 Multidimensional homogenized regions

The method exposed above used to obtain the homogeneous flux contributing to the discontinuity factors definition, can be generalized to multidimensional homogenized regions by alternatively solving coupled one-dimensional problems following the lines presented by Smith, (1986). To present the method, a two-dimensional homogenized region, like the one shown in Figure 6.4, is considered.

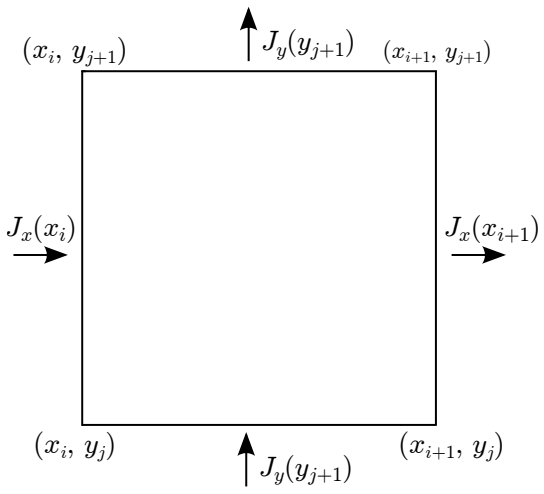

Figure 6.4: Two dimensional homogenized region.

The Reference Discontinuity Factors for the faces containing the vertices (x_i, y_j) and (x_i, y_{j+1}) (parallel to the y axis) are defined by

$$f^-_{g,\,i} = \frac{\int_{y_j}^{y_{j+1}} \phi^-_g(x_i, y)\,\mathrm{d}y}{\int_{y_j}^{y_{j+1}} \hat{\phi}^-_g(x_i, y)\,\mathrm{d}y}; \qquad f^+_{g,\,i-1} = \frac{\int_{y_j}^{y_{j+1}} \phi^+_g(x_i, y)\,\mathrm{d}y}{\int_{y_j}^{y_{j+1}} \hat{\phi}^+_g(x_i, y)\,\mathrm{d}y}\,. \tag{6.41}$$

The definition of the discontinuity factors for the other faces of the homogenized regions (parallel to the x axis) is similar. In order to calculate the discontinuity factors, the homogenized flux has to be calculated. Let's consider the neutron diffusion equation for the two-dimensional homogenized regions i

$$-\vec{\nabla}\hat{D}_i\vec{\nabla}\hat{\phi}(x,y) + \Sigma_{a,\,i}\hat{\phi}(x,y) = \nu\Sigma_{f,\,i}\hat{\phi}(x,y)\,. \tag{6.42}$$

Integrating along the y direction, equation (6.42) can be written as the one-dimensional problem

$$-\hat{D}_i\frac{\mathrm{d}^2}{\mathrm{d}x^2}\hat{\Phi}(x) + \left(\hat{\Sigma}_{a,\,i} - \frac{\nu\hat{\Sigma}_{f,\,i}}{\lambda}\right)\hat{\Phi}(x) = S(x)\,, \tag{6.43}$$

where the unknown, $\hat{\Phi}(x)$, is defined by

$$\hat{\Phi}(x) = \int_{y_i}^{y_{i+1}} \hat{\phi}(x,y)\mathrm{d}y\,,$$

and the leakage

$$S(x) = \hat{D}_i\int_{y_i}^{y_{i+1}} \frac{\mathrm{d}^2}{\mathrm{d}y^2}\hat{\phi}(x,y)\mathrm{d}y\,,$$

has been introduced, which is computed using the previously calculated heterogeneous neutron flux. The boundary conditions considered for this problem are as follows

$$\hat{J}_x(x_i) = -\hat{D}_i\frac{\mathrm{d}}{\mathrm{d}x}\hat{\Phi}(x_i) = \int_{y_j}^{y_{j+1}} \frac{\mathrm{d}}{\mathrm{d}x}\phi(x_i,y)\,\mathrm{d}y,$$
$$\hat{J}_x(x_{i+1}) = -\hat{D}_i\frac{\mathrm{d}}{\mathrm{d}x}\hat{\Phi}(x_{i+1}) = \int_{y_j}^{y_{j+1}} \frac{\mathrm{d}}{\mathrm{d}x}\phi(x_{i+1},y)\,\mathrm{d}y,$$

which are also obtained from the heterogeneous neutron flux.

The resulting problem is a one-dimensional source problem similar to the one exposed in Section 6.4.1, which is solved using the finite element method. A similar procedure is used to obtain the RDFs in the other faces of the region (parallel to the y axis).

6.5 Numerical Results

To assess the capabilities of the proposed interior penalty method with assembly discontinuity factors, a code has been implemented in the standard finite element library Deal.II (Bangerth, Hartmann, and Kanschat, 2007) using Lagrange polynomials.

To check the performance of the discontinuous Galerkin method in introducing the discontinuity factor conditions between the interior faces of adjacent nodes, first we will use the reference cross sections (RXSs) and reference assembly discontinuity factors (RDFs) computed from the heterogeneous flux. These results are complemented with the calculations using the homogenized cross sections (AXSs) and the assembly discontinuity factors (ADFs), calculated considering an isolated assembly with reflecting boundary conditions during the homogenization process.

Several one and two-dimensional benchmark problems have been analysed and the results obtained with the finite element method have been compared with the results obtained with the code PARCS (Downar et al., 2009). The one dimensional benchmarks are slabs of assemblies which are simplified representations of Boiling Water Reactor (BWR) configurations, while the two dimensional benchmark problems are two small subsets of the CISE core and the complete CISE core (Rahnema and Nichita, 1997).

6.5.1 One dimensional problems

Three different one dimensional problems representing BWR assemblies are studied. The benchmark is fully defined in Appendix B.5. Configurations are sorted by heterogeneities between assemblies. Configuration 1 is composed of similar assemblies, Configuration 2 puts together heterogeneous assemblies and configuration 3 joins very heterogeneous assemblies in an artificial way, which is used to test the method in an extreme heterogeneous situation. Zero-current boundary conditions are imposed at the edges of the system. All the calculation are made using cubic polynomials in the finite element method.

In addition to the explained finite element calculations, two more cases are presented for comparative purposes. The first one is done with the nodal code PARCS (Downar et al., 2009) using discontinuity factors. All PARCS calculations are made with 16 cells per assembly in order to achieve a reasonable accuracy for these small problems. The reference solution is obtained using an heterogeneous fine mesh calculation made with the finite element code.

Relative errors are condensed using the root mean square (RMS) as defined in equation (6.44)

$$\text{RMS} = \sqrt{\frac{1}{\sum_i V_i} \sum_i V_i \left(\frac{\varphi_{hom,i} - \varphi_{het,i}}{\varphi_{het,i}} \right)^2}, \tag{6.44}$$

where $\varphi_{hom,i}$ and $\varphi_{het,i}$ represent the homogeneous and the heterogeneous (reference) variable of interest (either fluxes or power averaged in homogenized region i). V_i represent the measure of the region i (longitude in 1D and area in 2D).

Figure 6.5 shows the fast and thermal fluxes for the homogenized reactor associated with Configuration 1, making use of the discontinuity factors and without using them. It is shown that a discontinuous solution for the flux is obtained with the interior penalty finite element method proposed here.

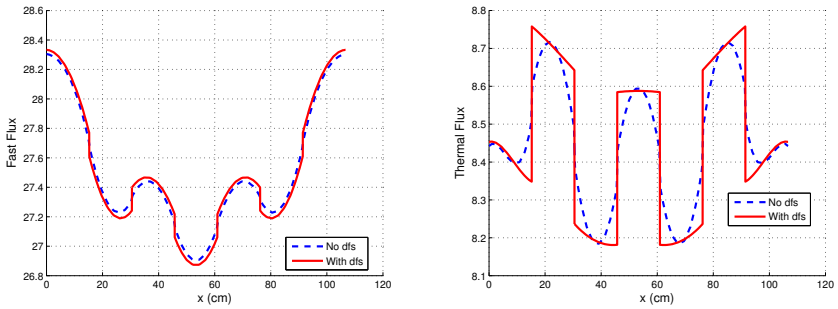

Figure 6.5: Fast and thermal homogeneous fluxes for the Configuration 1.

System k_{eff} and assembly averaged fluxes and power errors for configurations 1, 2 and 3 are given in Tables 6.1, 6.2, and 6.3, respectively. In Table 6.1 it is shown a very good behaviour for all the methods, being the solution with the RXS and RDFs the most accurate. It is worth to notice that this problem represents the less heterogeneous configuration, so the solution without discontinuity factors, even for the worst one, is obtained with very good accuracy.

Table 6.2 shows the results for a more heterogeneous configuration. For this problem, the use of discontinuity factors becomes necessary. We can observe a great improvement of the k_{eff} approximation, even if the errors in the flux are mostly the same as without discontinuity factors. Again, a good agreement is found between the finite element method with ADFs and PARCS with ADFs. RDFs present a null error as expected for one dimensional problems as the homogenization process is exact for these problems.

Table 6.1: Results for Configuration 1 core.

Method	Eigenvalue		Assembly Errors (%)		
	k_{eff}	Δk_{eff} (pcm)	Fast Flux	Thermal Flux	Power
FEM (No DFs)	1.31997	5	0.19	0.53	0.41
FEM (ADFs)	1.31991	1	0.05	0.06	0.04
PARCS (ADFs)	1.31990	2	0.05	0.04	0.03
FEM (RDFs)	1.31992	0	0.00	0.00	0.00
Heterogeneous	1.31992				

Table 6.2: Results for Configuration 2 core.

Method	Eigenvalue		Assembly Errors(%)		
	k_{eff}	Δk_{eff} (pcm)	Fast Flux	Thermal Flux	Power
FEM (No DFs)	1.10280	1736	3.46	3.70	4.31
FEM (ADFs)	1.11937	150	1.34	1.34	3.64
PARCS (ADFs)	1.11955	132	1.32	6.04	3.71
FEM (RDFs)	1.12087	0	0.00	0.00	0.16
Heterogeneous	1.12087				

For Configuration 3, the most heterogeneous among the ones chosen for the one-dimensional problems, we observed that more accurate calculations (higher order polynomial expansions for the FEM) are necessary in order to converge the method, so 5th order degree FEM has been added to the calculations. Using ADFs, we see that the FEM converges, when increasing the polynomial degree, to the same solution as PARCS with ADFs. Using the RDFs it is also necessary to go to 5th degree to achieve accurate results. This is due to the strong heterogeneity of the reactor, what makes also more challenging for the FEM to converge spatially (the homogenization error is larger for this configuration, but also the error due to the FEM approximation).

Table 6.3: Results for Configuration 3 core.

Method	Eigenvalue		Assembly Errors(%)		
	k_{eff}	Δk_{eff} (pcm)	Fast Flux	Thermal Flux	Power
No DFs; $p = 3$	1.01061	1125	4.56	15.34	10.87
No DFs; $p = 5$	1.01443	743	4.58	13.52	6.24
ADFs; $p = 3$	1.02498	312	1.86	15.29	3.29
ADFs; $p = 5$	1.02829	644	2.85	16.77	4.79
PARCS (ADFs)	1.02865	680	3.38	17.00	5.23
RDFs; $p = 3$	1.02187	2	0.01	0.02	0.02
RDFs; $p = 5$	1.02186	1	0.00	0.00	0.00
Heterogeneous	1.02185				

6.5.2 Multidimensional problems

The two-dimensional test problems chosen are based in the CISE benchmark (Rahnema and Nichita, 1997). They are fully defined in Appendix B.7. The layout for the CISE core, together with the assembly definition, are shown in Figure B.10, while the cross sections for the blade, water, the fuel A (fresh nuclear fuel) and the fuel B (depleted nuclear fuel) used in the tests are given in Table B.7.

First, a small subset composed by four assemblies surrounding an inserted control blade is considered, together with reflective boundary conditions. The geometry for the proposed problem, named *Small CISE*, is shown in Figure B.9a. Within this problem, the heterogeneities considered inside the reactor are taken into account. In order to analyse the method against a more heterogeneous problem, a non-realistic problem, called *Modified Small CISE*, is defined in Figure B.9b. This problem is similar to the small CISE, but the control blade inside the assemblies defined with material A is removed. This causes the flux to have a strong gradient on the interfaces, thus being more challenging for the homogenization procedure to preserve the properties of the original problem. The third problem to be considered is the original whole core CISE reactor (see Figure B.10), together with zero-flux boundary conditions.

An heterogeneous fine-mesh whole core calculation (Heterogeneous), with the fine mesh shown in Figure B.10b, is used as reference solution. Then, after the homogenization process, the different problems are solved using a coarse-mesh of one cell per assembly, together with the different homogenized parameters and discontinuity factors, both the isolated assembly homogenized data (ADFs),

and the reference homogenized data (RDFs). The calculations are complemented with the results obtained by PARCS with the ADFs (PARCS (ADFs)), in order to verify the introduction of the discontinuity factors into the FEM. The calculations with the Finite Element code, as in the previous section, were made using cubic polynomials.

The results for the small CISE benchmark are shown in Table 6.4. We can see that all the methods show very accurate solution. It is worth to note the agreement between the FEM and PARCS when using ADFs, being the error due mostly to the homogenization process, and corrected only by means of an improvement of the homogenized data.

Table 6.4: Results for small CISE benchmark.

Method	Eigenvalue		Assembly Errors(%)		
	k_{eff}	Δk_{eff} (pcm)	Fast Flux	Thermal Flux	Power
No DFs	0.83184	89	0.68	1.02	1.06
ADFs	0.83183	60	0.71	1.05	1.09
PARCS (ADFs)	0.83184	59	0.72	1.06	1.09
RDFs	0.83248	5	0.11	0.10	0.10
Heterogeneous	0.83243				

Table 6.5 shows the results for the Modified Small CISE benchmark. We can observe that the errors without using discontinuity factors are very big, while the introduction of the discontinuity factors mitigate the error due to the homogenization process. Comparing the solution of FEM with ADFs and PARCS with ADFs we observe that the two codes agree very well, and these errors can be reduced by means of improving the homogenization procedure, as we can see when we use the RXSs and RDFs.

Table 6.6 shows the results for the whole CISE reactor problem. The main differences between this problem and the previous ones is that here we use zero-flux boundary conditions, and that we have some assemblies (defining one layer of reflector) composed only by moderator. The use of zero-flux boundary conditions produce higher flux gradients close to the reflector, making the problem more challenging and thus requiring to increase the polynomial degree of the FEM. Moreover, reflector assemblies should be considered inside a macro-assembly while homogenizing the surrounding assemblies during the isolated assembly

homogenization process, otherwise the homogenization error close to the reflector will be also higher.

Table 6.5: Result for the modified small CISE.

Method	Eigenvalue		Assembly Errors(%)		
	k_{eff}	Δk_{eff} (pcm)	Fast Flux	Thermal Flux	Power
No DFs	0.94615	5341	6.37	11.33	7.90
ADFs	0.92720	3446	4.01	4.77	5.57
PARCS (ADFs)	0.92755	3481	4.06	4.45	5.30
RDFs	0.88863	411	1.78	2.31	2.20
Heterogeneous	0.89274				

Table 6.6: Results for CISE benchmark.

Method	Eigenvalue		Assembly Errors(%)		
	k_{eff}	Δk_{eff} (pcm)	Fast Flux	Thermal Flux	Power
No DFs; $p = 3$	0.94959	191	5.87	4.51	5.32
No DFs; $p = 5$	0.94955	195	5.66	4.28	5.08
ADFs; $p = 3$	0.95096	54	0.84	1.92	1.09
ADFs; $p = 5$	0.95090	60	0.89	2.11	1.15
PARCS (ADFs)	0.95078	72	1.00	2.38	1.16
RDFs; $p = 3$	0.95181	31	0.36	0.52	0.41
RDFs; $p = 5$	0.95176	26	0.47	0.49	0.49
Heterogeneous	0.95150				

It is observed that, even if the assembly errors are around 5% when the discontinuity factors are not used, we can decrease the error with the inclusion of the ADFs into the FEM. Again there is a good agreement between the FEM and PARCS when both use the same ADFs. Then, when using RXSs and RDFs we observe that, for degree $p = 3$, results show lower error in the power profile, while the errors in the flux are still quite large. This is due to different signs for the fast and for the thermal flux approximation errors, being cancelled when calculating the power. Increasing the polynomial degree in the spatial approximation for the RDFs solve the problem, giving a very good approximation (assembly errors smaller than 0.5%) for both fluxes and power profile.

In order to show the effects of the homogenization process, Figures 6.6 and 6.7 show the heterogeneous and homogenized solutions for the fast and the thermal neutron flux for the CISE reactor. It can be seen, that the homogenized calculation also obtains discontinuous neutron fluxes in the 2D CISE benchmark problem.

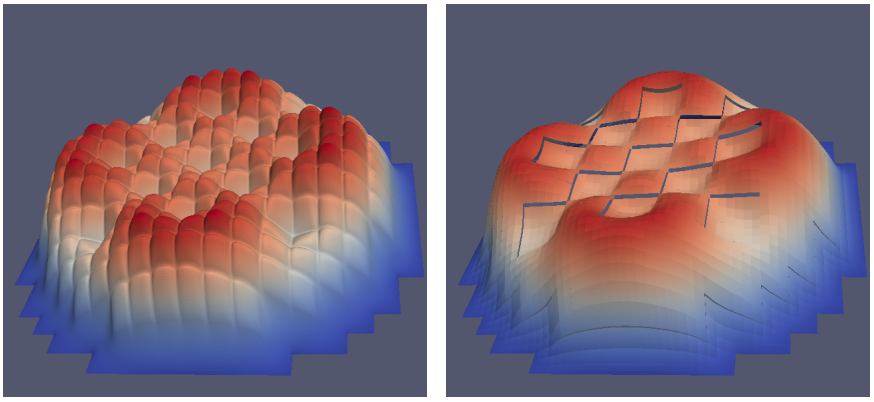

(a) Heterogeneous solution **(b)** Homogenized solution with ADFs

Figure 6.6: Fast flux for the CISE core.

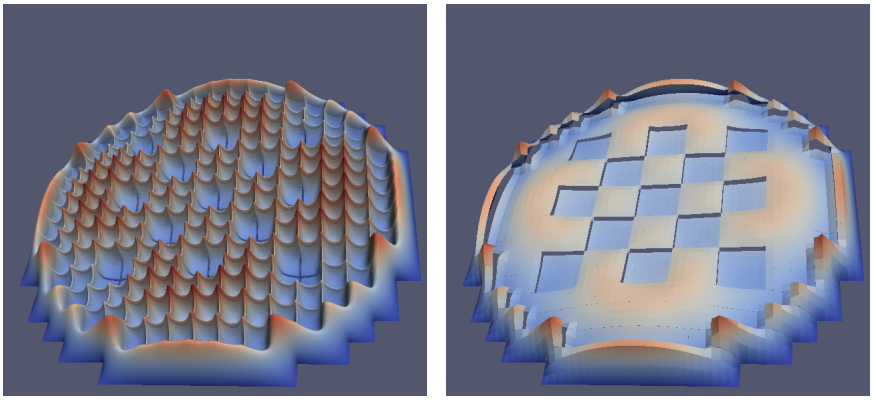

(a) Heterogeneous solution **(b)** Homogenized solution with ADFs

Figure 6.7: Thermal flux for the CISE core.

6.6 Homogenization strategy for Simplified Harmonic Equations (SP_N)

In this Section, we focus on the implementation of the flux discontinuity factors in the FEM the context of the SP_N approximation. We try to reduce the homogenization error using pin-wise homogenization. We use one dimensional geometries because the ambiguity in the definition of the flux discontinuity factors does not exist (Yu, Lu, and Chao, 2014; Yamamoto, Sakamoto, and Endo, 2016). As mentioned before, the one dimensional SP_N approximation is equivalent to the complete P_N approximation. We quantify the error of the proposed pin discontinuity factors and compare it to the usual assembly-wise homogenization.

6.6.1 Homogenization of cross sections

In order to simplify the notation here, the transport equation to be homogenized is considered in its mono-energetic formulation, and thus equation (5.1) can be written as

$$\left(\mu\frac{\mathrm{d}}{\mathrm{d}x}+\Sigma_t(x)\right)\psi(x,\mu)=\sum_{l=0}^{L}\frac{2l+1}{2}P_l(\mu)\Sigma_{sl}(x)\phi_l(x)+\frac{1}{\lambda}\chi(x)\nu\Sigma_f(x)\phi_0(x)\,, \tag{6.45}$$

and the SP_N approximation (5.6) is rewritten as

$$\begin{aligned}\frac{\mathrm{d}}{\mathrm{d}x}\left(\frac{n}{2n+1}\phi_{n-1}+\frac{n+1}{2n+1}\phi_{n+1}\right)+\left(\Sigma_t(x)-\delta_{n\leq L}\Sigma_{sn}(x)\right)\phi_n\\ =\frac{\delta_{n,0}}{\lambda}\chi(x)\nu\Sigma_f(x)\phi_0,\quad n=0,\,\ldots,\,N\,,\end{aligned} \tag{6.46}$$

where the lower and upper limits for the recurrence are $\phi_{-1}=\phi_{N+1}=0$. We consider the equations for the even and odd moments separately.

Our target is to find a homogenized equation for even indices moments as follows

$$\begin{aligned}\frac{\mathrm{d}}{\mathrm{d}x}\left(\frac{n}{2n+1}\hat{\phi}_{n-1}+\frac{n+1}{2n+1}\hat{\phi}_{n+1}\right)+\left(\hat{\Sigma}_t-\delta_{n\leq L}\hat{\Sigma}_{sn}\right)\hat{\phi}_n=\frac{\delta_{n,0}}{\hat{\lambda}}\hat{\chi}\hat{\nu}\hat{\Sigma}_f\hat{\phi}_0,\\ n=0,\,2,\,\ldots,\,N-1,\end{aligned} \tag{6.47}$$

which preserves local quantities over the smaller subdomains Ω_k, such as the average of the flux moments satisfies

$$\bar{\phi}_{k,n}:=\int_{\Omega_k}\phi_n\,\mathrm{d}x=\int_{\Omega_k}\hat{\phi}_n\,\mathrm{d}x,\qquad n=0,\,2,\,\ldots,\,N-1, \tag{6.48}$$

which implies that the diffusive pseudo-moments of equation (5.12) after the change of variables defined in equation (5.10) maintain

$$\int_{\Omega_k} u_n \,\mathrm{d}x = \int_{\Omega_k} \hat{u}_n \,\mathrm{d}x\,, \qquad\qquad n = 0,\, 2,\, \ldots,\, N-1, \tag{6.49}$$

and preserves the eigenvalue $\hat{\lambda} = \lambda$ of the original problem, using piecewise constant cross sections in the subdomains. Moreover, we introduce the concepts of *High Order* (HO) and *Low Order* (LO) operators, meaning that different approximations can be used to solve the equations at different scales, where an HO operator is more accurate using more functions to represent space, angle and energy, but more expensive in computational terms. A LO operator has lower accuracy in space, angle and energy, but is computationally less expensive. Thus, when we talk about a solution of the original problem, this should be obtained with a HO solver, while the solution of the homogenized problem is obtained by a LO solver.

A common strategy to obtain the homogenized parameters consists of integrating the original and the homogenized equations over each spatial subdomain, to obtain

$$\int_{\Omega_k} \frac{\mathrm{d}}{\mathrm{d}x}\left(\frac{n}{2n+1}\phi_{n-1} + \frac{n+1}{2n+1}\phi_{n+1}\right)\mathrm{d}x + \int_{\Omega_k} \left(\Sigma_t(x) - \delta_{n\leq L}\Sigma_{sn}(x)\right)\phi_n(x)\,\mathrm{d}x\mathrm{d}\mu\,\mathrm{d}x = \frac{\delta_{0,n}}{\lambda}\int_{\Omega_k} \chi(x)\nu\Sigma_f(x)\phi_0(x)\,\mathrm{d}x\,, \tag{6.50}$$

$$\int_{\Omega_k} \frac{\mathrm{d}}{\mathrm{d}x}\left(\frac{n}{2n+1}\hat{\phi}_{n-1} + \frac{n+1}{2n+1}\hat{\phi}_{n+1}\right)\mathrm{d}x + \left(\hat{\Sigma}_t - \delta_{n\leq L}\hat{\Sigma}_{sn}\right)\int_{\Omega_k} \hat{\phi}_n(x)\,\mathrm{d}x\mathrm{d}\mu\,\mathrm{d}x = \frac{\delta_{0,n}}{\hat{\lambda}}\hat{\chi}\hat{\nu}\hat{\Sigma}_f\int_{\Omega_k} \hat{\phi}_0(x)\,\mathrm{d}x\,. \tag{6.51}$$

Now we force equations (6.50) and (6.51) to be equal term by term, as follows

$$\int_{\Omega_k} \frac{\mathrm{d}}{\mathrm{d}x}\left(\frac{n}{2n+1}\phi_{n-1} + \frac{n+1}{2n+1}\phi_{n+1}\right)\mathrm{d}x = \int_{\Omega_k} \frac{\mathrm{d}}{\mathrm{d}x}\left(\frac{n}{2n+1}\hat{\phi}_{n-1} + \frac{n+1}{2n+1}\hat{\phi}_{n+1}\right)\mathrm{d}x\,, \tag{6.52}$$

$$\int_{\Omega_k} \left(\Sigma_t(x) - \delta_{n\leq L}\Sigma_{sn}(x)\right)\phi_n(x)\,\mathrm{d}x = \left(\hat{\Sigma}_t - \delta_{n\leq L}\hat{\Sigma}_{sn}\right)\int_{\Omega_k} \hat{\phi}_n(x)\,\mathrm{d}x\,, \tag{6.53}$$

$$\frac{\delta_{0,n}}{\lambda}\int_{\Omega_k} \frac{\chi(x)}{2}\nu\Sigma_f(x)\phi_0(x)\,\mathrm{d}x = \frac{\delta_{0,n}}{\hat{\lambda}}\hat{\chi}\hat{\nu}\hat{\Sigma}_f\int_{\Omega_k} \hat{\phi}_0(x)\,\mathrm{d}x\,, \tag{6.54}$$

to ensure that the solution of the homogenized equation reproduces the averages quantities of the heterogeneous solution in terms of reaction rates. We can see

that using equation (6.48) to preserve average flux moments, and imposing $\lambda = \hat{\lambda}$, we obtain from equation (6.54) that the homogenized fission cross section is defined by

$$\hat{\chi}\hat{\nu}\hat{\Sigma}_f = \frac{\int_{\Omega_k} \chi(x)\nu\Sigma_f(x)\phi_0(x)\,\mathrm{d}x}{\int_{\Omega_k} \hat{\phi}_0(x)\,\mathrm{d}x} = \frac{\int_{\Omega_k} \chi(x)\nu\Sigma_f(x)\phi_0(x)\,\mathrm{d}x}{\bar{\phi}_{k,0}(x)}\,, \tag{6.55}$$

and because the homogenized solution does not appear in this expression, we say that the homogenized fission cross section is independent of the LO solver. We apply the same procedure to the scattering term in equation (6.53) to obtain

$$\left(\hat{\Sigma}_t - \delta_{n\leq L}\hat{\Sigma}_{sn}\right) = \frac{\int_{\Omega_k} \left(\Sigma_t(x) - \delta_{n\leq L}\Sigma_{sn}(x)\right)\phi_n(x)\,\mathrm{d}x}{\int_{\Omega_k} \hat{\phi}_n(x)\,\mathrm{d}x} \tag{6.56}$$

$$= \frac{\int_{\Omega_k} \left(\Sigma_t(x) - \delta_{n\leq L}\Sigma_{sn}(x)\right)\phi_n(x)\,\mathrm{d}x}{\bar{\phi}_{k,n}(x)}\,. \tag{6.57}$$

But this definition of the homogenized cross section could produce non physical values, due to the fact that the denominator in the equation is not necessarily positive for all moments, $\bar{\phi}_n(x)$. This problem is exposed in Sanchez, (2009), where the proposed solution consists in using the zero moment homogenized flux for the denominator, obtaining

$$\left(\hat{\Sigma}_t - \delta_{n\leq L}\hat{\Sigma}_{sm}\right) = \frac{\int_{\Omega_k} \left(\Sigma_t(x) - \delta_{n\leq L}\Sigma_{sn}(x)\right)\phi_n(x)\,\mathrm{d}x}{\bar{\phi}_{k,0}(x)}\,. \tag{6.58}$$

Moreover, this approximation is exact for isotropic scattering problems because only zero order is considered for the homogenized cross section, and the error due to the change in the formula is preferred to the non-physical values obtained with negative or almost zero flux moments. We notice that the homogenized scattering cross section is also independent of the LO solver.

Last, we must deal with equation (6.52) involving the streaming terms in order to obtain a completely equivalent homogenized formulation. We integrate by parts equation (6.52) to obtain

$$\left[\!\left[\frac{n}{2n+1}\phi_{n-1} + \frac{n+1}{2n+1}\phi_{n+1}\right]\!\right]_{\Omega_k} = \left[\!\left[\frac{n}{2n+1}\hat{\phi}_{n-1} + \frac{n+1}{2n+1}\hat{\phi}_{n+1}\right]\!\right]_{\Omega_k}, \quad n = 0,\ 2,\ \ldots,\ N-1, \tag{6.59}$$

where the jump operator $[\![\cdot]\!]_{\Omega_k}$ is defined in Section 6.3. Because it must happen for all odd indices, and we use the closures $\phi_{-1} = \phi_{N+1} = 0$, this is equivalent to

ask for

$$[\![\phi_n]\!]_{\Omega_k} = \left[\!\!\left[\hat{\phi_n}\right]\!\!\right]_{\Omega_k}, \qquad n = 1, 3, \ldots, N. \tag{6.60}$$

To continue, we want to express the odd moments in terms of the even ones. In order to do this, we go back to equation (6.46) and consider the odd fluxes. For odd indices the source term is zero because of the isotropic representation of the fission term (only exists for the zero moment), so the odd fluxes satisfy the following equations

$$\phi_n = -\frac{1}{(\Sigma_t(x) - \delta_{n\leq L}\Sigma_{sn})}\frac{\mathrm{d}}{\mathrm{d}x}\left(\frac{n}{2n+1}\phi_{n-1} + \frac{n+1}{2n+1}\phi_{n+1}\right), \qquad n = 1, 3, \ldots, N, \tag{6.61}$$

that can be rewritten, using the definition of the diffusion-like coefficient and the change of variables (5.10), as follows

$$\phi_{n+1} = -D_n\frac{\mathrm{d}}{\mathrm{d}x}u_n, \quad D_n = \frac{1}{(2n+3)\left(\Sigma_t - \delta_{n\leq L}\Sigma_{sn}\right)}, \qquad n = 0, 2, \ldots, N-1. \tag{6.62}$$

Equation (6.60) will be satisfied if the heterogeneous and the homogeneous odd fluxes are equal pointwise at the interfaces, or average-wise for dimensions higher that 1. In terms of the even fluxes it reads as

$$-D_n\frac{\mathrm{d}}{\mathrm{d}x}u_n = -\hat{D}_n\frac{\mathrm{d}}{\mathrm{d}x}\hat{u}_n, \qquad n = 0, 2, \ldots, N-1.$$

For clarification, we notice that in the special case of $N = 1$, the original equation is the neutron diffusion equation, and the previous expression takes the form of preserving the neutron current, J, at the interfaces by

$$J := -D_0\frac{\mathrm{d}}{\mathrm{d}x}\phi_0 = -\hat{D}_0\frac{\mathrm{d}}{\mathrm{d}x}\hat{\phi}_0 := \hat{J}.$$

The main problem is that this condition must be satisfied on the two boundaries of each one of the K subdomains for one-dimension, for each of the $N/2$ even fluxes for each energy group, i.e. $K \times N \times G$ restrictions, but there is only one degree of freedom per subdomain, per even moment and per energy group, i.e. $K \times N/2 \times G$ degrees of freedom, that can be tuned to force this situation, i.e., the coefficients $\hat{D}_{n-1}$. Thus, we have more restrictions than degrees of freedoms and this can not be satisfied. Instead, we are going to use some extra parameters, called discontinuity factors, that add some extra degrees of freedom in order to recover some physical properties of the solution and minimize the homogenization error.

6.6.2 Interior Penalty-FEM for SP_N

For the spatial discretization of the diffusive eigenvalue problem corresponding to equation (5.15), a Discontinuous Galerkin finite element method is used extending the method presented in Section 6.3 for the SP_N equations. If discontinuity factors are not taken into account, the interior penalty finite element method can be formulated as follows. First, we choose a partition of the one-dimensional domain, $\mathcal{W}_h$, resulting in a splitting of the original domain defining the reactor Ω, into subdomains $\Omega_k = [e_{k-1},\, e_k]$, $k = 1,\, \ldots,\, K$, defining the mesh. Second, we use the set of partition nodes $\mathcal{E}_h = \mathcal{E}_h^0 \cup \mathcal{E}_h^\partial$. Now, problem (5.15) together with the continuity conditions for the moments and its derivatives, considering zero Dirichlet boundary conditions for clarity (for different boundary conditions, as the ones shown in Section 5.3.1, see Section 6.3), can be rewritten in a generic form as,

$$-\frac{\mathrm{d}}{\mathrm{d}x}\cdot D_n\frac{\mathrm{d}}{\mathrm{d}x}u_n + \Sigma\, u_n = q_n \quad \text{in each } \Omega_k \in \mathcal{W}_h\,, \tag{6.63}$$

$$\left[\!\left[u_n\right]\!\right]_e = 0 \quad \text{on each } e \in \mathcal{E}_h\,, \tag{6.64}$$

$$\left[\!\left[D_n\frac{\mathrm{d}}{\mathrm{d}x}u_n\right]\!\right]_e = 0 \quad \text{on each } e \in \mathcal{E}_h^0\,. \tag{6.65}$$

where the jumps $[\![\cdot]\!]$ are defined by

$$\begin{aligned}
\left[\!\left[u_n\right]\!\right]_e &= \mathbf{n}^- u_n^-(e) + \mathbf{n}^+ u_n^+(e) = u_n^- - u_n^+,\ \text{on } e \in \mathcal{E}_h^0,\\
\left[\!\left[u_n\right]\!\right]_e &= \begin{cases} \mathbf{n}^+ u_n^+(e_0) & = -u_n^+(e_0) \\ \mathbf{n}^- u_n^-(e_K) & = +u_n^-(e_K) \end{cases},\ \text{on } e \in \mathcal{E}_h^\partial,
\end{aligned} \tag{6.66}$$

where $u_n^\pm$ are the lateral limits of u_n in a particular node, and $\mathbf{n}^\pm$ are the normal vectors outward to the adjacent cells $-$ and $+$ at the shared node e, so $\mathbf{n}^- = +1$ and $\mathbf{n}^+ = -1$ in one-dimension. The indices for energy group g are avoided for simplicity of the notation, considering all the contributions coming from different energy and moments inside the source term q_n, together with the neutrons produced due to the fission terms. Standard Interior Penalty Finite Element Methods (IP-FEM) exist for the previous problem as follows (Brezzi et al., 2006b):

Find $u_n \in \mathrm{H}^1(\mathcal{W}_h)$ such that

$$\begin{aligned}
&\left(D_n\frac{\mathrm{d}}{\mathrm{d}x}u_n, \frac{\mathrm{d}}{\mathrm{d}x}v\right)_{\mathcal{W}_h} + (\Sigma u_n, v)_{\mathcal{W}_h} - \left(\left\{D_n\frac{\mathrm{d}}{\mathrm{d}x}u_n\right\}, [\![v]\!]\right)_{\mathcal{E}_h} \\
&\qquad + \left(s_1\left[\!\left[u_n\right]\!\right], [\![v]\!]\right)_{\mathcal{E}_h} = (q_n, v)_{\mathcal{W}_h}, \qquad \forall v \in \mathrm{H}^1(\mathcal{W}_h)\,,
\end{aligned} \tag{6.67}$$

where $\mathrm{H}^1(\mathcal{W}_h) := \left\{v \in \mathrm{L}^2(\Omega) : \quad v_{|\Omega_k} \in \mathrm{H}^1(\Omega_k) \quad \forall \Omega_k \in \mathcal{W}_h\right\}$, s_1 is a penalty parameter large enough to stabilize the problem, the averages $\{\cdot\}$ are defined by

$$\{u\} = \frac{1}{2}(u^- + u^+), \text{ on } e \in \mathcal{E}_h^0, \quad \{u\} = u, \text{ on } e \in \mathcal{E}_h^\partial. \tag{6.68}$$

Alternatively, using the edge operators over interior points, the problem can be rewritten as:
Find $u_n \in \mathrm{H}^1(\mathcal{W}_h)$ such that

$$\left(D_n \frac{\mathrm{d}}{\mathrm{d}x} u_n, \frac{\mathrm{d}}{\mathrm{d}x} v\right)_{\mathcal{W}_h} + (\Sigma u_n, v)_{\mathcal{W}_h} - \left(\left\{D_n \frac{\mathrm{d}}{\mathrm{d}x} u_n\right\}, [\![v]\!]\right)_{\mathcal{E}_h^0} + (s_1 [\![u_n]\!], [\![v]\!])_{\mathcal{E}_h^0}$$
$$+ D_n(e_0)\frac{\mathrm{d}}{\mathrm{d}x} u_n(e_0) v_(e_0) - D_n(e_K)\frac{\mathrm{d}}{\mathrm{d}x} u_n(e_K) v(e_K) = (q_n, v)_{\mathcal{W}_h}, \ \forall v \in \mathrm{H}^1(\mathcal{W}_h),$$

where we have used the boundary conditions $u(e_0) = 0$ and $u(e_K) = 0$. We notice that this formulation of the problem is the same as the one obtained in Section 6.3 for the neutron diffusion equation with zero flux boundary conditions. The notation for the d- and $(d-1)$-measures of the functions, that for our one-dimensional problem corresponds to integrals over the elements in $\mathcal{W}_h$ and the evaluation at the elements in $\mathcal{E}_h$, stands as follows

$$\begin{aligned}
(f,g)_{\mathcal{W}_h} &= \sum_{\Omega_k \in \mathcal{W}_h} (f,\, g)_{\Omega_k} = \sum_{\Omega_k \in \mathcal{W}_h} \int_{\Omega_k} f(x) g(x)\, \mathrm{d}x\,, \\
(f,g)_{\mathcal{E}_h} &= (f,g)_{\mathcal{E}_h^0} + (f,g)_{\mathcal{E}_h^\partial}\,, \\
(f,g)_{\mathcal{E}_h^0} &= \sum_{e \in \mathcal{E}_h^0} (f,\, g)_e = \sum_{e \in \mathcal{E}_h^0} f(e) g(e)\,, \\
(f,g)_{\mathcal{E}_h^\partial} &= \sum_{e \in \mathcal{E}_h^\partial} (f,\, g)_e = f(e_0) g(e_0) + f(e_K) g(e_K)\,.
\end{aligned} \tag{6.69}$$

This formulation is also called Incomplete Interior Penalty Galerkin method (IIPG). A more detailed description of the different operators for higher dimensions can be found in Brezzi et al., (2006b). Different formulations have also been proposed in Wang and Ragusa, (2010) and Turcksin and Ragusa, (2014), where the scheme is consistent with a transport formulation within the strategy of synthetic diffusion acceleration. The homogenization process and the inclusion of the discontinuity factors in the finite element method formulation is discussed in the next section.

6.6.3 Discontinuity factors for the Simplified P_N

In the generalized equivalence theory (Smith, 1986), which is an extension of Koebke's homogenization method (Wagner and Koebke, 1983), flux discontinuity factors (DFs) are introduced in the neutron diffusion theory and they improve the homogenization strategy stated before. In this theory, for a given interface node e limiting two adjacent homogenized subdomains, the energy-dependent discontinuity factors are defined as interface constants f_e^-, f_e^+, such that the scalar flux, ϕ_0, satisfies the following condition

$$f_e^- \hat{\phi}_0^-(e) = f_e^+ \hat{\phi}_0^+(e)\,, \tag{6.70}$$

where $\hat{\phi}_0^-$ and $\hat{\phi}_0^+$ are the lateral limits of the homogenized scalar flux viewed from the two different subdomains sharing this node. A possible definition of these discontinuity factors is

$$f_e^- = \frac{\phi_0^-(e)}{\hat{\phi}_0^-(e)}\,, \qquad f_e^+ = \frac{\phi_0^+(e)}{\hat{\phi}_0^+(e)}\,, \tag{6.71}$$

so continuity for the heterogeneous reconstructed zero-th order flux is enforced (Smith, 1986).

The angular flux in one-dimensional geometries, $\psi(x,\mu)$, can be projected onto the different diffusive moments of the SP_N equations, u_n. Then, a homogeneous problem must be solved in the homogenized subdomain using odd reference flux moments as boundary conditions to calculate the homogeneous even flux moments.

To calculate the discontinuity factors for the SP_N equations in the subdomain edge e, equation (6.71) can be extended to

$$f_{n,\,e}^+ = \frac{u_n^+(e)}{\hat{u}_n^+(e)}\,, \qquad f_{n,\,e}^- = \frac{u_n^-(e)}{\hat{u}_n^-(e)}\,, \qquad \text{for } n = 0,\,2,\,\ldots,\,N-1\,, \tag{6.72}$$

where u_n^- and u_n^+ are the left and right extremes of the reference heterogeneous diffusive moments defined in equation (5.10), extracted from the transport solution and $\hat{u}_n^-$ and $\hat{u}_n^+$ are the left and right extremes of the homogeneous diffusive moments calculated with the P_N approximation in the homogenized region. Thus, for a given node e shared by two adjacent homogenized regions, for the different moments we have the relationship

$$f_{n,\,e}^- \hat{u}_n^-(e) = f_{n,\,e}^+ \hat{u}_n^+(e)\,, \qquad \text{for } n = 0,\,2,\,\ldots,\,N-1\,, \tag{6.73}$$

It is worth to notice that the values of the homogenized solution appear explicitly in equation (6.73), and thus, the values of the discontinuity factors will depend

on the homogenized solution, which depends on the LO solver. Thus, the discontinuity factors depend on the LO solver that is going to be used when solving the homogenized equation.

At this point we need the value of the heterogeneous and homogeneous flux moments, $u_n(x)$ and $\hat{u}_n(x)$ respectively, to generate the homogenized cross sections and the discontinuity factors. Since the full heterogeneous solution is not known, these values must be determined by calculating each heterogeneous subdomain separately with a high order transport operator. These calculations are performed for a *reference problem* (Sanchez, 2009) whose solution is close enough to the solution that would be obtained if the entire heterogeneous system was calculated.

Usually, as it has been already mentioned in the case of the neutron diffusion equation, the reference problem is an isolated assembly with reflective boundary conditions. Then, the assembly homogenized cross sections are generated with assembly heterogeneous flux from the reference problem. The homogeneous flux is the solution of the reference homogeneous assembly with reflective boundary conditions and using the assembly homogenized cross sections. We can calculate Assembly Discontinuity Factors (ADFs) dividing the heterogeneous flux by the homogeneous flux. A scheme of the problems solved to calculate the ADFs is shown in Figure 6.8a. It must be noted that for a homogeneous reflective assembly, as the homogeneous reference problem, the fluxes are spatially constant and all the spherical harmonics expansion terms are zero except the first one. In this work, for homogenization at assembly level, the discontinuity factors for the moments greater than 0 are arbitrarily set to 1.0 .

Another possibility is to use the assembly heterogeneous results to compute pin homogenized parameters. In this way, we solve a homogeneous pin problem using the cross sections and current boundary conditions for the isolated heterogeneous assembly problem. Then, the Pin Discontinuity Factors (PDFs) are calculated by the ratio of the reference pin boundary flux values and the homogeneous reference problem boundary flux values. This procedure is schematised in Figure 6.8.

Finally, the heterogeneous flux calculated for the whole reactor can be used to generate reference cross sections and appropriate current boundary conditions. With the global k_{eff} and these cross sections the homogeneous flux can be generated in a particular region considered here as an assembly or a pin. Then, Reference Discontinuity Factors (RDFs) are generated using equation (6.72). This strategy corresponds to Figure 6.8c. This technique provides exact homogenized parameters, but it requires the solution of the whole heterogeneous problem to generate the homogenized parameters, what makes it of no practical use. However, it is

used here to verify that the discontinuity factors technique is successfully implemented within the interior penalty finite element method (IP-FEM), as it has been done for the neutron diffusion equation in Section 6.3

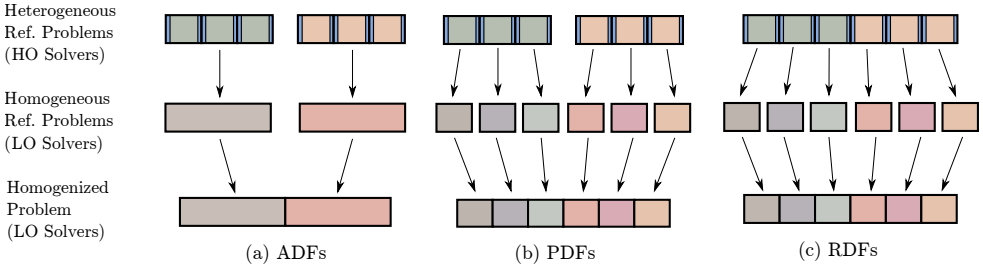

Figure 6.8: Scheme of homogenization strategies. The LO solvers for the *Homogeneous Ref. Problems* and for the *Homogenized problem* must be the same, due to the dependence of the discontinuity factors on the LO solver, at least for PDFs and RDFs (for ADFs the fluxes are constant and the method does not matter).

6.6.4 IP-FEM with discontinuity factors for SP_N

In this case, the reference situation is one assembly or a pin with suitable boundary conditions. Thus, the continuity condition for the flux will be forced to be discontinuous as in equation (6.73). This type of interface conditions leads to a slightly different problem from the one stated by equations (6.63), (6.64) and (6.65), i.e., the problem with discontinuity factors is of the form

$$-\frac{\mathrm{d}}{\mathrm{d}x}D_n\frac{\mathrm{d}}{\mathrm{d}x}u_n + \Sigma_n u_n = q_n \quad \text{in each } \Omega_k \in \mathcal{W}_h, \tag{6.74}$$

$$[\![u_n]\!]_{f,\,e} = 0 \quad \text{on each } e \in \mathcal{E}_h, \tag{6.75}$$

$$\left[\!\!\left[D_n\frac{\mathrm{d}}{\mathrm{d}x}u_n \right]\!\!\right]_e = 0 \quad \text{on each } e \in \mathcal{E}_h^0. \tag{6.76}$$

where the new jumps $[\![\cdot]\!]_f$ are defined as follows

$$\begin{aligned}
[\![u_n]\!]_f &= f^-_{n,\,e}\,\mathbf{n}^- u^-_n + f^+_{n,\,e}\,\mathbf{n}^+ u^+_n = f^-_{n,\,e}\,u^-_n - f^+_{n,\,e}\,u^+_n, \text{ on } e \in \mathcal{E}_h^0, \\
[\![u_n]\!]_f &= \begin{cases} f^-_{n,\,e_0}\,\mathbf{n}^+ u^+_n(e_0) & = -f^-_{n,\,e_0}\,u^+_n(e_0) \\ f^+_{n,\,e_K}\,\mathbf{n}^- u^-_n(e_K) & = +f^+_{n,\,e_K}\,u^-_n(e_K) \end{cases}, \text{ on } e \in \mathcal{E}_h^\partial,
\end{aligned} \tag{6.77}$$

where $f^+_{n,\,e}$ is generally different from $f^-_{n,\,e}$ for a particular edge e and even moment n, defining the jumps imposed to the solution, u_n. A scheme to approximate the

problem defined by equations (6.74), (6.75) and (6.76), has been implemented in an IP-FEM using a formulation based on equation (6.67) as follows

$$\left(D_n \frac{\mathrm{d}}{\mathrm{d}x} u_n, \frac{\mathrm{d}}{\mathrm{d}x} v_n\right)_{\mathcal{W}_h} + (\Sigma_n u_n, v_n)_{\mathcal{W}_h} - \left(\left\{D \frac{\mathrm{d}}{\mathrm{d}x} u_n\right\}, [\![v_n]\!]\right)_{\mathcal{E}_h} + \left(s_1 [\![u]\!]_f, [\![v_n]\!]\right)_{\mathcal{E}_h} = (q_n, v_n)_{\mathcal{W}_h}, \tag{6.78}$$

following analogous steps to the ones presented in Section 6.3 for the neutron diffusion equation.

6.7 Numerical Results for Pin-wise homogenization

To study the performance of the pin-wise homogenization method using the simplified spherical harmonics as the low order operator exposed above, two different one-dimensional reactor configurations based on the C5G7 benchmark (Lewis et al., 2001) are defined. The benchmark problems are fully defined in Appendix B.4. The first configuration is comprised of two assemblies and the second configuration has five assemblies with reflective boundary conditions as Figure B.4 shows. Each assembly consists of 17 pins, each pin is made of a layer of nuclear fuel surrounded by a thin layer of water.

Different strategies for the homogenization of the two reactor configurations are compared in this Section. These strategies are presented in Table 6.7. The reason for including RXS (reference cross sections without discontinuity factors) is to show that using better homogenized cross section does not correct the homogenization error alone, thus being advantageous the use of discontinuity factors even if the cross sections are just an approximation.

Table 6.7: Homogenization strategies.

No DFs	Problem without DFs and assembly homogenized cross sections.
RXSs	Problem without DFs and reference homogenized cross sections.
ADFs	Problem with assembly DFs and assembly homogenized cross sections.
PDFs	Problem with pin DFs and pin homogenized cross sections, they are calculated from an isolated assembly problem.
RDFs	Problem with reference DFs and reference homogenized cross sections.

To compare the solutions of the different homogenization strategies the maximum relative error in the scalar neutron flux, ε, the root mean square error of the

neutron power, RMS, defined in equation (6.44); and the absolute error for the multiplicative constant, Δk_{eff} (pcm), defined in Table 3.1; are used. The transport reference solution is calculated with a discrete ordinates code using a S_{96} approximation where the solution is fully converged. The transport reference results are also used to compute reference homogenized cross sections and reference discontinuity factors. The same code using a discrete ordinates approximations of order 96 is used to calculate isolated assembly heterogeneous fluxes to be able to calculate assembly and pin homogenization parameters.

6.7.1 Configuration 1

The reactor named Configuration 1 is composed of two different assemblies. Each assembly is formed by 17 equal pins. Figures 6.9a and 6.9b show the heterogeneous fluxes for the same transport approximations for $g = 1$ and $g = 7$ energy groups. Figures 6.9c and 6.9d show the relative errors for these energy groups. Looking at Figure 6.9a for the flux for $g = 1$, and its relative error in Figure 6.9c, we see that the error is mostly due to the the fact that the lower order approximations P_1, P_3 and P_5 do not capture the local behaviour of the solution in regions with water, where the flux is lower than in fuel regions for fast groups (low values of g). The same problem occurs when looking at the behaviour for $g = 7$ in Figures 6.9b and 6.9d, but this time because the flux is underestimated in the region with water, where the flux is larger than in regions with fuel for slow groups (high values of g). This behaviour is typical. Moreover, we also observe that the relative error is much bigger for $g = 7$ than for $g = 1$ (around one order of magnitude), but this is mainly due to the fact that the value of the flux is smaller (around one order of magnitude), and this means that the absolute value of the error is similar (of the same order). This effect is enhanced by the fact that strong heterogeneity in the cross sections in the thermal groups ($g > 5$) result in more heterogeneous thermal fluxes.

Table 6.8 shows a comparison of the heterogeneous results for this reactor, without any homogenization, for different order of P_N approximations to the neutron transport equation. In this comparison, the different k_{eff} for the different approximations are provided together with the difference with respect to the reference results, as well as the Root Mean Square error for the neutron power, and the maximum relative error (pointwise) for the fluxes for groups $g = 1$ and $g = 7$. It must be noted that the relative errors are much larger for the thermal groups ($g > 3$), i.e., the relative error for the $g = 7$ flux is locally above 35% for P_1, 25% for P_3, and 15% for P_5, as it has been explained before. Instead the pin averages power RMS errors are less than 0.4% for any of the approximations. The reason

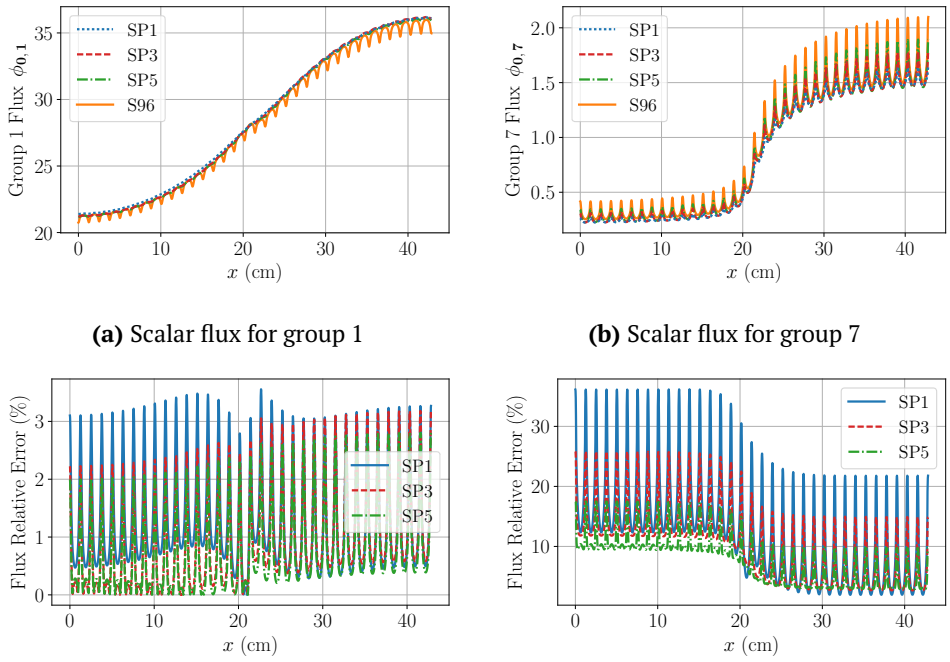

(a) Scalar flux for group 1

(b) Scalar flux for group 7

(c) Relative error for group 1

(d) Relative error for group 7

Figure 6.9: Comparison of results for heterogeneous fluxes and relative errors for Configuration 1.

for this is that the regions with water do not produce power (because there is not fission there), so the error in these regions does not directly affect the RMS error in the power (neither assembly-wise nor pin-wise). Nevertheless, we can observe that the error in the k_{eff} is very big for these approximations (above 900 pcm for $N \leq 5$) because this global parameter is affected by errors in the water regions through the balance equations. Increasing the order of the angular approximation for P_N affects mainly the value of the k_{eff} through better capturing of the behaviour in these regions.

Table 6.9 shows the assembly-wise homogenization results for different P_N approximations using different homogenization strategies defined in Table 6.7. At assembly level, the diffusion theory, P_1, results are accurate enough and increasing the number of spherical harmonics does not provide better results. This behaviour is explained by the fact that the assemblies are large enough to provide

Table 6.8: Comparison of heterogeneous results for Configuration 1.

	Eigenvalue		**Power RMS**		**Max. Rel. Error**	
	k_{eff}	Δk_{eff} (pcm)	Assembly (%)	Pin (%)	$g = 1$ (%)	$g = 7$ (%)
P_1	0.91154	1360	0.05	0.32	3.56	36.18
P_3	0.91411	1103	0.34	0.37	3.18	25.84
P_5	0.91610	904	0.30	0.32	2.80	17.49
S_{96}	0.92514					

precise average results with a LO solver such as the diffusion approximation, and the angular dependence does not have a strong effect average-wise for this size of the homogenized regions. However, reconstructed pin power results have RMS errors around 11%. This is explained by the assembly shape function (which is the heterogeneous power computed for an isolated assembly with reflexive boundary conditions) being inaccurate as it does not take into account influences of neighbouring assemblies. To improve these results a more sophisticated reconstruction method or pin homogenization strategy is necessary. We can also mention that using RXSs provide good results, even if no discontinuity factors are used. This is because the reconstruction has been done with the right shape for the local flux, which in practical reactor calculations is not available. Nevertheless, we observe that we must also use discontinuity factors together with the reference cross sections, RDFs, in order to completely reproduce the average values of the power and the k_{eff} of the original problem with a HO solver with the homogenized problem and a LO solver.

Last, pin-wise homogenization results are shown in Table 6.10. In this Table, we can observe a similar behaviour as for average-wise homogenization except that now the RMS error is reduced for pin-power averages. This is the main reason for using pin discontinuity factors. This comes from the choice of smaller domains for the homogenization, which requires that we correct the homogenization error at these scales. The RXSs and RDFs results behave analogously to the case of assembly-wise homogenization presented above.

Table 6.9: Comparison for assembly-wise homogenization results for Configuration 1.

Transport Approx.	Hom. Method	Eigenvalue		Power RMS	
		k_{eff}	Δk_{eff} (pcm)	Assembly (%)	Pin (%)
P_1	No DFs	0.92475	39	0.49	10.95
	ADFs	0.92547	33	0.10	10.90
	RXSs	0.92468	46	0.39	0.39
	RDFs	0.92514	0	0.00	0.00
P_3	No DFs	0.92514	0	0.06	10.91
	ADFs	0.92583	69	0.52	10.88
	RXSs	0.92507	7	0.04	0.04
	RDFs	0.92514	0	0.00	0.00
P_5	No DFs	0.92516	2	0.06	10.91
	ADFs	0.92585	71	0.53	10.88
	RXSs	0.92509	5	0.05	0.05
	RDFs	0.92514	0	0.00	0.00
Transport Reference		0.92514			

Table 6.10: Comparison for pin-wise homogenization results for Configuration 1.

Transport Approx.	Hom. Method	Eigenvalue		Power RMS	
		k_{eff}	Δk_{eff} (pcm)	Assembly (%)	Pin (%)
P_1	No DFs	0.92476	38	0.49	0.56
	PDFs	0.92547	33	0.10	0.44
	RXSs	0.92469	45	0.42	0.53
	RDFs	0.92514	0	0.00	0.00
P_3	No DFs	0.92515	1	0.05	0.15
	PDFs	0.92531	17	0.11	0.15
	RXSs	0.92508	6	0.02	0.17
	RDFs	0.92514	0	0.00	0.00
P_5	No DFs	0.92517	3	0.04	0.11
	PDFs	0.92533	19	0.12	0.17
	RXSs	0.92511	3	0.02	0.13
	RDFs	0.92514	0	0.00	0.00
Transport Reference		0.92514			

6.7.2 Configuration 2

The reactor named as Configuration 2 is composed of five assemblies with reflexive boundary conditions. Each assembly is composed of 17 pins describing an usual nuclear arrangement. This test is built to be more heterogeneous than the previous one, to be able to test the different homogenization methods in more realistic conditions, since the composition of each assembly will not be completely homogeneous.

First, we analyse the behaviour of the fluxes and the errors for different energy groups and different LO solvers (P_1, P_3, and P_5) without spatial homogenization. Figures 6.10a and 6.10b present the heterogeneous scalar fluxes, ϕ_0^g, of the groups $g = 1$ and $g = 7$ for different transport approximations. Figures 6.10c and 6.10d show the relative errors for these low order angular approximations. We see a similar behaviour as the one observed in the previous problem. In this way, the relative errors are larger for thermal groups $g > 5$. than for fast groups $g < 5$. Again we observe that this effect is higher in the regions with water and now also in regions with materials 5 and 6, which represent strong absorbers or fission chambers where almost no fission occurs. Again, the LO solvers are unable to fully capture the behaviour of the HO solution (S_{96}) in these regions.

Table 6.11 shows a comparison of the heterogeneous results, without any homogenization, for P_1, P_3, and P_5, approximations. This Table shows the same type of errors as Table 6.8. We can see the same behaviour, with larger point-wise flux maximum relative error for $g = 7$ than for $g = 1$, and large errors in the eigenvalue of the problem. We can also see that the average-wise error is larger for the power (pin-wise and assembly-wise), and that this error decreases when increasing the order of the LO solver. This suggests that for more realistic problems, there is actually a need of using LO solvers of slightly higher order for reducing both pin-wise and assembly-wise, RMS errors for average power.

Table 6.11: Comparison of heterogeneous results for Configuration 2.

	Eigenvalue		**Power RMS**		**Max. Rel. Error**	
	k_{eff}	Δk_{eff} (pcm)	Assembly (%)	Pin (%)	$g = 1$ (%)	$g = 7$ (%)
P_1	1.11869	1443	2.05	2.03	13.25	36.77
P_3	1.12290	1022	1.30	1.17	8.18	23.33
P_5	1.12649	663	0.75	0.68	5.04	13.83
S_{96}	1.13312					

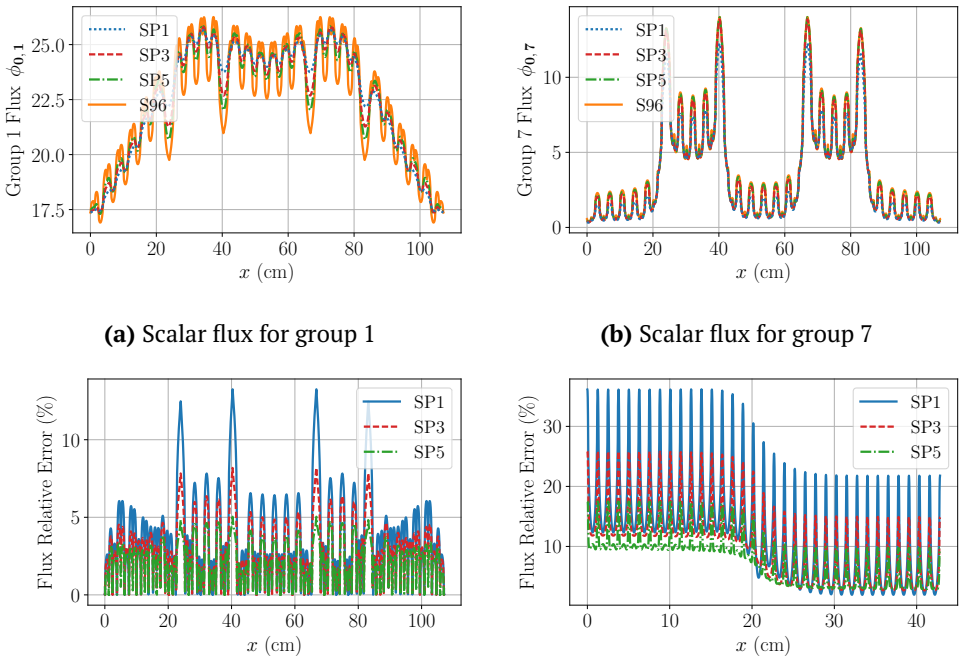

(a) Scalar flux for group 1

(b) Scalar flux for group 7

(c) Relative error for group 1

(d) Relative error for group 7

Figure 6.10: Comparison of results for heterogeneous fluxes and relative errors for Configuration 2.

Table 6.12 shows the assembly-wise homogenization results P_1, P_3 and P_5 approximations using the different strategies of homogenization defined in Table 6.7. As it occurs for reactor Configuration 1, for reactor Configuration 2 the computations at assembly level using ADFs, by means of the diffusion theory, P_1, are accurate enough and increasing the number of spherical harmonics in the transport approximation does not provide better results. In this case, the introduction of assembly discontinuity factors improves the obtained solution in terms of eigenvalue error and assembly averaged neutron error, while the pin-wise RMS error remains high, even if the order of the LO solver is increased up to P_5.

Results for pin-wise homogenization are shown in Table 6.13. We see that the use of pin-wise homogenization provides more accurate results, both in assembly and pin averaged power, specially if the proposed pin discontinuity factors are used. Increasing the number of spherical harmonics, N, reduces the eigenvalue

Table 6.12: Comparison for assembly-wise homogenization results for Configuration 2.

Transport Approx.	Hom. Method	Eigenvalue		Power RMS	
		k_{eff}	Δk_{eff} (pcm)	Assembly (%)	Pin (%)
P_1	No DFs	1.13462	150	1.20	14.82
	ADFs	1.13334	22	1.52	14.95
	RXSs	1.13368	56	3.16	2.55
	RDFs	1.13312	0	0.00	0.00
P_3	No DFs	1.13613	301	3.54	15.00
	ADFs	1.13392	80	0.95	14.89
	RXSs	1.13421	109	3.70	2.97
	RDFs	1.13312	0	0.00	0.00
P_5	No DFs	1.13618	306	3.55	15.00
	ADFs	1.13398	86	0.94	14.89
	RXSs	1.13426	114	3.71	2.98
	RDFs	1.13312	0	0.00	0.00
Transport Reference		1.13312			

error and pin averaged power errors because at pin scale the angular dependence is relevant. In this way, if the proposed pin discontinuity factors are used, the eigenvalue error can be reduced to 38 pcm and less than 1% in pin averaged power error results if one uses P_5 approximation.

Table 6.13: Comparison for pin-wise homogenization results for Configuration 2.

Transport Approx.	Hom. Method	Eigenvalue		Power RMS	
		k_{eff}	Δk_{eff} (pcm)	Assembly (%)	Pin (%)
P_1	No DFs	1.12458	854	1.66	1.66
	PDFs	1.13331	19	0.46	1.43
	RXSs	1.12436	876	1.64	1.67
	RDFs	1.13312	0	0.00	0.00
P_3	No DFs	1.12795	517	1.32	1.20
	PDFs	1.1335	55	0.89	0.92
	RXSs	1.12775	537	1.31	1.18
	RDFs	1.13312	0	0.00	0.00
P_5	No DFs	1.13053	259	1.03	0.94
	PDFs	1.1335	38	0.76	0.78
	RXSs	1.13033	279	1.02	0.93
	RDFs	1.13312	0	0.00	0.00
Transport Reference		1.13312			

7 Conclusions

The distribution of the neutron population in a nuclear reactor is described by the neutron transport equation. As the physics of a reactor is determined by the neutrons interactions with matter, this equation also predicts the quantity of fission reactions and thus, the power distribution, in the form of heat, produced inside the reactor core. The solution of this equation is the fundamental tool to predict the behaviour of a nuclear core. To solve the neutron transport equation we have to discretize it in terms of directions, energy, time and space. In this work, we have studied different approximations of this equation with a reasonable computational cost in order to simulate and evaluate the reactor performance.

In Chapter 3, we have presented an adaptive finite element algorithm for the static neutron diffusion equation, the Lambda modes problem. This method allows using high order finite elements with heterogeneous meshes. In this way, to increase the accuracy of the solution it is possible both to refine the spatial mesh and to increase the degree of the polynomials in the finite element method. Several numerical methods were established to solve the multiplicative constant of the reactor or the fundamental eigenvalue of the problem and its corresponding eigenvector, the stationary neutron flux. To study the performance of the method different benchmark problems have been analysed using different meshes and configurations of the computations. From all the analyses performed is concluded that the method converges if the mesh is refined or the degree of the polynomial expansions is increased, being the last strategy the most convenient one to obtain accurate results with a moderate computational cost.

Then, different preconditioning strategies for the system matrices arising in a high order finite element discretization of the neutron diffusion equation are studied. These preconditioners are based on domain decomposition techniques,

making use of a partition of the degrees of freedom on vertices, edges, faces and interiors ones, obtained through the identifications of the different shape functions with collocation points over each element. No improvement is observed in two-dimensional problems over traditional Jacobi preconditioners, due to the fact that the overhead cost of building and applying the preconditioner is not compensated by a significant improvement of the convergence ratio. Nevertheless, for large enough linear systems, as is the case for three dimensional problems, the preconditioners show an improvement of the convergence time for the studied linear systems, as well as for the memory usage, outperforming classical and widely used preconditioners as the Incomplete LU decomposition.

An additional feature studied in Section 3.8 is that the linear systems have been preprocessed with the Schur complement method, in order to reduce the memory usage and the CPU time for convergence, and these Schur matrices have then been preconditioned. We recall that this preprocessing technique, also known as static condensation, already represents an improvement in convergence rates over the classical methodology used for this problem. It is due to the fact that many linear systems have to be solved with the same coefficient matrices and different right hand sides during the application of the eigenvalue solver, thus, easily compensating initial cost of setting the Schur complement system.

As possible extensions, the application of these preconditioners for matrix-free algorithms are studied. A matrix-free application should consider the extra cost of applying the Schur complement system at each iteration and the problem of building the preconditioner without explicitly building the matrix. This method is used to efficiently accelerate the procedures of the neutron transport equation. Moreover, the construction of a preconditioner that performs equally well for different configurations of the same problem is of interest. The improvement for the convergence could be estimated a priory for the particular system in function of its size, thus choosing the optimal preconditioner for the particular situation.

Chapter 4 is devoted to the time dependent neutron diffusion equation. Many transients in nuclear power reactors involve the movement of the control rod banks. For the simulation of this kind of transients with the classical methods, it is necessary to define equivalent material properties corresponding to partially inserted cells during the movement of the control rods. Volume averaged and flux weighting techniques are used to define this equivalent cross-sections, but this procedure leads to non-physical behaviour of some magnitudes during the simulation when a small number of axial planes are used in the spatial discretization and this problem is known as the *rod-cusping effect*. To avoid it, a new method based on a high-order finite element method is proposed in this Chapter. In this new method, the spatial mesh is moved together with the control rods in such a

way that there is no partially inserted cells. The solutions of the physical magnitudes are transferred between different spatial meshes using a polynomial interpolation.

Also, numerical results show that the moving mesh method has a better performance than the traditional fixed mesh scheme when a small number of axial cells is used. Thus, the moving mesh scheme permits to use a coarser discretization and reduces the computational effort.

In Chapter 5, we have presented a simplified spherical harmonics approximation (SP_N) solver using a high order finite element discretization. The work has been centred in the comparisons between the diffusion equation, SP_1, and the more sophisticated SP_3 and SP_5 equations. To study the performance of the method to compute the multiplicative constant of the reactor and its corresponding stationary neutron flux, different benchmark problems have been analysed. From these analyses, it is concluded that when diffusion approximation does not give enough accurate results SP_3 is a convenient, computational cheap alternative to improve performance. However, SP_5 approximation does not worth the extra computational effort to solve this approximation for full reactor core problems.

A detailed description of a nuclear power reactor core taking into account the detailed composition of the different materials composing the fuel assemblies is a very expensive task from the computational point of view, even when a low order approximation of the neutron transport equation such as the neutron diffusion equation is used. Thus, a homogenized version of the core is generally used for whole core reactor calculations. In this way, the implementation of the Generalized Equivalence Theory in the Finite Element methods is discussed in Chapter 6. This homogenization theory makes use of flux discontinuity factors that introduces discontinuous solutions for the neutron flux. Flux discontinuity factors conditions were introduced for nodal methods because they do not force explicitly the continuity between subdomains. Here, we propose a discontinuous Galerkin method that introduces the flux discontinuity factors condition in a weak form, by means of an interior penalty method, obtaining discontinuous solutions for the neutronic flux. The performance of the method has been tested with 1D and 2D benchmark problems, using both reference homogenized cross sections together with reference discontinuity factors, and assembly cross sections together with assembly discontinuity factors obtained with the standard homogenization method. It is shown that the finite element method proposed has a very good performance, being the most part of the errors found due to the homogenization process. It has also been observed that the IP-FEM could need to increase the polynomial degree of the high order finite element method to more than $p = 3$ for some problems in order to achieve enough accuracy.

Moreover, Chapter 6 extends the generalized equivalence theory for the simplified spherical harmonics equations. This thesis proposes pin discontinuity factors for every even flux moment of the spherical harmonics approximation calculated from an isolated assembly transport calculation and the use of SP_3 or SP_5 approximations to the neutron transport equation for accurate reactor calculations. Numerical results show that low order spherical harmonics approximations cannot reproduce accurately sub-pin heterogeneities when solving for the whole domain. This strongly affects the approximation of the largest eigenvalue of the problem. In order to improve the approximation for the largest eigenvalue while keeping the computations efficient, the problem can be solved using a homogenization process with two different solvers at two different scales. In this way, assembly discontinuity factors correct some of the errors introduced during the homogenization process, and it produces acceptable eigenvalue and assembly averaged results using diffusion theory, even if they do not reconstruct precise pin averaged results. The proposed pin discontinuity factors produce accurate results for both pin and assembly averaged values without the use of reconstruction methods. Also, the homogenization methodology has been verified with the calculation of reference discontinuity factors, which fully reproduce average values with the homogenized problem.

Bibliography

Allaire, G. and Y. Capdeboscq (2000). "Homogenization of a spectral problem in neutronic multigroup diffusion". In: *Computer Methods in Applied Mechanics and Engineering* 187.1, pp. 91–117. doi: 10.1016/S0045-7825(99)00112-7 (cit. on p. 100).

Allaire, Grégoire and Guillaume Bal (1999). "Homogenization of the criticality spectral equation in neutron transport". In: *ESAIM: Mathematical Modelling and Numerical Analysis* 33.4, pp. 721–746 (cit. on p. 100).

American Nuclear Society (1977). *Argonne Code Center: benchmark problem book, ANL-7416(Suppl.2)*. Tech. rep. doi: 10.2172/5037820 (cit. on pp. 37, 56, 97, 177).

Arnold, D. N, F. Brezzi, B. Cockburn, and D. Marini (2000). *Discontinuous Galerkin methods for elliptic problems*. Ed. by B Cockburn, G Karniadakis, and C Shu. Vol. 11. Lect. Notes Comput. Sci. Eng. Berlin: Springer, pp. 89–101. doi: 10.1007/978-3-642-59721-3 (cit. on p. 105).

Arnold, D. N., F. Brezzi, B. Cockburn, and L. D. Marini (2002). "Unified analysis of discontinuous Galerkin methods for elliptic problems". In: *SIAM journal on numerical analysis* 39.5, pp. 1749–1779. doi: 10.1137/S0036142901384162 (cit. on p. 105).

Baker, C.M.J., A.G. Buchan, C.C. Pain, B.S. Tollit, M.A. Goffin, S. R. Merton, and P. Warner (2013). "Goal based mesh adaptivity for fixed source radiation transport calculations". In: *Annals of Nuclear Energy* 55, pp. 169–183. doi: 10.1016/j.anucene.2012.11.029 (cit. on p. 16).

Bangerth, W., R. Hartmann, and G. Kanschat (2007). "deal.II – a General Purpose Object Oriented Finite Element Library". In: *ACM Trans. Math. Softw.* 33.4, pp. 24/1–24/27. doi: 10.1145/1268776.1268779 (cit. on pp. 16, 46, 66, 117).

Bangerth, W. and O. Kayser-Herold (2009). "Data Structures and Requirements for hp Finite Element Software". In: *ACM Trans. Math. Softw.* 36.1, pp. 4/1–4/31. doi: 10.1145/1486525.1486529 (cit. on pp. 16, 27).

Barrault, M., B. Lathuiliere, P. Ramet, and J. Roman (2011). "Efficient parallel resolution of the simplified transport equations in mixed-dual formulation". In: *Journal of Computational Physics* 230.5, pp. 2004–2020. doi: 10.1016/j.jcp.2010.11.047 (cit. on pp. 45, 177).

Bennewitz, F., H. Finnemann, and M. R. Wagner. (1975). "Higher-Order Corrections in Nodal Reactor Computations". In: *Trans. Am. Nucl. Soc.* 22, p. 205 (cit. on p. 66).

Bernal, Á., R. Miró, D. Ginestar, and G. Verdú (2014). "Resolution of the generalized eigenvalue problem in the neutron diffusion equation discretized by the finite volume method". In: *Abstract and Applied Analysis* vol. 2014. doi: 10.1155/2014/913043 (cit. on pp. 16, 178).

Brantley, P. S. and E. W. Larsen (2000). "The simplified P_3 approximation". In: *Nuclear science and engineering* 134, pp. 1–21. doi: 10.13182/NSE134-01 (cit. on pp. 79, 86).

Brezzi, F., B. Cockburn, L. D. Marini, and E. Süli (2006a). "Stabilization mechanisms in discontinuous Galerkin finite element methods". In: *Computer Methods in Applied Mechanics and Engineering* 195.25, pp. 3293–3310. doi: 10.1016/j.cma.2005.06.015 (cit. on pp. 105, 108).

Brezzi, F., B. Cockburn, L. D. Marini, and E. Süli (2006b). "Stabilization mechanisms in discontinuous Galerkin finite element methods". In: *Computer Methods in Applied Mechanics and Engineering* 195.25, pp. 3293–3310. doi: 10.1016/j.cma.2005.06.015 (cit. on pp. 128, 129).

Bru, R., D. Ginestar, J. Marín, G. Verdú, J. Mas, and T. Manteuffel (2002). "Iterative schemes for the neutron diffusion equation". In: *Computers & Mathematics with Applications* 44.10, pp. 1307–1323. doi: 10.1016/S0898-1221(02)00258-4 (cit. on p. 60).

Cai, X. and M. Sarkis (1999). "A restricted additive Schwarz preconditioner for general sparse linear systems". In: *SIAM Journal on Scientific Computing* 21.2, pp. 792–797. doi: 10.1137/S106482759732678X (cit. on p. 51).

Capilla, M., C. F. Talavera, D. Ginestar, and G. Verdú (2005). "A nodal collocation method for the calculation of the lambda modes of the PL equations". In: *Annals of Nuclear Energy* 32.17, pp. 1825–1853. doi: 10.1016/j.anucene.2005.07.004 (cit. on pp. 82, 89, 167).

Carreño, A., A. Vidal-Ferràndiz, D. Ginestar, and G. Verdú (2017). "Spatial modes for the neutron diffusion equation and their computation". In: *Annals of Nuclear Energy* 110 Supplement C, pp. 1010–1022. doi: 10.1016/j.anucene.2017.08.018 (cit. on p. 13).

Carvalho, L. M., L. Giraud, and P. Le Tallec (2001). "Algebraic two-level preconditioners for the Schur complement method". In: *SIAM Journal on Scientific Computing* 22.6, pp. 1987–2005 (cit. on p. 51).

Chao, Y. (2016a). "A new and rigorous SPN theory for piecewise homogeneous regions". In: *Annals of Nuclear Energy* 96, pp. 112–125. doi: 10.1016/j.anucene.2016.06.010 (cit. on p. 101).

Chao, Y. (2016b). "A new SPn theory formulation with self-consistent physical assumptions on angular flux". In: *Annals of Nuclear Energy* 87, pp. 137–144 (cit. on p. 101).

Cho, N. Z., D. S. Kim, and K. T. Lee (2001). ""Three-dimensional reactor kinetics calculation in analytic function expansion nodal method". In: *Proceedings of the Winter Meeting of ANS*. Vol. 85. Reno, Nevada, USA, pp. 240–243 (cit. on p. 65).

Cossa, G., V. Giusti, and B. Montagnini (2010). "A Boundary Element-Response Matrix method for criticality diffusion problems in xyz geometry". In: *Annals of Nuclear Energy* 37.7, pp. 953–973. doi: 10.1016/j.anucene.2010.03.012 (cit. on pp. 45, 177).

Cullen, D. E. (2001). *Why are the Pn and Sn Methods Equivalent?* Tech. rep. UCRL-ID-145518. U.S. Department of Energy, Lawrence Livermore National Laboratory (cit. on p. 81).

Cuthill, E. and J. McKee (1969). "Reducing the bandwidth of sparse symmetric matrices". In: *Proceedings of the 1969 24th national conference*. ACM '69. New York, NY, USA: ACM, pp. 157–172. doi: 10.1145/800195.805928 (cit. on pp. 26, 64).

Dall'Osso, A. (2002). "Reducing rod cusping effect in nodal expansion method calculations". In: *Proceedings of the International Conference on the New Frontiers of Nuclear Technology: Reactor Physics, Safety and High-Performance Computing (PHYSOR), Seoul, Korea* (cit. on p. 66).

Davis, T. A. (2004). "Algorithm 832: UMFPACK V4.3—an Unsymmetric-pattern Multifrontal Method". In: *ACM Trans. Math. Softw.* 30.2, pp. 196–199. doi: 10.1145/992200.992206 (cit. on p. 45).

Demazière, C. (2014). *Modelling of Nuclear Reactors*. Lecture Notes. Gothenburg, Sweden: Division of Nuclear engineering, Department of Applied Physics, Chalmers University of Technology (cit. on pp. 4, 11).

Demmel, J. W., S. C. Eisenstat, J. R. Gilbert, X. S. Li, and J. W. H. Liu (1999). "A supernodal approach to sparse partial pivoting". In: *SIAM J. Matrix Analysis and Applications* 20.3, pp. 720–755. doi: 10.1137/S0895479895291765 (cit. on p. 45).

Downar, T. J., Yunlin Xu, V. Seker, and N. Hudson (2009). *PARCS v3.0 U.S. NRC Core Neutronics Simulator Theory Manual*. Tech. rep. Ann Arbor, USA: Department of Nuclear Engineering and Radiological Sciences, University of Michigan, pp. 1–129 (cit. on pp. 70, 77, 95, 117).

Dulla, S., E. H. Mund, and P. Ravetto (2008). "The quasi-static method revisited". In: *Progress in Nuclear Energy* 50.8, pp. 908–920 (cit. on p. 60).

Efstathiou, E. and M. J. Gander (2003). "Why Restricted Additive Schwarz Converges Faster than Additive Schwarz". In: *BIT Numerical Mathematics* 43.5, pp. 945–959. doi: 10.1023/B:BITN.0000014563.33622.1d (cit. on p. 51).

Epshteyn, Y. and B. Rivière (2007). "Estimation of penalty parameters for symmetric interior penalty Galerkin methods". In: *Journal of Computational and*

Applied Mathematics 206.2, pp. 843–872. doi: 10.1016/j.jcp.2014.06.034 (cit. on pp. 109, 112).

Ferguson, D. R. and K. L. Derstine (1977). "Optimized iteration strategies and data management considerations for fast reactor finite difference diffusion theory codes". In: *Nuclear Science and Engineering* 64.2, pp. 593–604. doi: 10.13182/NSE77-5 (cit. on p. 25).

Finnemann, H. (1975). *A consistent nodal method for the analysis of space-time effects in large LWR's*. Tech. rep. Technische Univ. Muenchen, Garching (F.R. Germany). Lab. fuer Reaktorregelung und Anlagensicherung (cit. on p. 15).

Gander, M. J. (2008). "Schwarz methods over the course of time". In: *Electronic Transactions on Numerical Analysis* 31, pp. 228–255 (cit. on p. 44).

Gast, R. (1958). *On the Equivalence of the Spherical Harmonics method and the discrete ordinate method using Gauss quadrature for the Boltzmann equation*. Tech. rep. WAPD-TM-118. Pittsburgh, United States: Westinghouse Electric Corp. Bettis Plant (cit. on p. 81).

Gehin, J. C. (1992). "A quasi-static polynomial nodal method for nuclear reactor analysis". PhD thesis. Massachusetts Institute of Technology. Dept. of Nuclear Engineering (cit. on p. 65).

Gelbard, E. M. (1960). *Application of spherical harmonics methods to reactor problems*. Tech. rep. WAPD-BT-20. Bettis Atomic Power Laboratory (cit. on p. 79).

Geuzaine, C. and J. Remacle (2009). "Gmsh: A 3-D finite element mesh generator with built-in pre- and post-processing facilities". In: *International Journal for Numerical Methods in Engineering* 79.11, pp. 1309–1331 (cit. on p. 73).

Gilbert, D., J. E. Roman, W. J. Garland, and W. F. S. Poehlman (2008). "Simulating control rod and fuel assembly motion using moving meshes". In: *Annals of Nuclear Energy* 35.2, pp. 291–303. doi: 10.1016/j.anucene.2007.06.007 (cit. on p. 64).

Ginestar, D. (1995). "Integración de la Ecuación de la Difusión Neutrónica en Geometrías Multidimensionales. Aplicación a Reactores Nucleares. Cálculo

de los Modos Lambda." PhD thesis. Universitat Politècnica de València. doi: 10.4995/Thesis/10251/4268 (cit. on p. 15).

Ginestar, D., J. Marín, and G. Verdú (2001). "Multilevel methods to solve the neutron diffusion equation". In: *Applied Mathematical Modelling* 25.6, pp. 463–477. doi: 10.1016/S0307-904X(00)00062-7 (cit. on p. 16).

Ginestar, D., G. Verdú, V. Vidal, R. Bru, J. Marín, and J. L. Muñoz-Cobo (1998). "High order backward discretization of the neutron diffusion equation". In: *Annals of Nuclear Energy* 25.1–3, pp. 47–64. doi: 10.1016/S0306-4549(97)00046-7 (cit. on pp. 60, 62).

Ginestar, D., R. Miró, G. Verdú, and T. Barrachina (2011). "Modal processing of the Local Power Range Monitors signals in BWR NPP". In: *Annals of Nuclear Energy* 38.11, pp. 2441–2455. doi: 10.1016/j.anucene.2011.07.010 (cit. on p. 13).

Golub, G. H. and J. H. Welsch (1969). "Calculation of Gauss Quadrature Rules". In: *Mathematics of Computation* 23.106, pp. 221–230. doi: 10.2307/2004418 (cit. on p. 22).

González-Pintor, S., D. Ginestar, and G. Verdú (2009). "High Order Finite Element Method for the Lambda modes problem on hexagonal geometry". In: *Annals of Nuclear Energy* 36.9, pp. 1450–1462. doi: 10.1016/j.anucene.2009.07.003 (cit. on pp. 16, 19).

González-Pintor, S., D. Ginestar, and G. Verdú (2012). "Modified Block Newton method for the lambda modes problem". In: *Nuclear Engineering and Design* 259, pp. 230–239. doi: 10.1016/j.nucengdes.2011.06.045 (cit. on p. 177).

González-Pintor, S., D. Ginestar, and G. Verdú (2014). "Preconditioning the solution of the time-dependent neutron diffusion equation by recycling Krylov subspaces". In: *International Journal of Computer Mathematics* 91.1, pp. 42–52. doi: 10.1080/00207160.2013.771181 (cit. on p. 60).

González-Pintor, S., G. Verdú, and D. Ginestar (2011). "Correction of the rod cusping effect for a high order finite element method". In: *Proceedings of the International Conference on Mathematics and Computational Methods Applied*

to Nuclear Science and Engineering (M&C 2011). Rio de Janeiro, RJ, Brazil, May 8-12, 2011, on CD-ROM, Latin American Section (LAS) / American Nuclear Society (ANS) (cit. on pp. 65, 73).

Hamilton, S. P. and T. M. Evans (2015). "Efficient solution of the simplified P_N equations". In: *Journal of Computational Physics* 284, pp. 155–170. doi: 10.1016/j.jcp.2014.12.014 (cit. on p. 83).

Hauck, C. and R. McClarren (2010). "Positive P_N Closures". In: *SIAM Journal on Scientific Computing* 32.5, pp. 2603–2626. doi: 10.1137/090764918 (cit. on p. 82).

Hébert, A. (1981). *Développement de la methode SPH: Homogénéisation de cellules dans un réseau non uniforme et calcul des paramètres de reflecteur*. Tech. rep. CEA-N-2209. Commissariat à l'Energie Atomique (cit. on p. 100).

Hébert, A. (1985). "Application of the Hermite Method for Finite Element Reactor Calculations". In: *Nuclear Science and Engineering* 91.1, pp. 34–58. doi: 10.13182/NSE85-A17127 (cit. on pp. 31, 173).

Hébert, A. (1987). "Development of the nodal collocation method for solving the neutron diffusion equation". In: *Annals of Nuclear Energy* 14.10, pp. 527–541. doi: 10.1016/0306-4549(87)90074-0 (cit. on p. 16).

Hébert, A. (1993). "A Consistent Technique for the Pin-by-Pin Homogenization of a Pressurized Water Reactor Assembly". In: *Nuclear Science and Engineering* 113.3, pp. 227–238. doi: 10.1017/CBO9781107415324.004 (cit. on p. 100).

Hébert, A. (2008). "A Raviart–Thomas–Schneider solution of the diffusion equation in hexagonal geometry". In: *Annals of Nuclear Energy* 35.3, pp. 363–376. doi: 10.1016/j.anucene.2007.07.016 (cit. on p. 16).

Hébert, A. and G. Mathonniere (1993). "Development of a third-generation superhomogénésation method for the homogenization of a pressurized water reactor assembly". In: *Nuclear science and engineering* 115.2, pp. 129–141. doi: 10.13182/NSE115-129 (cit. on p. 100).

Henry, A. F. (1975). *Nuclear-Reactor analysis*. Cambridge, MA, USA: MIT Press (cit. on pp. 15, 17, 81).

Hernandez, V., Jose E. Roman, and V. Vidal (2005). "SLEPc: A Scalable and Flexible Toolkit for the Solution of Eigenvalue Problems". In: *ACM Trans. Math. Software* 31.3, pp. 351–362 (cit. on pp. 17, 26).

Hinton, E., T. Rock, and O. C. Zienkiewicz (1976). "A note on mass lumping and related processes in the finite element method". In: *Earthquake Engineering & Structural Dynamics* 4.3, pp. 245–249. doi: 10.1002/eqe.4290040305 (cit. on p. 68).

Jamelot, E., A. M. Baudron, and J. J. Lautard (2012). "Domain Decomposition for the SPN Solver MINOS". In: *Transport Theory and Statistical Physics* 41.7, pp. 495–512. doi: 10.1080/00411450.2012.694827 (cit. on p. 45).

Jamelot, E. and P. Ciarlet (2013). "Fast non-overlapping Schwarz domain decomposition methods for solving the neutron diffusion equation". In: *Journal of Computational Physics* 241, pp. 445–463 (cit. on p. 45).

Karniadakis, G. E. and S. J. Sherwin (2005). *Spectral/hp element methods for computational fluid dynamics*. Numerical mathematics and scientific computation. Oxford, New York, Aukland: Oxford University Press (cit. on p. 67).

Kavenoky, A. (1978). "The SPH homogenization method". In: *Proc. Meeting Homogenization Methods in Reactor Physics*. IAEA-TECDOC-231. Lugano, Switzerland (cit. on p. 100).

Kelly, D. W., J. P. De S. R. Gago, O. C. Zienkiewicz, and I. Babuska (1983). "A posteriori error analysis and adaptive processes in the finite element method: Part I—error analysis". In: *International Journal for Numerical Methods in Engineering* 19.11, pp. 1593–1619. doi: 10.1002/nme.1620191103 (cit. on p. 27).

Keresztúri, A. and M. Telbisz (1992). "A Three Dimensional Hexagonal Kinetic Benchmark Problem". In: *2nd AER Symposium*. Paks, Hungary (cit. on p. 77).

Kim, Y. H. and N. Z. Cho (1990). "A bilinear weighting method for the control rod cusping problem in nodal methods". In: *Journal of Korean Nuclear Society* 22 (3), pp. 238–249 (cit. on p. 65).

Komatitsch, Di., G. Erlebacher, D. Göddeke, and D. Michéa (2010). "High-order finite-element seismic wave propagation modeling with MPI on a large GPU cluster". In: *Journal of Computational Physics* 229.20, pp. 7692–7714. doi: 10.1016/j.jcp.2010.06.024 (cit. on p. 42).

Kozlowski, T., Y. Xu, T. J. Downar, and D. Lee (2011). "Cell Homogenization Method for Pin-by-Pin Neutron Transport Calculations". In: *Nuclear science and engineering* 169.1, pp. 1–18. doi: 10.13182/NSE08-85 (cit. on p. 101).

Kronbichler, M. and K. Kormann (2012). "A generic interface for parallel cell-based finite element operator application". In: *Computers and Fluids* 63, pp. 135–147. doi: 10.1016/j.compfluid.2012.04.012 (cit. on pp. 42, 43).

Langenbuch, W. Maurer, and W. Werner (1977). "Coarse-Mesh Flux-Expansion Method for the Analysis of Space-Time Effects in Large Light Water Reactor Cores". In: *Nuclear Science and Engineering* 63.4, pp. 437–456. doi: 10.13182/NSE77-A27061 (cit. on pp. 75, 178).

Larsen, E. W., J. E. Morel, and J. M. McGhee (1996). "Asymptotic derivation of the multigroup P 1 and simplified P N equations with anisotropic scattering". In: *Nuclear science and engineering* 123.3, pp. 328–342 (cit. on p. 101).

Lesaint, P. and P. A. Raviart (1974). "On a Finite Element Method for Solving the Neutron Transport Equation". In: *Symposium on Mathematical Aspects of Finite Elements in Partial Differential Equations*. Univ. Paris VI, Labo. Analyse Numérique (cit. on p. 105).

Lewis, E. E. and W.F. Jr. Miller (1984). *Computational Methods of Neutron Transport*. New York, USA: John Wiley & Sons, Ltd. (cit. on pp. 6, 8, 9, 13, 80, 81).

Lewis, E. E., M. A. Smith, N. Tsoulfanidis, G. Palmiotti, T. A. Taiwo, and R. N. Blomquist (2001). *Benchmark specification for Deterministic 2-D/3-D MOX fuel assembly transport calculations without spatial homogenization (C5G7 MOX)*. Tech. rep. NEA/NSC/DOC (cit. on pp. 133, 171).

March-Leuba, J. and J.M. Rey (1993). "Coupled thermohydraulic-neutronic instabilities in boiling water nuclear reactors: a review of the state of the art". In: *Nuclear Engineering and Design* 145.1, pp. 97–111. doi: 10.1016/0029-5493(93)90061-D (cit. on p. 13).

McLane, V. (2000). *EXFOR Basics. A Short Guide to the Nuclear Reaction Data Exchange Format*. Tech. rep. BNL-NCS-63380-2000/05-Rev. Viena, Austria (cit. on p. 6).

Melenk, J.M., K. Gerdes, and C. Schwab (2001). "Fully discrete hp-finite elements: fast quadrature". In: *Computer Methods in Applied Mechanics and Engineering* 190.32, pp. 4339–4364. doi: 10.1016/S0045-7825(00)00322-4 (cit. on p. 42).

Miró, R., D. Ginestar, G. Verdú, and D. Hennig (2002). "A nodal modal method for the neutron diffusion equation. Application to BWR instabilities analysis". In: *Annals of Nuclear Energy* 29.10, pp. 1171–1194. doi: 10.1016/S0306-4549(01)00103-7 (cit. on pp. 13, 60, 178).

Müller, E. Z. and Z. J. Weiss (1991). "Benchmarking with the multigroup diffusion high-order response matrix method". In: *Annals of Nuclear Energy* 18.9, pp. 535–544. doi: 10.1016/0306-4549(91)90098-I (cit. on pp. 31, 173).

O'Dell, R D, F W Jr. Brinkley, and D R Marr (1982). *User's manual for ONEDANT: a code package for one-dimensional, diffusion-accelerated, neutral-particle transport*. doi: 10.2172/5226956 (cit. on pp. 89, 92).

Pardo, D., J. Álvarez Aramberri, M. Paszynski, L. Dalcin, and V.M. Calo (2015). "Impact of element-level static condensation on iterative solver performance". In: *Computers & Mathematics with Applications* 70.10, pp. 2331–2341. doi: 10.1016/j.camwa.2015.09.005 (cit. on p. 49).

Ragusa, J. C. (2010). "Application of h-, p-, and hp-Mesh Adaptation Techniques to the SP3 Equations". In: *Transport Theory and Statistical Physics* 39.2-4, pp. 234–254. doi: 10.1080/00411450.2010.533743 (cit. on p. 101).

Rahnema, F. and E. M. Nichita (1997). "Leakage corrected spatial (assembly) homogenization technique". In: *Annals of Nuclear Energy* 24.6, pp. 477–488. doi: 10.1016/S0306-4549(96)00084-9 (cit. on pp. 117, 120, 172, 175).

Rathkopf, J. A. and W. R. Martin (1986). "The finite element response matrix method for the solution of the neutron transport equation". In: *Progress in Nuclear Energy* 18.1, pp. 237–250 (cit. on p. 45).

Reed, W. H. and T. R. Hill (1973). *Triangular mesh methods for the neutron transport equation*. Tech. rep. LA-UR-73-479. Los Alamos, USA (cit. on p. 105).

Rivière, B. (2008). *Discontinuous Galerkin methods for solving elliptic and parabolic equations: theory and implementation*. Society for Industrial and Applied Mathematics (cit. on p. 108).

Ronen, Y., D. Shvarts, and J. J. Wagschal (1976). "A Comparison of Some Eigenvalues in Reactor Theory". In: *Nuclear Science and Engineering* 60.1, pp. 97–101. doi: 10.13182/NSE76-A26862 (cit. on p. 13).

Saad, Y. (2003). *Iterative Methods for Sparse Linear Systems*. 2nd edition. Philadelphia, PA, USA: Society for Industrial and Applied Mathematics (cit. on pp. 26, 44, 45, 47, 48, 51, 64).

Sanchez, R. (2009). "Assembly homogenization techniques for core calculations". In: *Progress in Nuclear Energy* 51.1, pp. 14–31. doi: 10.1016/j.pnucene.2008.01.009 (cit. on pp. 100, 126, 131).

Sanchez, R., G. Dante, and I. Zmijarevic (2013). "Diffusion Piecewise Homogenization via Flux Discontinuity Ratios". In: *Nuclear Engineering and Technology* 45.6, pp. 707–720. doi: 10.5516/NET.02.2013.518 (cit. on p. 100).

Schwarz, H. A. (1870). "Ueber einen Grenzübergang durch alternirendes Verfahren". In: *Vierteljahrsschrift der Naturforschenden Gesellschaft in Zürich*. Ed. by R. Wolf. Zürich: Zürcher u. Furrer. Chap. 15, pp. 272–286 (cit. on pp. 44, 51).

Shahbazi, K. (2005). "An explicit expression for the penalty parameter of the interior penalty method". In: *Journal of Computational Physics* 205.2, pp. 401–407. doi: 10.1016/j.jcp.2004.11.017 (cit. on pp. 109, 112).

Sherwin, S. J. and M. Casarin (2001). "Low-energy Basis Preconditioning for Elliptic Substructured Solvers Based on Unstructured Spectral/Hp Element Discretization". In: *J. Comput. Phys.* 171.1, pp. 394–417. doi: 10.1006/jcph.2001.6805 (cit. on p. 49).

Singh, T., T. Mazumdar, and P. Pandey (2014). "NEMSQR: A 3-D multi group diffusion theory code based on nodal expansion method for square geometry". In: *Annals of Nuclear Energy* 64, pp. 230–243 (cit. on p. 15).

Smith, B., P. Bjorstad, and W. Gropp (2004). *Domain decomposition: parallel multilevel methods for elliptic partial differential equations*. Cambridge university press (cit. on p. 44).

Smith, K. S. (1979). "An Analytic Nodal Method for Solving the Two-Group, Multidimensional, Static and Transient Neutron Diffusion Equations". PhD thesis. Massachusetts Institute of Technology, Dept. of Nuclear Engineering (cit. on pp. 16, 173).

Smith, K. S. (1986). "Assembly homogenization techniques for light water reactor analysis". In: *Progress in Nuclear Energy* 17.3, pp. 303 –335. doi: 10.1016/0149-1970(86)90035-1 (cit. on pp. 100, 102, 104, 113, 115, 130).

Smith, K. S., K.R. Rempe, J. D. Rhodes, and J. G. Stevens (1992). "Enhancements of the Studvick core management system". In: *Proceedings of the Topical Meeting on Advances in Reactor Physics*. Vol. 1. Charleston, SC, USA, pp. 117–128 (cit. on p. 65).

Stacey, W. M. (2007). *Nuclear Reactor Physics*. 2nd edition. Weinheim, Germany: John Wiley & Sons. doi: 10.1002/9783527611041 (cit. on pp. 4, 5, 14, 59, 84, 99).

Stewart, G. (2002). "A Krylov–Schur Algorithm for Large Eigenproblems". In: *SIAM Journal on Matrix Analysis and Applications* 23.3, pp. 601–614. doi: 10.1137/S0895479800371529 (cit. on p. 26).

Sun, S. and M. F. Wheeler (2005). "Symmetric and nonsymmetric discontinuous Galerkin methods for reactive transport in porous media". In: *SIAM Journal on Numerical Analysis* 43.1, pp. 195–219. doi: 10.1137/S003614290241708X (cit. on p. 109).

Theler, G. (2013). "Unstructured Grids and the Multigroup Neutron Diffusion Equation". In: *Science and Technology of Nuclear Installations* 2013. doi: 10.1155/2013/641863 (cit. on p. 16).

Trahan, T. J. and E. W. Larsen (2015). "Asymptotic, multigroup flux reconstruction and consistent discontinuity factors". In: *Journal of Nuclear Science and Technology* 52.7-8, pp. 917–931. doi: 10.1080/00223131.2015.1041568 (cit. on p. 100).

Turcksin, B. and J. C. Ragusa (2014). "Discontinuous diffusion synthetic acceleration for Sn transport on 2D arbitrary polygonal meshes". In: *Journal of Computational Physics* 274, pp. 356–369. doi: 10.1016/j.jcp.2014.05.044 (cit. on p. 129).

Turcksin, B., J. C. Ragusa, and W. Bangerth (2010). "Goal-oriented h-adaptivity for the multigroup SPn equations". In: *Nuclear Science and Engineering* 165.3, pp. 305–319 (cit. on p. 101).

Šolín, P., J. Červený, and I. Doležel (2008). "Arbitrary-level hanging nodes and automatic adaptivity in the hp-FEM". In: *Mathematics and Computers in Simulation* 77.1, pp. 117–132 (cit. on p. 60).

Velarde, G., C. Ahnert, and J. M. Aragonés (1978). "Analysis of the Eigenvalue in k, λ, γ, and α Applied to Some Fast- and Thermal-Neutron Systems". In: *Nuclear Science and Engineering* 66.3, pp. 284–294. doi: 10.13182/NSE78-A27213 (cit. on p. 13).

Verdú, G., D. Ginestar, V. Vidal, and J. L. Muñoz-Cobo (1994). "3D λ-modes of the neutron-diffusion equation". In: *Annals of Nuclear Energy* 21.7, pp. 405–421. doi: 10.1016/0306-4549(94)90041-8 (cit. on p. 16).

Verdú, G., D. Ginestar, V. Vidal, and J.L. Muñoz-Cobo (1995). "A consistent multidimensional nodal method for transient calculations". In: *Annals of Nuclear*

Energy 22.6, pp. 395–410. doi: 10.1016/0306-4549(94)00067-O (cit. on pp. 60, 178).

Verdú, G., R. Miró, D. Ginestar, and V. Vidal (1999). "The implicit restarted Arnoldi method, an efficient alternative to solve the neutron diffusion equation". In: *Annals of Nuclear Energy* 26.7, pp. 579–593. doi: 10.1016/S0306-4549(98)00077-2 (cit. on pp. 16, 26).

Verdú, G., D. Ginestar, R. Miró, and V. Vidal (2005). "Using the Jacobi–Davidson method to obtain the dominant Lambda modes of a nuclear power reactor". In: *Annals of Nuclear Energy* 32.11, pp. 1274–1296. doi: 10.1016/j.anucene.2005.03.002 (cit. on pp. 16, 26).

Vidal-Ferràndiz, A., R. Fayez, D. Ginestar, and G. Verdú (2014). "Solution of the Lambda modes problem of a nuclear power reactor using an h–p finite element method". In: *Annals of Nuclear Energy* 72, pp. 338–349. doi: 10.1016/j.anucene.2014.05.026 (cit. on pp. 17, 92, 114, 173).

Vidal-Ferràndiz, A., R. Fayez, D. Ginestar, and G. Verdú (2016a). "Moving meshes to solve the time-dependent neutron diffusion equation in hexagonal geometry". In: *Journal of Computational and Applied Mathematics* 291, pp. 197–208. doi: 10.1016/j.cam.2015.03.040 (cit. on p. 60).

Vidal-Ferràndiz, A., S. González-Pintor, D. Ginestar, G. Verdú, M. Asadzadeh, and C. Demazière (2016b). "Use of discontinuity factors in high-order finite element methods". In: *Annals of Nuclear Energy* 87, Part 2, pp. 728–738. doi: 10.1016/j.anucene.2015.06.021 (cit. on p. 101).

Vidal-Ferràndiz, A., S. González-Pintor, D. Ginestar, G. Verdú, and C. Demazière (2017). "Schwarz type preconditioners for the neutron diffusion equation". In: *Journal of Computational and Applied Mathematics* 309, pp. 563–574. doi: 10.1016/j.cam.2016.02.056 (cit. on p. 17).

Vidal-Ferràndiz, A., S. González-Pintor, D. Ginestar, G. Verdú, and C. Demazière (2018). "Pin-wise homogenization for SPN neutron transport approximation using the finite element method". In: *Journal of Computational and Applied Mathematics* 330 Supplement C, pp. 806–821. doi: 10.1016/j.cam.2017.06.023 (cit. on p. 101).

Wagner, M. R. and K. Koebke (1983). "Progress in nodal reactor analysis". In: *Atomkernenergie Kerntechnik. ANS topical meeting on advances in reactor computations; Salt Lake City, UT (USA)* 43.2, pp. 117–126 (cit. on pp. 100, 103, 130).

Wang, Y., W. Bangerth, and J. Ragusa (2009). "Three-dimensional h-adaptivity for the multigroup neutron diffusion equations". In: *Progress in Nuclear Energy* 51.3, pp. 543–555. doi: 10.1016/j.pnucene.2008.11.005 (cit. on pp. 16, 27, 31).

Wang, Y. and J. Ragusa (2009). "Application of hp adaptivity to the multigroup diffusion equations". In: *Nuclear Science and Engineering* 161.1, pp. 22–48. doi: 10.13182/NSE161-22 (cit. on p. 16).

Wang, Yaqi and Jean C Ragusa (2010). "Diffusion Synthetic Acceleration for High-Order Discontinuous Finite Element SN Transport Schemes and Application to Locally Refined Unstructured Meshes". In: *Nuclear Science and Engineering* 166.2, pp. 145–166. doi: 10.13182/NSE09-46 (cit. on p. 129).

Weinberg, A. M., P. Wigner, and E. K. Wigner (1958). *The physical theory of neutron chain reactors*. Chicago, USA: University of Chicago Press (cit. on p. 6).

Williams, Samuel, Leonid Oliker, Richard Vuduc, John Shalf, Katherine Yelick, and James Demmel (2007). "Optimization of Sparse Matrix-vector Multiplication on Emerging Multicore Platforms". In: *Proceedings of the 2007 ACM/IEEE Conference on Supercomputing*. SC '07. Reno, Nevada: ACM, 38:1–38:12. doi: 10.1145/1362622.1362674 (cit. on p. 43).

Yamamoto, A. (2004). "A Simple and Efficient Control Rod Cusping Model for Three-Dimensional Pin-by-Pin Core Calculations". In: *Nuclear Technology* 145.1, pp. 11–17. doi: 10.13182/NT145-11 (cit. on p. 64).

Yamamoto, A., T. Sakamoto, and T. Endo (2016). "Discontinuity Factors for Simplified P3 Theory". In: *Nuclear Science and Engineering* 183.1, pp. 39–51. doi: 10.13182/NSE15-102 (cit. on pp. 101, 124).

Yu, L. and Y. Chao (2015). "A unified generic theory on discontinuity factors in diffusion, SP_3 and transport calculations". In: *Annals of Nuclear Energy* 75, pp. 239–248 (cit. on p. 101).

Yu, L., D. Lu, and Y. A. Chao (2014). "The calculation method for SP3 discontinuity factor and its application". In: *Annals of Nuclear Energy* 69, pp. 14–24. doi: 10.1016/j.anucene.2014.01.032 (cit. on pp. 101, 124).

Zhang, Y., J. C. Ragusa, and J. E. Morel (2013). "Iterative performance of various formulations of the SPN equations". In: *Journal of Computational Physics* 252, pp. 558–572. doi: 10.1016/j.jcp.2013.06.009 (cit. on p. 101).

Zienkiewicz, O. C., R. L. Taylor, and J. Z. Zhu (2005). *The finite element method: its basis and fundamentals*. 7th Edition. Oxford: Butterworth-Heinemann. doi: 10.1016/B978-1-85617-633-0.00001-0 (cit. on pp. 19, 22, 62, 67).

A

Analytic Solution of an Homogeneous Reactor

A two dimensional rectangular homogeneous reactor with two energy groups cross sections is considered. The Lambda modes problem related to the neutron diffusion equation in a two-dimensional domain, $(x,\ y)$, is defined as

$$\begin{aligned} -\vec{\nabla} D_1 \vec{\nabla}\phi_1(x,\ y) + (\Sigma_{a1} + \Sigma_{12})\,\phi_1(x,\ y) &= \frac{1}{\lambda}\left(\nu\Sigma_{f1}\phi_1(x,\ y) + \nu\Sigma_{f2}\phi_2(x,\ y)\right)\,, \\ -\Sigma_{12}\phi_1(x,\ y) - \vec{\nabla} D_2 \vec{\nabla}\phi_2(x,\ y) + \Sigma_{a2}\phi_2(x,\ y) &= 0\,, \\ (x,\ y) &\in [0, L_1] \times [0, L_2]\,, \end{aligned} \tag{A.1}$$

with zero flux boundary conditions

$$\phi_g(0, y) = \phi_g(L_1, y) = 0\,, \qquad \phi_g(x, 0) = \phi_g(x, L_2) = 0\,, \qquad g = 1,\ 2\,. \tag{A.2}$$

Using the variables separation method,

$$\phi_g(x, y) = X_g(x) Y_g(y), \tag{A.3}$$

where X_g and Y_g are solutions of

$$\frac{\mathrm{d}^2 X_g}{\mathrm{d}x^2}(x) = \mu_x X_g(x), \qquad \frac{\mathrm{d}^2 Y_g}{\mathrm{d}y^2}(y) = \mu_y Y_g(y), \tag{A.4}$$

satisfying,

$$X_g(0) = X_g(L_1) = Y_g(0) = Y_g(L_2) = 0\,. \tag{A.5}$$

Thus, these functions have the general form,

$$\begin{aligned} X_g &= A_{g,x}\cos(\mu_x x) + B_{g,x}\sin(\mu_x x)\ , \\ Y_g &= A_{g,y}\cos(\mu_y y) + B_{g,y}\sin(\mu_y y)\,. \end{aligned} \tag{A.6}$$

Applying the boundary conditions defined in equation (A.2), it is found that

$$X(x) = B_{g,x}\sin\left(\frac{n\pi}{L_1}\right)\ , \qquad \mu_x = \frac{n\pi}{L_1}\,, \tag{A.7}$$

$$Y(y) = B_{g,y}\sin\left(\frac{m\pi}{L_2}\right)\ , \qquad \mu_x = \frac{m\pi}{L_2}\,, \tag{A.8}$$

and

$$\mu^2 = \mu_x^2 + \mu_y^2\,, \tag{A.9}$$

with $n, m \in \mathbb{N}$. Different values of n, m correspond to the different eigenvalues and eigenfunctions of the reactor. Using equation (A.3),

$$\phi_g(x,\ y) = k_g\sin(\mu_x)\sin(\mu_y)\,. \tag{A.10}$$

The equation (A.1) implies

$$\phi_1(x,y) = \frac{D_2\mu^2 + \Sigma_{a2}}{\Sigma_{12}}\,\phi_2(x,\ y)\,. \tag{A.11}$$

Solving the eigenvalue from equation (A.1), it is obtained

$$\lambda = \frac{\nu\Sigma_{f1}\left(D_2\mu^2 + \Sigma_{a2}\right) + \nu\Sigma_{f2}\Sigma_{12}}{\left(D_2\mu^2 + \Sigma_{a2}\right)\left(\Sigma_{a1} + \Sigma_{12} + D_1\mu^2\right)} \tag{A.12}$$

with the eigenfunctions

$$\phi_1(x,\ y) = k\left(\frac{D_2\mu^2 + \Sigma_{a2}}{\Sigma_{12}}\right)\sin(\mu_x x)\sin(\mu_y y)\,, \tag{A.13}$$

$$\phi_2(x,\ y) = k\sin(\mu_x x)\sin(\mu_y y)\,. \tag{A.14}$$

As the fluxes are defined up to a multiplicative constant k, these should be normalized with the criterion exposed in equation (3.28),

$$\begin{aligned} 1 &= \frac{1}{V_t}\int_V \left(\Sigma_{f1}|\phi_1| + \Sigma_{f2}|\phi_2|\right)\mathrm{d}V = \\ &= \frac{1}{L_1 L_2}\left(\Sigma_{f1}\frac{D_2\mu^2 + \Sigma_{a2}}{\Sigma_{12}} + \Sigma_{f2}\right)\int_0^{L_1}\mathrm{d}x\int_0^{L_2}\mathrm{d}y\,|\phi_2|\,. \end{aligned} \tag{A.15}$$

Hence, the normalized magnitudes obtained are

$$\phi_1(x,\, y) = \left(\frac{D_2\mu^2 + \Sigma_{a2}}{\Sigma_{f1}D_2\mu^2 + \Sigma_{f1}\Sigma_{a2} + \Sigma_{f2}\Sigma_{12}}\right)\left(\frac{\pi^2}{4}\right)\sin\left(\frac{n\pi}{L_1}x\right)\sin\left(\frac{m\pi}{L_2}y\right), \tag{A.16}$$

$$\phi_2(x,\, y) = \left(\frac{\Sigma_{12}}{\Sigma_{f1}D_2\mu^2 + \Sigma_{f1}\Sigma_{a2} + \Sigma_{f2}\Sigma_{12}}\right)\left(\frac{\pi^2}{4}\right)\sin\left(\frac{n\pi}{L_1}x\right)\sin\left(\frac{m\pi}{L_2}y\right), \tag{A.17}$$

$$P(x,\, y) = (\Sigma_{f1}\phi_1 + \Sigma_{f2}\phi_2) = \frac{\pi^2}{4}\sin\left(\frac{n\pi}{L_1}x\right)\sin\left(\frac{m\pi}{L_2}y\right). \tag{A.18}$$

This proves that the normalized neutron distribution in a homogeneous reactor does not depend on the nuclear properties of the material.

B

Benchmarks Definitions

Mathematical benchmarks, based on well defined problems with a complete set of input data and a unique solution, are widely used and accepted means of verifying the reliability of numerical simulations, i.e. to validate the accuracy, stability and efficiency of numerical nuclear codes. Problems are often very testing, but tend to be somewhat simplified, in order to make the analysis manageable to compare different models. Several realistic benchmarks have been defined in the literature. For completion purposes the definitions of the benchmarks used in this thesis are reproduced in here.

B.1 One Dimensional Homogeneous Reactor

A one dimensional homogeneous slab of 2 cm thick with vacuum boundary conditions is considered as Figure B.1. Its one-group nuclear cross sections are defined in Table B.1. This benchmark has the analytic solution for the full transport solution and the P_N approximations discussed in Capilla et al., (2005). This problem is also relevant because it shows a bad behaviour in the diffusions approximation because of the strong spatial variation of the neutronic flux.

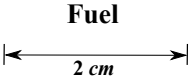

Figure B.1: Definition for the 1D homogeneous slab.

Table B.1: Cross Sections for the 1D reactor.

Material	Σ_t (1/cm)	Σ_s (1/cm)	$\nu\Sigma_f$ (1/cm)
Fuel	1.000	0.334	0.178

B.2 One Dimensional Heterogeneous Reactor

A more realistic example of a one dimensional problem is composed of a seven-region slab 18 cm thick, with vacuum boundary conditions for the leftmost and rightmost faces. The slab is comprised of a combination of fuel and reflector materials, as shown in Figure B.2. The reactor is solved with one energy group cross-sections shown in Table B.2.

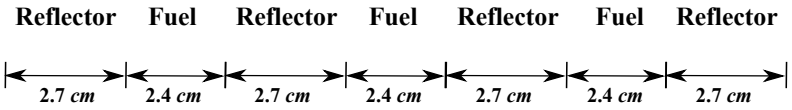

Figure B.2: One dimensional slab material disposition.

Table B.2: Cross Sections for the 1D reactor.

Material	Σ_t (1/cm)	Σ_s (1/cm)	$\nu\Sigma_f$ (1/cm)
Fuel	0.416667	0.334	0.178
Reflector	0.370370	0.334	0.000

B.3 One Dimensional Rod Ejection Problem

To validate the transient codes a simple and small one-dimensional reactor is defined. The reactor geometry is defined in Figure B.3 and the cross sections for the materials of each region are given in Table B.3. Precursor parameters and neutron velocities are given in Table B.4. Zero flux boundary conditions are imposed at the boundaries of the system.

The defined transient simulates a simplified model for a rod-ejection accident. The transient starts removing the control rod from time $0.0\,s$ to $4.0\,s$ with a constant velocity of $25\ cm/s$. Then the control rod is inserted again from $4.0\,s$ to $10\,s$ also with a constant velocity of $25\ cm/s$.

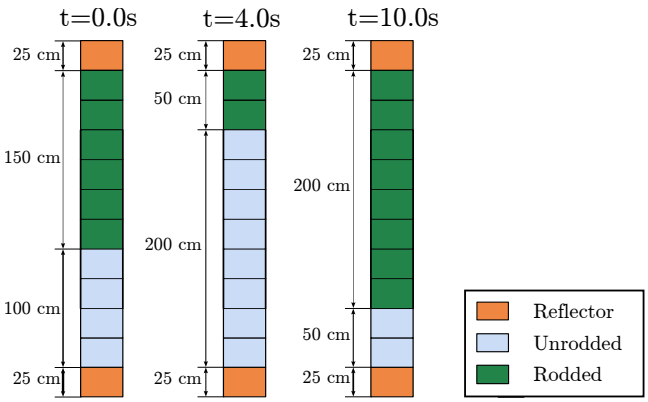

Figure B.3: Geometry of the 1D reactor problem.

Table B.3: Cross sections of the materials of the 1D reactor.

Material	g	$\mathbf{D_g}$ (cm)	$\boldsymbol{\Sigma_{ag}}$ (1/cm)	$\boldsymbol{\nu\Sigma_{fg}}$ (1/cm)	$\boldsymbol{\Sigma_{fg}}$ (1/cm)	$\boldsymbol{\Sigma_{12}}$ (1/cm)
Unrodded	1	1.40343	1.17659e−2	5.62285e−3	2.20503e−3	1.60795e−2
	2	0.32886	1.07186e−1	1.45865e−1	5.90546e−2	
Rodded	1	1.40343	1.17659e−2	5.60285e−3	2.19720e−3	1.60795e−2
	2	0.32886	1.07186e−1	1.45403e−1	5.88676e−2	
Reflector	1	0.93344	2.81676e−3	0.00000e+0	0.00000e+0	1.08805e−2
	2	0.95793	8.87200e−2	0.00000e+0	0.00000e+0	

Table B.4: Neutron precursors parameters for the reactor.

	Group 1	Group 2	Group 3	Group 4	Group 5	Group 6
β_p	0.000247	0.0013845	0.001222	0.026455	0.000832	0.000169
$\lambda_p\ (1/s)$	0.0127	0.0317	0.115	0.311	1.4	3.87
	$\mathrm{v}_1 = 1.27 \times 10^7$ cm/s		$\mathrm{v}_2 = 2.5 \times 10^5$ cm/s		$\beta = 0.0065$	

B.4 One Dimensional C5G7 Reactor

To study the performance of the homogenization methods, two different one-dimensional reactor configurations based on the C5G7 benchmark (Lewis et al., 2001) are defined. The first configuration is comprised of two assemblies and the second configuration has five assemblies of 21.42 cm wide with reflective boundary conditions as Figure B.4 shows. Each assembly consists of 17 pins of 1.26 cm wide, each pin is made of a layer of nuclear fuel of 1.08 cm, surrounded by a thin layer of water of 0.09 cm. The particular composition of each one of the assemblies can be found in Figure B.5 and the pins composition is presented in Figure B.6. Seven energy group cross sections for every material can be found in reference Lewis et al., (2001).

(a) Configuration 1

(b) Configuration 2

Figure B.4: Reactor configurations.

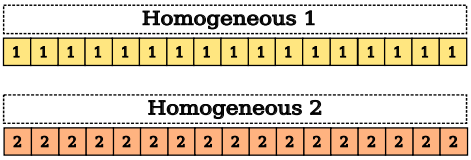

(a) Assemblies for Configuration 1

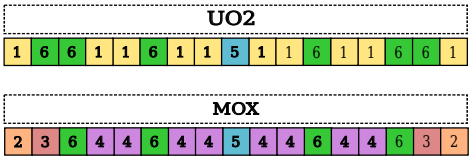

(b) Assemblies for Configuration 2

Figure B.5: Assemblies composition.

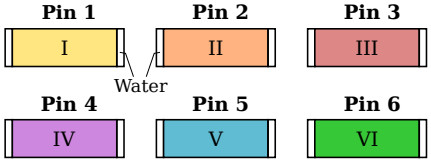

Figure B.6: Pins composition.

B.5 One Dimensional BWR Problems

One dimensional BWR problems composed of seven assemblies with heterogeneous pins extracted from Rahnema and Nichita, (1997). The reactor has three different configurations constructed by combining three different assemblies to represent a BWR assembly. The geometry of the assemblies and their configurations are shown in Figure B.7. Cross sections for each region of these assemblies are given in Table B.5. Configurations are sort by heterogeneities between assemblies. Configuration 1 is composed of similar assemblies, Configuration 2 puts together heterogeneous assemblies and Configuration 3 joins very heterogeneous assemblies in an artificial way, which is used to test the method in an extreme heterogeneous situation. Zero-current boundary conditions are imposed at the edges of the system.

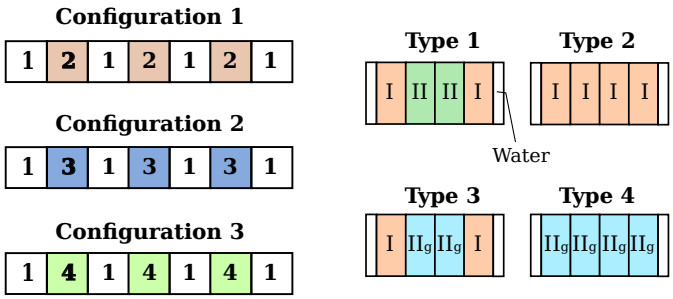

Figure B.7: Core and assemblies configurations for the 1D benchmark problems.

Table B.5: Material properties for the 1D BWR benchmark.

Material	Thickness (cm)	g	D_g (cm)	Σ_{ag} (1/cm)	$\nu\Sigma_{fg}$ (1/cm)	Σ_{12} (1/cm)
Water	1.158	1	1.7639	0.0003	0.0000	0.0380
		2	0.2278	0.0097	0.0000	
Fuel I	3.231	1	1.4730	0.0096	0.0067	0.0161
		2	0.3294	0.0764	0.1241	
Fuel II	3.231	1	1.4804	0.0101	0.0078	0.0156
		2	0.3362	0.0901	0.1542	
Fuel IIg	3.231	1	1.5342	0.0135	0.0056	0.0136
		2	0.3143	0.4873	0.0187	

B.6 Two Dimensional BIBLIS Reactor

The two dimensional BIBLIS problem is a realistic and highly non-separable 2-group problem representative of an actual operating pressurised water reactor (PWR). This problem is characterized by a *chequerboard effect* caused by fuel reloading. The realistic nature of this problem makes it an attractive test for coarse-mesh methods and it has already been used by several authors as Hébert, (1985); Smith, (1979); Müller and Weiss, (1991) and Vidal-Ferràndiz et al., (2014).

257 homogenized assemblies with widths of 23.1226 cm are present in the core including 64 cells modelling the reflector. Vacuum boundary conditions are applied at the external boundary. The definition of the 8 different materials and their cross sections are given in Figure B.8 and Table B.6. Reference solution for the fundamental mode are extracted from Müller and Weiss, (1991).

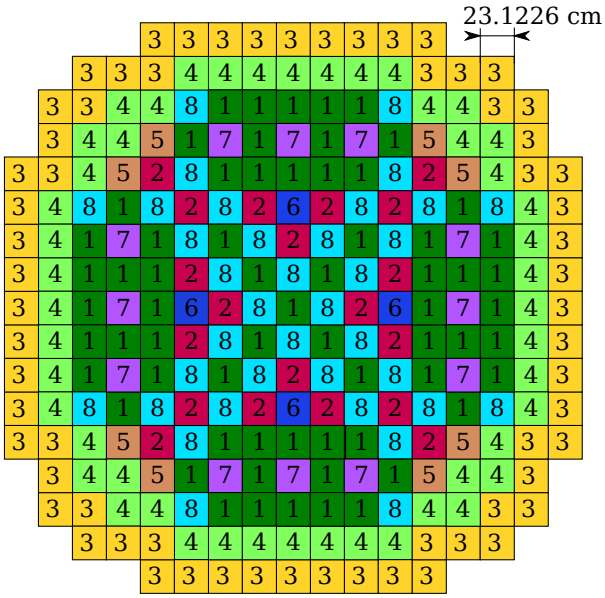

Figure B.8: BIBLIS reactor materials definition.

Table B.6: Macroscopic cross sections of the BIBLIS 2D reactor.

Material	**g**	$\mathbf{D_g}$ (cm)	$\boldsymbol{\Sigma_{ag}}$ (1/cm)	$\boldsymbol{\nu\Sigma_{fg}}$ (1/cm)	$\boldsymbol{\Sigma_{fg}}$ (1/cm)	$\boldsymbol{\Sigma_{12}}$ (1/cm)
1	1	1.4360	0.0095042	0.0058708	0.0023768	0.017754
	2	0.3635	0.0750580	0.0960670	0.0388940	
2	1	1.4366	0.0096785	0.0061908	0.0025064	0.017621
	2	0.3636	0.0784360	0.1035800	0.0419350	
3	1	1.3200	0.0026562	0.0000000	0.0000000	0.023106
	2	0.2772	0.0715960	0.0000000	0.0000000	
4	1	1.4389	0.0103630	0.0074527	0.0030173	0.017101
	2	0.3638	0.0914080	0.1323600	0.0535870	
5	1	1.4381	0.0100030	0.0061908	0.0025064	0.017290
	2	0.3665	0.0848280	0.1035800	0.0419350	
6	1	1.4385	0.0101320	0.0064285	0.0026026	0.017192
	2	0.3665	0.0873140	0.1091100	0.0441740	
7	1	1.4389	0.0101650	0.0061908	0.0025064	0.017125
	2	0.3679	0.0880240	0.1035800	0.0419350	
8	1	1.4393	0.0102940	0.0064285	0.0026026	0.017027
	2	0.3680	0.0905100	0.1091100	0.0441740	

B.7 2D CISE Benchmark

To evaluate the homogenization performance of the presented homogenization strategies a set two-dimensional test problems based in the CISE benchmark (Rahnema and Nichita, 1997) is chosen. The layout for the CISE core together with the assembly definition are shown in Figure B.10, while the cross sections for the blade, water, fresh nuclear fuel (fuel A) and depleted nuclear fuel (fuel B) used in the tests are given in Table B.7. ν is considered constant for all materials and energy groups.

Table B.7: Cross section values for CISE benchmarks.

Material	$\mathbf{D_1}$ (cm)	$\mathbf{D_2}$ (cm)	$\boldsymbol{\Sigma_{a1}}$ (1/cm)	$\boldsymbol{\Sigma_{a2}}$ (1/cm)	$\boldsymbol{\Sigma_{12}}$ (1/cm)	$\boldsymbol{\nu\Sigma_{f1}}$ (1/cm)	$\boldsymbol{\nu\Sigma_{f2}}$ (1/cm)
Water	2.0000	0.3000	0.0000	0.0100	0.0400	0.0000	0.0000
Fuel A	1.8000	0.5500	0.0080	0.0850	0.0120	0.0060	0.1100
Fuel B	1.8000	0.5500	0.0080	0.0850	0.0120	0.0050	0.1000
Blade	3.0000	0.1500	0.0800	1.0000	0.0000	0.0000	0.0000

Three problems are defined based on the CISE benchmark. First, a small subset composed by four assemblies surrounding an inserted control blade is considered, together with reflective boundary conditions. The geometry for the proposed problem, named *Small CISE*, is shown in Figure B.9a. Within this problem, the heterogeneities considered inside the reactor are taken into account. In order to analyse the method against a more heterogeneous problem, a non-realistic problem, called *Modified Small CISE*, is defined (see Figure B.9b). This problem is similar to the small CISE, but the control blade inside the assemblies defined with material A is removed. This causes the flux to have an strong gradient on the interfaces, thus being more challenging for the homogenization procedure to preserve the properties of the original problem. The third problem to be considered is the original whole core CISE reactor (see Figure B.10), together with zero-flux boundary conditions.

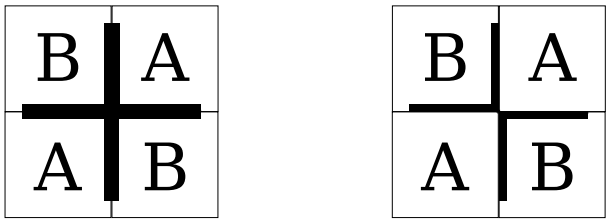

(a) Small CISE **(b)** Modified small CISE

Figure B.9: Definition of subsets of the CISE reactor

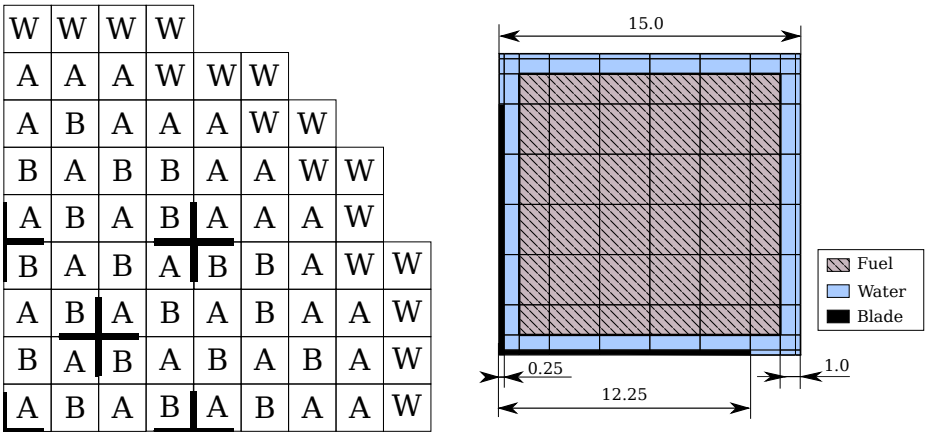

(a) Quarter of the whole core CISE reactor composition.

(b) Detailed view of the mesh used for the fine mesh heterogeneous calculation.

Figure B.10: CISE core and assembly definition.

B.8 3D IAEA PWR Reactor

The IAEA 3-D PWR problem has been a standard benchmark problem to measure the performance of neutron transport calculation methods. Its definition along with its reference results are found in (American Nuclear Society, 1977). This benchmark has been solved in numerous articles e.g. Cossa, Giusti, and Montagnini, (2010), Barrault et al., (2011) and González-Pintor, Ginestar, and Verdú, (2012). The core is composed by 177 fuel assemblies including nine fully rodded fuel assemblies and four partially rodded fuel assemblies. 64 reflector assemblies surround the core. The fuel assembly pitch is 20 cm and the active height of a fuel assembly is 340 cm. The thickness of axial reflector is 20cm. The definition of this reactor is given in Figure B.11 and the cross sections of the different materials are shown in Table B.8. The average number of neutrons born per fission, ν, is considered constant for all materials and energy groups. Albedo boundary conditions are used with a extrapolation distance of $2.13 \times D_g$.

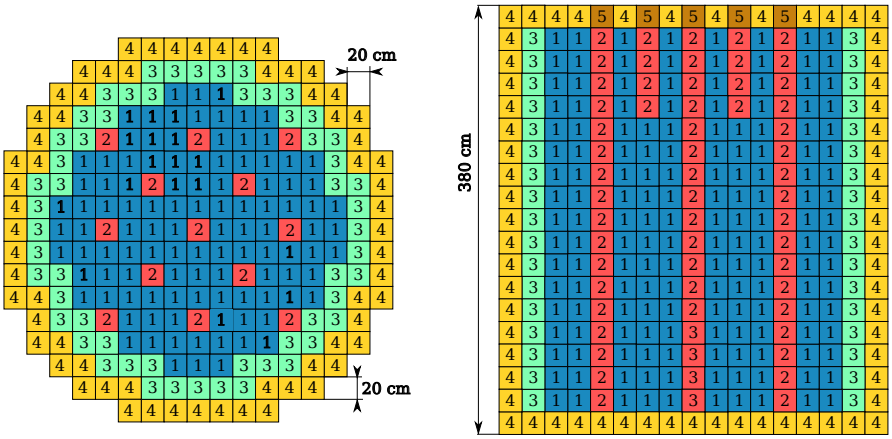

Figure B.11: Geometry and material definition of the IAEA 3D Reactor.

Table B.8: Macroscopic cross sections of the IAEA 3D reactor.

Material	$\mathbf{D_1}$ (cm)	$\mathbf{D_2}$ (cm)	$\boldsymbol{\Sigma_{a1}}$ (1/cm)	$\boldsymbol{\Sigma_{a2}}$ (1/cm)	$\boldsymbol{\Sigma_{s12}}$ (1/cm)	$\boldsymbol{\nu\Sigma_{f1}}$ (1/cm)	$\boldsymbol{\nu\Sigma_{f2}}$ (1/cm)
1 Fuel	1.50	0.40	0.010	0.085	0.020	0.00	0.135
2 Rodded Fuel	1.50	0.40	0.010	0.130	0.020	0.00	0.135
3 Exterior Fuel	1.50	0.40	0.010	0.080	0.020	0.00	0.135
4 Reflector	2.00	0.30	0.000	0.010	0.040	0.00	0.000
5 Rodded Reflector	2.00	0.30	0.000	0.055	0.040	0.00	0.000

B.9 3D Langenbuch Reactor

The Langenbuch reactor is a three dimensional small reactor composed of 77 fuel assemblies and 40 modelling the reflector as it is shown in Figure B.12. The assemblies have a size of 20×20 cm. Zero flux boundary values are applied at the frontier of the reactor. This problem is characterized by its small size for a three dimensional reactor and its symmetrical configuration. The fast resolution of the reactor makes it an attractive test. The reactor was defined in Langenbuch, Maurer, and Werner, (1977) and it has already been used by several authors as Verdú et al., (1995), Miró et al., (2002) and Bernal et al., (2014). The materials cross sections are exposed in Table B.9. ν is considered constant for all materials and energy groups. The transient was initiated by the withdrawal of a bank of four partially inserted control rods at a rate of 3 cm/s over $0 \geq t \geq 26.7$ s. A second bank of control rods is inserted at the same rate over $7.5 \geq t \geq 47.5$ s.

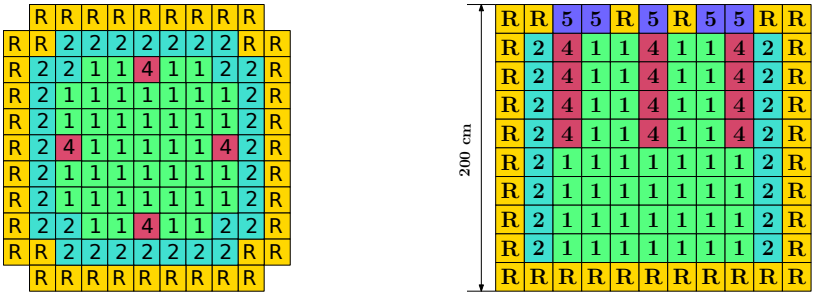

(a) Plant definition. **(b)** Axial definition

Figure B.12: Geometry and material definition of the Langenbuch 3D Reactor.

Table B.9: Cross sections definition of the Langenbuch reactor.

Material	Group	D_g (cm)	Σ_{ag} (1/cm)	$\nu\Sigma_{fg}$ (1/cm)	Σ_{s12} (1/cm)
1 – Fuel	1	1.423913	0.010402060	0.006477691	0.01755550
	2	0.356306	0.087662170	0.112732800	
2 – Fuel	1	1.425611	0.010992630	0.007503284	0.13780040
	2	0.350574	0.099256340	0.017177680	
3 – Absorbent	1	1.423913	0.010952060	0.006477691	0.11273228
	2	0.356306	0.091462170	0.017555500	
4 –Reflector	1	1.634227	0.002660573	0.000000000	0.02759693
	2	0.264002	0.049363510	0.000000000	

B.10 3D Small Hexagonal Rector

In order to test the codes in hexagonal reactors for static and time dependent applications a three dimension small reactor is defined. Figure B.13 shows the layout map of the core composed of 19 hexagonal assemblies, for which the hexagonal lattice pitch is 23.6 cm. The height of the reactor is 300 cm and 12 axial planes are considered, each one of 25 cm. The cross sections of the different materials composing the reactor are given in Table B.10. No data of Σ_{fg} is given because ν is considered constant for all materials and energy groups. The neutron precursors data used in this problem are given in Table B.11. Albedo boundary conditions are applied on the outer edge of the reflector cells. Extrapolation length is set to $2 \times D_g$.

The defined transient simulates a rod ejection accident as follows. Starting from the initial configuration, see Figure B.13, the rod 23 begins to be removed until it is completely removed at time $t = 0.15$ s remaining only the unrodded fuel. From $t = 0.15$ s until $t = 1.0$ s nothing happens. Then, the security system acts inserting the rods 22 at constant velocity of 25 cm/s until the bottom of the reactor is reached at $t = 9.0$ s.

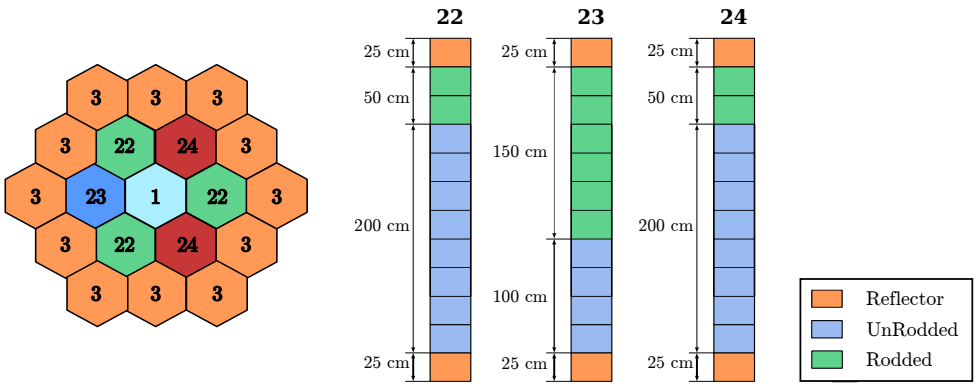

(a) Core definition. **(b)** Rods definition.

Figure B.13: Small 3D reactor geometry.

Table B.10: Cross section definition for the small 3D reactor.

Material	g	D_g (cm)	Σ_{ag} (1/cm)	$\nu\Sigma_{fg}$ (1/cm)	Σ_{fg} (1/cm)	Σ_{12} (1/cm)
Unrodded	1	1.40343	1.17659e-2	5.62285e-3	2.20504e-3	1.60795e-2
	2	0.32886	1.07186e-1	1.45865e-1	6.00267e-2	
Rodded	1	1.36764	1.39118e-2	5.37719e-3	2.10870e-3	1.35108e-2
	2	0.25108	9.96214e-2	1.15403e-1	4.74909e-2	
Reflector	1	0.93344	2.81676e-3	0.00000e+0	0.00000e+0	1.08805e-2
	2	0.95793	8.87200e-2	0.00000e+0	0.00000e+0	

Table B.11: Neutron precursors parameters for the reactor.

	Group 1	Group 2	Group 3	Group 4	Group 5	Group 6
β_p	0.000247	0.0013845	0.001222	0.026455	0.000832	0.000169
$\lambda_p\ (1/s)$	0.0127	0.0317	0.115	0.311	1.4	3.87
	$v_1 = 1.27 \times 10^7$ cm/s		$v_2 = 2.5 \times 10^5$ cm/s		$\beta = 0.0065$	

B.11 3D AER Benchmark

This benchmark corresponds to an asymmetric control rod ejection accident in a VVER-440 core. A plane of this reactor showing the geometry of the reactor and the disposition of materials together with the initial position of control rods are shown in Figure B.14. The hexagonal lattice pitch is 14.7 cm. Vacuum boundary conditions are applied at the frontier of the reactor. Cross section data are given in Table B.12. ν is considered constant for all materials and energy groups. Neutron precursors data are given in Table B.11.

The transient is defined as follows. The control rod denoted by number 26 is ejected in the first 0.08 seconds. Then, scram is initiated inserting the safety rods 23 and 25 at 1.0 s with constant velocity, the bottom position is reached at 11.0 s. The drop of control rod group 21 is also started at 1.0 s with the same velocity.

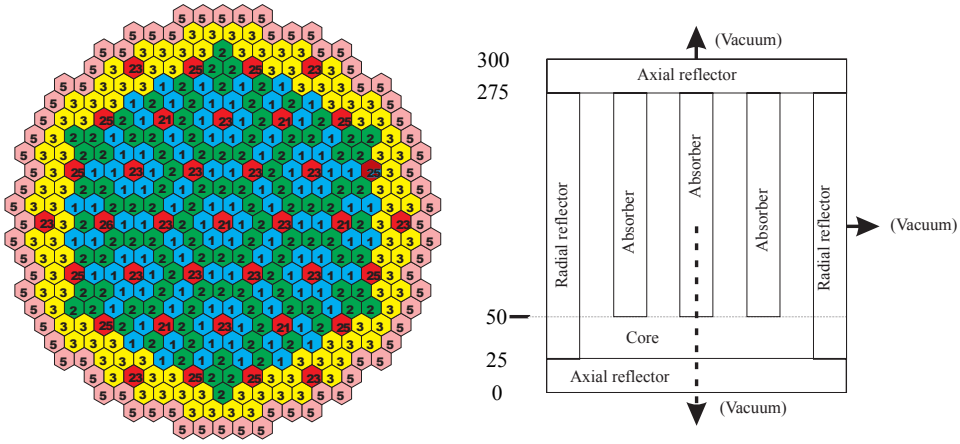

Figure B.14: Geometry of VVER 440 reactor core.

Table B.12: Cross section definition for the VVER 440.

Material	**g**	$\mathbf{D_g}$ (cm)	$\boldsymbol{\Sigma_{ag}}$ (1/cm)	$\boldsymbol{\nu\Sigma_{fg}}$ (1/cm)	$\boldsymbol{\Sigma_{12}}$ (1/cm)
1 – Fuel	1	1.3466	8.3620e−3	4.4339e−3	1.6893e−2
	2	3.7169e−1	6.4277e−2	7.3503e−2	
2 – Fuel	1	1.3377	8.7970e−3	5.5150e−3	1.5912e−2
	2	3.6918e−1	7.9361e−2	1.0545e−1	
3 – Fuel	1	1.3322	9.4700e−3	7.0120e−3	1.4888e−2
	2	3.6502e−1	1.0010e−1	1.4908e−1	
4 – Absorber	1	1.1953	1.3372e−2	0.0000	2.2264e−2
	2	1.9313e−1	1.3498e−1	0.0000	
5 – Radial Refl.	1	1.4485	9.2200e−2	0.0000	3.2262e−2
	2	2.5176e−1	3.2839e−2	0.0000	
6 – Axial Refl.	1	1.3413	2.1530e−3	0.0000	2.7148e−2
	2	2.4871e−1	6.4655e−2	0.0000	

The neutron transport equation describes the neutron population inside a nuclear reactor core. The stationary neutron diffusion equation is studied, the most useful approximation of the transport equation. This approximation leads to a differential eigenvalue problem. To solve the neutron diffusion equation a h-p finite element method is investigated.

Once the steady state neutron distribution is obtained, it is used as initial condition for the time integration of the diffusion equation. To test the behaviour of the method rod ejection accidents are numerically simulated. However, a non-physical behaviour appears when a cell is partially rodded, the rod cusping effect, which is solved using a moving mesh scheme. In other words, the mesh follows the movement of the control rod. Numerical results show that the rod cusping effect is corrected with this scheme.

After that, the simplified spherical harmonics approximation, SPN, is developed. This approximation extends the spherical harmonics approximation in one dimensional geometries to multidimensional geometries with strong assumptions. It improves the diffusion theory results but does not converge as N tends to infinity. The advantages and limitations of this approximation are tested on several reactors.

Finally, the spatial homogenization in the context of the finite element method is studied. Homogenization consists in replacing heterogeneous subdomains by homogeneous ones, in such a way that the homogenized problem provides fast and accurate average results. Discontinuous solutions are proposed in the Generalized Equivalence Theory. Here, a discontinuous Galerkin finite element method using interior penalty terms is developed. Also, the use of discontinuity factors for the correction of the homogenization error when using the SPN equations is investigated.